





# Grid integration aspects of wave energy



**Ollscoil  
Mhá Nuad**

Ollscoil na hÉireann  
Má Nuad

**Hafiz Ahsan Said**

A thesis submitted for the degree of  
*Doctor of Philosophy*

Maynooth University

Faculty of Science and Engineering, Electronic Engineering Department  
Centre for Ocean Energy Research

January 2024

Head of the department: Prof. Gerard Lacey  
Supervisor: **Prof. John V. Ringwood**



# Contents

<b>Abstract</b>	<b>v</b>
<b>Declaration of authorship</b>	<b>ix</b>
<b>Acknowledgements</b>	<b>xi</b>
<b>List of Figures</b>	<b>xiii</b>
<b>List of Tables</b>	<b>xix</b>
<b>List of acronyms</b>	<b>xxi</b>
<b>1 Introduction</b>	<b>1</b>
1.1 Motivation of the thesis . . . . .	2
1.2 Contributions of the thesis . . . . .	4
1.2.1 List of publications . . . . .	6
1.3 Thesis layout . . . . .	7
<b>I Combined resource exploitation and value of wave energy on the electricity grid</b>	<b>11</b>
<b>2 Combined resource exploitation: An Irish case study</b>	<b>13</b>
2.1 Resource data collation and power generation . . . . .	15
2.1.1 Choice of locations for data collection . . . . .	15
2.1.2 Wave data and power generation . . . . .	16
2.1.3 Tidal data and power generation . . . . .	17
2.1.4 Wind data and power generation . . . . .	18
2.1.5 Solar data and power generation . . . . .	19
2.2 Temporal complementarity analysis . . . . .	20
2.2.1 Total variation complementarity index . . . . .	20
2.2.2 Variance complementarity index . . . . .	21
2.2.3 Standard deviation complementarity index . . . . .	21
2.2.4 Complementarity results: An Irish case study . . . . .	21
2.3 Energy balance and balancing cost analysis . . . . .	24
2.4 Conclusions . . . . .	28

<b>II Preliminaries and state-of-the-art</b>	<b>31</b>
<b>3 Grid integration of wave energy and the associated power conversion system</b>	<b>33</b>
3.1 Typical wave energy conversion system . . . . .	33
3.1.1 Absorption . . . . .	34
3.1.2 PTO systems . . . . .	38
3.1.3 Power Conditioning . . . . .	40
3.2 The electric grid . . . . .	43
3.2.1 Grid operator's requirements . . . . .	47
3.3 Conclusions . . . . .	49
<b>4 Hydrodynamic WEC modelling</b>	<b>51</b>
4.1 Ocean waves . . . . .	53
4.1.1 Regular waves . . . . .	53
4.1.2 Irregular waves . . . . .	54
4.2 Linear WEC modelling . . . . .	55
4.2.1 Navier-Stokes equations . . . . .	56
4.2.2 Linear potential flow theory . . . . .	56
4.2.3 Cummins' equation . . . . .	61
4.2.4 Radiation convolution term approximation . . . . .	62
4.2.5 WEC state-space representation . . . . .	63
4.3 Hydrodynamic models: state-of-the-art . . . . .	64
4.4 Conclusions . . . . .	65
<b>5 Electrical systems modelling</b>	<b>67</b>
5.1 LPMG and Gen-SC model . . . . .	68
5.1.1 Park Transformation . . . . .	71
5.2 Grid-side converter (Grid-SC) model . . . . .	73
5.3 Ultra-capacitor-based storage subsystem model . . . . .	73
5.3.1 DC-DC buck-boost converter model . . . . .	74
5.4 Complete electrical system model . . . . .	75
5.5 Conclusions . . . . .	76
<b>III High-performance W2G control of a WEC</b>	<b>77</b>
<b>6 Device-side control</b>	<b>79</b>
6.1 Hydrodynamic control of a WEC . . . . .	80
6.1.1 Reactive controller: Impedance-matching principle . . . . .	80
6.1.2 Passive damping controller . . . . .	83
6.2 LiTe-Con . . . . .	83

6.2.1	Dynamic constraint handling mechanism: LiTe-Con+	86
6.3	Lyapunov-based Gen-SC Controller	90
6.3.1	Stability analysis	91
6.4	Results	92
6.5	Conclusions	97
<b>7</b>	<b>Storage and grid-side control</b>	<b>99</b>
7.1	Lyapunov-based Grid-SC controller	100
7.1.1	Grid Synchronisation and phase-locked loop	102
7.2	Storage system controller	103
7.3	Stability analysis	104
7.4	Energy management system	105
7.5	Results	107
7.6	Conclusions	111
<b>8</b>	<b>On the reactive power requirements of reactive hydrodynamic WEC control</b>	<b>113</b>
8.1	Reactive power peak phenomena	114
8.1.1	Notation and conventions	116
8.2	Optimal WEC control	116
8.2.1	Reactive PI control	117
8.3	Reactive power peak analysis	118
8.3.1	Preliminaries	119
8.3.2	Instantaneous power calculations	120
8.3.3	Energy results	125
8.4	Illustrative case studies	126
8.4.1	Matched cases	127
8.4.2	Mismatched cases	128
8.5	Discussion	135
8.5.1	Discussion of results	135
8.5.2	Effect of a non-ideal PTO	137
8.6	Conclusions	138
<b>IV</b>	<b>Conclusions and Future work</b>	<b>141</b>
<b>9</b>	<b>Conclusions</b>	<b>143</b>
9.1	Conclusions	143
9.2	Future work	145
	<b>Bibliography</b>	<b>149</b>





# Abstract

Traditional fossil fuel power plants release substantial amounts of greenhouse gases, primarily contributing to anthropogenic climate change. Integrating renewable energy sources into the energy supply systems is crucial to mitigate these environmental challenges. One untapped renewable energy source is wave energy, which can contribute to the transition towards a 100% renewable future.

Initially, this thesis presents a case for the potential value of adding wave energy to the electric grid by analysing the complementarity of the wave resource with other renewable energy modalities (wind, tidal and solar) and load requirements in the Island of Ireland. The analysis shows that wave energy has a role to play in the future Irish supply mix. Wave energy, like other renewable energy resources, presents a considerable challenge for integrating it into the power grid due to its intermittent, and relatively unpredictable nature. Wave energy grid integration entails several issues, including managing power output variability, effective control of the wave energy device and power converters, and optimal storage requirements. Additionally, an added complexity in wave energy grid integration lies in implementing reactive wave energy converter (WEC) control, which requires bi-directional power flow between the device and grid sides.

In general, many grid integration studies involving wave energy have deficiencies, such as simplified hydrodynamic and power converter models, simplified passive damping hydrodynamic control and relatively rudimentary PI power converter control. It is imperative to address the issues mentioned above to enhance the integration of wave energy into power grids, maximising power capture and the economic benefit of wave energy. To this end, this thesis presents a wave-to-grid (W2G) control framework for a direct-drive wave energy conversion system, including *control-oriented models* for each component in the powertrain and *high-performance controllers* for both device and grid sides, to achieve a range of control objectives. A short-term ultra-capacitor-based storage system supports both device-side (hydrodynamic control support) and grid-side (grid support during faults and power quality improvement) functionalities.

Additionally, the negative (reactive) power peaks are analysed by recognising the importance of reactive power requirements of reactive hydrodynamic WEC control and its implications for the powertrain equipment. As a result, this thesis provides analytical and simulation results regarding the excessive reactive power peaks requirements of hydrodynamic WEC control and offers recommendations on how to deal with them.



To Ammi, Abbu, Hajira  
and my family.  
**Thank you!**

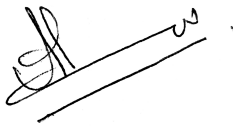


# Declaration of authorship

I, Hafiz Ahsan Said, declare that this thesis entitled "*Grid integration aspects of wave energy*" and the work presented in it are my own. I confirm that:

- This work was done wholly or mainly while in candidature for a research degree at this University.
- Where any part of this thesis has previously been submitted for a degree or any other qualification at this University or any other institution, this has been clearly stated.
- Where I have consulted the published work of others, this is always clearly attributed.
- Where I have quoted from the work of others, the source is always given. With the exception of such quotations, this thesis is entirely my own work.
- I have acknowledged all main sources of help.
- Where the thesis is based on work done by myself jointly with others, I have made clear exactly what was done by others and what I have contributed myself.

Date: 24/07/2023

Signature:  \_\_\_\_\_



# Acknowledgements

## Personal

First of all, I want to express my deepest gratitude to Prof. John Ringwood, my supervisor at COER, for granting me the opportunity to pursue my PhD and for his invaluable guidance on my research, technical writing, and presentation skills. The completion of this thesis is undeniably a result of his advice, feedback, and unwavering support. I also extend my thanks to all the staff members of the Electronic Engineering Department, especially Carrie Anne Barry, Ann Dempsey, Denis Buckley, and John Maloco, for their assistance with administrative and technical matters.

I extend my warmest thanks to the current and former members of the COER group for their valuable contributions to countless discussions and for making the time spent at the lab truly enjoyable: Yeraí Peña-Sanchez, Christian Windt, Mahdiyeh Farajvand, Andrei Ermakov, Bingyong Guo, Pedro Foraro, Fernando Jaramillo, LiGuo Wang, Kumars Mahmoodi, Augusto Sarda, Josefredo, Agustina Skiarski, Matheus Costa, Thalita Nazaré, Nahia Iturricastillo, Iain McLeod, Simon Thomas.

A very special thanks to my good friends and colleagues, Marco Rosati, Hasana Bagnall-Hare and Edoardo Pasta, for all the support and priceless advice while writing this thesis and, importantly, for their fantastic friendship during my PhD. I would also like to thank my collaborators Demián García-Violini, Nicolás Faedo and Tom Kelly for all their guidance and invaluable input during our collaborations.

Last but not least, I would like to extend my heartfelt thanks to my family, especially my parents, Rehan bhai, Bhabi Sofia, and Hajira, for their unwavering understanding, support, and patience throughout my PhD journey. Their encouragement and love have been invaluable to me.

## Institutional

I express my sincere gratitude to the Dept. of Electronic Engineering for supporting the first two years of my PhD through the Maynooth University Teaching Studentship (MUTS) scholarship. I am also thankful to MaREI, the Science Foundation Ireland (SFI) Research Centre for Energy, Climate and Marine, for their support in funding this research, under Grant No. 12/RC/2302\_P2. Additionally, I extend my thanks to the Irish Marine Institute, ERA database, and the authors of [1] for providing the renewable resource data fragments used in Chapter 2.





# List of Figures

1.1	Approximation of the average annual wave power density [kW/m] around the globe (adapted from [9]). . . . .	2
1.2	A comparison of the load demand and combined wave resource for 11 locations around Ireland for the year 2017. Note that the data is normalised to the maximum value of each time series. . . . .	3
2.1	Time series plot of normalised raw power available near Inishtrahull Sound for four different seasonal weeks of 2017. In the plots, highlighted sections indicate times of the week when complementarity benefits of combined resource exploitation may be gained. . . . .	14
2.2	Data collection locations around Ireland considered in this study. . . . .	16
2.3	Power matrix for the 750 kW Pelamis WEC [32]. . . . .	17
2.4	Generic 1.2 [MW] tidal turbine curve utilised in this chapter. . . . .	18
2.5	The W2E-215/9.0 (9 [MW]) [35] wind turbine power curve utilised in this study. . . . .	19
2.6	Seasonal complementarity among four resources around Ireland, considering all chosen data points in Fig. 2.2. . . . .	23
2.7	Standard deviation $\sigma_{\Delta}$ of the mismatch energy $\Delta(t)$ as a function of (a) wave fraction $\alpha$ (b) wind fraction $\beta$ (c) tidal fraction $\epsilon$ (d) solar fraction $\delta$ , in a 100% renewable-only scenario for IOI, based on daily time scale. . . . .	25
2.8	Generation and load profiles comparison for the optimal combination of all resources for Dec. 31, 2017. The highlighted yellow and red parts denote the prominent generation surplus and deficit regions, respectively. . . . .	26
2.9	Standard deviation $\sigma_{\Delta}$ of the mismatch energy $\Delta(t)$ as a function of (a) wave fraction $\alpha$ (b) wind fraction $\beta$ (c) tidal fraction $\epsilon$ (d) solar fraction $\delta$ , in a 100% renewable-only scenario for IOI, based on yearly time scale. . . . .	27
2.10	Generation and load profiles comparison for the optimal combination of all resources for 2017. The highlighted yellow and red parts denote the prominent generation surplus and deficit regions, respectively. . . . .	27
3.1	A typical W2G wave energy conversion system. . . . .	34

3.2	Types of wave absorbers (adapted from [43]): (a) Attenuator, (b) Pressure differential point absorber, (c) Overtopping, (d) Point absorber, (e) Oscillating wave surge converter (OWSC) (f) Oscillating water column (OWC). Note that the blue part of each sub-figure denotes the PTO system. . . . .	35
3.3	Recently developed wave absorbers. . . . .	37
3.4	Classification of energy storage systems [15]. . . . .	41
4.1	Ocean wave characteristics. The blue line represents the free surface, and SWL represents still water level or undisturbed free surface. . . .	53
4.2	Ocean wave characterisation using JONSWAP SDFs. (a) $H_s = 3$ [m], $\gamma = 3.3$ and $T_p \in [5, 10]$ [s] (b) $T_p = 10$ [s], $\gamma = 3.3$ and $H_s \in [1, 3.5]$ [m] (c) $H_s = 3$ [m], $T_p = 10$ [s] and $\gamma \in [1, 6]$ . . . . .	55
4.3	Example wave elevation time series $\eta(t)$ for a JONSWAP SDF with $H_s = 3$ [m], $T_p = 10$ [s] and $\gamma = 3.3$ . . . . .	55
4.4	Graphical representation of linear potential flow theory with the linear boundary conditions introduced in Section 4.2.2. . . . .	57
4.5	Schematic of the six degrees-of-freedom of a floating body. . . . .	59
4.6	Hydrodynamic coefficients of a 1-DoF (heave) point absorber, including geometry of the body (left), excitation effects in the frequency domain (centre) and radiation effects in the frequency domain (right). The operators $\Re\{\bullet\}$ and $\Im\{\bullet\}$ denote real and imaginary parts of $\{\bullet\}$ . . . . .	60
4.7	A comparison of IRF of parametric state space approximation vs Non-parametric radiation IRF for a 1-DoF heaving point absorber. . . . .	63
5.1	Reference W2G direct-drive configuration. . . . .	68
5.2	The schematics of WEC and PTO (LPMG) systems considered in this thesis. The acronym SWL stands for still water level. . . . .	69
5.3	The waveforms corresponding to phase 'a' of a generic rotary generator: (a) angular velocity $\omega_e(t)$ , (b) angular displacement $\theta(t)$ , and (c) the resulting 1- $\phi$ induced voltage $e_a(t)$ of the machine. . . . .	70
5.4	The waveforms corresponding to phase 'a' of an LPMG: (a) angular velocity $\omega_e(t) = \frac{\pi}{\tau}\dot{z}(t)$ , (b) angular displacement $\theta(t) = \frac{\pi}{\tau}z(t)$ , and (c) the resulting single phase induced voltage $e_a(t)$ of the machine. . . . .	70
6.1	Impedance-matching principle: (a) Equivalent circuit representation, (b) Impedance-matching feedback control structure. . . . .	81
6.2	Four quadrant electrical power flow naming convention in bi-directional power flow applications. The reactive power, in the hydrodynamic WEC control sense, lies in the shaded region (quadrants II and IV). . . . .	84

6.3	Frequency-response mappings of the LiTe-Con. In particular, the left column illustrates $H_{ff}^{LC}(\omega)$ (dashed line), together with the optimal feedforward mapping $H_{ff}^{opt}(\omega)$ (solid line). The right column depicts the force-to-velocity mapping associated with the LiTe-Con, i.e., $T_{fe \rightarrow v}^{LC}(\omega)$ (dashed line), along with the optimal force-to-velocity frequency response $T_{fe \rightarrow v}^{opt}(\omega)$ (solid line). The effect of the constraint handling mechanism for $k \in \{0.58, 0.4, 0.24, 0.13, 0.080\}$ , is depicted with dotted lines. . . . .	87
6.4	Optimised $k$ values for sea states with peak periods $T_p \in [5, 12]$ [s]. .	87
6.5	Envelope estimation algorithm. . . . .	88
6.6	Various possibilities for mapping $\mathcal{K}$ . . . . .	89
6.7	Device-side control structure including LiTe-Con+ (and LiTe-Con) and Gen-SC control. . . . .	90
6.8	Full-scale CorPower-like device considered in this case study. Dimensions are in metres. The acronym SWL stands for still water level and the letter G is used to denote the center of gravity of the device. . .	93
6.9	Performance comparison of LiTe-Con+, LiTe-Con and passive damping control for the totality of sea-states considered. (a) Absorbed power [kW], (b) Converted power [kW], (c) Peak-to-average power ratio of the converted power, and (d) Maximum PTO (control) force [N] . .	94
6.10	Comparative analysis of dynamic range for LiTe-Con+ and LiTe-Con for a sea-state with $H_s = 2$ [m], $T_p = 8.5$ [s] and $\gamma = 3.3$ . A histogram of operation range $[-1.5, 1.5]$ [m] with 500 bins is considered here. .	95
6.11	Tracking performance of the Gen-SC controller: (a) PTO force [N], (b) d-axis stator current [A], (c) q-axis stator current [A]. The highlighted sections are zoomed in plots presented on the right side of the respective plots. . . . .	96
7.1	Grid-SC control structure. . . . .	101
7.2	SRF-PLL structure for grid phase tracking. . . . .	102
7.3	W2G control block diagram. . . . .	104
7.4	Energy management system overview. . . . .	106
7.5	Tracking performance of the Grid-SC controller (a) d-axis current [A] (b) q-axis current [A]. . . . .	108
7.6	Tracking performance of the UC storage controller (a) Ultra-capacitor current [A] (b) DC bus voltage [V]. . . . .	108
7.7	Power quality plots (a) Three-phase injected current [A] (b) Scaled Phase A grid voltage [V] and Phase A current [A] (c) Frequency variations [Hz]. . . . .	109
7.8	Harmonic spectrum: (a) Magnitude of grid current harmonics (b) Magnitude of grid voltage harmonics. . . . .	110

7.9	LVRT response of the proposed control scheme under symmetrical 3-LG fault (a) PCC voltage [p.u.] (b) DC bus voltage [V] (c) Active power $P_g$ injected into the grid [kW] (d) Reactive power $Q_g$ injected into the grid [kVAR]. . . . .	111
7.10	LVRT response of the proposed control scheme under asymmetrical 1-LG fault (a) PCC voltage [p.u.] (b) DC bus voltage [V] (c) Active power $P_g$ injected into the grid [kW] (d) Reactive power $Q_g$ injected into the grid [kVAR]. . . . .	112
8.1	Active, and reactive, power flow regions for a wave energy converter under optimal control. . . . .	114
8.2	A typical instantaneous power flow profile for an optimally controlled WEC operating in irregular waves. The green shaded region represents active power flow region, while the red shaded region represents reactive power flow region. However, mean power flow (energy) is positive overall.	115
8.3	Maximum and minimum (normalised with respect to $P^u$ ) instantaneous power values for 500 random realisations of $L_f$ vectors according to a typical wave spectrum, for the device presented in Section 8.4, under optimal control conditions. A snippet of the time trace of instantaneous power, corresponding with the realisation linked to $P^u$ (centre) and $P^l$ (right), is presented, showing both maximum and minimum values attained (with circles). . . . .	123
8.4	Schematic diagram of cylindrical WEC with hemispherical bottom. All the relevant dimensions are shown in the schematic, with $R = 5$ [m]. SWL and CoM represent the still water level and centre of mass, respectively. . . . .	126
8.5	Peak power ratio $P_{ratio}$ , for the range of wave frequencies considered, for optimal controller (a). Monochromatic case (b). Panchromatic case. The vertical purple dotted line depicts the resonant frequency $\omega_r$ of the WEC. . . . .	127
8.6	Effects of parametric mismatch on peak power ratio $P_{ratio}$ for optimal controller under monochromatic waves: (a). Peak power ratio $P_{ratio}$ for the range of hydrostatic stiffness variations $\hat{K}_h \in [0.5K_h, 2K_h]$ [N/m], where $K_h = 7.8868 \times 10^5$ [N/m] (b). Peak power ratio $P_{ratio}$ for the range of mass variations $\hat{M} \in [0.5M, 2M]$ [kg], where $M = 6.6792 \times 10^5$ [kg] (c). Peak power ratio $P_{ratio}$ for the range of damping variations $\hat{B}_r(\omega) \in [0.5B_r(\omega), 2B_r(\omega)]$ [Ns/m]. $\omega_p$ represents wave frequency. . . . .	130

- 8.7 Effects of parametric mismatch on peak power ratio  $P_{\text{ratio}}$  for optimal controller under panchromatic waves: (a). Peak power ratio  $P_{\text{ratio}}$  for the range of hydrostatic stiffness variations  $\hat{K}_h \in [0.5K_h, 2K_h]$  [N/m], where  $K_h = 7.8868 \times 10^5$  [N/m] (b). Peak power ratio  $P_{\text{ratio}}$  for the range of mass variations  $\hat{M} \in [0.5M, 2M]$  [kg], where  $M = 6.6792 \times 10^5$  [kg] (c). Peak power ratio  $P_{\text{ratio}}$  for the range of damping variations  $\hat{B}_r(\omega) \in [0.5B_r(\omega), 2B_r(\omega)]$  [Ns/m].  $\omega_p$  represents peak wave spectrum frequency. . . . . 131
- 8.8 Effects of parametric mismatch on relative absorbed power  $P_{\text{abs}}/P_{\text{opt}}$  under panchromatic waves: (a).  $P_{\text{abs}}/P_{\text{opt}}$  for the range of hydrostatic stiffness variations  $\hat{K}_h \in [0.5K_h, 2K_h]$  [N/m], where  $K_h = 7.8868 \times 10^5$  [N/m] (b).  $P_{\text{abs}}/P_{\text{opt}}$  for the range of mass variations  $\hat{M} \in [0.5M, 2M]$  [kg], where  $M = 6.6792 \times 10^5$  [kg] (c).  $P_{\text{abs}}/P_{\text{opt}}$  for the range of damping variations  $\hat{B}_r(\omega) \in [0.5B_r(\omega), 2B_r(\omega)]$  [Ns/m].  $\omega_p$  depicts the peak frequency of a wave spectrum, and  $P_{\text{opt}}$  represents the optimal absorbed power for fully matched case. . . . . 132
- 8.9 Force-to-velocity mapping  $T(\omega)$  for the controllers considered here, *i.e.*, Optimal  $T_{f_e \rightarrow v}^{\text{opt}}$  (Black solid line), LiTeCon-V1  $T_{f_e \rightarrow v}^{\text{LCV1}}$  (blue dashed line), LiTeCon-V2  $T_{f_e \rightarrow v}^{\text{LCV2}}$  (orange dotted line), and Reactive PI  $T_{f_e \rightarrow v}^{\text{PI}}$  (yellow dash-dot line), respectively. The shaded green region represents the wave frequency range considered for the analysis, *i.e.*, the area of interest. . . . . 133
- 8.10 Effects of controller synthesis mismatch under monochromatic waves: (a) Peak power ratio  $P_{\text{ratio}}$  of three controllers for the range of wave frequencies considered. (b) Relative absorbed power  $P_{\text{abs}}/P_{\text{opt}}$  of the controllers for the range of wave frequencies considered. The vertical purple dotted line depicts the resonant frequency  $\omega_r$  of the WEC. . . 134
- 8.11 Effects of controller synthesis mismatch under panchromatic waves: (a) Peak power ratio  $P_{\text{ratio}}$  of the controllers for the range of wave frequencies considered. (b) Relative absorbed power  $P_{\text{abs}}/P_{\text{opt}}$  of the controllers for the range of wave frequencies considered. The vertical purple dotted line depicts the resonant frequency  $\omega_r$  of the WEC. . . 135
- 8.12 Occurrence probability of  $P_{\text{ratio}}$  values for both monochromatic and panchromatic cases. . . . . 136
- 8.13 Ranges of positive and negative energy absorption for non-ideal PTO case, using an efficiency-aware (moment-based), and efficiency-ignorant (reference) PI controller, using the methodology of [210] (left). Sample time trace of power flow with non-ideal PTO for an efficiency-ignorant (reference) PI controller, showing large excursions in reactive power flow (right). . . . . 138



# List of Tables

2.1	Complementarity indices for all raw resources at selected locations around Ireland. . . . .	22
2.2	Complementarity indices for various combinations of resource-mix for Island of Ireland. . . . .	23
3.1	Absorber-generator combinations used in the wave energy grid integration literature. Note: LPMG means linear permanent magnet generator, RPMSG means rotary permanent magnet synchronous generator, DFIG means doubly fed induction generator . . . . .	39
3.2	Reference guide to read Table 3.3 . . . . .	44
3.3	Review of power converters, W2G controllers, and energy storage for grid integration of wave energy. . . . .	45
3.4	Voltage variations allowed for Irish grid [12] and the UK grid [13]. . .	47
3.5	Frequency variations and time limits for the Irish grid [12]. . . . .	48
3.6	Frequency variations and time limits for the Irish grid [12]. . . . .	48
4.1	A review of hydrodynamic models used in the literature for grid integration of wave energy systems. Note: Linear-CD represents linear WEC model with constant damping coefficient term. . . . .	64
7.1	The Fault event times for both symmetric and asymmetric faults. . .	110





# List of acronyms

<b>AFE</b>	. . . . .	Active front End
<b>AWS</b>	. . . . .	Archimedes Wave Swing
<b>B2B</b>	. . . . .	Back-to-Back
<b>BC</b>	. . . . .	Boost Converter
<b>BEMs</b>	. . . . .	Boundary Element Methods
<b>CAES</b>	. . . . .	Compressed Air Energy Storage
<b>CFD</b>	. . . . .	Computational Fluid Dynamics
<b>DBES</b>	. . . . .	Distributed Battery Energy Storage System
<b>DBR</b>	. . . . .	Diode Bridge Rectifier
<b>DFIG</b>	. . . . .	Doubly-Fed Induction Generators
<b>DPTC-SVM</b>	. . .	Direct Power Control using Space Vector Modulation
<b>DoF</b>	. . . . .	Degree-of-Freedom
<b>EMS</b>	. . . . .	Energy Management System
<b>ESS</b>	. . . . .	Energy Storage System
<b>FFT</b>	. . . . .	Fast Fourier Transform
<b>FOAMM</b>	. . . . .	Finite Order Approximation by Moment-Matching
<b>FRT</b>	. . . . .	Fault Ride-Through
<b>FCSMPC</b>	. . . . .	Finite Control Set MPC
<b>FOC</b>	. . . . .	Field Oriented Control
<b>Gen-SC</b>	. . . . .	Generator-Side Converter
<b>Grid-SC</b>	. . . . .	Grid-Side Converter
<b>GSA</b>	. . . . .	Gravitational Search Algorithm
<b>HESS</b>	. . . . .	Hybrid Energy Storage System
<b>HVAC</b>	. . . . .	High Voltage Alternating Current
<b>HVDC</b>	. . . . .	High Voltage Direct Current
<b>HVDC-LLC</b>	. . .	HVDC with Line-Commutated Converters

<b>HVDC-VSC</b>	..	HVDC with Voltage Source Converters
<b>IOI</b>	..	Island Of Ireland
<b>IRF</b>	..	Impulse Response Function
<b>LPMG</b>	..	Linear Permanent Magnet Generator
<b>LiTe-Con</b>	..	<b>L</b> inear <b>T</b> ime invariant <b>C</b> ontroller
<b>LTI</b>	..	Linear Time Invariant
<b>LPT</b>	..	Linear Potential Theory
<b>LVRT</b>	..	Low Voltage Ride Through
<b>MMC</b>	..	Modular Multilevel Converter
<b>MPC</b>	..	Model Predictive Control
<b>NLVCS</b>	..	Non-Linear Vector Current Source
<b>NPC</b>	..	Neutral Point Clamped
<b>OWC</b>	..	Oscillating Water Column
<b>OWSC</b>	..	Oscillating Wave Surge Converter
<b>PMSG</b>	..	Permanent Magnet Synchronous Generator
<b>PTAP</b>	..	Peak-To-Average Power
<b>PM</b>	..	Pierson-Moskowitz
<b>PCC</b>	..	Point of Common Coupling
<b>PDLSPWM</b>	..	Phase Disposition Method of Level-Shifted PWM
<b>PTO</b>	..	Power Take-Off
<b>PI</b>	..	Proportional Integral
<b>SCIG</b>	..	Squirrel Cage Induction Generator
<b>SDF</b>	..	Spectral Density Function
<b>SISO</b>	..	Single-Input Single-Output
<b>SS</b>	..	State Space
<b>SMES</b>	..	Superconducting Magnetic Energy storage
<b>SWL</b>	..	Still Water Level
<b>SRF-PLL</b>	..	Synchronous Reference Frame Phase-Locked Loop
<b>TSOs</b>	..	Transmission System Operators
<b>UC</b>	..	Ultra-Capacitor
<b>USS</b>	..	Undersea storage system

<b>VSC</b>	. . . . .	Voltage Source Converter
<b>VSI</b>	. . . . .	Voltage Source Inverter
<b>WCA</b>	. . . . .	Water Cycle Algorithm
<b>WEC</b>	. . . . .	Wave Energy Converter
<b>W2G</b>	. . . . .	Wave-to-Grid



# 1

## Introduction

### Contents

---

<b>1.1 Motivation of the thesis</b> . . . . .	<b>2</b>
<b>1.2 Contributions of the thesis</b> . . . . .	<b>4</b>
1.2.1 List of publications . . . . .	6
<b>1.3 Thesis layout</b> . . . . .	<b>7</b>

---

Traditional fossil fuel power plants pose a significant threat to the modern world due to their high greenhouse gas emissions, contributing to anthropogenic climate change. Countries are turning to renewable energy solutions to meet their energy needs while combating climate change. One such solution is wave energy, which has gained attention in recent years and has led to the development of various wave energy systems [2]. The vast potential for clean energy [3, 4] and temporal complementarity with other renewable resources [5–7], such as wind and solar, make wave energy a promising option for transitioning to a 100% renewable future. Fig. 1.1 illustrates the wave energy resource distribution worldwide, and it is clear that the wave energy resource is a substantial source of untapped clean energy, and according to [8], the global wave energy resource has been estimated to be approximately 3.7 TW with an annual potential of about 32,000 TWh. Despite being one of the most abundant renewable resources, wave energy is still in its early stages of development. The reason for this is that energy extraction from reciprocating ocean waves is more complicated than other renewable energy modalities, such as solar and wind.

Due to the reciprocating nature of the wave resource, the power output of wave energy devices is not ideal from a grid integration perspective. Some grid integration

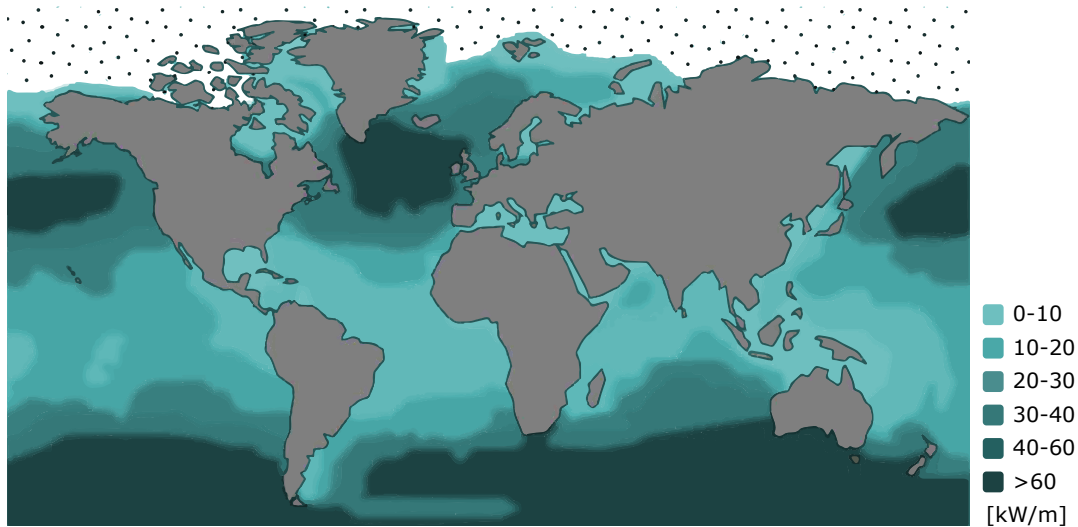


**Figure 1.1:** Approximation of the average annual wave power density [kW/m] around the globe (adapted from [9]).

experiences from wind can be ported to the wave energy case [10]. However, the penetration of wave energy into existing grid networks will directly depend upon the adverse effects it will have on the grid, and the availability of technology to tackle these effects [11]. Research and development in the field are crucial to overcoming wave energy integration challenges, including improving the efficiency and reliability of wave energy converters and developing advanced control strategies and storage solutions. Additionally, a supportive policy framework for developing and deploying wave energy is also essential, including creating regulations that promote the integration of wave energy into the power grid and providing financial incentives for developing wave energy projects.

To summarise, wave energy has the potential to play a significant role in the transition to a 100% renewable future, but there are still many challenges to overcome. With continued research and development and a supportive policy framework, wave energy can become a viable and sustainable source of clean energy that helps mitigate the impacts of climate change.

## 1.1 Motivation of the thesis

Incorporating wave energy into the current renewable generation mix provides complementary benefits, especially for the Irish jurisdiction [6]. Fig. 1.2 provides some insight into this complementarity between combined wave resource (for 11 locations<sup>1.1</sup>)

<sup>1.1</sup>The details of these locations can be found in the Chapter 2, Section 2.1.1

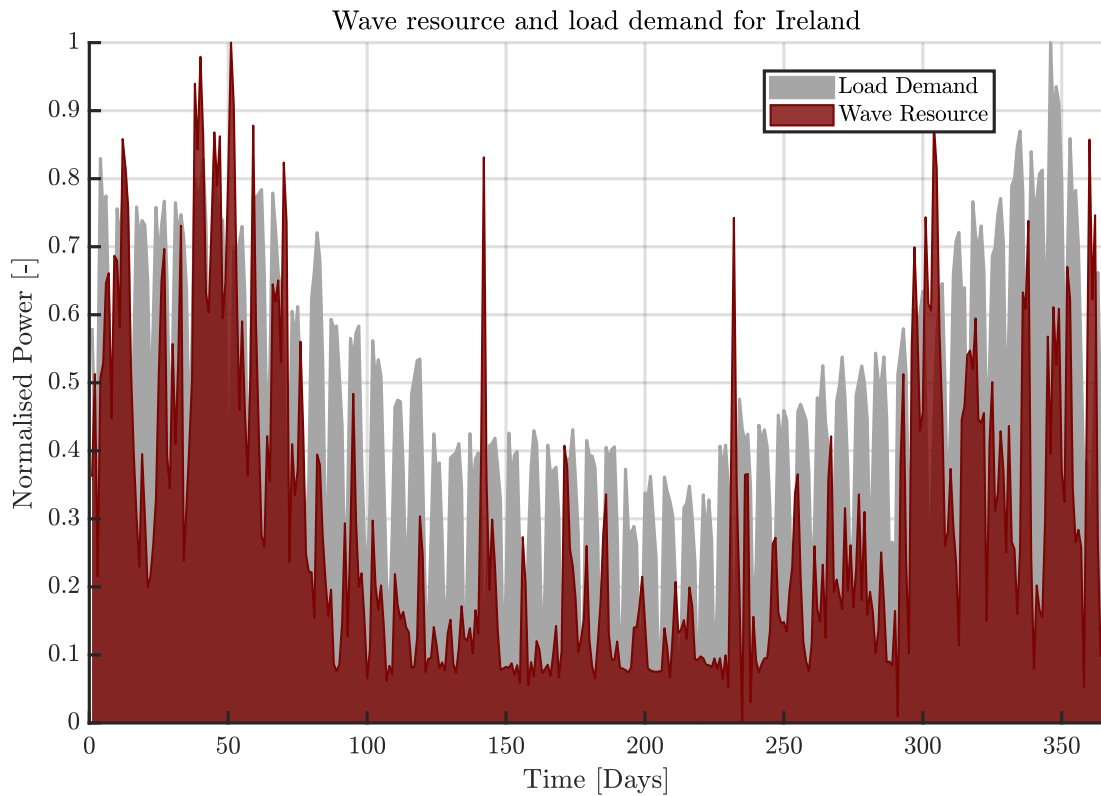


**Figure 1.2:** A comparison of the load demand and combined wave resource for 11 locations around Ireland for the year 2017. Note that the data is normalised to the maximum value of each time series.

and load demand for the Irish jurisdiction, and it is apparent that the wave resource has a natural seasonal complement to load demand, i.e., both have larger values in the winter and smaller values in the summer.

Like other renewable energy resources, such as wind and solar resources, wave resource is intermittent, relatively unpredictable and highly variable, which poses a significant challenge for grid integration. As discussed in the introduction to this chapter, the grid integration experience from wind energy can be ported through to the wave energy sector. However, wave energy provides additional challenges stemming from the energy-maximising reactive hydrodynamic wave energy converter (WEC) control. Additionally, wave-to-grid (W2G) control has device- and grid-side requirements, which must be fulfilled. On the device side, the focus is maximum power extraction from ocean waves while, on the grid side, the requirements are primarily concerned with power quality, imposed by the grid codes [12–14]. Furthermore, the reactive<sup>1,2</sup> (negative) power requirements of energy-maximising WEC controllers provide additional complexity, which is very specific to wave energy. Hence, a complete W2G control

<sup>1,2</sup>Note that the reactive power in the hydrodynamic WEC control sense is different from reactive power as defined for electrical power networks. For more details, see Chapter 8.

framework, which caters for both device- and grid-side requirements, is essential for wave energy grid integration.

The primary objective of this thesis is to analyse the system from wave-to-grid and to demonstrate the advantages of implementing a coordinated wave-to-grid (W2G) control framework. Previous research has predominantly examined individual subsystems of the wave-to-grid system, often overlooking the interconnected nature of the remaining subsystems within the wave-to-grid chain. For economic feasibility, the system from wave-to-grid needs to be considered as a whole. A complete wave-to-grid modelling and control framework is non-existent in the wave energy literature [15]. The main reason for this lack of modelling and control framework is the multi-disciplinary nature of the problem, which requires expertise from a wide range of disciplines, including hydrodynamics, mechanical, electrical and control systems fields. Generally, grid integration studies concerning wave energy either focus on the device side or the grid side, depending upon the area of expertise of the researchers. As part of the work undertaken by this thesis, a balanced W2G control-oriented modelling and *high-performance* control framework is developed that fulfils both device- and grid-side requirements. Moreover, realising the importance of reactive power requirements in energy-maximising wave energy converter control, and a poor understanding of the excessive reactive power peaks, analytical results are derived to understand the reactive power requirements and origins of excessive reactive power peaks and form an integral part of this thesis. Additionally, some other grid integration aspects, related to the value of wave energy on the electricity grid, are also discussed in this thesis.

## 1.2 Contributions of the thesis

In the preliminary stages of this thesis, explored in Chapter 2, a comprehensive complementarity analysis is conducted to assess the potential value of wave energy to the electric grid, with a particular focus on the Irish electric grid. This analysis encompasses the study of how wave energy complements other renewable resources such as tidal, wind, and solar energy, along with examining its alignment with the load demand on the Island of Ireland (work published in [16]).

Following the complementarity analysis in Chapter 2, in Chapter 3, an extensive examination of the current state of grid integration aspects of wave energy has been undertaken (work published in [15]). This comprehensive review encompasses several key facets: Firstly, a *novel classification* system for wave energy devices has been proposed. This classification is rooted in the distinctive characteristics of these devices, particularly focusing on their inertial characteristics. Furthermore, an investigation into the grid connection requirements stipulated by transmission system operators



(TSOs) for renewable energy resources has been conducted, which involves a detailed analysis of the specifications and standards that wave energy systems must adhere to for seamless integration into the power grid. In addition, a comprehensive review of existing grid integration studies has been carried out, with specific emphasis on power converter technology, control mechanisms, and storage systems designed to enhance power quality. This exploration delves into the technological landscape, evaluating the current state of power conversion methods and control strategies employed in grid-connected wave energy systems and exploring the role of energy storage in improving overall power quality for grid integration.

Developing a comprehensive wave-to-grid (W2G) model tailored for control-oriented grid integration studies constitutes a contribution of this thesis (works published in [17, 18]). This model encapsulates all components of a wave energy system connected to the grid, ensuring a well-balanced representation with fidelity. Firstly, in Chapter 4, unlike conventional literature that primarily features regular wave models, this W2G model incorporates irregular wave models. Furthermore, a linear WEC model that considers appropriate quantification of radiation forces, in contrast to the predominant mass-spring-damper models with constant damping found in the literature, is included. In Chapter 5, electrical components, such as generator and power converters, of the powertrain are modelled. Finally, the models for each wave-to-grid components are combined to form a control-oriented W2G model used for control design in Part III of the thesis.

In Part III, specifically Chapters 6 and 7, a major contribution was made where a high-performance W2G control framework is designed for a direct drive wave energy conversion system (works published in [18–20]). The W2G control framework consists of four parts: Firstly, a constrained reactive WEC hydrodynamic control, i.e. LiTe-Con (LiTe-Con+), in the W2G control framework, is introduced on the device side. The reactive WEC controller maximises energy absorption while providing a mechanism for dealing with position constraints essential for device safety. Secondly, Lyapunov-based nonlinear controllers for power converters in the powertrain are proposed on the grid side instead of PI controllers predominant in the literature. Thirdly, the framework includes the integration of a short-term storage subsystem, which serves a multifaceted purpose, offering support for reactive hydrodynamic control, contributing to power quality improvement, and providing fault ride-through (FRT) support during grid faults. Finally, an energy management system (EMS), as a supervisory control mechanism, is also a part of the framework, responsible for continuous W2G-controlled operation at all times by supervising storage and grid-side controls.

In Chapter 8, another major contribution of this thesis is the derivation of general analytical results for reactive-to-active power peaks for both monochromatic and

panchromatic wave excitation, which are then validated by a comprehensive set of simulations (work published in [21]). Moreover, the Chapter 8 also examines the various origins of system/controller mismatch, including modelling errors, controller synthesis inaccuracies, and non-ideal PTO behaviour, highlighting the consequences of such errors on reactive power flow levels.

### 1.2.1 List of publications

A list of peer-reviewed studies, that either make up the thesis core or are the outcome of work done as part of WEC modelling exercises, is provided in this section. The studies are arranged in chronological order. The abbreviated notation that follows indicates the status of a publication: (P) published, (Pr) in press, (A) accepted, (CA) conditionally accepted, (UR) under review, and (IP) in preparation. Additionally, if a publication is closely related to the contents of this thesis, i.e. if it includes essential information offered in this thesis, this is clarified by referencing a specific chapter or chapters.

#### Journal publications:

---

Status	Publication	Chapter/s
(P)	<b>Said H.A.</b> , Ringwood J.V. <i>Grid integration aspects of wave energy—Overview and perspectives</i> , IET Renewable Power Generation 2021;15:3045–64	2,3,4
(P)	Bingham, H.B., Yu, Y.H., Nielsen, K., Tran, T.T., Kim, K.H., Park, S., Hong, K., <b>Said, H.A.</b> , Kelly, T., Ringwood, J.V. and Read, RW. <i>Ocean Energy Systems Wave Energy Modeling Task 10.4: Numerical Modeling of a Fixed Oscillating Water Column</i> , Energies, 14(6), p.1718, 2021.	-
(P)	<b>Said, H.A.</b> , Garcia-Violini, D. and Ringwood, J.V., <i>Wave-to-grid (W2G) control of a wave energy converter</i> , Energy Conversion and Management: X, Vol.14, Paper 100190, pp 1-20, 2022.	4,5,6
(P)	<b>Said, H.A.</b> , Garcia-Violini, D., Fáedo, N., and Ringwood, J.V., <i>On the ratio of reactive to active power in WEC control</i> , IEEE Open Journal of Control Systems, Vol. 3, pp. 14-31, 2024.	7
(IP)	<b>Said, H.A.</b> , Costello, S.P. and Ringwood, J.V., <i>Combined resource exploitation and value of wave energy on the grid – An Irish case study</i> , Energy.	-
(IP)	Bingham, H.B., Yu, Y.H., Nielsen, K., Tran, T.T., Kim, K.H., Park, S., Hong, K., <b>Said, H.A.</b> , Kelly, T., Ringwood, J.V. and Read, RW, 2021. <i>Ocean Energy Systems Wave Energy Modeling Task 10.4: Numerical Modeling of DTU Oscillating Water Column</i> , Journal of Marine Science and Engineering.	-

**Conference publications:**

<b>Status</b>	<b>Publication</b>	<b>Chapter/s</b>
(P)	<b>Said, H.A.</b> and Ringwood, J.V., <i>Intelligent control of a DC microgrid consisting of Wave Energy Converter (WEC) and Hybrid Energy Storage System (HESS)</i> , Proceedings of the European Wave and Tidal Energy Conference (EWTEC) 2021, Plymouth, Sept. 2021, pp. 1884-1:1884-9.	5,6
(P)	Jain, J.K., Mason, O., <b>Said, H.A.</b> and Ringwood, J.V., <i>Limiting reactive power flow peaks in wave energy systems</i> , Proceedings of the 14th IFAC Conference on Control Applications in Marine Systems, Robotics, and Vehicles (CAMS), 2022, IFAC-PapersOnLine 55, no. 31: pp. 427-432.	-
(P)	<b>Said, H.A.</b> and Ringwood, J.V., <i>Low voltage ride-through (LVRT) capability enhancement of a grid-connected wave energy conversion system</i> , Proceedings of the Trends in Renewable Energies Offshore (RENEW), 2022, pp. 267-275	6
(P)	<b>Said, H.A.</b> , Garcia-Violini, D. and Ringwood, J.V., <i>An improved linear time-varying reactive hydrodynamic control for a grid-connected wave energy conversion system</i> , IEEE OCEANS, Limerick, June 2023, pp. 1-9.	5
(P)	Guo, B., Chen, S., <b>Said, H.A.</b> and Ringwood, J.V., <i>Wave-to-wire modelling of a vibro-impact wave energy converter for ocean data buoys</i> , 22 <sup>nd</sup> IFAC World Congress, Yokohama, July 2023, pp. 12593-12598.	-
(P)	<b>Said, H.A.</b> , Costello, S.P. and Ringwood, J.V., <i>On the complementarity of wave, tidal, wind and solar resources in Ireland</i> , Proceedings of the European Wave and Tidal Energy Conference (EWTEC), Bilbao, Sept 2023, pp. 340-1:340-6.	-
(P)	Rosati, M., <b>Said, H.A.</b> and Ringwood, J.V., <i>Wave-to-Wire Control of an Oscillating Water Column Wave Energy System Equipped with a Wells Turbine</i> , Proceedings of the European Wave and Tidal Energy Conference (EWTEC), Bilbao, Sept 2023, pp. 309-1:309-6.	-

### 1.3 Thesis layout

This section provides details about the organisation of the remainder of the thesis, divided into four parts given below:

- **Part I:** Combined resource exploitation and value of wave energy on the electricity grid (Chapter 2)
- **Part II:** Preliminaries and state-of-the-art (Chapters 3, 4, 5)

- **Part III:** High-performance W2G control of a WEC (Chapters 6, 7, 8)
- **Part IV:** Conclusions and future work (Chapter 9)

The broad contents of each chapter are laid out in the following:

- Chapter 2 presents a case study on the value of wave energy on the electric grid by utilising combined resource exploitation for the Island of Ireland, setting the context for the remainder of the thesis. In particular, the chapter focuses on the potential complementarity of combining multiple renewable energy modalities, including wave, wind, tidal and solar to meet the load requirements of Ireland. Additionally, a case is presented for the potential value of wave energy on the Irish electricity grid, in terms of reduced balancing requirements.
- Chapter 3 introduces a typical wave energy conversion system, including all powertrain components. Additionally, a detailed description of each element of the powertrain, as well as the role it plays in grid integration, is added in this chapter. Grid connection requirements, imposed by the grid codes for a grid connection of a renewable energy resource, are also introduced.
- Chapter 4 introduces the fundamentals of ocean waves and hydrodynamic WEC modelling, used throughout the thesis. Firstly, the numerical generation of regular and irregular waves is detailed. Secondly, WEC hydrodynamic modelling based on the linear potential flow theory is elaborated, including the formulation of a control-oriented state space model for a WEC. Finally, a review of the state-of-the-art hydrodynamic models, for grid-connected wave energy systems, is presented.
- Chapter 5 describes electrical system modelling for a direct-drive wave energy conversion system, which includes a linear permanent magnet generator (LPMG) model, back-to-back (B2B) power converter models and a model for a buck-boost converter connected to the ultra-capacitor based storage subsystem. A review of electrical systems models for grid-connected wave energy systems concludes this chapter.
- The device-side control component of the W2G control framework is presented in Chapter 6. Fundamentals of hydrodynamic WEC control, including formulations for passive and reactive hydrodynamic WEC control, are included. Additionally, a finite order realisation of reactive WEC control, namely LiTe-Con (Linear Time invariant Controller), is introduced. LiTe-Con provides a reference for generator-side converter (Gen-SC) control, which is then tracked by a Lyapunov-based controller for the Gen-SC. Finally, the capabilities of the device-side control system are illustrated by simulation results.

- Chapter 7 presents two additional components of the W2G control framework, i.e. grid-side converter (Grid-SC) control and storage subsystem control. Similar to Gen-SC control, Lyapunov-based nonlinear controllers are designed for the Grid-SC and the DC/DC buck-boost converter for the storage subsystem. The proper operation of the lower-level power converter controllers is also ensured by introducing an energy management system (EMS), which serves as a supervisory control mechanism. Finally, a set of simulation cases is used to evaluate the entire W2G control framework in light of device- and grid-side requirements.
- Chapter 8 proposes an analytical framework to understand reactive power peak phenomena and requirements for wave energy systems controlled via the reactive hydrodynamic WEC control. Furthermore, the consequences of excessive reactive power peaks, caused by modelling errors and controller synthesis errors, are illustrated. Illustrative case studies, through simulation, show validation of the analytical results and the effects of excessive reactive power peaks on the performance of a wave energy conversion system.
- Chapter 9 summarises the main conclusions of this thesis by critically analysing the results presented in each part of the thesis. Furthermore, future research directions are specified, along with a discussion on these future directions.



## **Part I**

# **Combined resource exploitation and value of wave energy on the electricity grid**





# 2

## Combined wave, tidal, wind and solar resource exploitation: An Irish case study

### Contents

---

<b>2.1</b>	<b>Resource data collation and power generation</b>	<b>15</b>
2.1.1	Choice of locations for data collection	15
2.1.2	Wave data and power generation	16
2.1.3	Tidal data and power generation	17
2.1.4	Wind data and power generation	18
2.1.5	Solar data and power generation	19
<b>2.2</b>	<b>Temporal complementarity analysis</b>	<b>20</b>
2.2.1	Total variation complementarity index	20
2.2.2	Variance complementarity index	21
2.2.3	Standard deviation complementarity index	21
2.2.4	Complementarity results: An Irish case study	21
<b>2.3</b>	<b>Energy balance and balancing cost analysis</b>	<b>24</b>
<b>2.4</b>	<b>Conclusions</b>	<b>28</b>

---

This chapter highlights the complementary benefits of integrating wave energy into the existing Irish renewable generation mix, currently primarily composed of wind and solar power plants. By incorporating new forms of renewable energy resources like wave and tidal energy, the transition to a fully renewable energy future can be facilitated due to the abundant availability of these resources [4] and the potential complementarity they offer. Utilising a diverse range of resources will enhance the

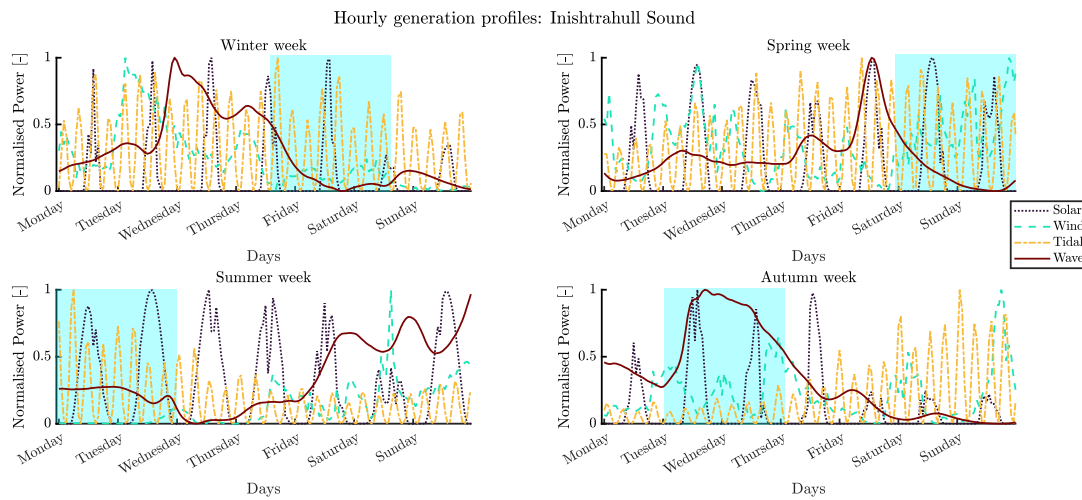


**Figure 2.1:** Time series plot of normalised raw power available near Inishtrahull Sound for four different seasonal weeks of 2017. In the plots, highlighted sections indicate times of the week when complementarity benefits of combined resource exploitation may be gained.

reliability of the energy supply system and contribute to lowering the overall cost of integrating renewable energy into the current generation mix.

In recent studies conducted for US and UK jurisdictions, efforts have been made to evaluate the temporal complementarity of (additional) multiple renewable energy resources, including wave and tidal energy [22, 23]. These studies have shown that marine renewable resources can offer substantial benefits to future power systems by reducing the need for balancing power and providing valuable capacity contributions. Ireland, with its island topography and abundant marine resources, has the potential to enjoy similar benefits through the combined exploitation of renewable resources. By way of example, Fig. 2.1 illustrates the renewable resource generation profiles at Inishtrahull Sound, Ireland, for four different weeks in 2017, with hourly resolution, highlighting the times of the week when certain resources are unavailable while others are available, leading to complementarity benefits. In the highlighted sections of Fig. 2.1, it can be observed that during the autumn week, wind and tidal resources are low, while wave and solar resources are available, providing complementary benefits. On the other hand, during the summer week, wind and wave resources are low, but tidal and solar resources offer complementary advantages. These examples demonstrate the potential benefits of combining different renewable resources to ensure a more consistent and reliable energy supply throughout the year, taking advantage of the varying availability of resources across different seasons. A reliable renewable energy supply can be achieved with sufficient storage, but this would be an extremely costly solution. However, with ambitious plans for offshore wind and hydrogen storage, Ireland is heading in that direction [24–26].

This chapter focuses on conducting a comprehensive complementarity assessment of four renewable resources, namely wave, tidal, wind, and solar, on the Island of Ireland (IOI), including Northern Ireland. The assessment utilises novel complementarity indices based on mathematical concepts, such as total variation, variance, and standard deviation [27]. These indices enable the evaluation of complementarity among multiple (more than two) resources. Furthermore, the chapter provides a preliminary balancing cost analysis in order to find an optimal resource combination to provide for Ireland's 100% load demand.

The remainder of the chapter is organised as follows: Section 2.1 describes the data collection and power generation profiles for all four resources, while Section 2.2 details the methodology used here to assess complementarity, including various complementarity indices used as well as the results for the complementarity assessment. Mismatch energy and balancing cost analysis is presented in Section 2.3. Finally, Section 2.4 concludes this study.

## 2.1 Resource data collation and power generation

This section details the choice of data locations around Ireland, data collation for each raw renewable resource, and calculation of respective power time-series.

### 2.1.1 Choice of locations for data collection

In order to assess the potential of the four renewable resources (wave, tidal, wind, and solar), it is crucial to gather relevant data. In this study, the selection of data locations is based on identifying potential tidal sites around the IOI, as tidal resources (in terms of both resource availability, and measurement points) are considered the limiting factor compared to wind, solar, and wave resources, which are present in most coastal locations in Ireland. The chosen data locations are depicted as coloured circles in Fig. 2.2. By selecting the same locations for each resource, there are several advantages, including the possibility of co-locating power plants that can leverage shared electrical infrastructure and other synergies. The data for each resource was obtained from two primary sources: the Marine Institute [28], and a high-resolution solar and wind dataset provided in [1]. It should be noted that the data from these two sources could only be obtained for a single overlapping year, which, in this case, is 2017. This single overlapping year provides a consistent basis for comparing and evaluating the complementarity among the different resources.

While the Marine Institute served as the primary source for tidal and wave data, it was discovered that the wave dataset provided by the Institute for the nominated tidal

locations (as depicted in Fig. 2.2) was not suitable due to the influence of wind on tide effects [29], i.e. waves generated by the interaction of wind and tide, at these tidal locations. To address this limitation, additional wave data were collected from the ERA5 database [30], specifically for sites further offshore. These additional wave data points are represented by black dots (M2-M6) in Fig. 2.2. By incorporating these offshore wave data points, the dataset became more comprehensive, considering the wave conditions that are not influenced by wind-on-tide effects. All the datasets used in the study are modelled data, although they have been validated against different metrics to ensure their accuracy and reliability.

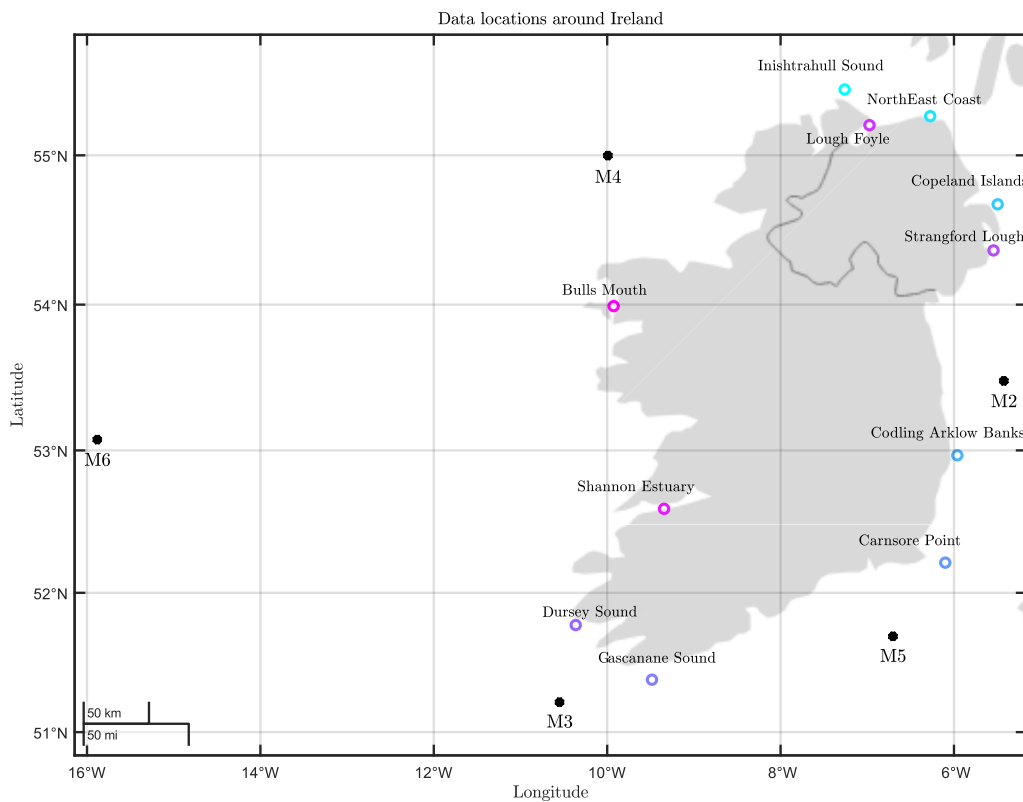


**Figure 2.2:** Data collection locations around Ireland considered in this study.

## 2.1.2 Wave data and power generation

As mentioned in Section 2.1.1, the Marine Institute and ERA5 database was utilised to obtain wave data for this project, including mean wave period  $T_m$  and significant wave height  $H_s$ . The data was available at an hourly resolution, providing a time series covering the entire year of 2017, representing one data point for each of  $T_m$  and  $H_s$  at each hour. Calculating the extracted power from wave energy devices poses challenges due to the lack of standardised wave technology and the diverse operating principles of

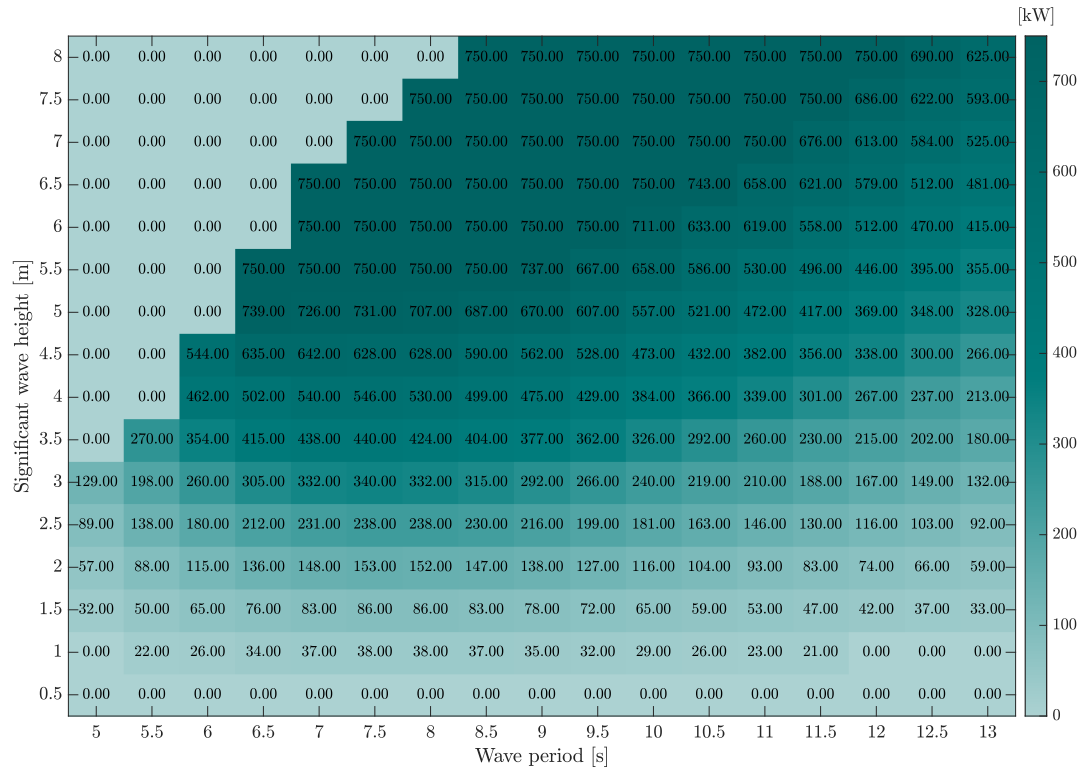


**Figure 2.3:** Power matrix for the 750 kW Pelamis WEC [32].

available devices [31]. Consequently, establishing a uniform measure of the extracted power for wave energy remains a complex task. In this study, the 750 MW Pelamis WEC [32] was selected as the reference device due to its well-documented power production characteristics. The power production of the Pelamis converter is described in a published power matrix, as shown in Fig. 2.3. While there may be generic concerns regarding power matrix representations [33], using this matrix allows for standard analysis and comparison in this study, with simplicity and computability as priorities.

### 2.1.3 Tidal data and power generation

The tidal data used in this study was also obtained from the Marine Institute and consisted of an hourly time series covering one year, i.e. 2017. The dataset provided information on various parameters, including surface current velocities in the eastward direction ( $u$ ) and northward direction ( $v$ ). Additionally, depth-averaged velocities in both the eastward and northward directions were also included in the dataset.

To convert tidal stream kinetic energy into electrical power, tidal devices, somewhat similar to marine versions of horizontal-axis wind turbines, are utilised in this study. The instantaneous kinetic energy available in the tidal stream is given by  $P_c(t) = \frac{1}{2}A_t v^3(t)$ , where  $r = 1030 \text{ kg/m}^3$  represents the density of seawater,  $A_t$  is the cross-sectional

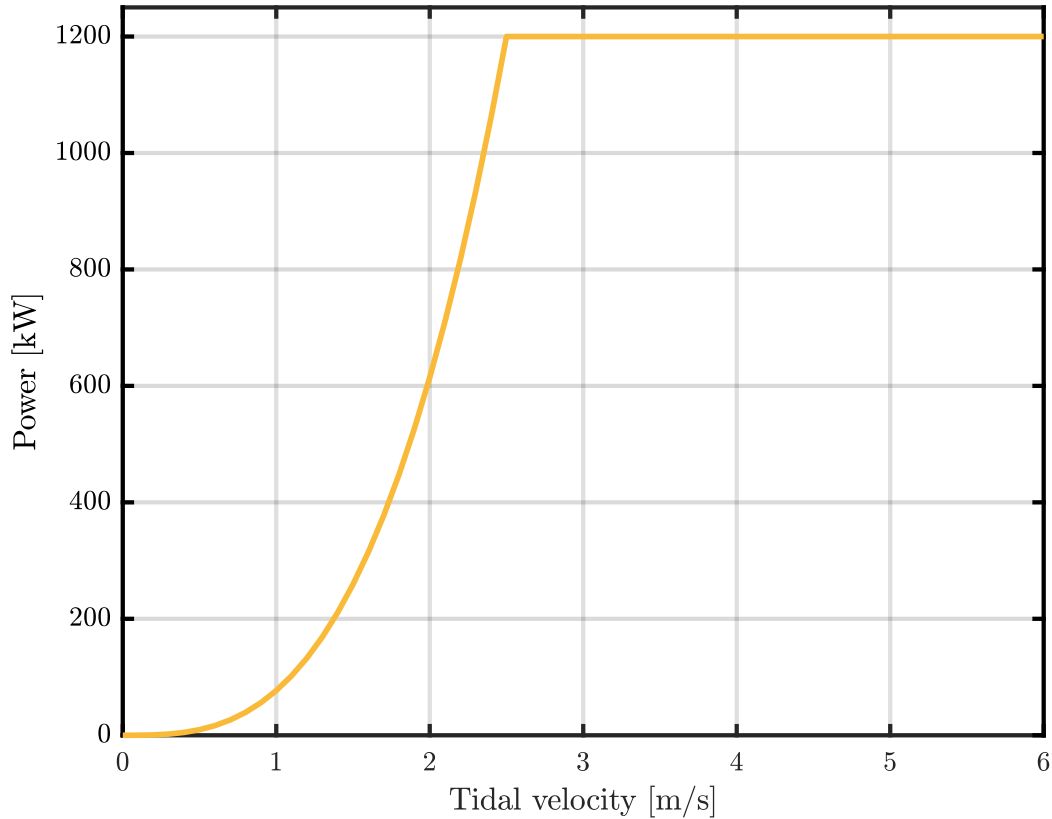


**Figure 2.4:** Generic 1.2 [MW] tidal turbine curve utilised in this chapter.

area swept by the rotor, and  $v(t)$  is the velocity of the water stream. However, the tidal turbine can only capture a portion of this energy, which depends on its technical characteristics. The following equation expresses this relationship:

$$P_{\text{tidal}} = C_p P_c, \quad (2.1)$$

where  $C_p$  is the power coefficient, which is influenced by the blade pitch angle and tip speed ratio. For this study, a value of  $C_p = 0.45$  is assumed [34]. The resulting power curve for the tidal device is shown in Fig. 2.4.

### 2.1.4 Wind data and power generation

Wind data, provided by the authors of [1], is also in the form of an hourly time series. Data from various locations across IOI was selected to mitigate the direct correlation in available wind power, providing spatial diversity. This spatial diversity helps ensure more consistent and reliable wind power utilisation. However, it is essential to note that large weather systems can still result in some degree of direct correlation between different locations.

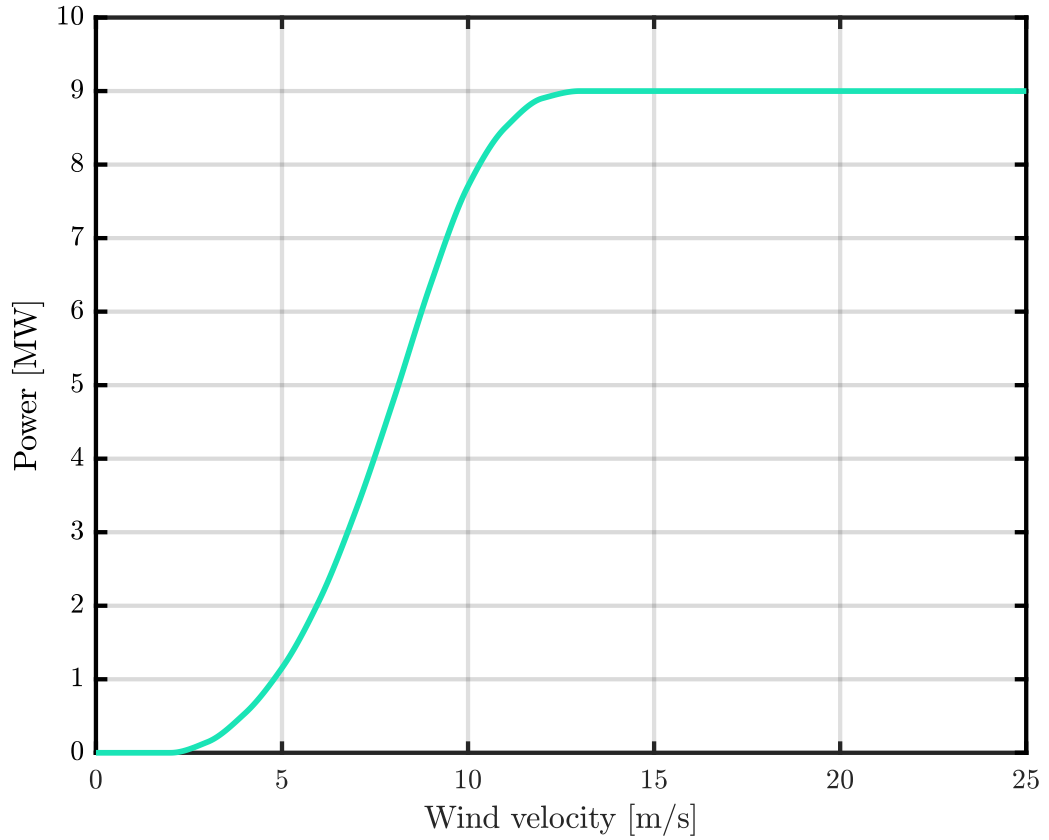


**Figure 2.5:** The W2E-215/9.0 (9 [MW]) [35] wind turbine power curve utilised in this study.

The power extracted from wind can be estimated using established power curves based on wind turbine technology. In this study, a representative wind turbine model, specifically the W2E-215/9.0 (9 [MW]) [35], has been chosen. The power curve associated with this wind turbine model is shown in Figure 2.5.

### 2.1.5 Solar data and power generation

The solar data provided in [1] consists of hourly measurements for the year 2017. Solar data exhibit a high level of predictability, following a diurnal pattern with higher solar irradiance levels occurring during the summer months. To estimate the power generation from a photovoltaic (PV) system at a specific time  $t$ , the solar irradiance ( $G_{irr}$ ) and the air temperature ( $T_{air}$ ) are taken into account [36]. The relationship can be expressed as:

$$P_{solar} = \eta_p G_{irr}(t) [1 - \mu(T_{air}(t) - T_{STC}) - \mu C G_{irr}(t)], \quad (2.2)$$

where  $\eta_p$  represents a production parameter, which considers the PV array surface area and the efficiencies of the inverter and generator.  $\mu$  and  $C$  are efficiency reduction

factors that depend on the temperature and irradiance, respectively.  $T_{\text{STC}}$  is the standard test condition temperature corresponding to the photovoltaic cell [37].

## 2.2 Temporal complementarity analysis

The concept of energetic complementarity refers to the synergistic collaboration of multiple variable renewable energy sources to enhance the reliability of the energy system and minimise periods of insufficient energy generation. By assessing the complementarity of renewable energy resources, it becomes possible to determine the optimal combination of these resources to meet the energy demand for a specific area. This analysis is crucial for designing an efficient and reliable energy mix that effectively fulfils the load requirements in a given jurisdiction.

Traditional correlation-based metrics are unsuitable when assessing the complementarity of all four resources, since they only allow complementarity calculations for up to two resources. To overcome this limitation, novel complementarity metrics, based on the mathematical concepts of total variation, standard deviation, and variance, have been proposed in [27], which provide the advantage of evaluating the complementarity among more than two resources. The details of each metric will be discussed in the following subsections.

### 2.2.1 Total variation complementarity index

The total variation complementarity index is derived from the mathematical concept of *total variation*. For  $n$  functions  $f_i$ , where  $i = 1, 2, \dots, n$ , the general formulation of the total variation complementarity index,  $\Phi$ , over a time interval  $[a, b]$  is given by:

$$\Phi(f_i) = 1 - \frac{\bigvee_b^a(f_1 + f_2 + \dots + f_n)}{\bigvee_b^a(f_1) + \bigvee_b^a(f_2) + \dots + \bigvee_b^a(f_n)}, \quad (2.3)$$

with,

$$\bigvee_b^a = \sup \sum_{j=1}^m |f(t_j) - f(t_{j-1})|, \quad (2.4)$$

defined as the total variation of a function  $f(t)$ . The supremum is taken over all possible finite partitions  $a = t_1 < \dots < t_n = b$  over the interval  $[a, b]$ . The complementarity metric  $\Phi(f_i)$  takes values between 0 and 1, where  $\Phi(f_i) = 1$  indicates perfect complementarity, and  $\Phi(f_i) = 0$  represents no complementarity (similar to a high level of correlation). The index  $\Phi$  is sensitive to the scale of the variables, depends on the persistence (autocorrelation) of the series (not just their cross-correlation), and can be applied to more than two variables<sup>2.1</sup>.

<sup>2.1</sup>For a detailed discussion on the characteristics of this metric, please refer to [27].



### 2.2.2 Variance complementarity index

By considering variance, the variance complementarity index accounts for the variability and spread of the variables, offering a more appropriate evaluation of complementarity compared to correlation. In this metric, Eq. (2.3) can be modified by substituting the total variation with the variance ( $\sigma^2$ ), as follows:

$$\Phi_v(f_i) = 1 - \frac{\sigma^2(f_1 + f_2 + \dots + f_n)}{\sigma^2(f_1) + \sigma^2(f_2) + \dots + \sigma^2(f_n)}, \quad (2.5)$$

where  $-1 < \Phi_v < 1$ . For consistent analysis with other metrics,  $\Phi_v$  is re-scaled as follows:

$$\hat{\Phi} = \frac{(\Phi_v + 1)}{2}, \quad (2.6)$$

with  $0 < \hat{\Phi} < 1$ . Originally,  $\hat{\Phi}$  is designed for only two resources by applying the above definition to two time series, resulting in a correlation-based metric [27]. However, in this chapter, we employ the generalised description presented in Eq. (2.5), and utilise this metric to evaluate complementarity among all four resources.

### 2.2.3 Standard deviation complementarity index

The standard deviation complementarity index, denoted by  $\Phi_s$ , is calculated by replacing the total variation in Eq (2.3) with the standard deviation  $\sigma$ , as follows:

$$\Phi_s(f_i) = 1 - \frac{\sigma(f_1 + f_2 + \dots + f_n)}{\sigma(f_1) + \sigma(f_2) + \dots + \sigma(f_n)}, \quad (2.7)$$

where  $0 < \Phi_s < 1$ . The  $\Phi_s$  metric measures the variability of the sum using the standard deviation and retains the same unit as the original variables, unlike the squared values in  $\Phi_v$ .

### 2.2.4 Complementarity results: An Irish case study

In order to showcase the potential complementarity among resources, the above-mentioned metrics are computed for diverse locations across IOI, considering a range of time scales and combinations of resources. The analysis employs all three complementarity indices, namely  $\Phi$ ,  $\Phi_s$ , and  $\hat{\Phi}$ . To ensure a consistent magnitude scale for assessing complementarity, the time series data for each resource is normalised to its maximum value. This normalisation procedure guarantees fair comparisons and evaluation of complementarity among the various resources.

Table 2.1 presents the complementarity quantification, utilising the indices mentioned above, among all resources (raw data) for 2017, categorised by location. The table indicates that the complementarity among the four resources is consistent across all

**Table 2.1:** Complementarity indices for all raw resources at selected locations around Ireland.

Locations	$\Phi$	$\Phi_s$	$\hat{\Phi}$
Inishtrahull Sound	0.270	0.500	0.569
NorthEast Coast	0.271	0.499	0.570
Copeland Islands	0.257	0.439	0.528
Codling Arklow Banks	0.258	0.463	0.522
Carnsore Point	0.253	0.465	0.534
Gascanane Sound	0.231	0.467	0.555
Dursey Sound	0.190	0.464	0.556
Strangford Lough	0.239	0.431	0.563
Lough Foyle	0.206	0.464	0.563
Shannon Estuary	0.247	0.438	0.526
Bulls Mouth	0.222	0.477	0.549

sites, with only slight variations in the complementarity index values. For example, the minimum value of the total variation complementarity index,  $\Phi$ , is 0.190 in Dursey Sound, while the maximum value is 0.271 on the North-East Coast. The metrics  $\Phi_s$  and  $\hat{\Phi}$  also displayed similar variations. However, it is important to note that metrics based on standard deviation and variance, i.e.  $\Phi_s$  and  $\hat{\Phi}$ , have a tendency to overestimate complementarity, which is consistent with findings in [27]. In this case,  $\hat{\Phi}$  yields the highest values, primarily due to the re-scaling process in (2.6).

Fig. 2.6 illustrates the comparative analysis of the three indices on a seasonal timescale, combining data from all locations to highlight seasonal complementarity. Once again,  $\Phi$  consistently shows a pattern with slight variations ranging from 0.33 to 0.37, indicating the highest complementarity during summer. On the other hand,  $\Phi_s$  and  $\hat{\Phi}$  exhibit larger variations compared to  $\Phi$ , with lower values in the winter and higher values in the spring and summer seasons. The larger variations in  $\Phi_s$  and  $\hat{\Phi}$  can be attributed to the nature of the solar resource during the winter season, where its availability is significantly lower, resulting in greater sensitivity to data variations for these metrics.

Table 2.2 presents the complementarity indices for various resource mix configurations on the IOI, demonstrating the impact of different resource combinations. The table clearly shows that increased diversity in the resource mix corresponds to higher levels of complementarity. When considering  $\Phi$  as a metric, complementarity is lower for resource mixes comprising only two resources, but progressively increases with the addition of third and fourth resources. Including marine energy sources, such as wave and tidal, to the wind-solar mix enhances overall complementarity. The highest

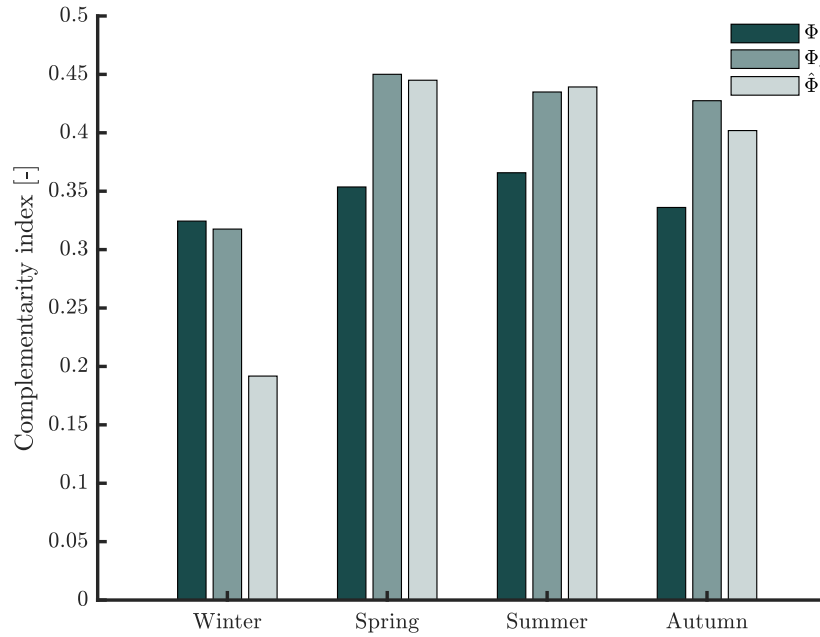


**Figure 2.6:** Seasonal complementarity among four resources around Ireland, considering all chosen data points in Fig. 2.2.

complementarity is achieved when all four resources are included, as indicated by the highlighted text in green. It is worth noting that  $\Phi_s$  and  $\hat{\Phi}$  tend to overestimate complementarity for different resource mixes and exhibit greater sensitivity to adding new resources to the mix.

**Table 2.2:** Complementarity indices for various combinations of resource-mix for Island of Ireland.

Resource Mix	$\Phi$	$\Phi_s$	$\hat{\Phi}$
Wave-wind	0.1055	0.0776	0.1920
Wave-tidal	0.0755	0.3135	0.5347
Wave-solar	0.0753	0.3632	0.6031
Wind-tidal	0.1930	0.2617	0.5101
Wind-solar	0.2232	0.3567	0.5891
Tidal-solar	0.1890	0.2689	0.4985
Wave-wind-tidal	0.2647	0.0417	0.2597
Wave-wind-solar	0.2647	0.0420	0.4223
Wind-tidal-solar	0.3217	0.1478	0.5835
Wave-wind-tidal-solar	0.3470	0.4554	0.4447

The complementarity analysis suggests that introducing more diversity into the electricity generation mix in Ireland can yield several potential benefits. By incorporating

marine energy sources, such as wave and tidal energy, the availability and continuity of renewable generation profiles can be enhanced, complementing the intermittent nature of wind and solar energy. This diversification of the supply systems through marine energy integration can reduce the reliance on extensive energy storage solutions to mitigate the temporal variabilities associated with renewables. The increased complementarity among different renewable resources contributes to a more balanced and consistent electricity supply, reducing the need for large-scale energy storage. However, further quantitative analysis is needed to fully evaluate these potential benefits and their implications for the overall energy system in Ireland.

Additionally, this study highlights a different approach to quantifying complementarity, which has traditionally been approached through the lens of *negative correlation* in the existing literature [27, 38, 39]. The total variation-based index,  $\Phi$ , provides a consistent measure of complementarity by considering the regularity of the sum of variables as a fundamental concept. In contrast, metrics based on standard deviation and variance, such as  $\Phi_s$  and  $\hat{\Phi}$ , have shown to be more sensitive to variations in the time-series data.

## 2.3 Energy balance and balancing cost analysis

This section provides the analysis to find a seasonal optimal mix among wave, tidal, wind and solar generation in a 100% renewable energy scenario for the island of Ireland, without consideration of storage. Based on the data presented in Section 2.1, it is straightforward to quantify an optimal mix, utilising energy balance,  $\Delta(t)$ , as follows:

$$\Delta(t) = P_{\text{mix}}(t) - \langle P_{\text{load}}(t) \rangle, \quad (2.8)$$

with,

$$P_{\text{mix}}(t) = \alpha \langle P_{\text{wave}}(t) \rangle + \beta \langle P_{\text{wind}}(t) \rangle + \epsilon \langle P_{\text{tidal}}(t) \rangle + \delta \langle P_{\text{solar}}(t) \rangle, \quad (2.9)$$

the power generation from the combined system and  $P_{\text{load}}(t)$  is the load demand. The operator  $\langle \cdot \rangle$  represents a normalised time-series to its maximum, while the coefficients  $\alpha$ ,  $\beta$ ,  $\epsilon$  and  $\delta$  represent how much of the load is, on average, covered by wave, wind, tidal and solar power generation, respectively. For a 100% renewable scenario, the above coefficients are constrained to  $\alpha + \beta + \epsilon + \delta = 1$ , i.e. sum of the resource combination is always 100%.

The relative values of power generation and load can result in either a positive or negative balance, depending on whether the generation exceeds or falls short of the load, respectively. In the examined scenarios, the capacities are adjusted to match the electricity load throughout 2017, resulting in a balanced situation. The variability

of the energy balance is further analysed using the standard deviation of the energy balance ( $\sigma_{\Delta}$ ) values over this period. This metric is commonly used [40, 41] in studies exploring *100% renewable-only* scenarios. Therefore, the  $\sigma_{\Delta}$  can be interpreted as a simple measure balancing costs, defined as follows:

$$\sigma_{\Delta} = \sqrt{\langle \Delta^2 \rangle - \langle \Delta \rangle^2}. \quad (2.10)$$

In the following discussion, we will consider balancing costs and the standard deviation of the energy balance interchangeably. It is vital to assess balancing costs at different temporal scales to fully understand the performance of the system. In the following, we examine all possible energy mix scenarios by varying the sharing coefficients ( $\alpha$ ,  $\beta$ ,  $\epsilon$  and  $\delta$ ) between 0 and 1 for daily, and annual, temporal scales.

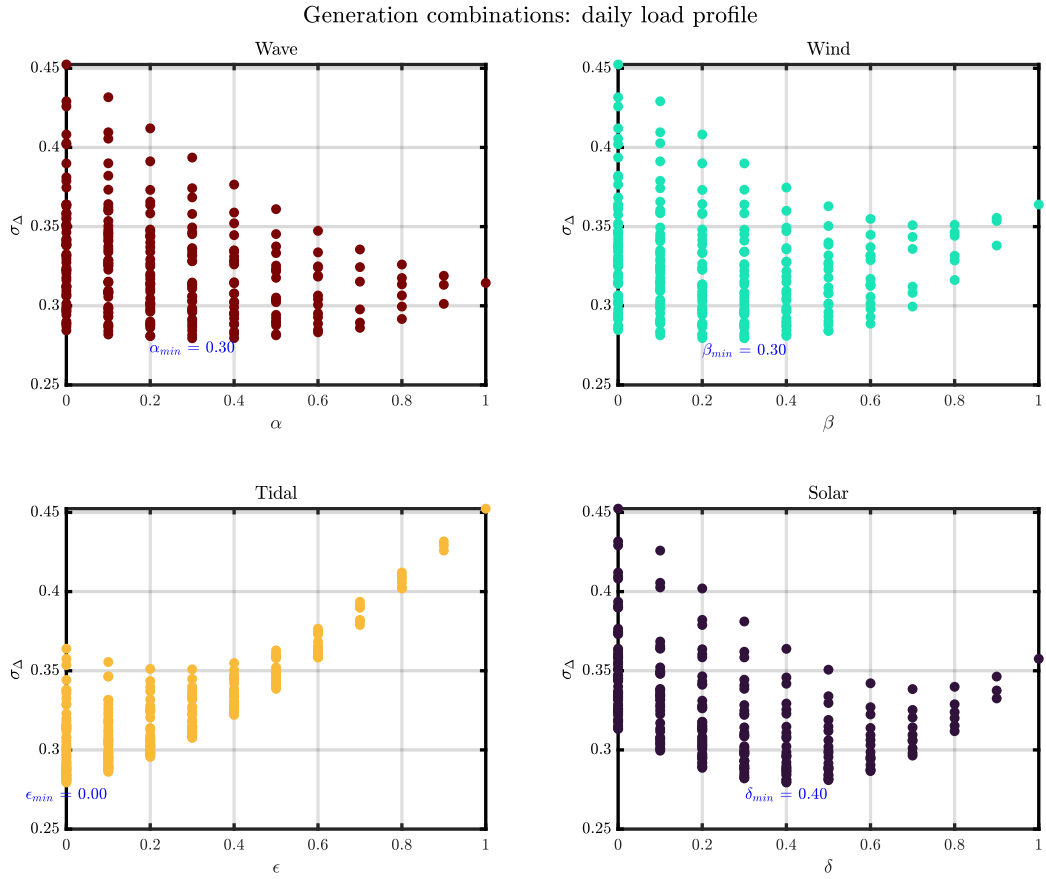


**Figure 2.7:** Standard deviation  $\sigma_{\Delta}$  of the mismatch energy  $\Delta(t)$  as a function of (a) wave fraction  $\alpha$  (b) wind fraction  $\beta$  (c) tidal fraction  $\epsilon$  (d) solar fraction  $\delta$ , in a 100% renewable-only scenario for IOI, based on daily time scale.

For example, Fig. 2.7 presents the standard deviation  $\sigma_{\Delta}$  of the mismatch energy  $\Delta(t)$  and respective generation combinations of all four resources to match a daily load profile. For this particular day (December 31, 2017), the optimal combination,

with the lowest  $\sigma_{\Delta}$ , is 30%-30%-40% wave-wind-solar. Adding tidal in the mix, for this particular day (December 31, 2017), always results in an increased  $\sigma_{\Delta}$ , as shown in Fig. 2.7(c). However, it is worth noting that the results vary for different days, depending on the seasons, in the year 2017. The resultant generation profile for the optimal combination found in Fig. 2.7 is compared with the load profile in Fig. 2.8. It is evident from Fig. 2.8 that the optimal generation-mix can supply load demand for some times of the day but struggles to match the load demand during peak hours.

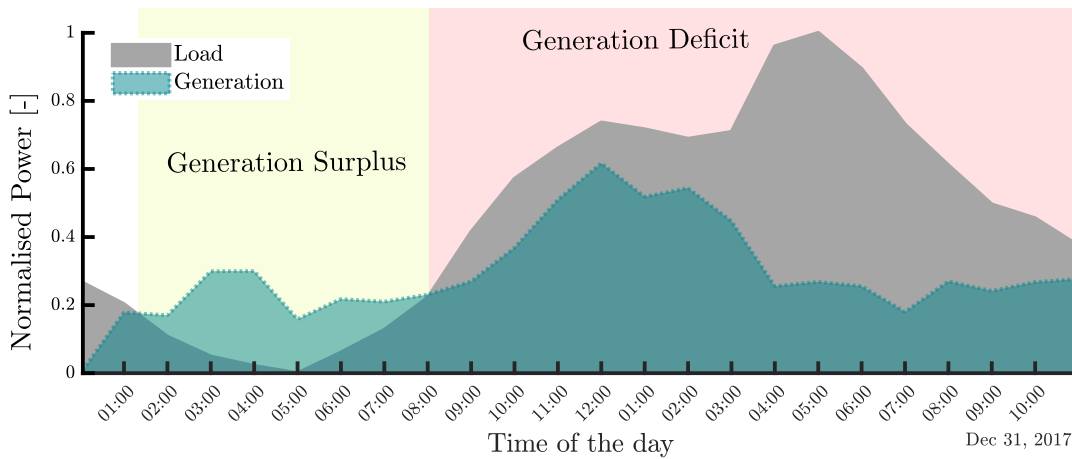


**Figure 2.8:** Generation and load profiles comparison for the optimal combination of all resources for Dec. 31, 2017. The highlighted yellow and red parts denote the prominent generation surplus and deficit regions, respectively.

On the other hand, a scatter plot of various combinations of the four resources to match a yearly load profile, in terms of the standard deviation  $\sigma_{\Delta}$  of the mismatch energy  $\Delta(t)$ , is presented in Fig. 2.9. It is important to note that the annual load profile data is available at an hourly resolution so, to smooth the load demand curve, a 7-day (weekly) moving average is applied before the analysis. In this case, 60%-40% wave-wind results in the lowest standard deviation  $\sigma_{\Delta}$ , which is consistent with the results presented in [6]. Thus, utilising this optimal combination results in the lowest balancing costs. The comparison of the resultant generation profile and annual load profile is presented in Fig. 2.10, showing the patterns of generation surplus and deficit throughout the year. Surprisingly, the addition of solar and/or tidal in the generation-mix results in an increased  $\sigma_{\Delta}$  for 2017.

The preliminary results presented in this section have some limitations, described below:

- Using standard deviation ( $\sigma_{\Delta}$ ) as a simple balancing cost metric may pose some challenges in this context. While  $\sigma_{\Delta}$  does measure the variability between the generation profile and the load profile, it may not provide an accurate representation of the actual balancing costs. For instance, a generation surplus

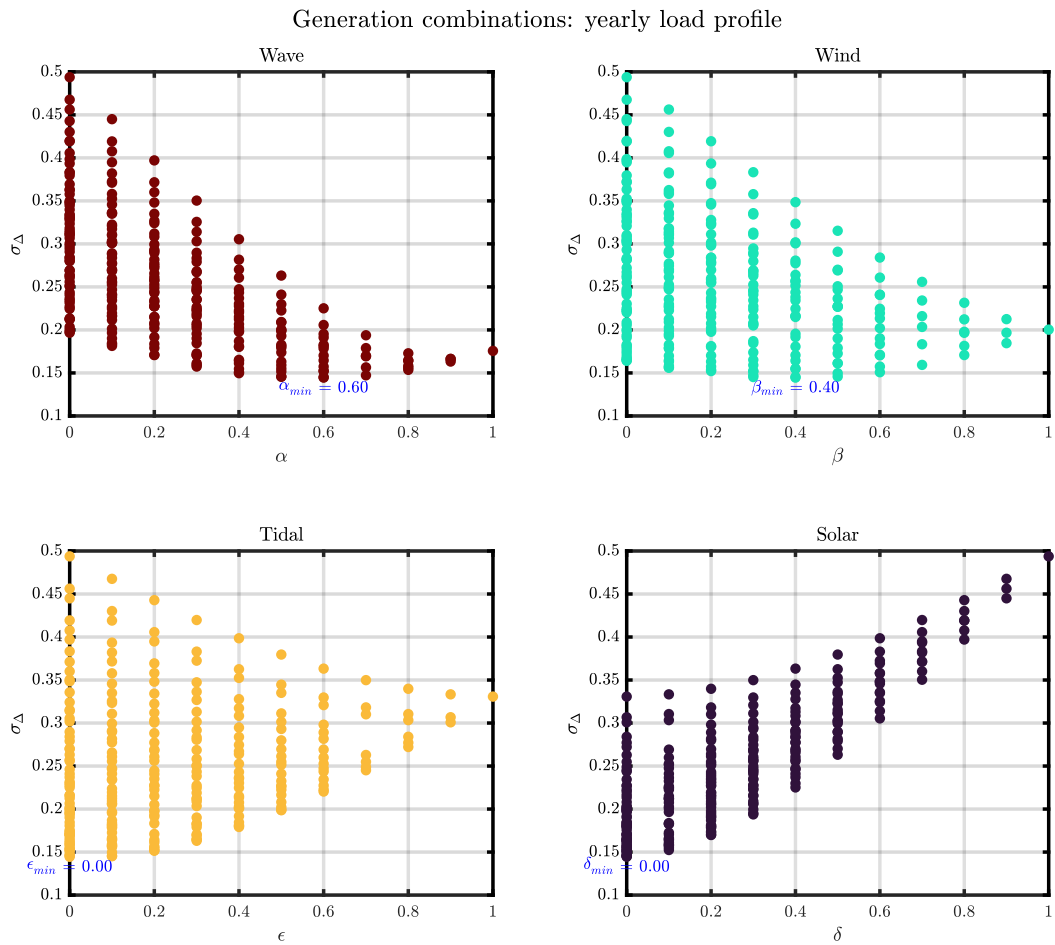


**Figure 2.9:** Standard deviation  $\sigma_{\Delta}$  of the mismatch energy  $\Delta(t)$  as a function of (a) wave fraction  $\alpha$  (b) wind fraction  $\beta$  (c) tidal fraction  $\epsilon$  (d) solar fraction  $\delta$ , in a 100% renewable-only scenario for IOI, based on yearly time scale.

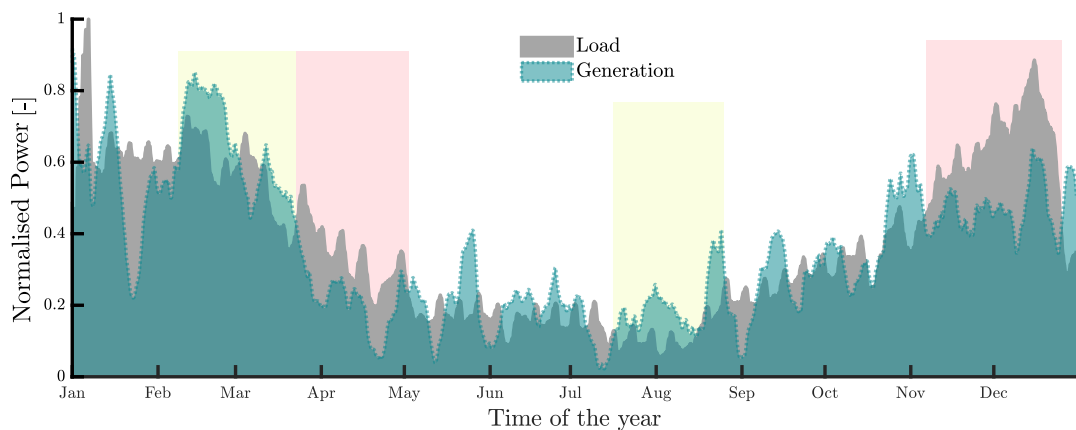


**Figure 2.10:** Generation and load profiles comparison for the optimal combination of all resources for 2017. The highlighted yellow and red parts denote the prominent generation surplus and deficit regions, respectively.

that matches the load curve for a specific time, and can be used for spinning reserve, might result in an increased  $\sigma_{\Delta}$  even though the load demand is adequately met. Therefore, relying solely on  $\sigma_{\Delta}$  as a measure of balancing costs may not accurately reflect the actual costs associated with balancing the generation and load profiles.

- One limitation of the analysis is the use of resource data without any constraint on each resource, which may lead to the identification of an optimal combination that is not practically feasible. For instance, the analysis shows that a 40% solar contribution is optimal in the generation mix for a particular daily load profile (see Fig. 2.7), which may not be feasible in reality [42], highlighting the infeasibility of the proposed 40% solar contribution. Similar arguments can be made for the tidal resource as well.
- The data used for the analysis is only available for year 2017, which is not sufficient for the analysis.

While acknowledging the limitations of the balancing cost analysis, it is essential to recognise that wave energy can still contribute significantly to reducing balancing costs and ensuring a consistent output power in a *wind-dominated* Irish power system. Furthermore, it is possible to meet the electricity demand in Ireland through wave and wind resources only since both of these resources are available in abundance. However, further analysis, with improved balancing cost metrics, more data, and constraints on tidal and solar, is needed to fully evaluate the potential benefits of adding wave energy to the generation mix and its implications for the overall energy system in Ireland.

## 2.4 Conclusions

This chapter focuses on conducting a complementarity assessment of four renewable energy resources on the Island of Ireland, namely wave, wind, tidal, and solar. The evaluation utilises three complementarity indices, namely  $\Phi$ ,  $\Phi_s$ , and  $\hat{\Phi}$ , enabling the simultaneous assessment of complementarity among multiple resources. The obtained results exhibit consistent trends across the three metrics under various test conditions. Among the three indices, the total variation complementarity index  $\Phi$  demonstrates greater reliability and consistency compared to  $\Phi_s$  and  $\hat{\Phi}$ . These latter metrics tend to overestimate complementarity and display higher sensitivity to variations in the time-series data.

The complementarity results also reveal a positive correlation between complementarity and the diversity of supply systems. By integrating marine energy resources such



as wave and tidal power into the wind-solar mix, the IOI energy supply system can potentially benefit from reduced storage and reserve requirements. This finding particularly suggests that including the wave energy resource can enhance the overall resilience and efficiency of the Irish energy supply, offering potential advantages in terms of system reliability and stability.

Despite its limitations, the preliminary balancing costs analysis highlights the value of incorporating wave energy into the predominantly wind-powered Irish electricity system. In particular, the incorporation of wave energy into the generation mix has the potential to reduce balancing costs by reducing the variability associated with the intermittent renewable energy sources.



## **Part II**

### **Preliminaries and state-of-the-art**



# 3

## Grid integration of wave energy and the associated power conversion system

### Contents

---

<b>3.1 Typical wave energy conversion system</b> . . . . .	<b>33</b>
3.1.1 Absorption . . . . .	34
3.1.2 PTO systems . . . . .	38
3.1.3 Power Conditioning . . . . .	40
<b>3.2 The electric grid</b> . . . . .	<b>43</b>
3.2.1 Grid operator's requirements . . . . .	47
<b>3.3 Conclusions</b> . . . . .	<b>49</b>

---

This chapter introduces a typical W2G wave energy conversion system, along with grid integration requirements imposed by the grid codes [12, 13]. All the W2G powertrain components, including wave absorbers, PTO systems, power converters, and storage technologies, are examined. Additionally, a state-of-the-art review of the aforementioned powertrain components and control possibilities for each stage of the powertrain is also presented.

### 3.1 Typical wave energy conversion system

A typical W2G wave energy conversion system is presented in Fig. 3.1, showing the power flow from the ocean waves to the electricity grid. It is clear that extracting useful energy from ocean waves requires multiple stages. The various stages include

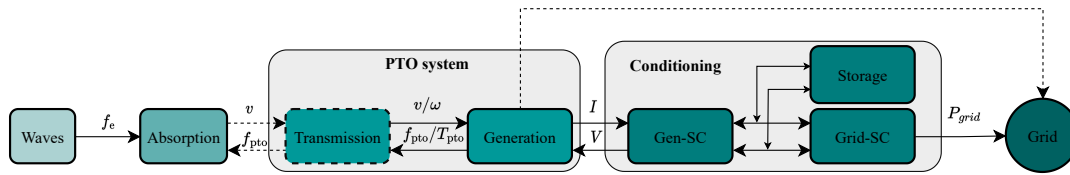


**Figure 3.1:** A typical W2G wave energy conversion system.

the absorption stage, a PTO system (transmission and generation stages) and a power conditioning stage. For a grid-connected wave energy conversion system, all of these stages must work in harmony to provide good-quality power to the grid. The details of each stage of the powertrain are given in the following sections.

### 3.1.1 Absorption

The absorption stage of the W2G powertrain concerns the wave absorber technology used to harness the wave energy resource. As, to date, no profitable standard wave absorber geometry exists, numerous developers, researchers, and innovators have proposed various wave absorber concepts [31]. In the literature, several possible classifications for wave absorbers have been proposed. In particular, wave absorber types may be categorised in relation to (i) size and orientation with respect to the incoming waves, (ii) operating principle, and (iii) proximity to the coast. Fig. 3.2 depicts some popular wave absorber types available in the literature. However, none of the current wave absorbers classifications considers the grid integration perspective. The grid integration process is likely to be more straightforward for wave absorbers with a more steady power output, since less power conditioning is needed. Wave absorbers, whose spectral properties are similar to those of low-pass filters, are desirable for grid integration. Therefore, suitable inertial characteristics of the wave absorbers are essential, and, moreover, a distinct classification based on the inertial characteristics of wave absorbers is needed. However, the PTO that each wave absorber utilises also affects the inertial properties of the wave energy conversion system. For example, certain PTOs, are designed to work with specific types of wave absorbers, such as those for overtopping wave absorbers with reservoirs and hydro turbines, and OWCs with generator/turbine sets. On the other hand, other PTO mechanisms, such as hydraulic PTOs and direct drive PTOs are more ‘*generic*’ and can be utilised with a variety of wave absorbers. In this context, as an alternative to the somewhat standard classifications for wave absorbers, the following classification can be adopted [15, 44, 45]:

1. Absorbers with dedicated PTOs

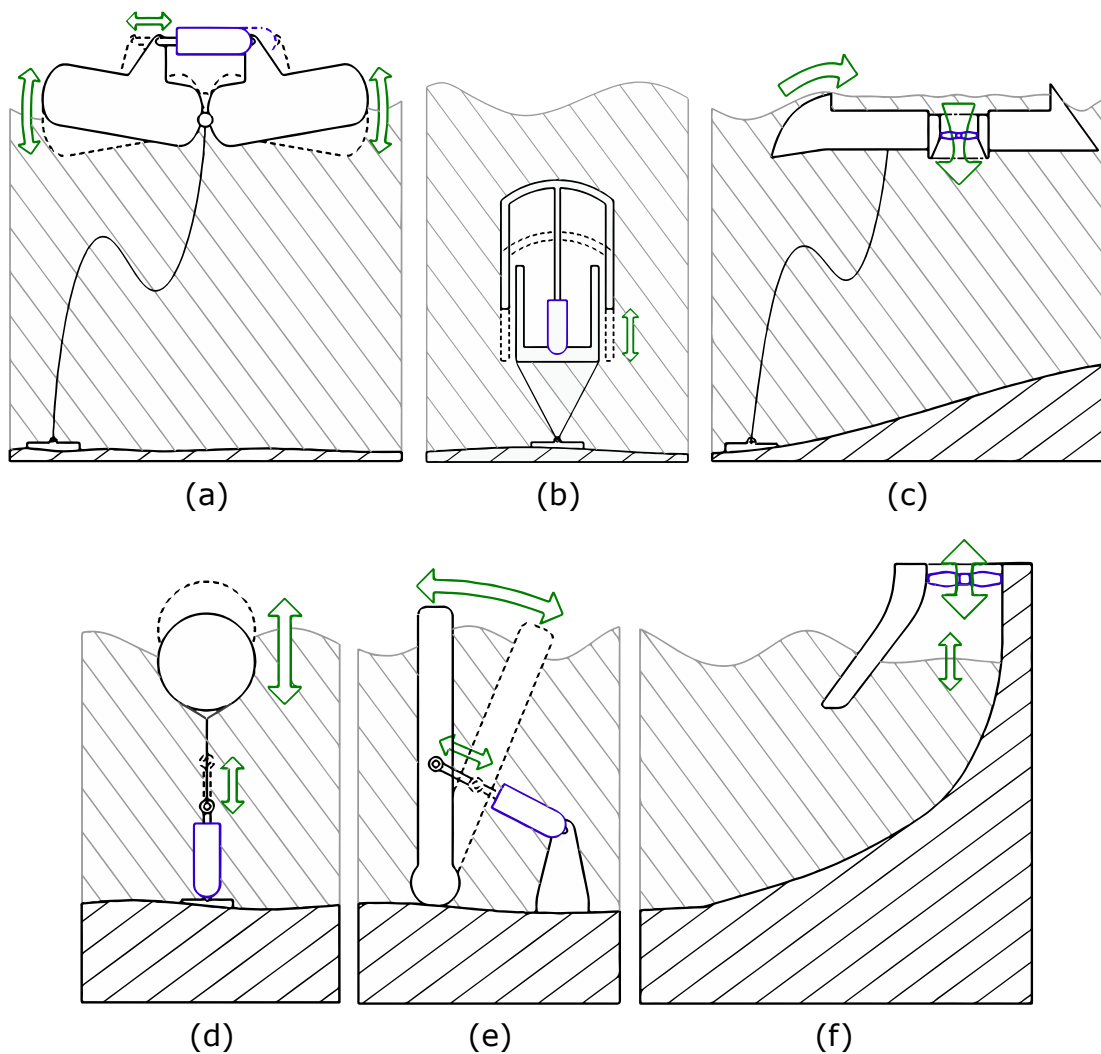


**Figure 3.2:** Types of wave absorbers (adapted from [43]): (a) Attenuator, (b) Pressure differential point absorber, (c) Overtopping, (d) Point absorber, (e) Oscillating wave surge converter (OWSC) (f) Oscillating water column (OWC). Note that the blue part of each sub-figure denotes the PTO system.

- (a) OWC with turbine/generator
- (b) Overtopping with reservoir/hydro turbine

## 2. Absorbers with generic PTOs

- (a) Point absorbers
- (b) Attenuators
- (c) OWSC
- (d) Other devices

### 3.1.1.1 Absorbers with dedicated PTOs

**OWC with turbine/generator:** Oscillating water column (OWC) wave absorbers use air in a hollow chamber that is compressed and decompressed by waves to generate energy (see Fig. 3.2(f)). The airflow spins an air turbine (Wells/axial-flow impulse/radial-flow impulse) [46], which drives an electric generator. While impulse turbines are relatively slow and need 6-8 pole generators, Wells turbines can drive low pole (2-4 pole) high-speed generators [45]. The selection of an air turbine for an OWC mainly depends on the pressure levels in the OWC chamber [47, 48]. Due to the highly variable thermodynamic conditions in the air chamber, a broad operating speed range is needed. Therefore, variable speed generators, such as doubly-fed induction generators (DFIGs) [49], or permanent magnet synchronous generators (PMSGs) [50], should be used with OWCs. The electro-mechanical PTO system (turbine and generator) provides the inertial response of OWC-based wave energy conversion systems. Examples of OWCs are LIMPET, OE buoy and Mutriku WECs [51–53].

**Overtopping with reservoir/hydro turbine:** The working principle of the overtopping wave absorber is very similar to a hydroelectric dam. Incident waves flow onto the ramp, and the water is captured in a reservoir which is then used to drive a low-head turbine as shown in Fig. 3.2(c). Key advantages of using the overtopping wave absorber include unidirectional power flux, and the presence of a reservoir, allowing the use of a constant speed turbine/generator set with this wave absorber. The presence of the reservoir 'storage' also smooths the resource variability effects on the generator and improves inertial characteristics. The nominal speed of conventional hydro turbines is of the order of 100-300 rpm, which is relatively low and requires a carefully designed gearing mechanism if used with overtopping wave absorbers [45]. Wave Dragon is an example of an overtopping wave absorber [54].

### 3.1.1.2 Absorbers with generic PTOs

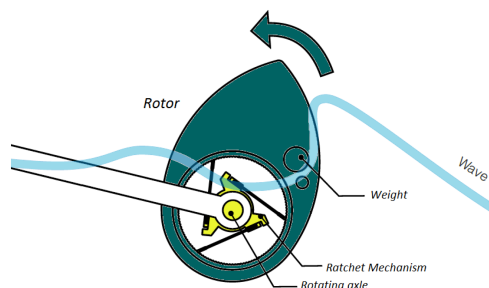
**Point absorber:** Point absorbers can be submerged or floating. Point absorbers are either single-body, bottom referenced (e.g., Fig. 3.2(d)) or multi-body, self-referenced (e.g., Fig. 3.2(b)), and the relative motion between the moving part and the fixed reference part (self or bottom) produces energy. The CorPower wave absorber [55] and the Archimedes wave swing (AWS) [56] are two examples of bottom referenced point absorbers, while the WaveBob [57] is a self-referenced device.



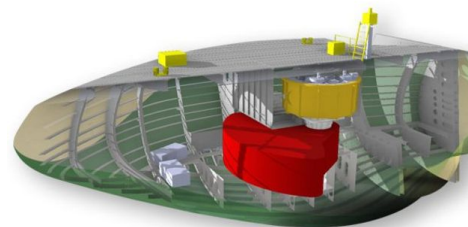
**OWSC:** Oscillating wave surge converters (OWSCs) are oscillating absorbers placed on the sea bed in shallow waters. The 'flap' of the surge converter swings back and forth like an inverted pendulum attached to a pivot, as depicted in Fig. 3.2(e). The Oyster, by Aquamarine Power Ltd., is an example of an OWSC wave absorber [58].

**Attenuators:** Attenuators are floating devices that are placed on the sea surface, parallel to the direction of the incident waves. These wave absorbers generate energy through the relative motion of two arms, or more, (e.g, see Fig. 3.2(a)). The (4 body) Pelamis is an example of an attenuator wave absorber [59], with the (2 body) MOcean [60] being a more recent evolution.

**Other absorbers:** Less established wave absorber technologies [61], which include wave rotors [62, 63] and rotating masses [64], are considered in this paragraph. The operating principles of these wave absorbers differ from the more well-established designs presented in Fig. 3.2. For example Weptos wave rotor [62] (see Fig. 3.3(a)) is composed of several rotors that swivel around a common axle, which is connected to a PTO mechanism. The absorbed energy from the device is transferred to the PTO through the common axle. Another example of wave rotor absorber is the Atargis CycWEC (cyclorotor) [65], which uses lift forces on hydrofoils to extract energy from ocean waves. On the other hand, in rotating mass devices, a heavy mass is displaced by the incoming waves, which then drives a rotating generator to produce electrical energy. This oscillating heavy mass improves the inertial properties of the rotating mass devices, actively contributing to the inertia of the wave energy conversion system. An example of a rotating mass device is Wello Penguin [64], shown in Fig. 3.3(b).



(a) Weptos wave rotor [62], based on the original Salter Duck [66].



(b) Wello Penguin [64].

**Figure 3.3:** Recently developed wave absorbers.

### 3.1.2 PTO systems

The PTO system is a critical part of the W2G powertrain. Like wave absorbers, a wide variety of PTO systems are reported in the literature. In addition to the absorber-specific PTOs described in Section 3.1.1.1, many PTOs can be used with different types of wave absorbers. From a grid integration perspective, such PTOs are categorised as ‘*generic PTOs*’ here. The generic PTOs are broadly classified into two categories:

1. Hydraulic PTOs
2. Direct drive PTOs

#### 3.1.2.1 Hydraulic PTOs

A hydraulic PTO has easy power flow rectification and high force density even at low speeds, making it one of the most widely used PTO mechanisms [67]. The components of a typical hydraulic transmission system are hydraulic motors, hydraulic reservoirs, rectifying valves, accumulators, and hydraulic cylinders. The hydraulic cylinders provide a link between the absorber and the hydraulic circuit. Through rectifying valves, the reciprocating device motion is converted into unidirectional motion. The hydraulic cylinders push the fluid into accumulators, which serve as short-term storage and provide relatively smooth fluid flow to drive the hydraulic motor; therefore, a constant speed generator, such as a squirrel cage induction generator (SCIG), may be used [68]. As a result, a hydraulic PTO coupled with a SCIG allows for the possibility of direct grid connection, rather than via converter connection [69].

#### 3.1.2.2 Direct drive PTOs

Direct drive PTOs do not have a transmission stage and, thus, have a direct mechanical connection with the wave absorber. Direct drive PTOs utilise PMSGs in linear or rotary configurations. In [70], Baker’s analysis found LPMGs to be the most appropriate option for direct drive PTOs. In the linear generator case, the WEC is mechanically linked to the translator of the generator [71]. In the case of rotary generators, the fundamental motion of the wave absorber determines whether or not to use an intermediary mechanism to convert the absorber’s motion into rotary generator motion. For example, the fundamental motion of the wave rotors is rotary and, therefore, they do not require any additional mechanism to use rotary generators, except when it is needed for a specific control strategy, such as latching or declutching control [63]. On the other hand, when the fundamental motion of the absorber is not rotary, intermediary mechanisms, such as gears, rack and pinion mechanisms, pulleys etc., are employed to convert absorber motion into rotary motion. Examples of such

mechanisms include a cascade gearing mechanism in [55], and rack and pinion in [72]. Recent developments in generator technologies, such as vernier hybrid machines (VHM), use a magnetic gearing mechanism instead of mechanical gears, e.g. PTO system for MOcean WEC [73]. Due to the variable speed nature of these generators, their inertial performance is substandard. The lack of inertial storage makes grid connection challenging and requires the wave energy conversion system to handle high peak torque pulses, leading to increased ratings for power conditioning components [45]. It is worth mentioning that the classification presented here aims to understand the inertial characteristics of wave energy conversion systems from a grid integration perspective and, ultimately, to show that the inertial characteristics depend on both the absorber and its PTO mechanism. It should also be noted that a specific type of wave absorber may be combined with different types of PTO mechanisms. For instance, point absorbers may have direct drive, as in [55], or a hydraulic PTO [74]. Therefore, Table 3.1 presents absorber-PTO combinations from the wave energy literature from a grid integration perspective and does not include all the possible absorber-PTO combinations available in the broader wave energy literature<sup>3.1</sup>.

**Table 3.1:** Absorber-generator combinations used in the wave energy grid integration literature. Note: LPMG means linear permanent magnet generator, RPMSG means rotary permanent magnet synchronous generator, DFIG means doubly fed induction generator

Ref. No.	Wave absorber	Generator	Frequency
[76–92]	AWS	LPMG	17
[93–99]	Point Absorber	LPMG	7
[100–104]	Point Absorber	Rotary generators	5
[105–107]	OWC	RPMSG	3
[49, 108–110]	OWC	DFIG	5
[111]	OWSC	LPMG	1
[112]	Overtopping	Rotary generator	1

It is clear from Table 3.1 that variable speed generators, such as LPMGs or RPMSGs, are the most commonly used generators, due to the inherent variability associated with the wave resource. Furthermore, Table 3.1 also shows that the most frequently selected wave absorbers for grid integration studies are point absorbers. In [76–92], the AWS wave absorber is studied. The AWS utilises a direct drive PTO (an LPMG), as shown in Table 3.1. The benefits of all-electric direct drive PTOs, such as simple control and the removal of pneumatic and hydraulic stages from the powertrain, are covered in detail in [93, 101, 113–115]. A comparison of LPMGs and RPMSGs is presented in [116].

<sup>3.1</sup>For detailed absorbers and PTOs classifications, readers are referred to [31, 75]

All-electric direct drive PTOs are also used with other point absorbers, where a linear or rotary generator is used with back-to-back (B2B) power converters. On the other hand, wave absorbers, such as OWCs, OWSCs and overtopping absorbers, also use variable speed generators, i.e. DFIGs and RPMSGs, but are less common in the literature.

### 3.1.3 Power Conditioning

The power conditioning stage includes storage and power converter technologies used for power quality improvement, which are discussed in detail in the following sections.

#### 3.1.3.1 Energy storage systems

An integral part of the W2G powertrain is the energy storage system (ESS). Like other renewable energy technologies, grid-connected wave energy systems typically have lower inertia than traditional generators due to the inclusion of power converters in the W2G powertrain [117]. Therefore, ESSs are required to improve the inertial performance of wave energy systems by mitigating the effects of variability and intermittency associated with the wave resource. Also, ESSs are essential for reactively controlled WECs, due to the negative (reactive) power requirements of reactive hydrodynamic WEC control, an issue unique to wave energy systems, discussed in Part III of this thesis.

From a grid integration of renewable energy technologies perspective, the main focus of the ESSs is to improve power quality by performing power smoothing, short-duration fluctuation suppression, and voltage and frequency regulation. Various ESSs are available in the literature, depending upon the requirements and applications for which they are used, with a review of marine renewable ESSs available in [118]. Typically, ESSs can be categorised as follows:

- Mechanical ESSs
- Thermal ESSs
- Electrical ESSs
- Chemical ESSs

**Mechanical ESSs:** As shown in Fig. 3.4, mechanical storage technologies include compressed air energy storage (CAES), pumped hydro storage, and flywheels. Due to the larger physical size of the storage component, mechanical ESSs typically have higher power ratings. Fast response times and high energy density are necessary for grid integration purposes. Therefore, flywheels can be useful for wave energy applications, even though their high self-discharge losses may be an obstacle [119].

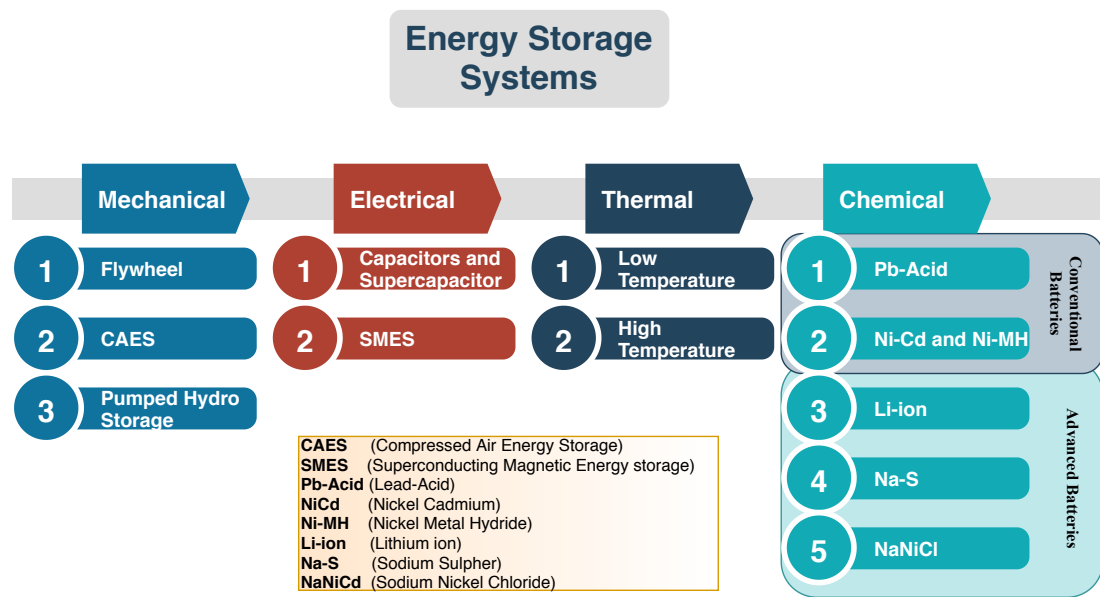


**Figure 3.4:** Classification of energy storage systems [15].

**Electrical ESSs:** Electrical storage technologies are frequently used for grid integration of renewable energy sources. Examples of these technologies are supercapacitors, capacitors, and superconducting magnetic energy storage (SMES), as shown in Fig. 3.4. Despite their poor self-discharge response, these devices are suitable for grid integration and power quality improvement applications due to their higher cycle efficiency and peak power deliverability [120, 121].

**Thermal ESSs:** Thermal ESSs are broadly classified into low-temperature and high-temperature thermal ESSs. Despite having high energy density, low-temperature thermal ESSs, such as cryogenic ESSs, are not considered an appropriate option for grid integration of wave energy due to their lower efficiency and early development stage [119]. On the other hand, although high-temperature systems, such as latent heat storage are already in use for solar thermal applications, their lower efficiency at this early development stage makes them difficult to incorporate into grid integration technologies [122].

**Chemical ESSs** Chemical ESSs are divided into conventional and advanced batteries and are the most frequently used ESSs in various application areas, including mobile phones, electric vehicles, etc. [120]. Lead-acid (Pb-acid), Nickel Cadmium (NiCd) and Nickel-Metal Hydride (Ni-MH) batteries are examples of conventional batteries that are mature technologies, and are used in a diverse range of applications. On the other hand, Lithium-ion (Li-ion), Sodium Sulphur (Na-S), and Sodium Nickel Chloride (NaNiCl) batteries are examples of advanced

batteries. Li-ion is the most widely used battery storage technology, used in virtually every portable electronic device using batteries [123]. In addition to the technologies mentioned above, chemical storage encompasses electrochemical energy storage systems. Among these electrochemical ESSs are fuel cells, which come in various forms and are used in multiple applications, including grid integration, due to their fast response characteristics. Thus, fuel cells play a crucial role in the grid integration of renewable energy, voltage control, and frequency regulation [123].

The utilisation of ESSs for wave energy grid integration is mainly concerned with power quality improvement, as documented in a number of WEC grid integration studies [98, 99, 102, 103]. Hence, the choice of storage technology, and its energy capacity, is informed by the wave climate at a deployment site, as well as the requirements of the W2G controllers. Furthermore, ESSs can also be used for virtual inertia emulation for wave energy systems, as shown by Parwal et al. in [124], by providing virtual inertia through a virtual excitation controller. A review of literature regarding wave energy grid integration indicates that most works use DC-link capacitors as a short-term storage component between the B2B power converters (e.g., see Table 3.3). However, the use of other storage technologies has also been reported in the literature, such as super-capacitors [103], pumped undersea storage system (USS) [99] or a combination of two storage technologies to form a hybrid energy storage system (HESS) [17, 125].

### 3.1.3.2 Power converters and their control

Wave energy systems have power intermittency issues due to the inherent irregularity of the wave resource [126] and, consequently, they cannot be directly connected to the grid. Therefore, a power conversion system is required for the grid-connection of a wave energy conversion system. The power conversion system, along with its control, makes it possible for a wave energy system to be connected to the grid [98].

A review of grid integration studies of wave energy, in terms of power converter technology, W2G control techniques, and storage systems is presented in Table 3.3. The majority of the studies reviewed in Table 3.3 utilise a B2B AC/DC/AC power converter topology in their grid-connected wave energy systems to allow for power conditioning. Moreover, other power converter topologies, such as the diode bridge rectifier (DBR) and boost converter combination [80, 95] on the device side, and modular multilevel converter (MMC) [96, 99] and neutral point clamped (NPC) inverters [95] on the grid side, are also reported. From a control perspective, the literature review on grid integration studies, schematically summarised in Table 3.3, highlights some significant limitations, in terms of W2G control techniques. In particular, simplified passive

damping hydrodynamic WEC control and relatively rudimentary PI power converter control are the default controller choices. Depending upon the area of expertise of the researchers, the focus of the studies changes from the hydrodynamic side to the electrical side. For example, in [76–85, 93, 94, 102, 114, 125, 127–132], the focus is on maximum power extraction from waves (hydrodynamic control). Hydrodynamic WEC controllers are broadly categorised into passive damping and reactive controllers. The difference between reactive and passive controllers lies in the bidirectional power flow requirement, meaning that reactive controllers require bidirectional power flow, whereas passive controllers do not have such a bidirectional power flow requirement. In [133], a review of hydrodynamic WEC controllers is presented. Complex-conjugate [93] and phase and amplitude control [114] strategies are also classified as reactive. Table 3.3 also reflects the default choice of hydrodynamic control for grid integration studies is passive damping. However, in [101], while the authors simulate both passive and reactive hydrodynamic WEC controllers for the device side, only a passive controller is implemented in a grid-connected case study. On the other hand, power converters and their control are given substantially less consideration, and mostly PI control is used for power converters in the powertrain (see Table 3.3).

## 3.2 The electric grid

This section discusses the last part of the W2G powertrain, i.e. the electric grid. In particular, grid connection requirements imposed by the transmission system operators (TSOs), via the grid codes are described here. Several components comprise an electric grid, including generating stations (thermal, hydro, solar, wind, wave power etc.), transmission lines, and distribution systems. All of these components must operate in tandem to provide consumers with consistent power. The electricity is generated at the generating stations, which can be conventional or renewable power plants. Since most generating stations are situated far from the densely populated areas where electricity is consumed, they need to transmit the generated electricity over long distances to reach load centres. To this end, transformers are employed at the generating stations to step up the voltage to minimise the losses within the transmission lines. When the generated electricity reaches populated areas (load centres), transformers are again utilised to step down the voltage to a safer and more practical voltage for consumers. As Section 3.1.1 outlines, wave absorbers can be deployed onshore or offshore. Establishing a grid connection for onshore devices is relatively straightforward, given their proximity to existing infrastructure. However, the situation is more complex for offshore devices. In this case, a comprehensive electrical infrastructure, particularly a transmission system, is essential to transport the generated electricity from the

**Table 3.2:** Reference guide to read Table 3.3

Column	Brief description																		
Ref. No.	List of studies reviewed.																		
Power converter Topology	Types of power converter technology use for device- and grid-sides.																		
Control techniques	Types of W2G powertrain controllers, divided into hydrodynamic/turbine control (HDC/TC), Gen-SC control and Grid-SC control.																		
Storage	Type of storage component used.																		
-	No information is provided in the study.																		
Abbreviations	<table border="0"> <tbody> <tr> <td><b>DBR</b> Diode Bridge Rectifier</td> <td><b>AFE</b> Active front End</td> </tr> <tr> <td><b>BC</b> Boost Converter</td> <td><b>MMC</b> Modular Multilevel Converter</td> </tr> <tr> <td><b>Gen-SC</b> Generator Side Converter</td> <td><b>NLVCS</b> Non-Linear Vector Current Source</td> </tr> <tr> <td><b>VSI</b> Voltage Source Inverter</td> <td><b>MPC</b> Model Predictive Control</td> </tr> <tr> <td><b>DBES</b> Distributed Battery Energy Storage System</td> <td><b>USS</b> Undersea storage system</td> </tr> <tr> <td><b>LVRT</b> Low Voltage Ride-Through</td> <td><b>PDLSPWM</b> Phase Disposition Method of Level-Shifted PWM</td> </tr> <tr> <td><b>GSA</b> Gravitational Search Algorithm</td> <td><b>FCSMPC</b> Finite Control Set MPC</td> </tr> <tr> <td><b>WCA</b> Water Cycle Algorithm</td> <td><b>FOC</b> Field Oriented Control</td> </tr> <tr> <td><b>PCC</b> Point of Common Coupling</td> <td><b>DPTC-SVM</b> Direct Power Control using Space Vector Modulation</td> </tr> </tbody> </table>	<b>DBR</b> Diode Bridge Rectifier	<b>AFE</b> Active front End	<b>BC</b> Boost Converter	<b>MMC</b> Modular Multilevel Converter	<b>Gen-SC</b> Generator Side Converter	<b>NLVCS</b> Non-Linear Vector Current Source	<b>VSI</b> Voltage Source Inverter	<b>MPC</b> Model Predictive Control	<b>DBES</b> Distributed Battery Energy Storage System	<b>USS</b> Undersea storage system	<b>LVRT</b> Low Voltage Ride-Through	<b>PDLSPWM</b> Phase Disposition Method of Level-Shifted PWM	<b>GSA</b> Gravitational Search Algorithm	<b>FCSMPC</b> Finite Control Set MPC	<b>WCA</b> Water Cycle Algorithm	<b>FOC</b> Field Oriented Control	<b>PCC</b> Point of Common Coupling	<b>DPTC-SVM</b> Direct Power Control using Space Vector Modulation
<b>DBR</b> Diode Bridge Rectifier	<b>AFE</b> Active front End																		
<b>BC</b> Boost Converter	<b>MMC</b> Modular Multilevel Converter																		
<b>Gen-SC</b> Generator Side Converter	<b>NLVCS</b> Non-Linear Vector Current Source																		
<b>VSI</b> Voltage Source Inverter	<b>MPC</b> Model Predictive Control																		
<b>DBES</b> Distributed Battery Energy Storage System	<b>USS</b> Undersea storage system																		
<b>LVRT</b> Low Voltage Ride-Through	<b>PDLSPWM</b> Phase Disposition Method of Level-Shifted PWM																		
<b>GSA</b> Gravitational Search Algorithm	<b>FCSMPC</b> Finite Control Set MPC																		
<b>WCA</b> Water Cycle Algorithm	<b>FOC</b> Field Oriented Control																		
<b>PCC</b> Point of Common Coupling	<b>DPTC-SVM</b> Direct Power Control using Space Vector Modulation																		

offshore location to a connection point with the local grid. The most common way to transport is via sub-sea power cables [134]. Two technologies commonly transport electrical energy and are usually used to link offshore wind farms to the grid: alternating current (AC) and direct current (DC). Wave farms will also be expected to use similar infrastructure.

**AC connection:** Opting for an AC connection is a logical decision when connecting AC-producing wave farms to the AC electric grid. Utilising the internal wave farm voltage for transmission eliminates the necessity for offshore transformers. While this configuration offers the advantage of not requiring offshore transmission equipment, it comes with two significant drawbacks: capacity issues of sub-sea



### 3. Grid integration of wave energy and the associated power conversion system 45

**Table 3.3:** Review of power converters, W2G controllers, and energy storage for grid integration of wave energy.

Ref. No.	Power converter topology			Control techniques			Storage
	Device-side	Grid-side		HDC/TC	Gen-SC	Grid-SC	
[80]	DBR and BC	Inverter		Passive damping	PI	PI	DC-link Capacitor
[76]	AC/DC converter	Inverter		Passive damping	PI	PI	DC-link Capacitor
[79]	AC/DC converter	Inverter		Optimal passive	PI	PI	DC-link Capacitor
[81]	Active rectifier	Inverter		Optimal passive	PI	PI	DC-link Capacitor & DBES
[82]	AC/DC VSC	DC/AC VSC		MPPT	PI	PI	DC-link Capacitor
[83]	AC/DC converter	BBC		Passive damping	GSA PI	GSA PI	-
[85]	AC/DC converter	DC/AC Inverter		Passive damping	WCA PI	WCA PI	DC-link Capacitor
[86–88]	Active rectifier	Inverter		Passive damping	PI	PI	DC-link Capacitor and Supercapacitor
[125]	AC/DC converter	DC/AC Inverter		Passive damping	PI	PI	Battery and Supercapacitor HESS
[93]	AC/DC converter	DC/AC Inverter		Passive and ACC	-	-	DC-link Capacitor
[94]	Active rectifier	DC/AC Inverter		MPC with Cu-losses	PI	PI	DC-link Capacitor
[95]	DBR and BC	NPC Inverter			DC voltage control	Predictive current control	DC-link Capacitor
[96]	Active rectifier	MMC		Passive damping	PI	NLVCS control	DC-link Capacitor
[97, 98]	AC/DC rectifier	VSI		Passive damping	PI	PI	DC-link Capacitor
[99]	AC/DC converter	MMC inverter		Optimal passive	PI	PDLSPWM & PSCB control	USS
[100]	AC/DC converter	DC/AC Inverter		Threshold control & Equivalent saturation control	-	-	-
[101]	AC/DC converter	DC/AC Inverter		Passive & reactive loading	FOC based PI	AFE based PI	DC-link Capacitor
[102]	AC/DC converter	DC/AC Inverter		Passive & reactive loading with saturation	FOC based PI	Droop control	Ideal short-term ESS
[103]	AC/DC converter	DC/AC Inverter		Max. power extraction control	-	-	Super-capacitor
[105, 106]	Active rectifier	2-level VSI		Turbine speed control	FCSMPC	FCSMPC	Battery in [105] & Super-capacitor in [106]
[107]	AC/DC converter	DC/AC Inverter		Torque control	FOC based PI	LVRT control	Super-capacitor
[49, 108]	AC/DC rectifier	DC/AC Inverter		Air flow control	PI	PI	DC-link Capacitor
[109, 110]	AC/DC rectifier	DC/AC Inverter		Air flow control	Neural control	Neural control	DC-link Capacitor
[111]	AC/DC converter	DC/AC Inverter		-	Hysteresis band control	PI	DC-link Capacitor
[111]	-	DC/AC Inverter		-	-	DPTC-SVM	DC-link Capacitor

cables and increased Ohmic losses ( $I^2R$ ). These limitations restrict the feasibility of such connections to a range of 10-15 km offshore.

Mitigating Ohmic losses often involves stepping up the voltage, a commonly employed practice. This necessitates the installation of a transformer (substation) at the offshore farm location. While this approach effectively reduces Ohmic losses, it comes at the cost of implementing a costly offshore substation to accommodate the transformer. With high voltage cables, the transmission length of the system is no longer restricted by Ohmic resistance but rather by the electrical characteristics of insulated cables. The dielectric insulation, acting as a capacitor under alternating current, introduces a limitation as the realignment of electric dipoles during voltage changes produces heat, resulting in a loss of active power. Transmission of high voltage AC (HVAC) is economically feasible for distances up to 50-100 km [134].

**High Voltage Direct Current (HVDC) connection:** Conversion to DC is necessary to cover distances beyond the practical reach of medium and high-voltage AC. This conversion occurs at an offshore converter and transformer station, with a subsequent conversion back from DC to AC at the onshore grid connection point. Currently, two conversion systems are in operation: conventional HVDC with line-commutated converters (HVDC-LCC) and HVDC plus with voltage source converters (HVDC-VSC). Conventional HVDC-LCC system is typically employed for transporting electrical energy over extensive distances [135]. However, the HVDC-LCC system requires capacitive compensation equipment, i.e. STATCOMs, to compensate for the reactive power requirement of the grid. On the other hand, HVDC-VSC technology, which employs IEGTs or IGBTs, allows for active and reactive power control on both sides (not possible with an LCC system), providing more flexibility. Hence, HVDC-VSC is preferable over distances larger than 50 km [135].

A wave energy conversion system produces intermittent power as a result of irregular (panchromatic) waves. If a wave farm is connected to the grid without an appropriate power conditioning system, these power oscillations can be damaging to the grid. Any power plant requiring a grid connection is required to comply with grid codes that impose restrictions on power quality. These requirements are presented in the following sections.

### 3.2.1 Grid operator's requirements

Grid regulations, which regulate all parts of a grid, including planning, design, connection requirements, and operational activities, were created due to the complexity of electrical networks. Grid codes have also been updated to reflect the changes brought about by the surge of renewable energy penetration due to the growth in their generation capacity and intermittent nature. For instance, these specifications, for wind farms, are reviewed in [136]. TSOs in every country specify the grid-codes. For example, EirGrid specifies Irish grid codes [12], National Grid ESO specifies UK grid codes [13], and National Transmission and Dispatch Company (NTDC) specifies grid codes in Pakistan [137].

**Voltage variations:** For a new power plant to be connected to a grid, grid codes specify allowable voltage variations. Voltage variations can be categorised into long-term and short-term variations. Table 3.4 presents the long-term voltage variations allowed for Irish and UK jurisdictions. Table 3.4 shows that the voltage variations are specified in terms of a percentage/range of the nominal grid voltage at the grid connection point. Short-term variations, however, relate

**Table 3.4:** Voltage variations allowed for Irish grid [12] and the UK grid [13].

Grid connection voltage		Nominal operating ranges	
Ireland	UK	Ireland	UK
110kV	132kV	105-120kV	132kV $\pm 10\%$
220kV	275kV	210-240kV	275kV $\pm 10\%$
400kV	400kV	370-410kV	400kV $\pm 5\%$

to the power quality issues, such as sag, swell and interruption. IEEE standard 1159-2009 [138], revised in 2019 [139], further categorises short-term variations into instantaneous, momentary, and temporary, depending upon the duration of these variations. Additionally, harmonics, phase imbalance and flicker issues can distort voltage waveform quality. In the wave energy literature, flicker estimation has been the primary focus, estimated by the international electrotechnical commission (IEC) standard 61400-21. For example, in [126], flicker evaluation was carried out at several levels using assessment charts. Blavette et al. [140] developed a simplified approach to flicker estimation for wave energy farms. The effects of wave farms on the grid in terms of flicker are explored in [141, 142], and it is demonstrated that the number of WECs in a wave farm directly influences the amount of flicker present in that wave farm power output.

**Frequency variations:** In electric grids, frequency stability is paramount, since a slight variation in the frequency can have significant implications for the power network. Therefore, grid codes set out strict operating frequency ranges for a new power plant grid connection, as presented in Table 3.5 for the Irish grid. Even under fault conditions, the power plant must be connected to the grid for a specified duration.

**Table 3.5:** Frequency variations and time limits for the Irish grid [12].

Sr. No.	Frequency limits [Hz]	Time duration
1.	49.5-50.5	Continuous
2.	47.5-52.0	60 minutes
3.	47.0-47.5	20 seconds

**FRT requirements:** Another critical requirement, specified by the grid codes for a new plant requiring grid connection, is the fault ride-through (FRT) capability. In essence, the grid requires power plants to be connected to the grid under voltage dips. During voltage dips, generation plants increase electrical reactive power injection to the grid to compensate for voltage dips caused by fault conditions, which induces peak currents potentially harmful to the equipment. The plant can be disconnected from the grid as a straightforward solution, but this is not ideal as it may lead to a chain reaction of disconnection, which may cause the entire grid network to collapse [14]. The FRT requirements, for the Irish grid, are laid out in Table 3.6.

**Table 3.6:** Frequency variations and time limits for the Irish grid [12].

Voltage dip	FRT times [ms]		
	110kV	220kV	400kV
95% (5% retained)	150	150	150
50% (50% retained)	450	450	450

**Active and reactive power responses:** A power generating plant's active and reactive power responses are essential because they guarantee grid stability during a fault. In this regard, grid codes place strict restrictions on a generating station's ability to respond to power demands, especially for renewable plants [143]. For instance, under Irish grid codes, wind power plants must provide active power support. They should restore their active power output to 90% of the rated value within one second of the voltage recovery at 0.9 per unit (pu) [12]. In this regard,

the active power control of the plant offers frequency stability. During voltage dips and other faults, generating stations must support voltage regulation and inject electrical reactive power into the grid.

Currently, these regulations apply to wind turbines subject to European grid codes [143–145], and wave energy devices will be subject to similar restrictions after incorporation into the grid.

### **3.3 Conclusions**

This chapter introduces W2G powertrain components for wave energy systems, including wave absorbers, PTO systems, power converters, storage systems, and the electric grid. In particular, a classification of wave absorbers based on their inertial characteristics from a grid integration perspective is presented. It is concluded that the inertial characteristics of a wave energy system depend on the wave absorber type and the PTO system it uses.

The power conditioning stage encompasses power converters and storage systems, which are discussed in detail. Additionally, a review of the literature is presented in terms of control of various powertrain stages, power converter topologies and the type of storage component used. Although several grid integration studies are available in the literature, most studies focus only on one part of the powertrain. Additionally, a complete W2G control framework, tackling both device- and grid-side requirements/constraints, is currently non-existent in the literature. In particular, the reactive hydrodynamic control implementation for grid-connected wave energy systems is not available in the literature.

Finally, grid connection requirements are discussed, including voltage, frequency, and FRT requirements imposed by the grid codes. These grid requirements are expected to evolve as more wave energy is integrated into the grid.

Drawing from the discussion in this section, Part III of this thesis presents a complete W2G control framework, addressing both device- and grid-side requirements.



# 4

## Hydrodynamic WEC modelling

### Contents

---

<b>4.1</b>	<b>Ocean waves</b>	<b>53</b>
4.1.1	Regular waves	53
4.1.2	Irregular waves	54
<b>4.2</b>	<b>Linear WEC modelling</b>	<b>55</b>
4.2.1	Navier-Stokes equations	56
4.2.2	Linear potential flow theory	56
4.2.3	Cummins' equation	61
4.2.4	Radiation convolution term approximation	62
4.2.5	WEC state-space representation	63
<b>4.3</b>	<b>Hydrodynamic models: state-of-the-art</b>	<b>64</b>
<b>4.4</b>	<b>Conclusions</b>	<b>65</b>

---

As described in Chapter 1, one of the objectives of the thesis is to provide a computationally efficient W2G model suitable for control applications. However, most of the literature on grid integration of wave energy still uses simplified linear WEC models, where radiation forces are not modelled accurately (see Section 4.3). Consequently, there is a need for WEC models that include proper radiation force quantification in the literature concerning wave energy grid integration.

Although linear WEC models provide a reasonably accurate description of linear WEC dynamics, they can be limiting under certain conditions, for certain devices. For instance, the energy-maximising WEC control often exaggerates device motion, violating the small device motion assumption of the linear potential flow theory, as detailed in Section 4.2.2. Therefore, the assumptions on which linear models are based

can be violated when using them to design WEC controllers, creating a modelling paradox [146]. Since this thesis analyses a grid-connected WEC under controlled conditions, using a linear WEC model may not be appropriate. Nevertheless, at this stage, linear models that properly quantify radiation forces provide an improvement in the literature regarding grid integration of wave energy, in which the *simplified* mass-spring-damper model is still the most commonly used WEC model (see Section 4.3). Therefore, assessing the W2G controlled performance of a grid-connected wave energy conversion system with linear WEC models is essential before implementing nonlinear WEC models. Additionally, if the device is a cylindrical WEC (linear Froude-Krylov forces) with a rounded bottom (little viscous drag), like the device used in Chapter 8 (see Fig. 8.4), then the hydrodynamic model may be predominantly linear, especially for small/moderate motion.

Nonlinear WEC models, which include typical nonlinearities associated with WEC hydrodynamics, can be more accurate at capturing the motion of a WEC. However, these models are more computationally intensive and may be unsuitable for control design. Furthermore, the dominant nonlinear terms depend on the WEC type and its specific geometry [147]; therefore, a unique nonlinear WEC description cannot be found in the literature. On the other hand, Cummins' equation [148] can be considered a general description for linear WECs as it is widely used in the literature for various types of WECs. Additionally, linear WEC models, with correctly modelled radiation forces, offer a reasonable compromise between accuracy and computational efficiency, especially for specific types of devices. Therefore, in this thesis, linear WEC hydrodynamic models are used in the complete W2G modelling to balance computational effort and model fidelity. In this regard, this chapter introduces a linear WEC model and the assumptions associated with the model to better understand the limitations of the final (linear) WEC model.

This chapter is organised as follows: the mathematical representation of (regular and irregular) ocean waves is described in Section 4.1. Then, Section 4.2 provides an introduction to linear WEC modelling based on the linear potential theory (LPT) assumptions [149]. In particular, Cummins' equation [148], which is the most widely used linear description of the wave/WEC dynamic interaction in the WEC control literature, is derived from Navier-Stokes equations using the LPT assumptions. Additionally, a suitable state-space representation for WEC control design is detailed. Furthermore, a review of hydrodynamic models used for grid integration of WECs is included in Section 4.3. Finally, Section 4.4 concludes this chapter.



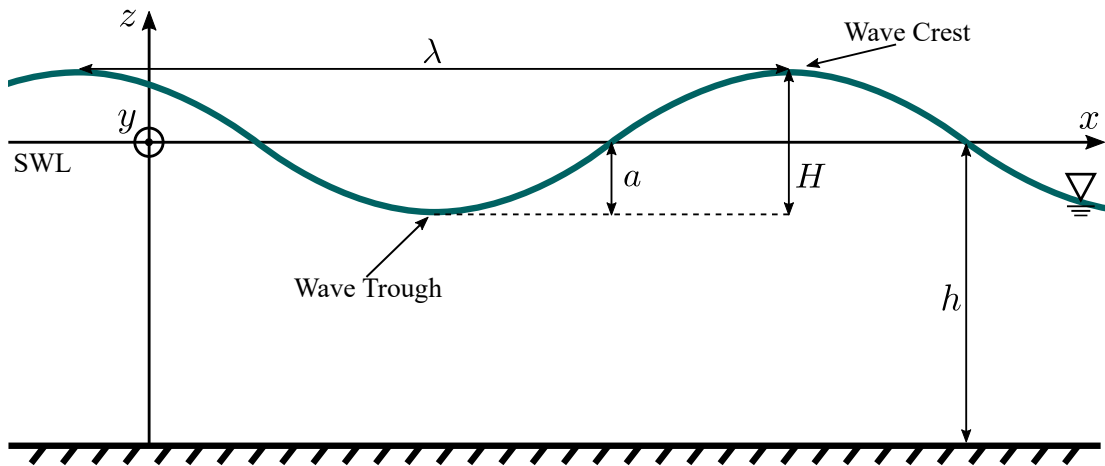


**Figure 4.1:** Ocean wave characteristics. The blue line represents the free surface, and SWL represents still water level or undisturbed free surface.

## 4.1 Ocean waves

Ocean waves can be represented mathematically in various ways, from a simple monochromatic representation (a single sinusoid with constant phase and amplitude) to a highly complex irregular, three-dimensional, nonlinear representation. Due to the complexities involved in nonlinear wave characterisations, numerous theories have been proposed in the ocean engineering literature. In this section (and in this thesis), first order waves are considered, which are derived from linear wave theory or Airy's wave theory (as credited to the mathematician George Airy) [150]. This theory is used to describe wind generated waves propagating on a free surface.

Fig. 4.1 illustrates the wave characteristics under linear wave theory, where  $\lambda$  represents wavelength,  $H = 2a$  represents wave height, with  $a$  being the wave amplitude, and  $h$  is the depth of water. Furthermore, Fig. 4.1 also illustrates the coordinate system considered here, where the  $x$ -axis denotes the direction of wave propagation, the  $y$ -axis is out of the page, and the  $z$ -axis is perpendicular to the free surface. Even though linear wave theory only describes waves with  $H/\lambda \ll 1$  (i.e., waves for which the wave height is significantly smaller than the wavelength), it provides a suitable description of the typical operational wave resource in most cases, since WECs mainly operate in power-production model in light to moderate sea-states (i.e.,  $H/\lambda \ll 1$ ) [2].

### 4.1.1 Regular waves

Regular (monochromatic) waves have a single frequency  $\omega$  (or, alternatively, a period  $T = 2\pi/\omega$ ). Assuming *long-crested* (or planar) waves, i.e. waves which stretch only in the  $z$ -direction in Fig. 4.1, the two-dimensional representation, in time and space, of the free surface elevation  $\eta$  can be written as

$$\eta(x, t) = \frac{H}{2} \cos(\omega t + \phi_w(x, \omega)), \quad (4.1)$$

with  $\phi_w$  represents a phase shift, depending upon the spatial coordinate  $x$  and  $\omega$ . Regular (monochromatic) waves do not generally represent real sea-states; however, they are useful for deriving theoretical results in the frequency domain. For instance, regular waves are used for deriving the impedance matching principle, which provides theoretical foundations for energy maximising WEC control [151], along with the determination of other fundamental results for ocean devices.

### 4.1.2 Irregular waves

Due to the intrinsic limitations associated with regular waves, regarding the misrepresentation of ocean waves, irregular waves based on a stochastic description are needed. In particular, the free surface elevation  $\eta$  for irregular waves is generated using a spectral density function (SDF) representing a real sea state. Some examples of such SDFs include the JONSWAP spectrum for waves with fetch limitations [152], the Bretschneider spectrum for developing seas [153] and Pierson-Moskowitz (PM) spectrum for fully-developed seas [154]. The irregular wave spectrum is generally characterised by significant wave height  $H_s$  and peak wave period  $T_p$  (or peak wave frequency  $\omega_p$ ). For example, a JONSWAP SDF can be written as

$$S_\eta(\omega) = \frac{\alpha g^2}{\omega^5} e^{\frac{5}{4}(\frac{\omega_p}{\omega})} \gamma^{r(\omega)}, \quad (4.2)$$

where  $g$  is the gravitational acceleration,  $\alpha$  is a constant and  $r(\omega)$  is a frequency-dependent function determined using the JONSWAP experimental data [152] as follows:

$$r(\omega) = \exp \left[ \frac{(\omega - \omega_p)^2}{2\sigma^2\omega_p^2} \right]. \quad (4.3)$$

Additionally,  $\gamma$  is the *peak-shape (or peak-enhancement)* parameter, which represents the *peakiness* of the wave spectrum.

Fig. 4.2 illustrates the effects of various parameters on the shape of a JONSWAP spectrum. Specifically, Fig. 4.2(a) presents the impact of variations in the peak wave period  $T_p$ , Fig. 4.2(b) depicts the effect of significant wave height  $H_s$  variations and Fig. 4.2(c) shows the impact of peak-shape parameter  $\gamma$  variations, respectively.

To compute the free surface elevation time series  $\eta(t)$  from an SDF, various methods are available in the literature, such as a superposition of harmonic components with random phases/amplitudes schemes [155]. Another alternative is to use a white noise signal filtered by the wave spectrum by utilising the inverse Fourier transform as

$$\eta(t) = \mathcal{F}^{-1}(S_\eta(\omega)S_{wn}(\omega)), \quad (4.4)$$

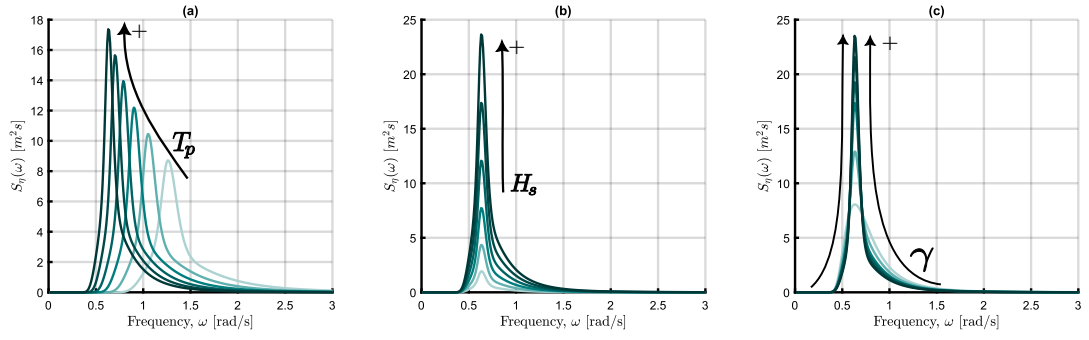


**Figure 4.2:** Ocean wave characterisation using JONSWAP SDFs. (a)  $H_s = 3$  [m],  $\gamma = 3.3$  and  $T_p \in [5, 10]$  [s] (b)  $T_p = 10$  [s],  $\gamma = 3.3$  and  $H_s \in [1, 3.5]$  [m] (c)  $H_s = 3$  [m],  $T_p = 10$  [s] and  $\gamma \in [1, 6]$ .

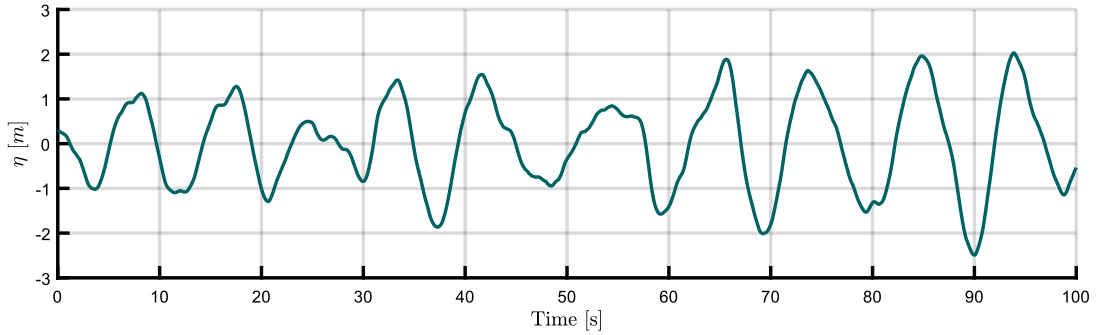


**Figure 4.3:** Example wave elevation time series  $\eta(t)$  for a JONSWAP SDF with  $H_s = 3$  [m],  $T_p = 10$  [s] and  $\gamma = 3.3$ .

where  $\mathcal{F}^{-1}$  represents inverse Fourier transform,  $S_{wn}(\omega)$  denotes power spectral density of a white noise signal with mean value  $\approx 1$ , i.e.  $\frac{1}{n_{wn}} \sum_{i=1}^{n_{wn}} S_{wn}(\omega) \approx 1$  and  $S_\eta(\omega)$  is the target wave SDF (e.g., a JONSWAP or a PM SDF). Fig. 4.3 shows the free surface elevation time series,  $\eta(t)$ , generated using (4.4) with a JONSWAP spectrum with  $H_s = 3$  [m],  $T_p = 10$  [s] and  $\gamma = 3.3$ .

## 4.2 Linear WEC modelling

In this section, linear hydrodynamic WEC modelling is presented, starting from the Navier-Stokes equations [156] to all the way to the Cummins equation [148], with a focus on the assumptions made to achieve a linear WEC representation. Additionally, the state-space formulation of the wave energy converter which lends itself to control design, is also discussed.

### 4.2.1 Navier-Stokes equations

Navier-Stokes equations describe the motion of fluids and fluid-structure interactions in a set of nonlinear partial differential equations. Essentially, equations describe the complex behaviour of fluids from first principles, such as the conservation of mass and Newton's second law of motion. The conservation of mass and momentum can be expressed as follows:

$$\frac{\partial \rho}{\partial t} + \dot{\nabla}(\rho \boldsymbol{\nu}_f) = 0 \quad (4.5a)$$

$$\frac{\partial \boldsymbol{\nu}_f}{\partial t} + \boldsymbol{\nu}_f^\top \nabla \boldsymbol{\nu}_f = \mathbf{f} - \frac{1}{\rho} \nabla p + \frac{\mu_f}{\rho} \nabla^2 \boldsymbol{\nu}_f, \quad (4.5b)$$

where  $\rho$ ,  $\boldsymbol{\nu}_f$ ,  $p$ ,  $\mathbf{f}$  and  $\mu_f$  represent fluid density, flow velocity field, pressure, external force per unit mass and fluid viscosity, respectively. Additionally, the operators  $\dot{\nabla}$ ,  $\nabla$  and  $\nabla^2$  represent divergence, gradient and Laplacian, respectively. A numerical discretisation method is required to obtain a solution since there is no analytical solution to the Navier-Stokes equations. Therefore, numerical modelling approaches, such as computational fluid dynamics (CFD) and smoothed-particle hydrodynamics (SPH), are commonly used to approximate Navier-Stokes equations, in the literature [157]. However, CFD based modelling methods are computationally expensive and they cannot be used for control purposes, not least due to their nonparametric form. By simplifying the system of equations (4.5) under LPT assumptions detailed in Section 4.2.2, LPT avoids the computational cost associated with CFD approaches to solving the hydrodynamic wave-structure interactions.

### 4.2.2 Linear potential flow theory

In order to simplify the Navier-Stokes equations, linear potential flow theory considers some assumptions, which are listed below:

#### Assumptions:

- A1:** The fluid (sea water) is incompressible, i.e.  $\frac{\partial \rho}{\partial t} = 0$  in (4.5a).
- A2:** The fluid is inviscid (frictionless), i.e.  $\mu_f = 0$  in (4.5b).
- A3:** The fluid flow is irrotational, i.e.  $\nabla \times \boldsymbol{\nu}_f = 0$ .
- A4:** The amplitude of body motion is small as compared to the dimensions of the body.
- A5:** Linear wave theory holds, i.e. the wave amplitude is small compared to the wavelength.

Utilising the aforementioned linear potential flow assumptions, the velocity field  $\boldsymbol{\nu}_f$  in (4.5) can be described using a scalar potential function  $\phi_f$ , which is obtained by solving a Laplace equation

$$\nabla^2 \phi_f = 0. \quad (4.6)$$

Moreover, assumption **A2**, i.e. that the fluid is inviscid, results in the loss of the last term in Eq. (4.5b). Therefore, Bernoulli's equation can be obtained by integrating Eq. (4.5b), and defining gravitational force as an external force, as

$$\frac{p}{\rho} + \frac{\partial \phi_f}{\partial t} + \frac{1}{2} (\nabla \phi_f)^2 + gz = C_{\text{int}}, \quad (4.7)$$

where  $C_{\text{int}}$  is a constant of integration. A set of boundary conditions must be defined in order to determine the fluid pressure and velocity potential. These boundary conditions, for linear potential flow theory<sup>4.1</sup>, are explained in the following:

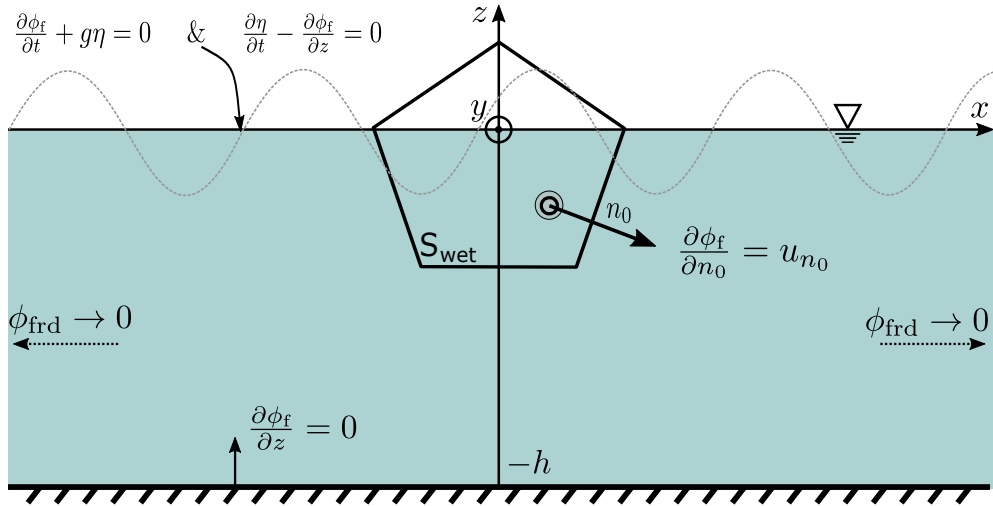


**Figure 4.4:** Graphical representation of linear potential flow theory with the linear boundary conditions introduced in Section 4.2.2.

**B1:** The kinematic boundary condition assumes that a fluid particle on the free surface stays on the free surface. Therefore, the fluid velocity normal to the free surface must be equal to the free surface velocity. The linearised boundary condition can be written as

$$\frac{\partial \eta}{\partial t} - \frac{\partial \phi_f}{\partial z} = 0 \quad \text{at } z = 0. \quad (4.8)$$

<sup>4.1</sup>For nonlinear boundary conditions description, readers are referred to [149, 158].

**B2:** According to the linear dynamic boundary condition, the fluid pressure must be equal to atmospheric pressure  $p_{\text{atm}}$ . Mathematically, this condition can be described as

$$\frac{\partial \phi_f}{\partial t} + g\eta = 0 \quad \text{at } z = 0. \quad (4.9)$$

**B3:** The impermeability and flatness of the seabed is assumed, which means that the fluid neither enters nor leaves the seabed. Mathematically, this boundary condition is written as

$$\frac{\partial \phi_f}{\partial z} = 0 \quad \text{at } z = -h. \quad (4.10)$$

**B4:** Similar to **B3**, impermeability of the floating body is assumed, resulting in the fluid velocity component normal to the surface of the floating body ( $u_{n_0}$ ) must be equal to the body velocity in the same direction, i.e.

$$\frac{\partial \phi_f}{\partial n_0} = u_{n_0} \quad \text{on the body surface.} \quad (4.11)$$

**B5:** This boundary condition describes the decaying amplitude of the wave field, i.e. the following condition holds as the distance from the oscillatory body increases:

$$\phi_{\text{frd}} \rightarrow 0 \quad \text{as} \quad r_d \rightarrow \infty, \quad (4.12)$$

with  $r_d$  representing the radial distance, and  $\phi_{\text{frd}} = \phi_{\text{fr}} + \phi_{\text{fd}}$  termed the perturbation potential, with  $\phi_{\text{fr}}$  radiation and  $\phi_{\text{fd}}$  diffraction potentials, respectively.

So-called boundary element methods (BEMs) are based on the above boundary conditions and Laplace equation (4.6) to numerically solve for potential flow  $\phi_f$  [159].

#### 4.2.2.1 Hydrodynamic forces in linear potential flow theory

Fig. 4.5 shows a schematic illustration of a floating body's six degrees-of-freedom (DoF). These DoFs include three translational motions in the  $xyz$ - directions, i.e. surge, sway and heave, respectively, and three rotational motions around the  $xyz$ -axes, which are roll, pitch and yaw, respectively.

According to Newton's second law of motion, the equation of motion of a floating body can be described, in time domain, as

$$M\ddot{z}(t) = \sum f_i(t), \quad (4.13)$$

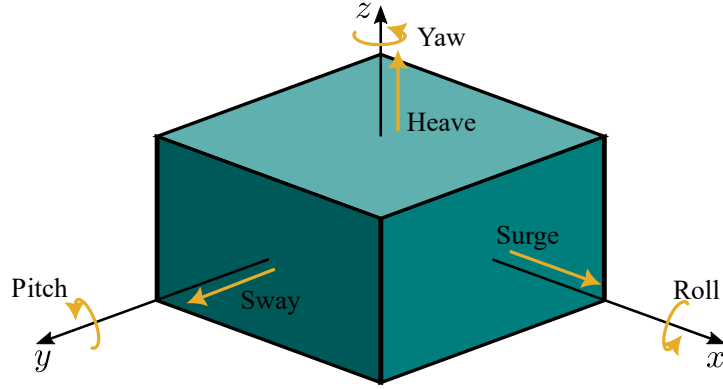


**Figure 4.5:** Schematic of the six degrees-of-freedom of a floating body.

where  $f_i(t) \in \mathbb{R}^6$  are the force vectors and moments acting on the floating body for the different modes of motion and  $\ddot{z}(t)$  denotes the body acceleration as a function of time.  $M \in \mathbb{R}^{6 \times 6}$  is the generalised mass-inertia matrix defined as

$$M = \begin{bmatrix} m & 0 & 0 & 0 & mz_g & -my_g \\ 0 & m & 0 & mz_g & 0 & -mx_g \\ 0 & 0 & m & my_g & -mx_g & 0 \\ 0 & -mz_g & my_g & i_{xx} & -i_{xy} & -i_{xz} \\ mz_g & 0 & mx_g & -i_{yx} & i_{yy} & -i_{yz} \\ -my_g & mx_g & 0 & -i_{zx} & -i_{zy} & i_{zz} \end{bmatrix}, \quad (4.14)$$

where  $m$  is the mass of the body,  $(x_g, y_g, z_g)$  the coordinates of the centre of gravity, and  $i_{ij}$  are the moments of inertia about the different axes if  $i = j$ , and if  $i \neq j$ , it represents the products of inertia with respect to the centre of mass. Under the LPT assumptions, the total force acting on the floating body can be expressed as the sum of all the forces. Therefore, Eq. (4.13) can be modified as

$$M\ddot{z}(t) = f_e(t) + f_r(t) + f_h(t) + f_{\text{ext}}(t), \quad (4.15)$$

where  $f_e(t)$  is the excitation force due to incoming wave field,  $f_r(t)$  is the radiation force generated by the oscillations of the floating body,  $f_h(t)$  is the hydrostatic stiffness force, and  $f_{\text{ext}}(t)$  represents any external force, such as a PTO force ( $f_{\text{pto}}(t)$ ) and/or mooring force ( $f_{\text{moor}}(t)$ ). In the frequency domain, Eq. (4.15) can be equivalently expressed as

$$M\ddot{Z}(\omega) = F_e(\omega) + F_r(\omega) + F_h(\omega) + F_{\text{ext}}(\omega). \quad (4.16)$$

The details of each force in Eq. (4.15) is given in the following paragraphs.

**Excitation force:** The excitation force on a floating body is the force acting on the body due to the incoming wave field. Under the LPT assumptions presented

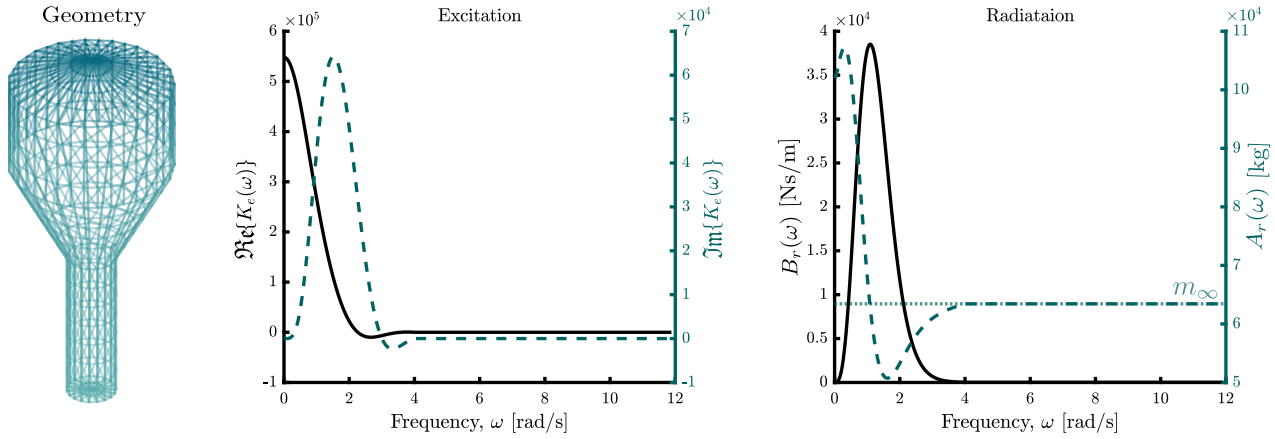


**Figure 4.6:** Hydrodynamic coefficients of a 1-DoF (heave) point absorber, including geometry of the body (left), excitation effects in the frequency domain (centre) and radiation effects in the frequency domain (right). The operators  $\Re\{\bullet\}$  and  $\Im\{\bullet\}$  denote real and imaginary parts of  $\{\bullet\}$ .

in Section 4.2.2, the excitation force is the superposition of dynamic Froude-Krylov<sup>4.2</sup> (FK) and diffraction effects [160]. Furthermore, the diffraction effects are negligible compared to the FK effects due to Assumption **A4**. In the time domain, the excitation force  $f_e(t)$  can be computed from the wave surface elevation  $\eta(t)$  as

$$f_e(t) = \int_{-\infty}^{\infty} k_e(t - \tau)\eta(\tau)d\tau, \quad (4.17)$$

where  $k_e(t) \in \mathbb{R}^6$  is the excitation impulse response function (IRF).  $k_e(t)$  can be conveniently calculated through the frequency domain equivalent  $K_e(\omega)$ , which is computed using BEM codes, such as Nemoh [161]. Fig. 4.6(centre) illustrates the real and imaginary parts of the  $K_e(\omega)$  for a point absorber constrained to move in 1-DoF, i.e. heave. It is worth mentioning that although the excitation IRF  $k_e(t)$  is easy to compute, it masks one peculiar property, i.e. non-causality, meaning that it requires future knowledge of the free-surface elevation. It is quite intuitive to understand the non-causality of the mapping  $\eta \mapsto f_e$  since the fluid (sea water, in this case) beneath the free surface is a continuum, the body feels the pressure caused by approaching wave particle velocities well in advance of the actual arrival of the wave at the body centre [162]. Therefore, although  $k_e(t)$  is real valued, it is non-causal; in other words,  $k_e(t) \neq 0$  for  $t < 0$ .

**Radiation force:** The hydrodynamic fluid force induced due to the oscillating motion of the body in generating waves is called the radiation force. Under the LPT assumptions, the radiation force  $f_r(t)$  can be expressed as

<sup>4.2</sup>For a detailed discussion of FK effects, readers are referred to [160].



$$f_r(t) = -m_\infty \ddot{z} - \int_{-\infty}^t k_r(t-\tau) \dot{z}(\tau) d\tau, \quad (4.18)$$

where  $k_r(t) \in \mathbb{R}^{6 \times 6}$  represents the (causal) radiation IRF, and  $m_\infty \in \mathbb{R}^{6 \times 6}$  represents the added mass at infinite frequency.  $k_r(t)$  can be effectively described, in the frequency domain, by means of Ogilvie's relations [163], as:

$$\begin{cases} A_r(\omega) = m_\infty - \frac{1}{\omega} \int_0^\infty k_r(t) \sin(\omega t) dt \\ B_r(\omega) = \int_0^\infty k_r(t) \cos(\omega t) dt \end{cases}, \quad (4.19)$$

with  $A_r(\omega) \in \mathbb{R}^{6 \times 6}$  and  $B_r(\omega) \in \mathbb{R}^{6 \times 6}$  denoting the so-called radiation added-mass and damping, respectively. In addition, it must be noted that Eq. (4.19) verifies that  $m_\infty = \lim_{\omega \rightarrow \infty} A_r(\omega)$ . Then, using Eq. (4.19), the full frequency domain characterisation of  $k_r(t)$  is given by:

$$K_r(\omega) = B_r(\omega) + j\omega [A_r(\omega) - m_\infty]. \quad (4.20)$$

Fig. 4.6(right) shows  $A_r(\omega)$  and  $B_r(\omega)$  for a heaving point absorber as a specific example of frequency domain characterisation.

**Hydrostatic stiffness force:** A mismatch between gravitational and buoyancy forces results in hydrostatic stiffness (restoring) force. According to linear potential flow theory, the hydrostatic stiffness force  $f_h$  is given as

$$f_h = -K_h z(t), \quad (4.21)$$

with  $K_h \in \mathbb{R}^{6 \times 6}$  and  $z(t)$  denote hydrostatic stiffness coefficient matrix and body displacement, respectively.

### 4.2.3 Cummins' equation

The Cummins' equation, first introduced in [148], can be obtained by using the hydrodynamic forces explained in Section 4.2.2.1 and the equation of motion (4.13) as

$$(M + m_\infty) \ddot{z}(t) = -K_h z(t) - k_r(t) * \dot{z}(t) + k_e(t) * \eta(t) + f_{\text{ext}}(t), \quad (4.22)$$

where  $*$  represents the convolution operator. From a system dynamic perspective, the excitation force term ' $k_e(t) * \eta(t)$ ' can be considered as an external input since it does not depend on the internal variables of the system in (4.22). Additionally, by filtering the generated free-surface elevation, the wave excitation force  $f_e(t)$  can be computed numerically. In particular,  $f_e(t)$  is directly obtained by performing a

convolution operation between the excitation IRF  $k_e(t)$  and the free-surface elevation  $\eta(t)$  (computed through an SDF, as explained in Section 4.1.2). Equation (4.22) still contains a non-parametric radiation convolution term ' $k_r(t) * \dot{z}(t)$ ', and solving a convolution term can be computationally expensive. Therefore, having a convolution term in (4.22) is not ideal, from a control design perspective. Generally, in the wave energy literature, the radiation convolution term is approximated by a finite-order linear time-invariant (LTI) system [164], as detailed in the following Section 4.2.4.

#### 4.2.4 Radiation convolution term approximation

As described in Section 4.2.3, the radiation convolution term in (4.22) poses some disadvantages from simulation and control design perspectives. Firstly, numerically solving a convolution term is a computationally inefficient task from a simulation point of view. Secondly, model-based control strategies typically require a parametric model of the system for control design, and it is not ideal to have a non-parametric convolution term in the model. In order to overcome these shortcomings, a parametric LTI approximation is usually computed using a variety of toolboxes/methods in a variety of ocean engineering applications, including wave energy. Some of the most widely used toolboxes include frequency domain identification (FDI) toolbox [165] developed at the Norwegian University of Science and Technology, WEC-Sim toolbox [166] and finite-order approximation by moment-matching (FOAMM) toolbox [167] developed at the Centre for Ocean Energy Research (COER), Maynooth University. Additionally, Prony's method [168] is also commonly used in wave energy literature, but it does not have a dedicated toolbox. Irrespective of the method/toolbox used, the final goal is to approximate radiation convolution term  $k_r(t) * \dot{z}(t)$  in (4.22) with a finite order LTI system. In this thesis, the FOAMM toolbox is used to approximate the radiation convolution term due to one key advantage, i.e. it provides an identified system with an exact match for specific key frequencies selected by the user. The input to the FOAMM toolbox is a radiation damping vector, frequency vector, and added mass vector for a given mode of motion obtained through BEM tools, such as Nemoh or WAMIT. The FOAMM toolbox returns a state space approximation in the following form:

$$\dot{\mathcal{X}}_r(t) = \mathcal{A}_r \mathcal{X}_r(t) + \mathcal{B}_r \dot{z}(t) \quad (4.23a)$$

$$f_{rc}(t) = \mathcal{C}_r \mathcal{X}_r(t) + \mathcal{D}_r \dot{z}(t) \approx k_r(t) * \dot{z}(t), \quad (4.23b)$$

where  $\mathcal{X}_r(t) \in \mathbb{R}^{n_r}$  is the state vector of the radiation convolution state-space representation, and the matrices  $\mathcal{A}_r \in \mathbb{R}^{n_r \times n_r}$ ,  $\mathcal{B}_r \in \mathbb{R}^{n_r \times n_D}$ ,  $\mathcal{C}_r \in \mathbb{R}^{n_D \times n_r}$ , and  $\mathcal{D}_r \in \mathbb{R}^{n_D}$ , with  $n_D$  is the number of DoF for the device under analysis. By way

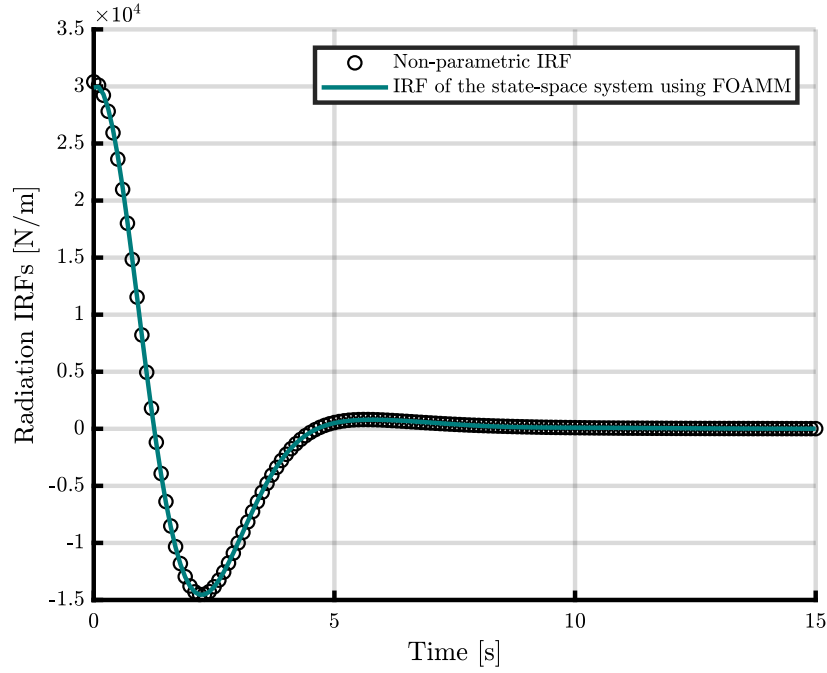


**Figure 4.7:** A comparison of IRF of parametric state space approximation vs Non-parametric radiation IRF for a 1-DoF heaving point absorber.

of example, Fig. 4.7 presents a comparison of non-parametric and (approximated) parametric IRFs computed through FOAMM toolbox for a 1-DoF point absorber (geometry shown in Fig. 4.6), and it is clear that the FOAMM toolbox provides a satisfactory approximation of the radiation convolution term, with a 6<sup>th</sup> order state-space representation in this case.

#### 4.2.5 WEC state-space representation

Obtaining an overall state-space representation of a WEC becomes straightforward once a parametric approximation of the radiation convolution term in (4.22) is found. For the sake of simplicity, the external forces are initially assumed zero, i.e.  $f_{\text{ext}} = 0$ . The analogous state-space representation of Eq. (4.22) is defined as

$$\Sigma : \begin{cases} \dot{x}(t) = Ax(t) + Bf_e(t) \\ y(t) = Cx(t) + Df_e(t) \end{cases}, \quad (4.24)$$

where  $x(t) = [z(t) \ \dot{z}(t) \ \mathcal{X}_r(t)]^T \in \mathbb{R}^{n_{ss}}$ ,  $y(t) = [z(t) \ \dot{z}(t) \ \ddot{z}(t)]^T \in \mathbb{R}^{3n_D}$ , and the matrices  $A \in \mathbb{R}^{n_{ss} \times n_{ss}}$ ,  $B \in \mathbb{R}^{n_{ss} \times n_D}$ ,  $C \in \mathbb{R}^{3n_D \times n_{ss}}$ , and  $D \in \mathbb{R}^{3n_D \times n_D}$  are given by

$$\begin{aligned} A &= \begin{bmatrix} 0 & \mathbb{I}_{n_D} & 0 \\ -\mathcal{M}K_h & 0 & -\mathcal{M}\mathcal{C}_r \\ 0 & \mathcal{B}_r & \mathcal{A}_r \end{bmatrix}, B = \begin{bmatrix} 0 \\ \mathcal{M} \\ 0 \end{bmatrix}, \\ C &= \begin{bmatrix} \mathbb{I}_{n_D} & 0 & 0 \\ 0 & \mathbb{I}_{n_D} & 0 \\ -\mathcal{M}K_h & 0 & -\mathcal{M}\mathcal{C}_r \end{bmatrix} \text{ and } D = \begin{bmatrix} 0 \\ 0 \\ \mathcal{M} \end{bmatrix}, \end{aligned} \quad (4.25)$$

with  $\mathcal{M} = (M + m_\infty)^{-1}$ . The symbol  $\mathbb{I}_{n_D}$  denotes an identity matrix of size  $n_D$ , and the symbol 0 stands for any zero element dimensioned according to the context.

It is worth mentioning that the LTI system  $\Sigma$  in (4.24) presents a general linear model description for a multiple DoF WEC with three outputs, i.e. displacement, velocity and acceleration. However, getting a *reduced* order model for a WEC with less modes of motion (DoFs) is straightforward, depending upon the application. This can be achieved by considering only a limited number of DoFs with specific outputs. The most commonly used WEC model in this thesis is the 1-DoF (heave) model, with WEC velocity as the system output, variation of the system  $\Sigma$  in (4.24).

### 4.3 Hydrodynamic models: state-of-the-art

This section reviews the state-of-the-art hydrodynamic models in the literature concerning wave energy grid integration. Although the linear WEC model, given in Eq. (4.24), presents a general linear model for various wave absorbers, the linear WEC representation may change slightly depending upon the type of WEC, e.g. an OWC has an air chamber, whose dynamics must be included in the WEC model. In the literature concerning wave energy grid integration, most studies use simplified variations of the linear WEC model in Eq. (4.24). In most cases, the radiation force is simplified by using a constant radiation coefficient rather than frequency-dependent

**Table 4.1:** A review of hydrodynamic models used in the literature for grid integration of wave energy systems. Note: Linear-CD represents linear WEC model with constant damping coefficient term.

Ref. No.	Hydrodynamic model	Frequency
[76–88, 90, 92, 99, 103]	Linear-CD	17
[89, 93, 94, 96, 100–102, 104, 111]	Linear	9
[91]	Nonlinear	1
[49, 95, 97, 98, 105, 106, 108–110]	No model information	9

radiation damping. The constant radiation damping coefficient is used to avoid the requirement for a radiation convolution term approximation, resulting in effectively a so-called *mass-spring-damper* model of a WEC. Table 4.1 shows the state-of-the-art hydrodynamic models used for grid integration of wave energy conversion systems. It is evident from Table 4.1 that the most frequent hydrodynamic WEC model in the literature is a linear WEC model with a *simplified* radiation force term as, for example, in [76–88, 90, 92, 99, 103]. Table 4.1 also shows that linear WEC models with appropriate radiation force terms are used in [89, 93, 94, 96, 100–102, 104, 111]. In a recent study [91], authors used a nonlinear model for the AWS WEC-based grid-connected wave energy system. However, a passive damping hydrodynamic control is used for maximum power extraction from waves, which has significantly lower power absorption capability compared to a reactive controller [18]. Additionally, in [49, 95, 97, 98, 105, 106, 108–110], there is no hydrodynamic model information available. Depending on the type of WEC, the input to the electrical part of the powertrain is different. For point absorber WECs, a WEC output power curve is used as input to the electrical part of the powertrain [95, 97, 98]. For OWCs, on the other hand, air flow velocity is typically used as an input to the air turbine, which drives an electric generator [49, 105, 106, 108–110].

## 4.4 Conclusions

This chapter introduces mathematical representations of ocean waves (regular and irregular) and provides the basics of linear hydrodynamic WEC modelling. In particular, linear potential assumptions and boundary conditions are specified to achieve the well-known non-parametric Cummins' equation. Additionally, parametric approximation of the radiation convolution term is computed through the FOAMM toolbox, which is used to get an overall state-space representation of a WEC essential for control applications. Finally, a review of the literature is presented, focusing on the hydrodynamic WEC models used for grid integration of wave energy systems, which shows that the most commonly utilised WEC models are simplified linear WEC models, which use a constant radiation damping term.



# 5

## Electrical systems modelling

### Contents

---

<b>5.1 LPMG and Gen-SC model</b> . . . . .	<b>68</b>
5.1.1 Park Transformation . . . . .	71
<b>5.2 Grid-side converter (Grid-SC) model</b> . . . . .	<b>73</b>
<b>5.3 Ultra-capacitor-based storage subsystem model</b> . . . . .	<b>73</b>
5.3.1 DC-DC buck-boost converter model . . . . .	74
<b>5.4 Complete electrical system model</b> . . . . .	<b>75</b>
<b>5.5 Conclusions</b> . . . . .	<b>76</b>

---

This chapter provides electrical systems modelling for a direct-drive wave energy conversion system with a linear permanent magnet generator (LPMG) as a PTO mechanism. As discussed in Chapter 3, various powertrain configurations are available in the literature depending upon the type of wave absorption and PTO technology. In this thesis, a direct-drive scheme with a LPMG PTO is chosen due to its simplicity (no gearbox/stator brushes), reasonable efficiencies at lower speeds, and higher force density of a LPMG than a generic rotary generator, making it suitable for wave energy applications [78].

In addition to the WEC and LPMG, the direct-drive configuration includes full-scale back-to-back (B2B) power converters with a DC link in between that isolates the device and grid sides. Furthermore, a short-term storage subsystem based on an ultra-capacitor (UC) is also a part of the W2G powertrain, which is essential for W2G controlled operation. As shown in Fig. 5.1, the W2G system consists of three subsystems: device-side, grid-side and storage subsystems. First, the device-side

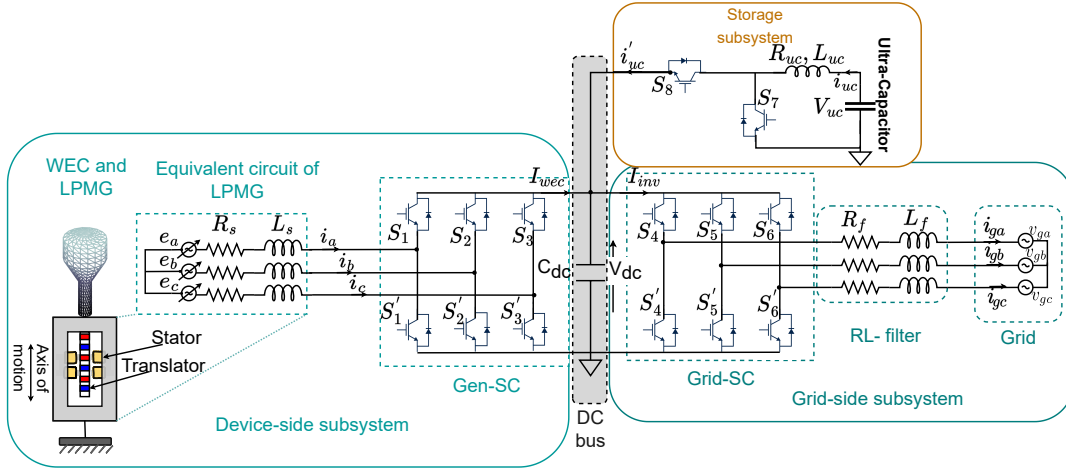


**Figure 5.1:** Reference W2G direct-drive configuration.

subsystem includes a WEC (heaving point absorber), an LPMG as PTO and an active rectifier, also referred to as a generator-side converter (Gen-SC). Secondly, the grid-side subsystem consists of a three-phase (3- $\phi$ ) inverter referred to as a grid-side converter (Grid-SC) and the electric grid. Finally, the storage subsystem includes an ultra-capacitor connected to the DC-bus via a DC/DC buck-boost converter, as depicted in Fig. 5.1. The following sections describe the dynamic models for each electrical component of the W2G powertrain.

## 5.1 LPMG and Gen-SC model

A LPMG is best suited as a power-take-off (PTO) mechanism for the direct-drive wave energy applications due to its high force density and reasonable low-speed efficiency, as noted in [78]. Fig. 5.2 shows a heaving point absorber WEC connected to the translator of a LPMG considered here. The dynamic model of the LPMG closely resembles that of a rotary permanent magnet generator (RPMG), with the exception of the translator motion, which reciprocates instead of rotating like the rotor in a rotary generator and can be represented by a set of symmetrical equations in  $abc$  frame of reference, as follows:

$$\mathbf{e}_{abc} - R_s \mathbf{i}_{abc} - L_s \frac{d\mathbf{i}_{abc}}{dt} = \mathbf{v}_{abc}, \quad (5.1)$$

where  $\mathbf{e}_{abc} = [e_a, e_b, e_c]^T$ ,  $\mathbf{i}_{abc} = [i_a, i_b, i_c]^T$ , and  $\mathbf{v}_{abc} = [v_a, v_b, v_c]^T$  are the induced voltages, currents in each phase of the stator, and terminal voltages in the  $abc$  frame



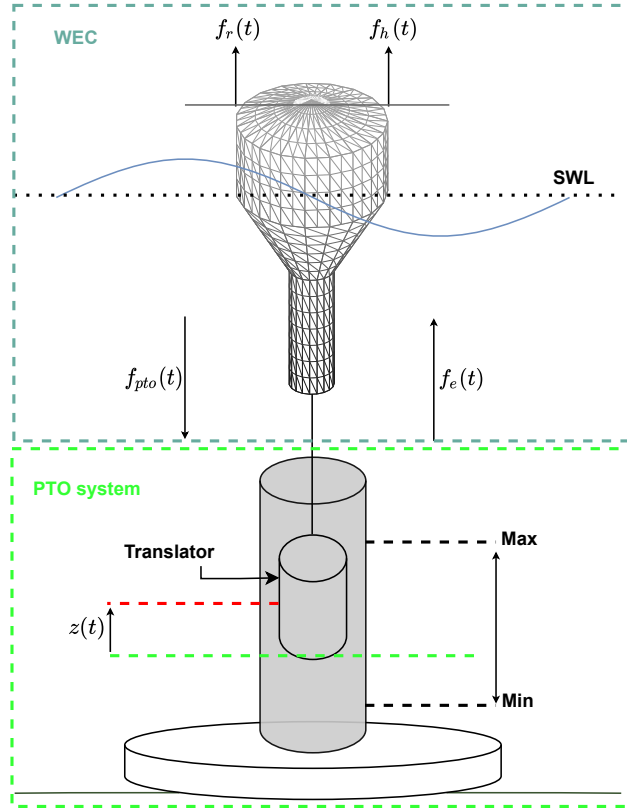


**Figure 5.2:** The schematics of WEC and PTO (LPMG) systems considered in this thesis. The acronym SWL stands for still water level.

of reference, respectively. For a sinusoidally wound stator, the induced voltages  $\mathbf{e}_{abc}$  in the LPMG depends on the heave displacement  $z(t)$  and velocity  $\dot{z}(t)$ , i.e.

$$\begin{bmatrix} e_a(t) \\ e_b(t) \\ e_c(t) \end{bmatrix} = \begin{bmatrix} \dot{z}(t) \frac{\pi}{\tau} \psi_{PM} \sin(\frac{\pi}{\tau} z(t)) \\ \dot{z}(t) \frac{\pi}{\tau} \psi_{PM} \sin(\frac{\pi}{\tau} z(t) - \frac{2\pi}{3}) \\ \dot{z}(t) \frac{\pi}{\tau} \psi_{PM} \sin(\frac{\pi}{\tau} z(t) - \frac{4\pi}{3}) \end{bmatrix}, \quad (5.2)$$

where  $\psi_{PM}$  is the permanent magnet flux linkage and  $\tau$  is the pole pitch of the LPMG. On the other hand, in rotary generators, the induced voltages depend on the angular velocity of the rotor. For example, phase 'a' of a rotary generator is presented as

$$\begin{aligned} e_a(t) &= \omega_e(t) \psi_{PM} \sin(\theta(t)), \\ \theta(t) &= \int_0^t \omega_e(\tau) d\tau. \end{aligned} \quad (5.3)$$

Under constant rotational speed, Fig. 5.3 shows the induced voltage in phase 'a' of a generic rotary generator, which is sinusoidal. For a LPMG, on the other hand, the translator has a reciprocating motion, which leads to reciprocating displacement and velocity. By way of example, Fig. 5.4 shows the amplitude modulated waveform of the phase 'a' induced voltage for a sinusoidally changing displacement and velocity corresponding to monochromatic (regular) wave excitation.

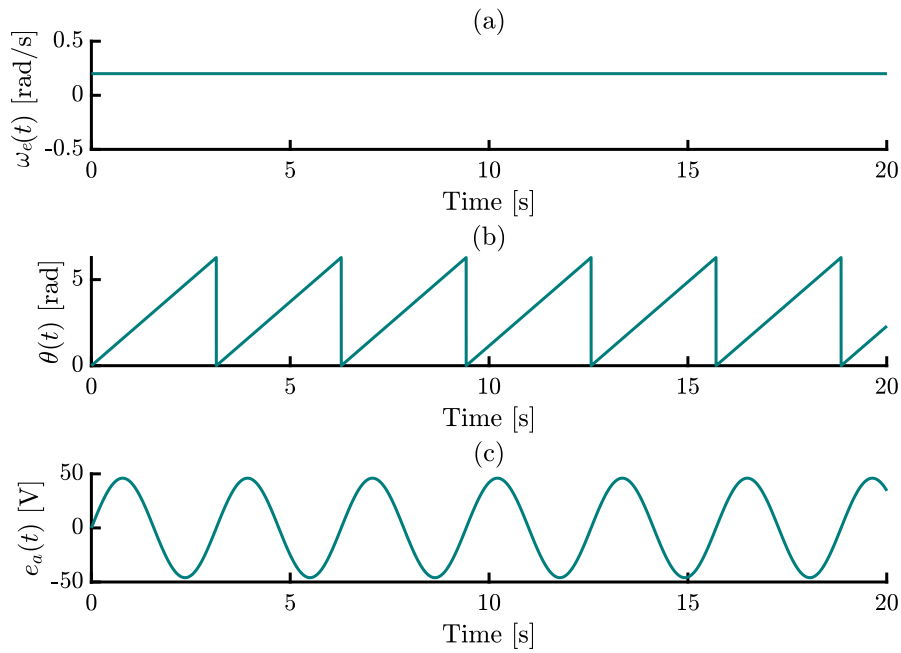


**Figure 5.3:** The waveforms corresponding to phase ‘a’ of a generic rotary generator: (a) angular velocity  $\omega_e(t)$ , (b) angular displacement  $\theta(t)$ , and (c) the resulting 1- $\phi$  induced voltage  $e_a(t)$  of the machine.

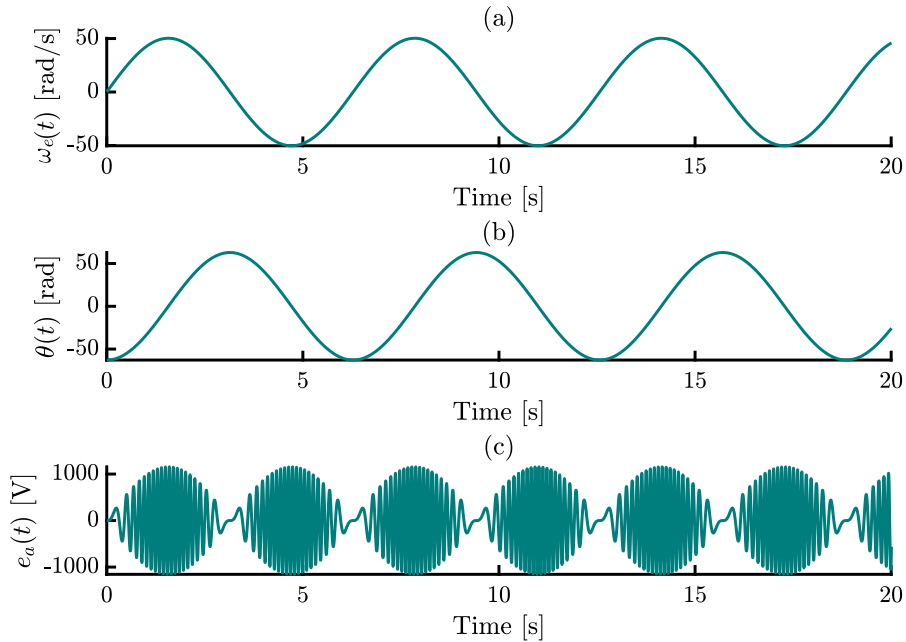


**Figure 5.4:** The waveforms corresponding to phase ‘a’ of an LPMG: (a) angular velocity  $\omega_e(t) = \frac{\pi}{\tau} \dot{z}(t)$ , (b) angular displacement  $\theta(t) = \frac{\pi}{\tau} z(t)$ , and (c) the resulting single phase induced voltage  $e_a(t)$  of the machine.

### 5.1.1 Park Transformation

The utilisation of the  $d$ - $q$  (Park) transformation [169] allows for the representation of a balanced three-phase system using a two-phase system [170], where the transformation matrix is dependent on the electrical angular position  $\theta(t)$ . In the context of a LPMG, the angular position is influenced by the heave displacement of the translator, as indicated below:

$$\theta(t) = \frac{\pi}{\tau} z(t). \quad (5.4)$$

The transformation matrix  $\mathcal{T}_{abc/dq0}$  to convert  $abc$  quantities into  $d$ - $q$  form is as:

$$\mathcal{T}_{abc/dq0} = \frac{2}{3} \begin{bmatrix} \cos(\theta(t)) & \cos(\theta(t) - \frac{2\pi}{3}) & \cos(\theta(t) - \frac{4\pi}{3}) \\ -\sin(\theta(t)) & -\sin(\theta(t) - \frac{2\pi}{3}) & -\sin(\theta(t) - \frac{4\pi}{3}) \\ 1/2 & 1/2 & 1/2 \end{bmatrix}. \quad (5.5)$$

Using this transformation, the  $d$ - $q$  model for the LPMG is [171]:

$$\begin{bmatrix} L_{ds} \\ L_{qs} \end{bmatrix} \frac{d}{dt} \begin{bmatrix} i_{ds}(t) \\ i_{qs}(t) \end{bmatrix} = \begin{bmatrix} e_{ds}(t) \\ e_{qs}(t) \end{bmatrix} - \begin{bmatrix} v_{ds}(t) \\ v_{qs}(t) \end{bmatrix} - \omega_e \begin{bmatrix} L_{ds} \\ L_{qs} \end{bmatrix} \begin{bmatrix} -i_{qs}(t) \\ i_{ds}(t) \end{bmatrix} - R_s \begin{bmatrix} i_{ds}(t) \\ i_{qs}(t) \end{bmatrix}, \quad (5.6)$$

where

$$\omega_e = \frac{\pi}{\tau} \dot{z}(t), \quad (5.7)$$

and

$$\begin{bmatrix} e_{ds}(t) \\ e_{qs}(t) \end{bmatrix} = \begin{bmatrix} 0 \\ \psi_{PM}\omega_e \end{bmatrix}, \quad (5.8)$$

where  $\omega_e$  and  $\psi_{PM}$  represent electrical angular speed of stator variables and permanent magnet flux linkage, respectively. The  $d$ - and  $q$ -axis flux linkages for the LPMG are given below<sup>5.1</sup>:

$$\begin{aligned} \psi_{ds} &= L_{ds}i_{ds} - \psi_{PM} \\ \psi_{qs} &= L_{qs}i_{qs} \end{aligned} \quad (5.9)$$

The PTO force produced by the LPMG, depends on the stator currents, the flux linkage and the pole pitch as:

$$f_{pto} = 1.5 \frac{\pi}{\tau} (\psi_{ds}i_{qs} - \psi_{qs}i_{ds}) \quad (5.10)$$

Using the flux relations given in (5.9),  $f_{pto}(t)$  can be obtained as:

$$f_{pto} = 1.5 \frac{\pi}{\tau} ((L_{ds} - L_{qs})i_{ds}i_{qs} - \psi_{PM}i_{qs}) \quad (5.11)$$

<sup>5.1</sup>From now on, the dependence on  $t$  is dropped when clear from context.

By utilising Eq. (5.11), it can be inferred that the developed force of an LPMG is composed of two distinct components. The first term represents the reluctance force attributed to saliency, while the second term represents the magnetic force generated by the permanent magnet. In the case of a surface mount LPMG machine considered here, where the air gap is uniform, the  $d$ - and  $q$ -axis inductances are equal, i.e.  $L_{ds} = L_{qs} = L_s$ , thereby simplifying the model in (5.6) and  $f_{pto}(t)$  in (5.11) as:

$$\frac{di_{ds}}{dt} = -\frac{R_s}{L_s}i_{ds} + \omega_e i_{qs} - \frac{1}{L_s}v_{ds}, \quad (5.12)$$

$$\frac{di_{qs}}{dt} = -\omega_e i_{ds} - \frac{R_s}{L_s}i_{qs} - \frac{\omega_e}{L_s}\psi_{PM} - \frac{1}{L_s}v_{qs}, \quad (5.13)$$

with,

$$f_{pto} = -1.5\frac{\pi}{\tau}\psi_{PM}i_{qs}. \quad (5.14)$$

The stator  $d$ - and  $q$ -axis voltages, which serve as the inputs to the Gen-SC and can be controlled separately, are now expressed in terms of corresponding control actions of the Gen-SC [172, 173], as outlined below:

$$v_{ds} = v_{dc}u_{ds}, \quad v_{qs} = v_{dc}u_{qs}, \quad \text{and} \quad I_{wec} = u_{ds}i_{ds} + u_{qs}i_{qs} \quad (5.15)$$

where  $u_{ds}$  and  $u_{qs}$  are the Park transformation of the switch position function  $S_i$ ,  $\forall i = 1, 2, 3$  (see Fig. 5.1) with

$$S_i = \begin{cases} 1 & \text{if } S_i \text{ is ON and } S'_i \text{ is OFF} \\ 0 & \text{if } S_i \text{ is OFF and } S'_i \text{ is ON} \end{cases}. \quad (5.16)$$

Substituting the values of  $v_{ds}$  and  $v_{qs}$  from (5.15) into (5.12) and (5.13), the unified model of the LPMG and Gen-SC combination is obtained as follows:

$$\frac{di_{ds}}{dt} = -\frac{R_s}{L_s}i_{ds} + \omega_e i_{qs} - \frac{1}{L_s}v_{dc}u_{ds}, \quad (5.17)$$

$$\frac{di_{qs}}{dt} = -\omega_e i_{ds} - \frac{R_s}{L_s}i_{qs} - \frac{\omega_e}{L_s}\psi_{PM} - \frac{1}{L_s}v_{dc}u_{qs}. \quad (5.18)$$

## 5.2 Grid-side converter (Grid-SC) model

In Fig. 5.1, the DC/AC inverter (Grid-SC) is depicted on the right-hand side. Like the Gen-SC, it consists of six insulated-gate bipolar transistors (IGBTs) and is a three-legged, three-phase voltage source converter. The dynamic model of the Grid-SC in the  $abc$  frame can be derived [172, 174] by applying Kirchhoff's laws, as:

$$L_f \frac{d\mathbf{i}_{g(abc)}}{dt} = v_{dc}[S_j] - \mathbf{v}_{g(abc)} - R_f \mathbf{i}_{g(abc)} \quad (5.19)$$

where,  $\mathbf{i}_{g(abc)} = [i_{ga}, i_{gb}, i_{gc}]^T$  represents the three-phase grid currents, while  $\mathbf{v}_{g(abc)} = [v_{ga}, v_{gb}, v_{gc}]^T$  represents the sinusoidal three-phase grid voltages. The parameters  $R_f$  and  $L_f$  correspond to the filter resistance and inductance, respectively. The function  $S_j$  in Eq. (5.19), where  $j = 4, 5, 6$ , represents the switch position function, defined as follows:

$$S_j = \begin{cases} 1 & \text{if } S_j \text{ is ON and } S'_j \text{ is OFF} \\ 0 & \text{if } S_j \text{ is OFF and } S'_j \text{ is ON} \end{cases} \quad (5.20)$$

In order to facilitate control synthesis, the triphase representation in Eq. (5.20) is often transformed into the  $d$ - $q$  frame. The  $d$ - $q$  frame is linked to the grid voltage and rotates synchronously with the grid voltage frequency  $\omega_o$  (in this case  $\omega_o = 314.159$  [rad/s], since the grid frequency is 50 [Hz]). This transformation results in the following model for the Grid-SC [172]:

$$\frac{di_{dg}}{dt} = -\frac{V_{dg}}{L_f} + \omega_o i_{qg} - \frac{R_f}{L_f} i_{dg} + \frac{v_{dc}}{L_f} u_{dg}, \quad (5.21)$$

$$\frac{di_{qg}}{dt} = -\frac{V_{qg}}{L_f} - \omega_o i_{dg} - \frac{R_f}{L_f} i_{qg} + \frac{v_{dc}}{L_f} u_{qg}, \quad (5.22)$$

where  $i_{dg, qg}$  represent grid currents in the  $d$ - $q$  synchronous frame,  $V_{dg, qg}$  represent the  $d$ - $q$  grid voltages, and  $u_{dg, qg}$  denotes the  $d$ - $q$  components of  $S_j$ .

## 5.3 Ultra-capacitor-based storage subsystem model

The use of a UC-based storage system is crucial for W2G-controlled operation due to the following reasons:

1. The WEC hydrodynamic control principle is based on amplifying the device motion in resonance with the wave resource, resulting in increased variability in the WEC output power under controlled WEC conditions; therefore, to meet the power quality requirements imposed by grid codes, which prohibit direct feeding of highly variable WEC output power into the grid, the UC storage

system is used to reduce the variability in the WEC electrical output power, thus increasing the value of the grid-connected wave power.

2. Secondly, the reactive hydrodynamic LiTe-Con (Linear Time invariant Controller) implementation on the device side, based on the complex-conjugate (impedance matching) principle<sup>5.2</sup>, requires power from the grid side in some cases, necessitating the use of the storage system to meet the negative (reactive) power requirements of LiTe-Con and regulate the DC bus voltage.
3. Finally, the UC storage system is also utilised to support the grid during voltage sags.

In this way, the UC storage system allows for decoupled controllers on either side of the DC bus. A detailed description of each task, and how they are accomplished using UC storage, can be found in Chapter 7 of the thesis.

To facilitate proper functioning of the UC in the W2G system, the UC is connected to the DC-bus through a DC/DC buck-boost converter. The buck-boost converter controls the direction of power flow, allowing power to flow from the DC-bus to the UC or from the UC to the DC-bus, depending on the system requirements. The dynamic model of the DC/DC buck-boost converter is detailed in the following subsection.

### 5.3.1 DC-DC buck-boost converter model

The buck-boost converter operates in both boost and buck mode, depending upon the direction of power flow. During discharge mode, the UC supplies power to the DC-bus, and the buck-boost converter operates as a boost converter ( $S_7$  ON,  $S_8$  OFF in Fig. 5.1). Conversely, during charge mode, the converter operates in buck mode ( $S_7$  OFF,  $S_8$  ON in Fig. 5.1) as power flows from the DC-bus to the UC. The converter buck and boost modes are modelled separately and combined to form a complete model. The dynamic model for the buck-boost converter during discharge (boost) mode can be easily derived [174, 175] as:

$$\frac{di_{uc}}{dt} = \frac{V_{uc}}{L_{uc}} - \frac{R_{uc}}{L_{uc}}i_{uc} - (1 - u_7)\frac{v_{dc}}{L_{uc}}, \quad (5.23)$$

$$i'_{uc} = (1 - u_7)i_{uc}, \quad (5.24)$$

during charge (buck) mode, on the other hand, the model is:

$$\frac{di_{uc}}{dt} = \frac{V_{uc}}{L_{uc}} - \frac{R_{uc}}{L_{uc}}i_{uc} - u_8\frac{v_{dc}}{L_{uc}}, \quad (5.25)$$

---

<sup>5.2</sup>For a complete description of impedance matching principle for WEC control, please refer to Section 6.1.1 in Chapter 6 of the thesis.

$$i'_{uc} = u_8 i_{uc}, \quad (5.26)$$

where  $V_{uc}$ ,  $L_{uc}$ , and  $R_{uc}$  denote UC voltage, inductance and equivalent series resistance, respectively,  $i_{uc}$  and  $i'_{uc}$  are the UC input and output currents. Additionally, the control signals for switches  $S_7$  and  $S_8$  (see Fig. 5.1) are denoted as  $u_7$  and  $u_8$ , respectively. For simplicity, a signal  $u_{78}$  is introduced as:

$$u_{78} = K(1 - u_7) + (1 - K)u_8, \quad (5.27)$$

with  $K$  defined as:

$$K = \begin{cases} 1 & \text{if } S_7 \text{ is ON and } S_8 \text{ is OFF (Boost mode)} \\ 0 & \text{if } S_7 \text{ is OFF and } S_8 \text{ is ON (Buck mode)} \end{cases}. \quad (5.28)$$

Finally, the simplified model for the DC/DC buck-boost converter, using  $u_{78}$  from (5.28), is given below:

$$\frac{di_{uc}}{dt} = \frac{V_{uc}}{L_{uc}} - \frac{R_{uc}}{L_{uc}} i_{uc} - \frac{v_{dc}}{L_{uc}} u_{78}, \quad (5.29)$$

$$i'_{uc} = u_{78} i_{uc}. \quad (5.30)$$

## 5.4 Complete electrical system model

The complete electrical system model for the direct-drive W2G structure is obtained by combining the mathematical models derived in Sections 5.1, 5.2, and 5.3.1, which represent the LPMG and Gen-SC combination, Grid-SC, and buck-boost converter, respectively. From Fig. 5.1, it follows that:

$$C_{dc} \frac{dv_{dc}}{dt} = I_{wec} + i'_{uc} - I_{inv}, \quad (5.31)$$

and, substituting Eqs. (5.15) and (5.30) in Eq. (5.31), gives:

$$\frac{dv_{dc}}{dt} = \frac{1}{C_{dc}} [(u_{ds} i_{ds} + u_{qs} i_{qs}) + u_{78} i_{uc} - I_{inv}]. \quad (5.32)$$

To ease control design, averaged models<sup>5.3</sup> are often used for power converters. The process of averaging involves replacing all the model variables with their average values over a switching period, while ignoring their high-frequency components, resulting in simplified models that are faster to compute [177, 178]. This modelling technique determines the state model for each possible circuit configuration and then combines all these elementary models into a unified one through a duty ratio.

<sup>5.3</sup>The interested reader is referred to [176–178] for comprehensive description of averaging methods for power converter models.

The averaged models are useful for control applications due to their simplicity and fast computational times [176]. In this regard, we define averaged state variables as  $x_1 = \langle i_{ds} \rangle$ ,  $x_2 = \langle i_{qs} \rangle$ ,  $x_3 = \langle i_{dg} \rangle$ ,  $x_4 = \langle i_{qg} \rangle$ ,  $x_5 = \langle i_{uc} \rangle$  and  $x_6 = \langle v_{dc} \rangle$ , where the operator  $\langle \bullet \rangle$  represents the average value over a switching period. Combining Eqs. (5.17), (5.18), (5.21), (5.22), (5.29) and (5.32) results in the following complete electrical system model:

$$\frac{dx_1}{dt} = -\frac{R_s}{L_s}x_1 + \omega_e x_2 - \frac{x_6}{L_s}\mu_{ds} \quad (5.33)$$

$$\frac{dx_2}{dt} = -\omega_e x_1 - \frac{R_s}{L_s}x_2 - \frac{\omega_e}{L_s}\psi_{PM} - \frac{x_6}{L_s}\mu_{qs} \quad (5.34)$$

$$\frac{dx_3}{dt} = -\frac{V_{dg}}{L_f} + \omega_o x_4 - \frac{R_f}{L_f}x_3 + \frac{x_6}{L_f}\mu_{dg} \quad (5.35)$$

$$\frac{dx_4}{dt} = -\frac{V_{qg}}{L_f} - \omega_o x_3 - \frac{R_f}{L_f}x_4 + \frac{x_6}{L_f}\mu_{qg} \quad (5.36)$$

$$\frac{dx_5}{dt} = \frac{V_{uc}}{L_{uc}} - \frac{R_{uc}}{L_{uc}}x_4 - \frac{x_6}{L_{uc}}\mu_{78} \quad (5.37)$$

$$\frac{dx_6}{dt} = \frac{1}{C_{dc}}[\mu_{ds}x_1 + \mu_{qs}x_2 + \mu_{78}x_5 - I_{inv}] \quad (5.38)$$

where,  $\mu_{ds}$  and  $\mu_{qs}$  are the duty ratios of the Gen-SC,  $\mu_{dg}$  and  $\mu_{qg}$  are the duty ratios of the Grid-SC, and  $\mu_{67}$  is the duty ratio of the buck-boost converter. These averaged power converter models are utilised for W2G control design due to their computational efficiency and simplicity, compared to full-circuit power converter models.

## 5.5 Conclusions

This chapter presents a comprehensive model for the electrical components of a direct-drive wave energy conversion system. It begins with an introduction to the LPMG model and highlights the differences between a rotary PMG and a linear PMG. The LPMG model assumes a balanced three-phase LPMG system, which is transformed into a two-phase  $d$ - $q$  system using the Park transformation. A combined LPMG-Gen-SC model is then derived. A dynamic model for the Grid-SC is developed on the grid side, while a DC/DC buck-boost converter model, used with the UC-based storage subsystem, is also presented. Finally, a complete model for the electrical part of the powertrain is derived by utilising the state-space averaging method.

The combined hydrodynamic and electrical system models presented in Chapter 4 and Chapter 5, respectively, form a complete W2G system model for a direct-drive wave energy conversion system, used for the W2G control design in Part III of this thesis.



## **Part III**

# **High-performance W2G control of a WEC**



# 6

## Device-side control

### Contents

---

<b>6.1 Hydrodynamic control of a WEC</b> . . . . .	<b>80</b>
6.1.1 Reactive controller: Impedance-matching principle . . . . .	80
6.1.2 Passive damping controller . . . . .	83
<b>6.2 LiTe-Con</b> . . . . .	<b>83</b>
6.2.1 Dynamic constraint handling mechanism: LiTe-Con+ . . . . .	86
<b>6.3 Lyapunov-based Gen-SC Controller</b> . . . . .	<b>90</b>
6.3.1 Stability analysis . . . . .	91
<b>6.4 Results</b> . . . . .	<b>92</b>
<b>6.5 Conclusions</b> . . . . .	<b>97</b>

---

Like the W2G powertrain, the W2G control framework features device-side, grid-side, and storage subsystem controllers. This chapter focuses on the device-side control part of the overall W2G control framework, which is further divided into two parts: the hydrodynamic controller and the Gen-SC controller. The hydrodynamic controller generates the PTO force reference, which the Gen-SC controller then tracks by controlling the LPMG stator current.

The main objective of this chapter is to describe, in detail, both parts of the device-side control. Specifically, the basics of hydrodynamic WEC controllers (both reactive and passive) are introduced in the Section 6.1. Section 6.2 then describes a finite order LTI realisation, i.e. LiTe-Con, of the theoretical broadband optimal impedance-matching condition, including static and dynamic position constraint handling mechanisms, and provides a PTO force reference  $f_{pto}^{ref}(t)$  for the Gen-SC controller. In Section 6.3, a

Lyapunov-based controller is designed for the Gen-SC, which tracks the PTO force reference  $f_{\text{pto}}^{\text{ref}}(t)$  provided by the LiTe-Con. Section 6.4 presents results for the device-side control system, while Section 6.5 concludes this chapter.

## 6.1 Hydrodynamic control of a WEC

In order to maximise energy absorption from ocean waves, hydrodynamic WEC controllers actively manipulate the motion of the WEC, utilising existing capital infrastructure to maximise energy capture, thereby enhancing the economic performance of the system [151]. Hydrodynamic WEC controllers can be broadly categorised into reactive and passive damping WEC controllers. The key distinction between reactive and passive controllers lies in the bi-directional power flow requirement. Reactive controllers necessitate bi-directional power flow, while passive controllers do not have such a requirement for bi-directional power flow. Both reactive and passive damping controllers are discussed, in detail, in the following subsections.

### 6.1.1 Reactive controller: Impedance-matching principle

Within the wave energy control literature, one of the most fundamental results is a rather simplistic solution to the problem of energy maximisation from WEC infrastructure. The impedance-matching principle relies heavily on a frequency-domain description of a WEC. Therefore, applying the Fourier transform to the linear Cummins' equation, defined in (4.22), results in the following:

$$j\omega(M + m_{\infty})\dot{Z}(\omega) + K_r(\omega)\dot{Z}(\omega) + \frac{K_h}{j\omega}\dot{Z}(\omega) = F_e(\omega) - F_{\text{pto}}(\omega), \quad (6.1)$$

where  $F_{\text{pto}}(\omega)$  and  $\dot{Z}(\omega) = V(\omega)$  denotes the Fourier transform of the PTO force (control input) and velocity, respectively. It is worth noting that from now on, a 1-DoF heaving point absorber WEC with a direct-drive PTO is considered in this part of the thesis, unless stated otherwise. From (6.1), it follows that

$$V(\omega) = G(j\omega) [F_e(\omega) - F_{\text{pto}}(\omega)] = \frac{1}{Z_i(\omega)} [F_e(\omega) - F_{\text{pto}}(\omega)], \quad (6.2)$$

with  $Z_i(\omega)$  defined as

$$Z_i(\omega) = B_r(\omega) + j\omega \left( M + A_r(\omega) - \frac{K_h}{\omega^2} \right), \quad (6.3)$$

representing the *intrinsic impedance* of the WEC.  $G(j\omega)$  represents the frequency-domain mapping of the WEC dynamics. Naturally, the concept of intrinsic impedance resembles the well-known ('internal impedance') representation in electrical engineering

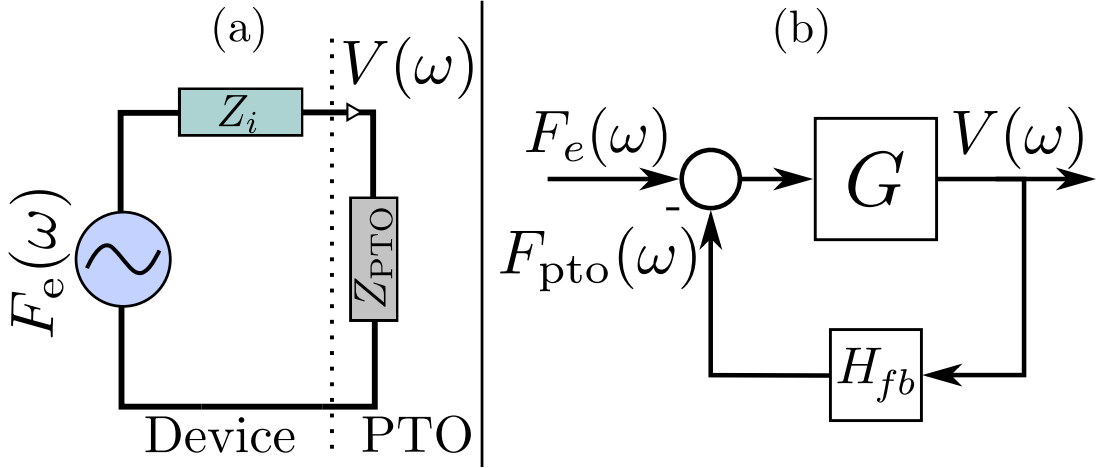


**Figure 6.1:** Impedance-matching principle: (a) Equivalent circuit representation, (b) Impedance-matching feedback control structure.

and circuit theory, i.e. the WEC system can be equivalently depicted by a circuit representation, as shown in Fig. 6.1(a). Hence, the PTO can be considered as a ‘load’, and the control force  $F_{pto}(\omega)$ , applied by the PTO, is designed to achieve maximum power transfer to the load. Hence, the *maximum power transfer* or impedance-matching principle [179], from circuit theory, can be directly applied, which states that the load impedance  $Z_{pto}(\omega)$  must be equal to the complex-conjugate of the source impedance  $Z_i(\omega)$  for maximum power transfer to the load. In other words, the control force that maximises the power transfer, is given by:

$$F_{pto}(\omega) = Z_{pto}(\omega)V(\omega) = Z_i^*(\omega)V(\omega), \quad (6.4)$$

where  $Z_i^*(\omega)$  denotes the complex-conjugate of the intrinsic impedance  $Z_i(\omega)$ . Analogously, the impedance-matching condition can be expressed, in terms of an optimal velocity profile, with a purely real mapping, guaranteeing a zero-phase-locking condition between the device velocity  $V(\omega)$  and  $F_e(\omega)$  as:

$$V^{opt}(\omega) = \frac{1}{Z_i(\omega) + Z_i^*(\omega)} F_e(\omega) = \frac{1}{2B_r(\omega)} F_e(\omega). \quad (6.5)$$

Thus, Eqs. (6.4) and (6.5) define the well-established impedance-matching or *complex-conjugate* condition [180], which is generally expressed in a feedback control form as  $H_{fb}(\omega) = Z_i^*(\omega)$ , where the controller  $H_{fb}(\omega)$  is placed in the feedback path, as shown in Fig. 6.1(b). Thus, Eq. (6.4) presents an appealing solution, largely due to its simplicity and its close association with well-established theories in the field of analogue circuits. However, despite these advantages, there are various issues related to the control specification given in (6.4), which create obstacles to the smooth implementation of this potentially valuable principle. These obstacles are detailed below:

- The impedance-matching conditions in (6.4) and (6.5) are frequency dependent, meaning that either the controller handles only a single frequency, or a representative key frequency for a broadband sea, as in the case of approximate complex-conjugate (ACC) control [128], or the controller is adapted with respect to frequency, for instance in the simple and effective controller [181].
- Another obstacle in implementing the impedance-matching (complex-conjugate) controller is consideration, or lack thereof, of the physical constraints of the system, such as position, velocity and PTO control force constraints. Consequently, successfully implementing the impedance-matching controller may require unrealistic device motion, velocity and PTO force values.
- The anti-causality of  $Z_i^*(\omega)$  in (6.4) creates a hindrance to the implementation of the controller, and requires future knowledge of excitation force  $f_e(t)$  for specific controller structures [151]. In the case of regular (monochromatic) waves, the excitation force is easily determined since it only comprises a single harmonic component (a single sinusoid). However, irregular waves present a more significant challenge as they contain multiple harmonic components, making the determination of the excitation force more difficult.
- In Fig. 6.1(a), the signs of PTO force and velocity can be opposite, which may require the PTO to supply power during certain parts of the sinusoidal cycle. This situation can place specific demands on PTO systems, which include facilitating bidirectional power flow and managing peak reactive power<sup>6.1</sup>, which can be significantly greater than active power, in some cases. The optimal *passive* PTO system would not need to supply power, but it may result in suboptimal control.

Even though the impedance-matching condition in (6.4) may not be practically feasible due to the various reasons discussed above, it does provide an intuitive approach to describe the fundamental dynamics of maximum energy absorption from ocean waves. Utilising the impedance-matching condition, in (6.4), several control strategies have been proposed for WECs [151], ranging from relatively *simple* WEC controllers [182] to optimisation-based WEC controllers [183].

---

<sup>6.1</sup>The topic of reactive power peak requirements in hydrodynamic WEC control is treated extensively in Chapter 8 of this thesis.

### 6.1.2 Passive damping controller

A passive damping controller, also referred to as resistive loading (RL) controller, is the default choice of hydrodynamic control in the literature concerning grid-connected wave energy conversion systems (see Table 3.3). As the name suggested, a passive damping controller does not require bidirectional power flow as in a reactive hydrodynamic controller and, consequently, a *passive* PTO system can be utilised. However, this may result in a suboptimal control with significantly less power absorption capabilities (see Section 6.4).

The PTO reference force  $f_{pto}^{ref}$  generated from RL control [94] is given by:

$$f_{pto}^{ref} = |Z_i(\omega_{pk})|\dot{z} \quad (6.6)$$

with,

$$|Z_i(\omega_{pk})| = \sqrt{B_r(\omega_{pk})^2 + \omega_{pk}(M + A_r(\omega_{pk}) - \frac{K_h}{\omega_{pk}})^2}, \quad (6.7)$$

where the optimal PTO resistance is specified at a chosen frequency  $\omega_{pk}$ , where  $\omega_{pk}$  is typically the peak of the input wave spectrum.

## 6.2 LiTe-Con

The LiTe-Con energy maximising controller, proposed in [184], aims to synthesise the optimal condition for maximising absorbed energy in the frequency domain, which is given by the impedance-matching principle. This control approach is highly effective and suitable for realistic scenarios due to its broadband nature and the inclusion of a constraint handling mechanism, as demonstrated in [184, 185]. In comparison to optimisation-based controllers [186], LiTe-Con is computationally simpler. Among simple WEC controllers, based on the impedance-matching principle without the inclusion of optimisation routines, LiTe-Con provides the best performance in terms of maximum power capture and constraint handling, as shown in [182]. LiTe-Con, being a feedforward controller, can effectively address the limitations of feedback impedance-matching-based controllers, such as stability and constraint handling, making it appealing for realistic WEC control implementation where WEC motion is significantly exaggerated. LiTe-Con is chosen as the reactive hydrodynamic WEC controller in this thesis, due to its aforementioned advantages.

LiTe-Con is classified as a reactive controller, which requires ‘reactive power’ from the DC-link at specific instances to operate correctly. It is important to note that this ‘reactive power’ is distinct from reactive electrical power, so a clear differentiation must be made when discussing reactive power in the hydrodynamic control context,

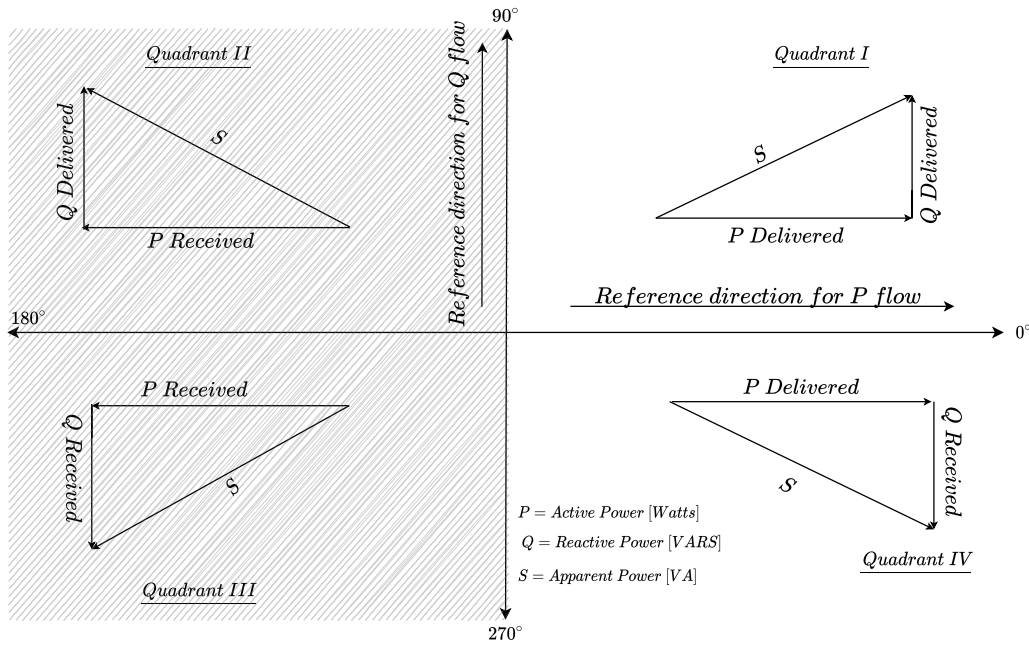


**Figure 6.2:** Four quadrant electrical power flow naming convention in bi-directional power flow applications. The reactive power, in the hydrodynamic WEC control sense, lies in the shaded region (quadrants II and IV).

compared to the reactive power in electrical networks. Fig. 6.2 depicts the convention for *electrical power* flow, both for active power  $P$  and reactive power  $Q$ , in bi-directional power flow applications. In the reactive hydrodynamic control of a WEC, the required reactive power from the grid-side is, in fact, negative electrical power, which lies in the second and third quadrant, as illustrated by the shaded region in the Fig. 6.2. For further details regarding the reactive power peaks phenomenon in hydrodynamic WEC control, readers are referred to the Chapter 8 (Section 8.1) of this thesis. From now on, in this chapter, reactive power in the hydrodynamic context will be referred to as '*reactive mechanical power*'. In contrast, reactive power in the electrical sense will be referred to as '*reactive electrical power*'.

As discussed in Section 6.1, standard results for impedance-matching-based control cannot be straightforwardly implementable in practice and require practical considerations for implementation [182]. Aiming to find an implementable structure for WEC control, and considering the impedance-matching condition, the frequency-domain description of the system  $G_0(s)$  can be, in general, expressed as<sup>6.2</sup>:

$$G_0(s) \Big|_{s=j\omega} = \Re\{G\} + j\Im\{G\}. \quad (6.8)$$

<sup>6.2</sup>For the sake of simplicity of notation, let  $\Re\{G\} = \Re\{G(j\omega)\}$  and  $\Im\{G\} = \Im\{G(j\omega)\}$  denote the *real-part* and *imaginary-part* operators, respectively.



Consequently, an alternative expression for the optimal relationship between  $F_e(\omega)$  and  $V^{opt}(\omega)$  (force-to-velocity mapping), as given in (6.5), can be obtained as:

$$\frac{V^{opt}(\omega)}{F_e(\omega)} = T_{f_e \rightarrow v}^{opt}(\omega) = \frac{\Re(G)^2 + \Im(G)^2}{2\Re(G)}. \quad (6.9)$$

By utilising the definitions provided in Eqs. (6.8) and (6.9), it is possible to express the optimal feedforward controller that satisfies the impedance-matching condition as:

$$H_{ff}(\omega) = \frac{\Re(G) + j\Im(G)}{2\Re(G)}, \quad (6.10)$$

such that:

$$T_{f_e \rightarrow v}^{opt}(\omega) = (1 - H_{ff}(\omega)) G_0(j\omega). \quad (6.11)$$

The LiTe-Con method aims to approximate the frequency-domain mapping  $H_{ff}(\omega)$  using a parametric LTI-stable and implementable dynamical system  $H_{ff}^{LC}(s)$  through the use of system identification algorithms [164, 187, 188], i.e.:

$$H_{ff}^{LC}(s) \Big|_{s=j\omega} \approx H_{ff}(\omega), \quad (6.12)$$

for  $\omega \in \mathcal{W} = [\omega_l, \omega_u]$ , which represents the target frequency band for controller approximation.  $H_{ff}^{LC}(s)$  represents the LiTe-Con feedforward mapping. The LiTe-Con offers a comprehensive control solution, effectively addressing panchromatic sea-states characterised by a power spectral density predominantly confined within  $\mathcal{W} = [\omega_l, \omega_u]$ . Tuning the LiTe-Con involves a global approximation using  $\|\cdot\|_2$ . To meet this requirement, the following condition must be fulfilled:

$$\|H_{ff}^{LC}(j\omega) - H_{f_{ex} \rightarrow f_u}^{opt}(\omega)\|_2 < \epsilon, \quad (6.13)$$

where  $\epsilon$  represents an *acceptability* level, serving as a design criterion. The controller's *acceptability* relies on power absorption within the frequency band  $\mathcal{W} = [\omega_l, \omega_u]$ , making it a crucial design parameter aimed at maximising power absorption. When implementing LiTe-Con in a practical setting, it is crucial to have a constraint handling mechanism in place, to avoid causing damage to the mechanical system. In [184], a constraint handling mechanism is proposed that involves the use of a constant value  $k \in [0, 1]$ . This mechanism ensures that the resulting control force reference  $f_{pto}^{ref}(t)$  for Gen-SC control can be expressed as:

$$f_{pto}^{ref}(t) = [kH_{ff}^{LC}(s) + (1 - k)] f_e(t), \quad (6.14)$$

Eq. (6.14) suggests that, for the target frequency band  $\mathcal{W}$ , the LiTe-Con controller matches the optimal expression in equation (6.9) when  $k = 1$ . Conversely, when

$k = 0$ , the output of the force-to-velocity mapping is set to zero, thereby halting the device motion (assuming ideal estimation of  $f_e(t)$ ), as illustrated in Fig. 6.3 for a heaving point absorber WEC (geometry presented in Fig. 6.8). In particular, Fig. 6.3 presents two plots side-by-side, with the left plot showing the frequency response of the LiTe-Con controller feedforward mapping  $H_{ff}^{LC}(\omega)$ , as well as the optimal (target) feedforward controller mapping  $H_{ff}^{opt}(\omega)$ . The right plot shows the force-to-velocity mapping of the overall system including LiTe-Con controller  $T_{f_e \rightarrow v}^{LC}(\omega)$ , along with the optimal (target) force-to-velocity response  $T_{f_e \rightarrow v}^{opt}(\omega)$ . The yellow shaded region in the Fig. 6.3 represents the frequency range that was chosen for controller synthesis, i.e.  $\mathcal{W}$ , which correspond to the panchromatic sea-states, where the power spectral density is mainly contained within  $\mathcal{W} = [\omega_l, \omega_u]$ . Moreover, the impact of varying the constant value  $k$ , used for constraint handling, is demonstrated on both frequency response mappings. It is worth noting that the device motion (displacement) is limited to the operational range of  $[-1.5, 1.5]$  [m]. In the constrained LiTe-Con case, the appropriate values of  $k$  are determined through exhaustive simulations for each sea state considered, assuming full knowledge of the excitation force. Specifically, for each sea state with peak period  $T_p \in [5, 12]$  [s], the resulting optimised values of  $k$ , that maintain operation within the physical constraints of the device, are shown in Fig. 6.4.

### 6.2.1 Dynamic constraint handling mechanism: LiTe-Con+

In the LiTe-Con+ control strategy for WEC systems [189], a dynamic constraint handling mechanism is introduced to address the limitations of the static gain-based constraint handling used in the LiTe-Con. While the LiTe-Con has shown effectiveness in various operating scenarios, its conservative constraint handling can limit control performance, particularly in scenarios where displacement limits are frequently reached. The LiTe-Con+ addresses this limitation by using an online estimation of the envelope of the excitation force to implement a time-variant constraint handling strategy. Since the excitation force is an exogenous factor that does not depend on the instantaneous dynamics of the system under linear operating conditions, the constraint handling action can be decoupled from the system motion, simplifying stability considerations. By using real-time estimates of the excitation force envelope, the LiTe-Con+ can provide more effective control, leading to increased energy absorption.

It is important to note that the main distinction between the LiTe-Con, given in Eq. (6.14), and the LiTe-Con+ lies in the nature of the adjustment of the gain parameter  $k$ . In the LiTe-Con+, the gain used for constraint handling is a time-varying one, which is determined dynamically and updated continuously over time, as explained in the following.

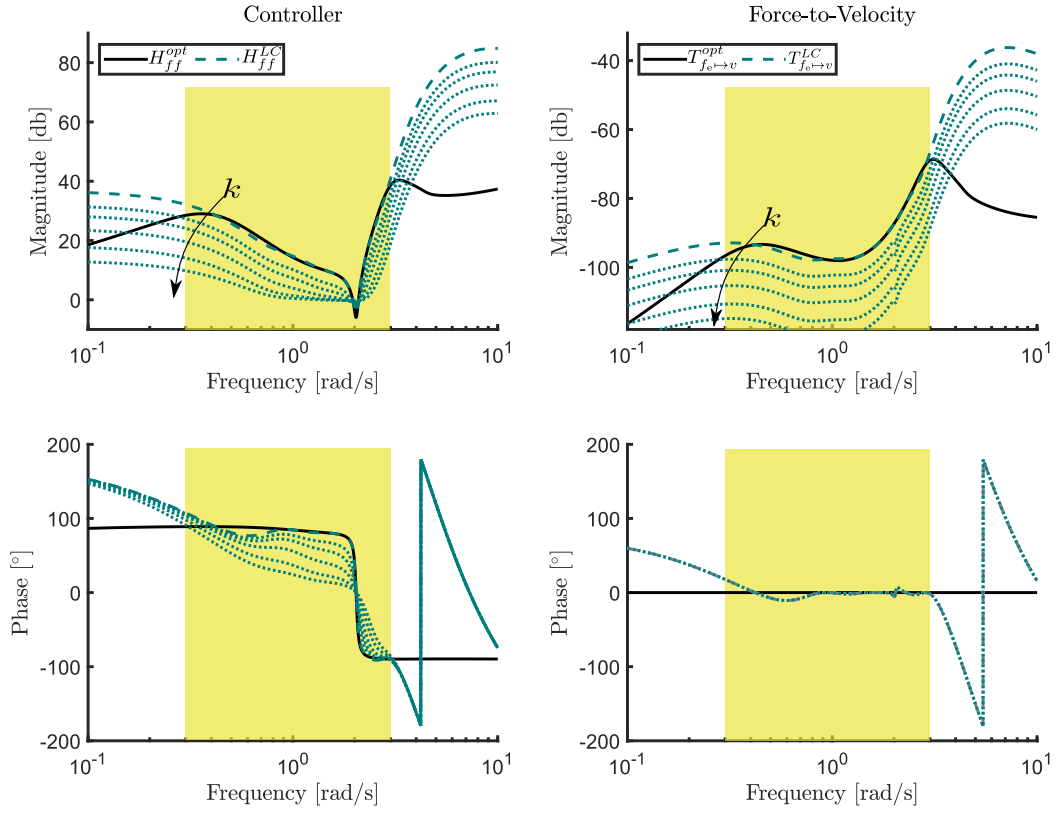


**Figure 6.3:** Frequency-response mappings of the LiTe-Con. In particular, the left column illustrates  $H_{\text{ff}}^{LC}(\omega)$  (dashed line), together with the optimal feedforward mapping  $H_{\text{ff}}^{\text{opt}}(\omega)$  (solid line). The right column depicts the force-to-velocity mapping associated with the LiTe-Con, i.e.,  $T_{\text{fe} \rightarrow \text{v}}^{LC}(\omega)$  (dashed line), along with the optimal force-to-velocity frequency response  $T_{\text{fe} \rightarrow \text{v}}^{\text{opt}}(\omega)$  (solid line). The effect of the constraint handling mechanism for  $k \in \{0.58, 0.4, 0.24, 0.13, 0.080\}$ , is depicted with dotted lines.

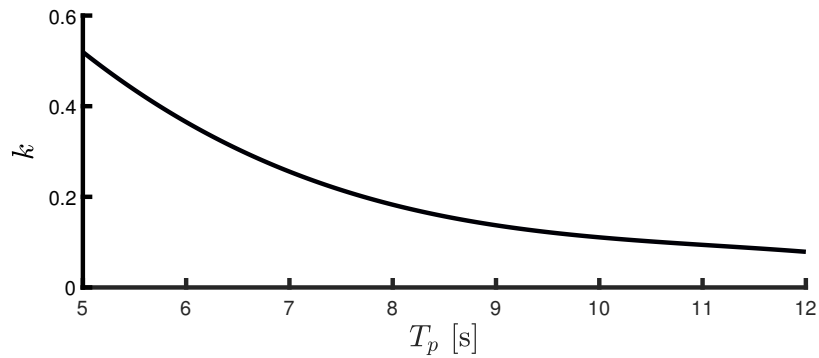


**Figure 6.4:** Optimised  $k$  values for sea states with peak periods  $T_p \in [5, 12]$  [s].

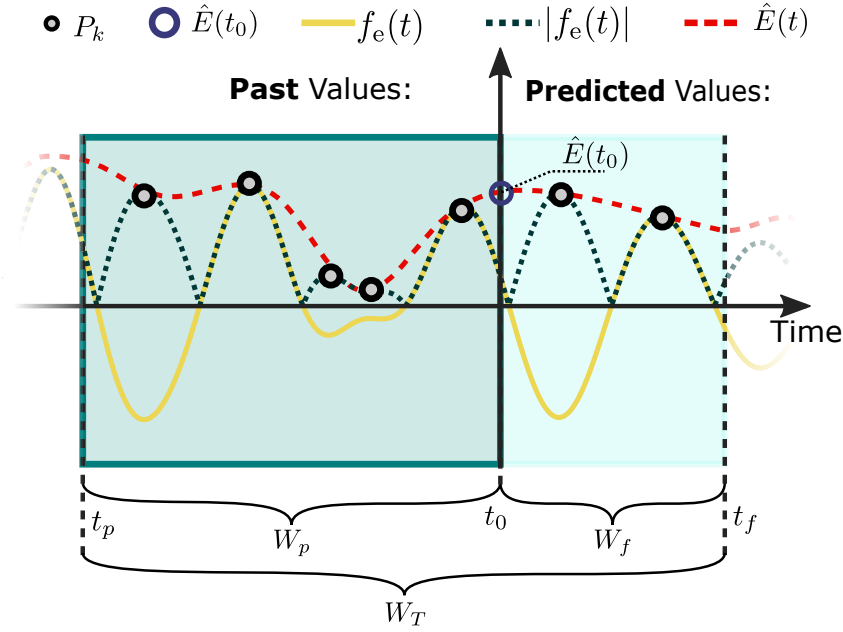


**Figure 6.5:** Envelope estimation algorithm.

**Envelope estimation:** The LiTe-Con+ control strategy adapts the constraint handling gain  $k$  based on online estimation of the envelope of the excitation force  $f_e(t)$ . Considering the excitation force can be assumed to be a quasi-periodic non-stationary process [181], given by:

$$f_e(t) \approx E(t) \cos\left(\int \omega_e(t) dt\right), \quad (6.15)$$

where  $E(t)$  denotes the instantaneous amplitude of  $f_e(t)$ . To estimate  $E(t)$ , a methodology, presented in [189], is employed, resulting in an amplitude estimation denoted as  $\hat{E}(t)$ . The envelope estimation approach involves interpolating the set of local maxima of  $|f_e(t)|$ ,  $P_k$ , within a time window that spans both past and, if available, future values of  $f_e(t)$ , for which a forecasting strategy can be used. Fig. 6.5 illustrates the typical steps involved in estimating the envelope. The key components of the algorithm include identifying the set of local maxima  $P_k$  within the time window, obtaining the absolute value of  $f_e(t)$ , and determining the current time  $t_0$  and the envelope estimate  $\hat{E}(t_0)$ .

It should be noted that the time windows for past and predicted values have lengths of  $W_p$  and  $W_f$ , respectively, and the total length of the time window is  $W_T = W_p + W_f$ , as depicted in Fig. 6.5. Finally, the estimate  $\hat{E}(t)$  can be obtained by interpolating the set of local maxima  $P_k$ , using standard interpolation techniques like cubic spline interpolation.

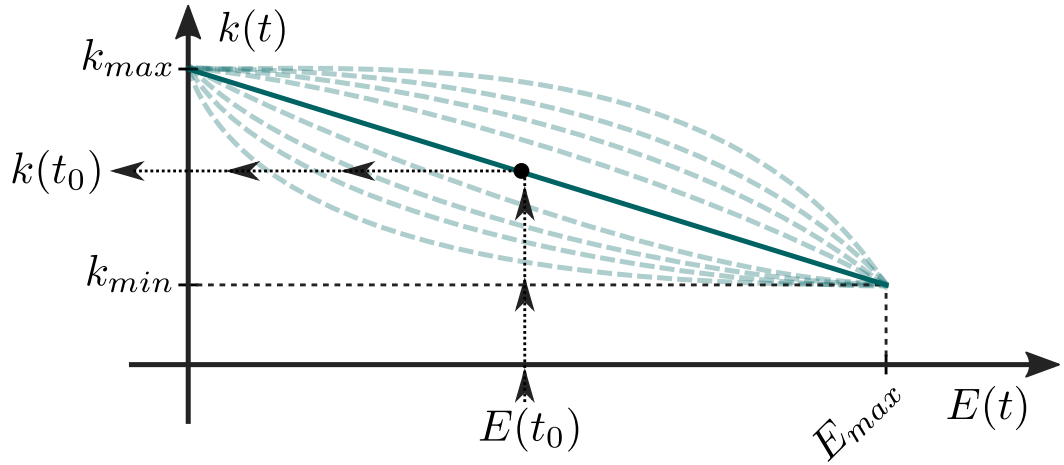


**Figure 6.6:** Various possibilities for mapping  $\mathcal{K}$ .

**Dynamical mapping and constraint gain:** To achieve the desired time-varying modulation of the gain  $k$ , and obtain a time-varying version of (6.14), a mapping  $\mathcal{K} : \mathbb{R}^+ \mapsto [k_{min}, k_{max}]$  is necessary. This mapping transforms the estimated envelope into the resulting modulation of  $k$ . Three tuning parameters are used to define this mapping:  $E_{max}$ , which is an estimate of the expected maximum value of the envelope, and  $k_{min}$  and  $k_{max}$ , which are the minimum and maximum interval limits for the modulation of  $k(t)$ , respectively. A set of curves, given by the exponential family, is used to define the mapping:

$$\mathcal{K} : k(t) = \begin{cases} \kappa_1 e^{\kappa_2 \hat{E}(t)} + \kappa_3 & \text{if } 0 \leq \hat{E}(t) \leq E_{max} \\ k_{min} & \text{if } \hat{E}(t) > E_{max} \end{cases}, \quad (6.16)$$

which is shown in Fig. 6.6, and depending on the mapping,  $\kappa_1$ ,  $\kappa_2$ , and  $\kappa_3 \in \mathbb{R}$ , in (6.16) can be easily fitted using basic curve fitting algorithms, with  $E_{max}$ ,  $k_{min}$ , and  $k_{max}$ . In this case, a linear mapping is used, which is illustrated by a solid green line in Fig. 6.6.

Now, Eq. (6.14) can be updated to show the time-varying constraint handling gain  $k(t)$  as follows:

$$f_{pto}^{ref}(t) = [k(t)H_{ff}^{LC}(s) + (1 - k(t))] f_e(t). \quad (6.17)$$

Hence, Eq. (6.17) provides a PTO force reference generated by the LiTe-Con+ with time-varying  $k(t)$ , which will be tracked by a Gen-SC controller presented in the following section.

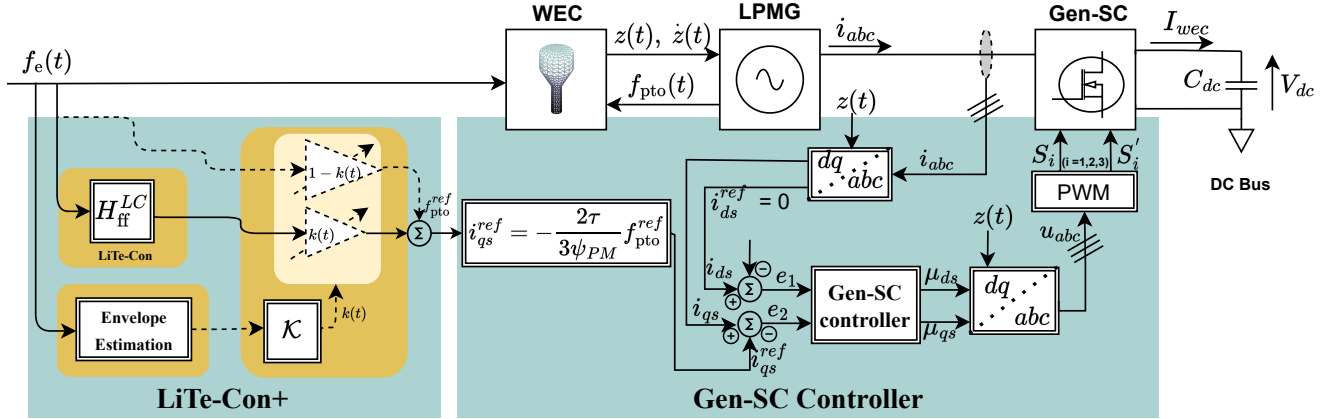


**Figure 6.7:** Device-side control structure including LiTe-Con+ (and LiTe-Con) and Gen-SC control.

### 6.3 Lyapunov-based Gen-SC Controller

For the Gen-SC, as well as other power converters in the complete W2G system, Lyapunov control is chosen, since the power converters are intrinsically nonlinear, with Lyapunov control being especially effective for nonlinear systems. Among the typical nonlinear controllers used for power converter control, Lyapunov-based stabilising control is computationally efficient and ensures the stability of the system using the Lyapunov stability criterion [190]. The theoretical development and application of various Lyapunov-based techniques to a wide range of practical engineering systems, such as electric machines and robotic systems, are presented in [191]. The control objectives of Gen-SC control can be summarised as follows:

1. Maximum power extraction from the waves by tracking a reference PTO force  $f_{pto}^{ref}(t)$  generated through hydrodynamic (LiTe-Con+/LiTe-Con/passive damping) WEC controllers.
2. Generator Copper (Cu)-loss minimisation by regulating the LPMG stator  $d$ -axis current  $i_{ds}$  to zero.

Fig. 6.7 shows the device-side control structure, including the hydrodynamic LiTe-Con+ controllers. The LPMG  $d$ - and  $q$ -axis currents are controlled via the Gen-SC. In this regard, it is evident, from Eq. (5.14), that the force generated by the LPMG can be controlled with only  $q$ -axis current  $i_{qs}$ . Therefore,  $i_{qs}^{ref}$  is generated by using Eq. (5.14) as:

$$i_{qs}^{ref} = -\frac{2\tau}{3\psi_{PM}} f_{pto}^{ref}, \quad (6.18)$$

where  $f_{pto}^{ref}$  represents the PTO force reference generated by the hydrodynamic controllers, i.e. Eq. (6.17) for LiTe-Con+, Eq. (6.14) for LiTe-Con, and Eq. (6.6) for passive damping controllers, respectively. Additionally,  $i_{ds}^{ref}$  is set to zero, to minimise generator Cu-losses. To this end, the following tracking error signals are introduced:

$$e_1 = x_1 - i_{ds}^{ref}, \quad (6.19)$$

$$e_2 = x_2 - i_{qs}^{ref}. \quad (6.20)$$

To achieve control objectives 1 and 2, listed above,  $e_1$  and  $e_2$  must be regulated to zero. Using (5.33) and (5.34), the dynamics of  $e_1$  and  $e_2$  can be derived as:

$$\dot{e}_1 = -\frac{R_s}{L_s}x_1 + \omega_e x_2 - \frac{1}{L_s}x_6\mu_{ds} - \dot{i}_{ds}^{ref}, \quad (6.21)$$

$$\dot{e}_2 = -\omega_e x_1 - \frac{R_s}{L_s}x_2 - \frac{\omega_e}{L_s}\psi_{PM} - \frac{1}{L_s}x_6\mu_{qs} - \dot{i}_{qs}^{ref}. \quad (6.22)$$

To drive  $e_1$  and  $e_2$  to zero,  $\dot{e}_1$  and  $\dot{e}_2$  are forced to behave as:

$$\dot{e}_1 = -c_1 e_1, \quad (6.23)$$

$$\dot{e}_2 = -c_2 e_2, \quad (6.24)$$

where  $c_1 > 0$  and  $c_2 > 0$  are design parameters. Then, the comparison of Eqs. (6.21) and (6.22) with Eqs. (6.23) and (6.24), respectively, results in the following control laws for the Gen-SC:

$$\mu_{ds} = \frac{1}{x_6}[-R_s x_1 + \omega_e L_s x_2 + c_1 e_1 L_s - L_s \dot{i}_{ds}^{ref}], \quad (6.25)$$

$$\mu_{qs} = \frac{1}{x_6}[-\omega_e L_s x_1 - R_s x_2 - \omega_e \psi_{PM} + c_2 e_2 L_s - L_s \dot{i}_{qs}^{ref}]. \quad (6.26)$$

### 6.3.1 Stability analysis

The stability of the Gen-SC control system is established by utilising Lyapunov stability criteria. In particular, it is investigated that the controllers presented in Eqs. (6.25) and (6.26), can force the state variations (errors), denoted as  $e_1$  and  $e_2$ , to converge to zero. The system is considered asymptotically stable if the proposed Lyapunov function  $V_1(\mathbf{e})$ , where  $\mathbf{e} = [e_1 \ e_2]^T$ , satisfies the following properties:

$$\begin{cases} V(0) = 0; \\ V(\mathbf{e}) > 0, \quad \forall \mathbf{e} \neq 0; \\ V(\mathbf{e}) = 0, \quad \text{as } \|\mathbf{e}\| = 0; \\ \dot{V}(\mathbf{e}) < 0, \quad \forall \mathbf{e} \neq 0. \end{cases} \quad (6.27)$$

A typical choice of a candidate Lyapunov function is a quadratic form of state variations (errors  $\mathbf{e}$ ). In this case, the Lyapunov function is chosen as  $V_1(\mathbf{e}) = \frac{1}{2}\mathbf{e}^T\mathbf{Q}_1\mathbf{e}$ , where  $\mathbf{Q}_1 \in \mathbb{R}^{2 \times 2}$  is a symmetric positive definite matrix. The selection of  $\mathbf{Q}_1$  allows some flexibility in choosing the candidate Lyapunov function [192]. For simplicity, we consider  $\mathbf{Q}_1 = \mathbb{I}_2 \in \mathbb{R}^{2 \times 2}$ , resulting in the following energy-like quadratic Lyapunov function for the Gen-SC system.

$$V_1(\mathbf{e}) = \frac{1}{2}(e_1^2 + e_2^2). \quad (6.28)$$

It is evident that the Lyapunov function  $V_1(\mathbf{e})$  satisfies the first three stability properties as expressed in (6.27). The fourth property in (6.27) can be achieved by employing the control laws derived in Eqs. (6.25) and (6.26). In order for the system to be asymptotically stable, the time derivative of  $V_1(\mathbf{e})$ , denoted as  $\dot{V}_1(\mathbf{e})$ , must be negative definite, i.e.  $\dot{V}_1(\mathbf{e}) < 0$ . By differentiating (6.28), we obtain:

$$\dot{V}_1(\mathbf{e}) = e_1\dot{e}_1 + e_2\dot{e}_2 \quad (6.29)$$

Substituting expressions for  $\dot{e}_1$  and  $\dot{e}_2$  from (6.23) and (6.24), respectively, into (6.29) yields:

$$\dot{V}_1(\mathbf{e}) = -c_1e_1^2 - c_2e_2^2. \quad (6.30)$$

Equation (6.30) shows that  $\dot{V}_1(\mathbf{e}) < 0$ ; thus, asymptotically stability of the equilibrium  $[e_1, e_2]^T = [0, 0]^T$ , is achieved.

## 6.4 Results

This section provides the performance assessment of the device-side control part of the high-performance W2G control scheme, for a direct-drive wave energy conversion system. The WEC geometry considered here, along with its dimensions, is shown in Fig. 6.8. For numerical simulation, the sea states (irregular waves) under consideration, based on a JONSWAP spectrum [123], have a fixed significant wave height of  $H_s = 2$  [m], with the peak wave period  $T_p \in [5, 12]$  [s], and a peak shape parameter  $\gamma = 3.3$ . In order to obtain statistically consistent results, a total of 20 realisations



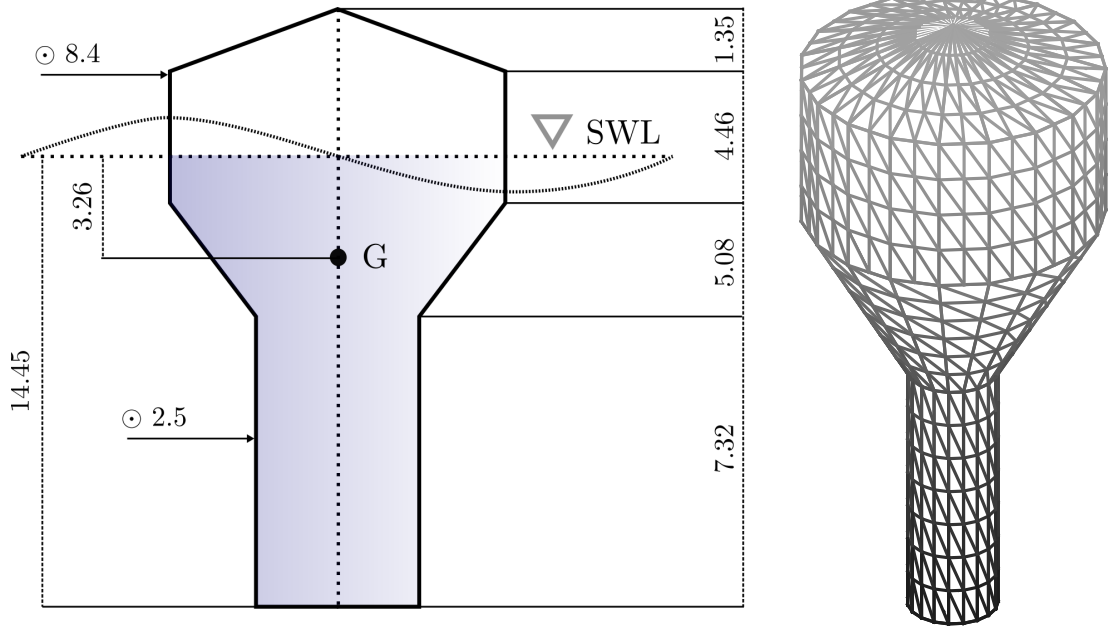


**Figure 6.8:** Full-scale CorPower-like device considered in this case study. Dimensions are in metres. The acronym SWL stands for still water level and the letter G is used to denote the center of gravity of the device.

are considered for each sea state, with each realisation having a duration of 200 times the peak wave period  $T_p$ .

In the following, a series of plots is presented to illustrate the behaviour of various parameters for the considered range of wave periods, i.e.  $T_p \in [5, 12]$  [s]. These plots depict the absorbed power, converted power, peak-to-average power (PTAP) ratio for the converted power, and the maximum PTO force. The absorbed hydrodynamic power represents the mechanical output of the WEC, while the converted power corresponds to the electrical power generated by the PTO, measured at the output of the Gen-SC. The obtained results, using LiTe-Con+ and LiTe-Con, are compared with benchmark passive damping (resistive loading) control, commonly used in the literature for grid integration of WECs. The comparison is illustrated in Fig. 6.9. In particular, Fig. 6.9(a) compares the absorbed hydrodynamic power for all the controllers considered here. The LiTe-Con+ and LiTe-Con outperform the passive damping controller, due to their broadband reactive nature, which is particularly effective for realistic irregular waves. Additionally, the dynamic constraint handling mechanism of LiTe-Con+ manages to use the operational range very effectively, and it performs better than the LiTe-Con which has a static constraint handling mechanism, for the same position constraint limits, i.e.  $[-1.5, 1.5]$  [m]. As a result, the converted power is significantly greater for both reactive controllers, i.e. LiTe-Con+ and LiTe-Con, compared to the passive damping controller, as illustrated in Fig. 6.9(b). However, for longer wave periods

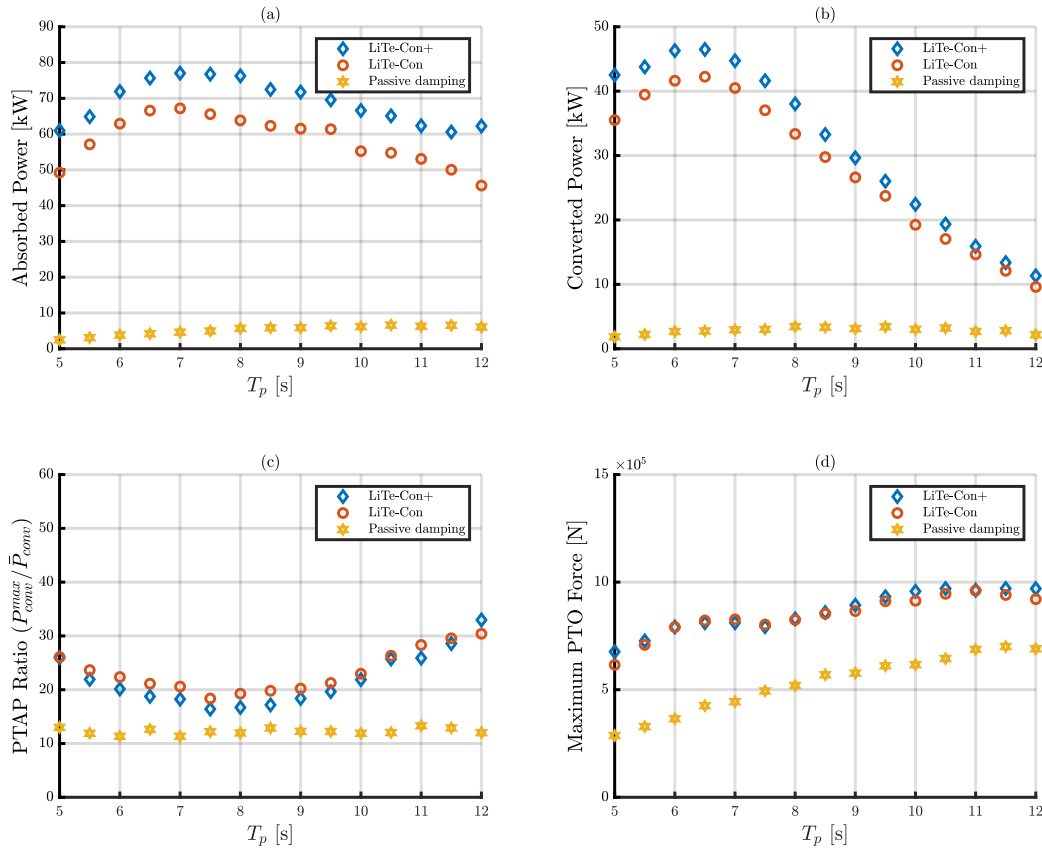


**Figure 6.9:** Performance comparison of LiTe-Con+, LiTe-Con and passive damping control for the totality of sea-states considered. (a) Absorbed power [kW], (b) Converted power [kW], (c) Peak-to-average power ratio of the converted power, and (d) Maximum PTO (control) force [N]

( $T_p > 10$  [s]), there is a significant drop in converted power for both LiTe-Con+ and LiTe-Con, due to increased Cu-losses in the LPMG stator, which are not accounted for in the LiTe-Con/LiTe-Con+ hydrodynamic model. The increase in Cu-losses for longer periods can be attributed to the increased PTO force requirements of both LiTe-Con+ and LiTe-Con, resulting in increased stator current and increased Cu-losses. This phenomenon of increased Cu-losses at longer periods is also reported in the literature, e.g., in [94, 193, 194]. Fig. 6.9(c) shows the PTAP ratios for the three hydrodynamic WEC controllers, which illustrate that the passive damping controller has the lowest PTAP ratios (around 10), consistent with this type of controller [194]. On the other hand, the PTAP ratios for both LiTe-Con+ and LiTe-Con are consistently higher than the passive damping controller, for the range of wave periods considered here, due to their multi-frequency reactive nature. For periods  $T_p > 10$  [s], the PTAP ratios for LiTe-Con+ and LiTe-Con increase significantly due to increased PTO force requirements. However, it is essential to note that the increase in PTAP ratios comes with a significant increase in absorbed power (see Fig. 6.9(a)). Furthermore,

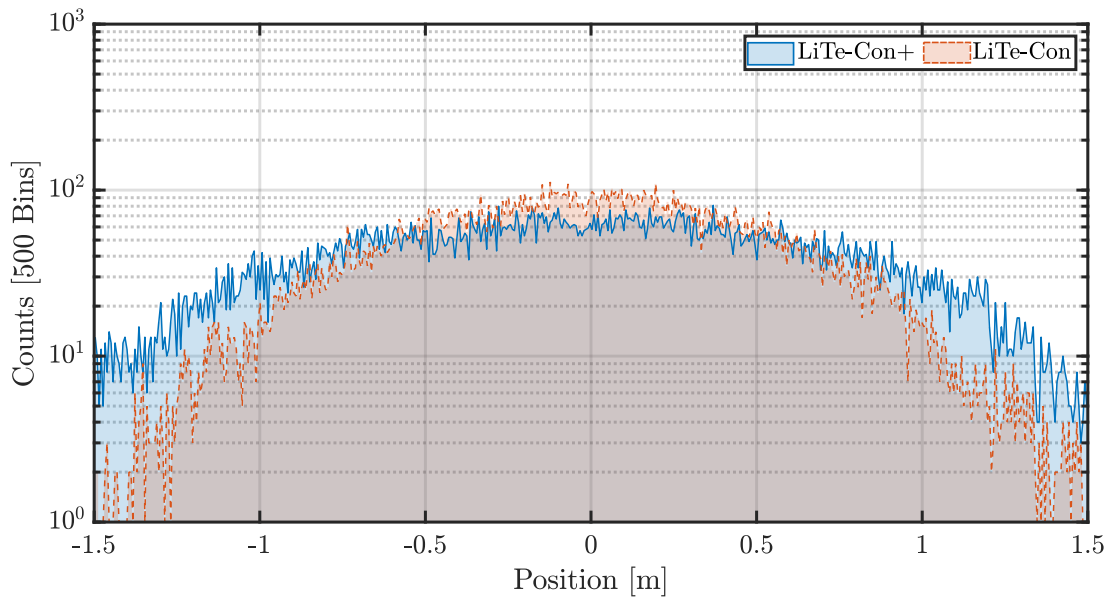


**Figure 6.10:** Comparative analysis of dynamic range for LiTe-Con+ and LiTe-Con for a sea-state with  $H_s = 2$  [m],  $T_p = 8.5$  [s] and  $\gamma = 3.3$ . A histogram of operation range  $[-1.5, 1.5]$  [m] with 500 bins is considered here.

Fig. 6.9(c) also depicts another interesting result: PTAP ratios for LiTe-Con+ are lower than that of LiTe-Con, due to better power absorption capability owing to the improved time-varying constraint handling mechanism. Finally, Fig. 6.9(d) presents the peak PTO force requirements of the three hydrodynamic controllers. As expected, LiTe-Con+ and LiTe-Con require more peak PTO forces than the passive damping controller, due to their broadband reactive nature.

The enhanced performance of the LiTe-Con+ controller can be attributed to its superior utilisation of the operational range, as demonstrated in Fig. 6.10. Specifically, a histogram is presented in Fig. 5.10 to visualise the operational range of both LiTe-Con+ and LiTe-Con controllers. The histogram consists of 500 bins covering a range of  $[-1.5, 1.5]$  [m], and illustrates the frequency of device displacement occurrences within each bin, for both controllers. The histogram highlights the significant improvement in operational range utilisation achieved by the LiTe-Con+ controller, compared to LiTe-Con, by employing a dynamic constraint handling mechanism, with an increased frequency of occurrence around the constraint limits of  $-1.5$  [m] and  $1.5$  [m]. Hence, the LiTe-Con+ reacts promptly to changes in the excitation force, while staying within its operating limits, and making optimal use of its operating range.

Naturally, the enhanced power capture performance of the LiTe-Con+ and LiTe-Con controllers come with increased capital costs. First, the higher PTO force requirement has implications for the necessary rating of the LPMG, resulting in higher costs for the PTO system. Additionally, higher PTAP values, particularly at longer wave periods,

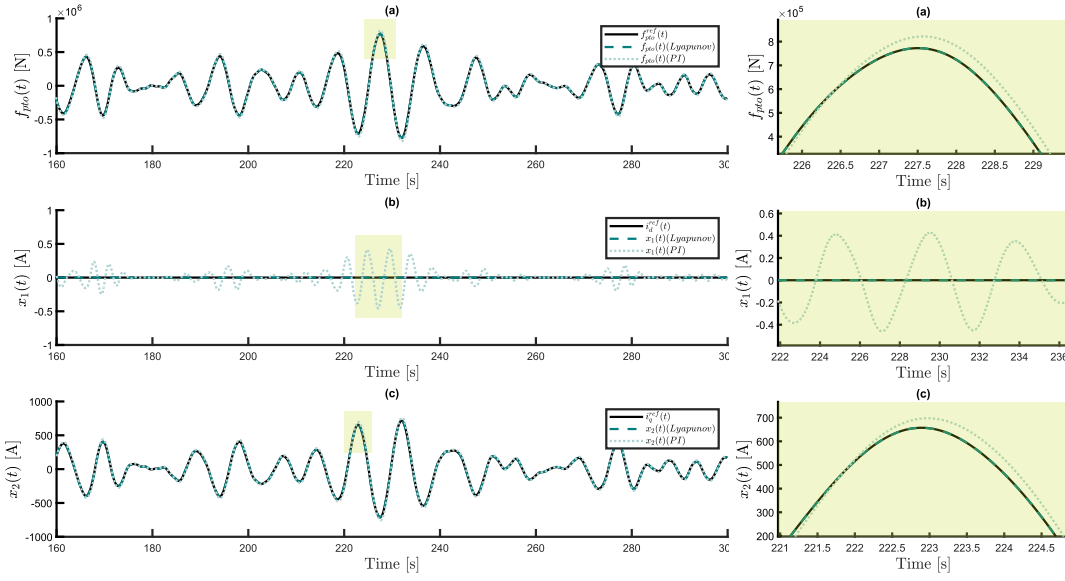


**Figure 6.11:** Tracking performance of the Gen-SC controller: (a) PTO force [N], (b) d-axis stator current [A], (c) q-axis stator current [A]. The highlighted sections are zoomed in plots presented on the right side of the respective plots.

necessitate higher ratings for the power conversion and storage systems. These factors contribute to elevated equipment costs within the powertrain, leading to higher capital expenditure. It is important to note that optimisation-based controllers, such as model predictive control (MPC), can incorporate constraints on maximum PTO force and Cu-losses more elegantly, reducing both the PTO force requirements and associated losses [94]. However, such formulations introduce additional computational complexity and may not be well-suited for real-time implementation due to increased computational costs. Furthermore, it should be acknowledged that there is a trade-off between performance, constraint handling, and powertrain equipment costs. While optimisation-based controllers may offer economic benefits by incorporating constraints on peak PTO force, reactive power, and stator current requirements [195–197], the main advantage of LiTe-Con (LiTe-Con+) is that it is a fixed LTI controller, which is computationally simpler, but may also be more attractive to industrial practitioners. In the following, typical tracking performance of the Lyapunov-based Gen-SC controller is evaluated using time series plots, for a single sea state. The properties of the sea state under consideration are a peak wave period of  $T_p = 8.5$  [s], which is the average value between the extremes of the complete wave period range of [5, 12] [s], and a significant wave height of  $H_s = 2$  [m]. The tracking performance of the Lyapunov-based Gen-SC controller is illustrated in Fig. 6.11 (a), (b), and (c), clearly demonstrating that the PTO force reference, provided by the LiTe-Con controller, is accurately tracked by the actual PTO force  $f_{pto}(t)$ , achieved by tracking the stator q-axis current  $x_2(t)$

of the LPMG to its reference  $i_{qs}^{ref}(t)$ . Additionally, the control strategy effectively minimises Cu-losses in the generator by regulating the d-axis current  $x_1(t)$  to zero. It is worth noting that Fig. 6.11 (a), (b), and (c) also depict the tracking performance of an alternative Proportional-Integral (PI) controller, predominant in the literature concerning wave energy grid integration, which exhibits inferior performance compared to the Lyapunov-based control in accurately tracking the reference signals. While the Lyapunov controller demonstrates good tracking performance, it is crucial to recognise that the objective of extracting maximum power from the waves relies heavily on the quality of the PTO force reference  $f_{pto}^{ref}$  generated by the hydrodynamic control, which is depicted in Fig. 6.9(a), where it can be observed that the power absorbed by the wave energy conversion system is consistently lower for a passive damping controller, in comparison to the LiTe-Con and LiTe-Con+ controllers, irrespective of the type of controller employed for the Gen-SC.

## 6.5 Conclusions

This chapter presents the device-side control part of the high-performance W2G controller for a direct-drive heaving point absorber-based wave energy conversion system. First, the principle of impedance-matching, which provides basics for the WEC hydrodynamic control, including finite-order sub-optimal realisation, such as a passive damping hydrodynamic controller, is introduced. Then, a panchromatic finite-order approximation of the impedance-matching condition, i.e. LiTe-Con (and LiTe-Con+), is presented, which is utilised to provide a PTO force reference to the Gen-SC controller for maximum power extraction from waves. The use of LiTe-Con (and LiTe-Con+) enables the wave energy conversion system to extract more power from waves compared to a passive damping controller. Additionally, both LiTe-Con and LiTe-Con+ also provide position constraint handling mechanisms, while no such mechanism is available in passive damping control. Utilising time-varying (dynamic) constraint handling in the LiTe-Con+ leads to superior power absorption performance compared to LiTe-Con, achieved by effectively utilising the operational range of the system, while ensuring that the device remains within its position constraints.

While the reactive broadband controllers (LiTe-Con and LiTe-Con+) offer the advantage of delivering more power compared to passive damping control, there are certain implications to consider in terms of equipment ratings and costs. The reactive mechanical power requirements of LiTe-Con (and LiTe-Con+), and higher PTAP ratios for the converted power, result in increased rating requirements for the PTO and power conversion equipment in the powertrain. This consideration highlights the need to limit the amount of reactive mechanical (negative electrical) power transmitted to

the WEC from the DC link, as it affects the overall system performance and equipment ratings. However, imposing a constraint on reactive mechanical power introduces nonlinearity and significantly increases the control complexity. In the case of relatively *simple* WEC controllers [182], such as LiTe-Con, the focus is on maintaining low complexity, but with effective constraint handling. Nonetheless, more sophisticated controllers, such as pseudo-spectral and MPC, offer possibilities for addressing these constraints at the expense of increased computational complexity [195–197]. These advanced control strategies provide avenues for optimising the system performance while effectively managing equipment ratings and costs.

Lyapunov-based nonlinear controllers are used here for Gen-SC control to track the PTO force reference provided by the hydrodynamic controllers, demonstrating overall better tracking performance than PI controllers, commonly used in the literature regarding wave energy grid integration. Furthermore, the Lyapunov-based control synthesis procedure not only achieves desirable control performance but also *guarantees* the stability of the electrical section of the device-side subsystem.

# 7

## Storage and grid-side control

### Contents

---

<b>7.1 Lyapunov-based Grid-SC controller</b> . . . . .	<b>100</b>
7.1.1 Grid Synchronisation and phase-locked loop . . . . .	102
<b>7.2 Storage system controller</b> . . . . .	<b>103</b>
<b>7.3 Stability analysis</b> . . . . .	<b>104</b>
<b>7.4 Energy management system</b> . . . . .	<b>105</b>
<b>7.5 Results</b> . . . . .	<b>107</b>
<b>7.6 Conclusions</b> . . . . .	<b>111</b>

---

As mentioned in Chapter 6, the W2G control framework includes device-side, grid-side, and storage subsystem controllers. This chapter focuses on the grid-side and storage subsystem control parts of the overall W2G control framework in addition to the energy management system (EMS), which provides a supervisory control mechanism for both grid-side and storage controllers. The control objectives of the Grid-SC controller include maximum active power injection and zero reactive electrical power injection (unity power factor control), which are achieved by tracking  $i_{dg}^{ref}$  and  $i_{qg}^{ref}$  currents provided by the EMS. On the other hand, the storage system controller tracks  $v_{uc}^{ref}$ , also provided by the EMS, and achieves the following control objectives:

1. **DC bus voltage regulation:** The storage system controller absorbs peaks in the output power generated by the wave energy converter (WEC), denoted as  $P_{wec}$ , and regulates the DC bus voltage. This helps improve power quality by smoothing out fluctuations in power output.

2. **Reactive hydrodynamic control support:** The storage system controller provides negative (reactive) power to the device-side, enabling support for reactive hydrodynamic control strategies, i.e. LiTe-Con and LiTe-Con+.
3. **Grid low-voltage ride-through (LVRT) support:** During grid fault events, the storage system controller ensures that the system remains connected to the grid and provides support to ride through low-voltage conditions.

The primary objective of this chapter is to provide a comprehensive description of the grid-side control, storage control, and the EMS. Specifically, the Lyapunov-based nonlinear controllers for grid-side converter (Grid-SC), along with synchronous reference phased locked loop (SRF-PLL) for grid phase tracking, are detailed in Section 7.1. Section 7.2 then describes a Lyapunov-based controller for the buck-boost converter connected to the UC-storage subsystem, performing DC bus voltage regulation, reactive hydrodynamic control support, and grid support during grid faults. In Section 7.4, a supervisory EMS is presented, which ensures optimal operation of storage and Grid-SC controllers by providing the current references for grid-side and storage controllers. Section 7.5 presents results for both control systems, while Section 7.6 concludes this chapter.

## 7.1 Lyapunov-based Grid-SC controller

The Grid-SC control is responsible for maximum active power and zero reactive electrical power (unity power factor) injection into the grid. A synchronous reference frame phase-locked loop (SRF-PLL) is utilised for grid phase tracking to ensure proper synchronisation with the grid voltage. Details of the SRF-PLL can be found in Section 7.1.1. The  $d$ - $q$ -axis current references, denoted as  $i_{dg}^{ref}$  and  $i_{qg}^{ref}$ , are determined by the EMS discussed in Section 7.4. Specifically,  $i_{dg}^{ref}$  is responsible for achieving maximum active power injection to the grid, contributing to efficient energy transfer. On the other hand, the value of  $i_{qg}^{ref}$  depends on the operating mode, varying between normal grid operation and fault conditions, as provided by the EMS. Under normal grid operation,  $i_{qg}^{ref}$  is set to zero for unity power factor control, while  $i_{qg}^{ref}$  is not zero during grid faults as determined by the EMS to support grid fault. The Grid-SC control structure is shown in Fig. 7.1.

The current tracking errors are defined as:

$$e_3 = x_3 - i_{dg}^{ref} \quad (7.1)$$

$$e_4 = x_4 - i_{qg}^{ref} \quad (7.2)$$



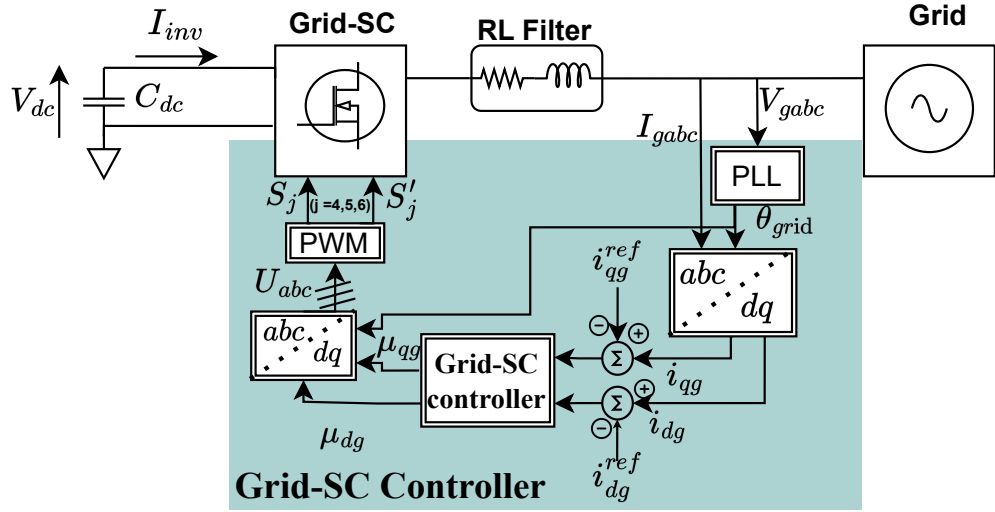


**Figure 7.1:** Grid-SC control structure.

To achieve the control objectives of maximum active power injection and zero reactive power injection into grid,  $e_3$  and  $e_4$  must be regulated to zero. Using (5.35) and (5.36), the dynamics of  $e_3$  and  $e_4$  can be derived as:

$$\dot{e}_3 = -\frac{V_{dg}}{L_f} - \frac{R_f}{L_f}x_3 + \omega_o x_4 + \frac{x_6}{L_f}\mu_{dg} - \dot{i}_{dg}^{ref} \quad (7.3)$$

$$\dot{e}_4 = -\frac{V_{qg}}{L_f} - \omega_o x_3 - \frac{R_f}{L_f}x_4 + \frac{x_6}{L_f}\mu_{qg} - \dot{i}_{qg}^{ref} \quad (7.4)$$

To drive errors  $e_3$  and  $e_4$  asymptotically to zero,  $\dot{e}_3$  and  $\dot{e}_4$  are forced to behave as:

$$\dot{e}_3 = -c_3 e_3 \quad (7.5)$$

$$\dot{e}_4 = -c_4 e_4 \quad (7.6)$$

where,  $c_3 > 0$  and  $c_4 > 0$ , are controller design parameters. Comparing Eqs. (7.3) and (7.4) to Eqs. (7.5) and (7.6) results in the following control laws for the Grid-SC:

$$\mu_{dg} = \frac{1}{x_6} [V_{dg} + R_f x_3 - \omega_o L_f x_4 - c_3 e_3 L_f + L_f \dot{i}_{dg}^{ref}] \quad (7.7)$$

$$\mu_{qg} = \frac{1}{x_6} [V_{qg} + \omega_o L_f x_3 + R_f x_4 - c_4 e_4 L_f + L_f \dot{i}_{qg}^{ref}] \quad (7.8)$$

### 7.1.1 Grid Synchronisation and phase-locked loop

A synchronous reference frame phase-locked loop (SRF-PLL) is used to estimate the frequency and phase of the grid. The SRF-PLL is a closed-loop feedback control system designed to synchronise its output signal with the reference input signal, which in this case, is the grid voltage. Ideal grid conditions are assumed, i.e. the grid is supposed to be a sinusoidal voltage source with constant frequency. A synchronous reference frame PLL is employed here due to its simplicity and accuracy for estimating the grid phase under ideal grid conditions [198]. The structure of an SRF-PLL is shown in Fig. 7.2, which includes various components, such as a phase detector, low-pass filter, and voltage-controlled oscillator (VCO), working together to track and synchronise the grid frequency and phase. By accurately estimating the grid frequency and phase, the SRF-PLL ensures proper synchronisation of the Grid-SC with the grid voltage, enabling effective control and operation of the system.

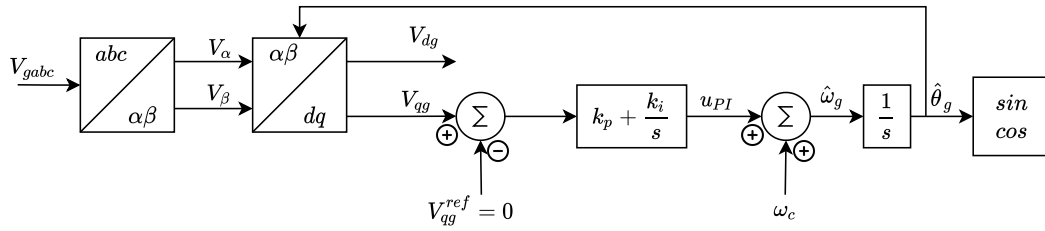


**Figure 7.2:** SRF-PLL structure for grid phase tracking.

The following 3-phase input grid voltages are assumed:

$$\begin{aligned} v_{ga} &= V_g \sin(\theta_g) \\ v_{gb} &= V_g \sin\left(\theta_g - \frac{2\pi}{3}\right) \\ v_{gc} &= V_g \sin\left(\theta_g - \frac{4\pi}{3}\right), \end{aligned} \quad (7.9)$$

where  $V_g$  and  $\theta_g$  denote the amplitude and phase of three-phase grid voltages, respectively. Using Park [169] and Clarke [199] transformations, the  $d$ -axis voltage  $V_{dg}$  is aligned with  $V_g$ , while  $V_{qg}$  is orthogonal to the  $d$ -axis. The phase error information is contained in  $V_{qg}$ , and a PI controller is used to regulate it.

$$G_c(s) = \frac{k_p s + k_i}{s}. \quad (7.10)$$

The output of the PI controller  $u_{PI}$  is an actuation signal, added to the centre frequency  $\omega_c$ . The second sum block in Fig. 7.2 generates the estimated frequency in radians,

which is then used to estimate the phase angle  $\hat{\theta}_g$  through the voltage-controlled oscillator. The closed-loop transfer function of the PLL system is obtained as follows:

$$G_{CL}(s) = \frac{V_g(k_p s + k_i)}{s^2 + V_g k_p s + V_g k_i}. \quad (7.11)$$

The closed-loop transfer function  $G_{CL}(s)$  in (7.11) can be represented as a second-order transfer function of the form:

$$G_{CL}(s) = \frac{2\zeta\omega_n s + \omega_n^2}{s^2 + 2\zeta\omega_n s + \omega_n^2}, \quad (7.12)$$

with

$$\omega_n = \sqrt{V_g k_i}, \quad \text{and} \quad \zeta = \frac{V_g k_p}{2\sqrt{V_g k_i}}, \quad (7.13)$$

where  $\omega_n$  is the bandwidth of the closed-loop PLL system, and  $\zeta$  is the damping ratio. The controller gains in Eq. (7.10) are tuned to minimise the phase error, which is the main objective of the PI controller. The PI controller acts as a low-pass filter to attenuate measurement noise, with design criteria employed to balance fast-tracking and noise rejection. It is worth noting that increasing the PLL bandwidth leads to a faster response time but poor filtering ability.

## 7.2 Storage system controller

The control of the DC/DC buck-boost converter plays a crucial role in the operation of the UC storage system within the W2G control scheme. The UC storage system is responsible for performing three essential tasks. Firstly, it supports reactive hydrodynamic control using, for example, LiTe-Con or LiTe-Con+, by supplying reactive mechanical power to the LPMG, when required, enabling reactive hydrodynamic control implementation in the W2G control framework. Secondly, DC bus voltage regulation is achieved indirectly by tracking the UC reference current  $I_{uc}^{ref}$ , ensuring that the DC bus voltage remains within the desired operating range. Thirdly, the UC storage system provides grid support during grid faults by supplying reactive electrical power. To achieve these tasks, the UC reference current  $I_{uc}^{ref}$  is generated by a supervisory EMS, detailed in Section 7.4, which employs a rule-based strategy to determine the appropriate reference current for the UC storage system. The complete W2G control block diagram, including the storage controller structure, is shown in Fig. 7.3.

The following tracking error is defined for UC-storage converter control:

$$e_5 = x_5 - I_{uc}^{ref}. \quad (7.14)$$

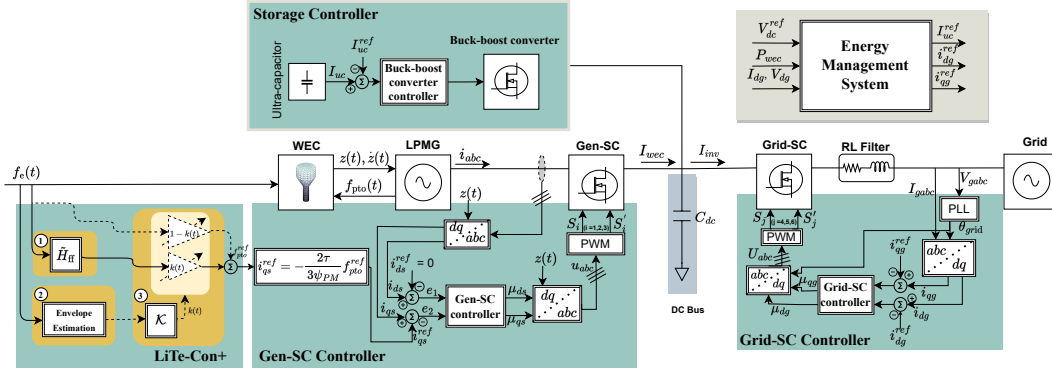


Figure 7.3: W2G control block diagram.

Using Eq. (5.37), the dynamics of  $e_5$  are derived as:

$$\dot{e}_5 = \frac{V_{uc}}{L_{uc}} - \frac{R_{uc}}{L_{uc}}x_5 - \mu_{78} \frac{x_6}{L_{uc}} - \dot{I}_{uc}^{ref}. \quad (7.15)$$

To regulate  $e_5$  to zero,  $\dot{e}_5$  is enforced to behave as:

$$\dot{e}_5 = -c_5 e_5 + e_6, \quad (7.16)$$

where,  $c_5 > 0$  is an additional design parameter.  $e_6$  is now defined as the DC bus voltage error, as follows:

$$e_6 = x_6 - V_{dc}^{ref}. \quad (7.17)$$

The control law  $\mu_{78}$  is easily obtained by comparing Eqs. (7.15) and (7.16) as:

$$\mu_{78} = \frac{1}{x_6} [(V_{uc} - R_{uc})x_5 + c_5 e_5 L_{uc} - e_6 L_{uc} - L_{uc} \dot{I}_{uc}^{ref}]. \quad (7.18)$$

It is worth mentioning that  $e_6$  is introduced in (7.18) as an extra term to adjust the DC bus voltage. The incorporation of  $e_6$  in (7.18) enables an indirect control of the DC bus voltage through the UC-based buck-boost converter controller. The dynamics of  $e_6$  will be introduced later.

## 7.3 Stability analysis

Similar to the Gen-SC controller, the stability of the Grid-SC and storage system controllers can be established using the Lyapunov stability criterion. In this regard, a commulative Lyapunov candidate function for the electrical components of the W2G powertrain (both device- and grid-sides), using (6.28), as follows:

$$V_c(\mathbf{e}) = V_1(\mathbf{e}) + \frac{1}{2}(e_3^2 + e_4^2 + e_5^2 + e_6^2). \quad (7.19)$$

It is worth noting that  $V_c(\mathbf{e})$  possess the first three properties expressed in (6.27). To satisfy the fourth property, i.e.  $\dot{V}_c(\mathbf{e}) < 0, \forall \mathbf{e} \neq 0$ , differentiating (7.19) yields:

$$\dot{V}_c(\mathbf{e}) = \dot{V}_1(\mathbf{e}) + (e_3\dot{e}_3 + e_4\dot{e}_4 + e_5\dot{e}_5 + e_6\dot{e}_6). \quad (7.20)$$

Using (6.29) results in

$$\dot{V}_c(\mathbf{e}) = (e_1\dot{e}_1 + e_2\dot{e}_2 + e_3\dot{e}_3 + e_4\dot{e}_4 + e_5\dot{e}_5 + e_6\dot{e}_6). \quad (7.21)$$

Substituting expressions for  $\dot{e}_1, \dot{e}_2, \dot{e}_3, \dot{e}_4$ , and  $\dot{e}_5$  from (6.23), (6.24), (7.5), (7.6) and (7.16), respectively, into (7.21) leads to the following:

$$\dot{V}_c(\mathbf{e}) = -c_1e_1^2 - c_2e_2^2 - c_3e_3^2 - c_4e_4^2 - c_5e_5^2 + e_6(e_5 + \dot{e}_6). \quad (7.22)$$

To verify that  $\dot{V}_c(\mathbf{e}) < 0$ ,  $\dot{e}_6$  is defined as follows:

$$\dot{e}_6 = -c_6e_6 - e_5, \quad (7.23)$$

where  $c_6 > 0$  is yet another design parameter. Utilising (7.16),  $\dot{V}_c(\mathbf{e})$  is updated as:

$$\dot{V}_c(\mathbf{e}) = -c_1e_1^2 - c_2e_2^2 - c_3e_3^2 - c_4e_4^2 - c_5e_5^2 - c_6e_6^2. \quad (7.24)$$

Eq. (7.24) indicates that  $\dot{V}_c(\mathbf{e}) < 0$ , implying that the equilibrium,  $[e_1, e_2, e_3, e_4, e_5, e_6]^\top = [0, 0, 0, 0, 0, 0]^\top$ , is asymptotically stable. It is important to note that DC bus voltage  $V_{dc}^{bus}$  regulation is achieved indirectly by controlling the UC current  $I_{uc}$ . Specifically, the convergence of the error  $e_6$  depends on the convergence of  $e_5$ , and introducing  $e_6$  indirectly imposes a constraint on  $e_5$ .

## 7.4 Energy management system

The energy management system (EMS) serves as a supervisory control mechanism in the overall W2G control scheme. The EMS plays a vital role in coordinating the operation of the storage converter (DC/DC buck-boost converter) and Grid-SC controllers, ensuring continuous and controlled W2G operation and responding effectively to normal and fault conditions. The flowchart, shown in Fig. 7.4, illustrates the operation of the EMS under both normal operating conditions and during fault events.

During normal grid operation, the main objective of the EMS is to ensure that the UC storage fulfils two tasks: (1) regulating the DC bus voltage and (2) providing support for reactive hydrodynamic Lite-Con (and LiTe-Con+) control. Furthermore, the EMS supplies the current references, i.e.  $i_{dg}^{ref}$  and  $i_{qg}^{ref}$ , to the Grid-SC controller,

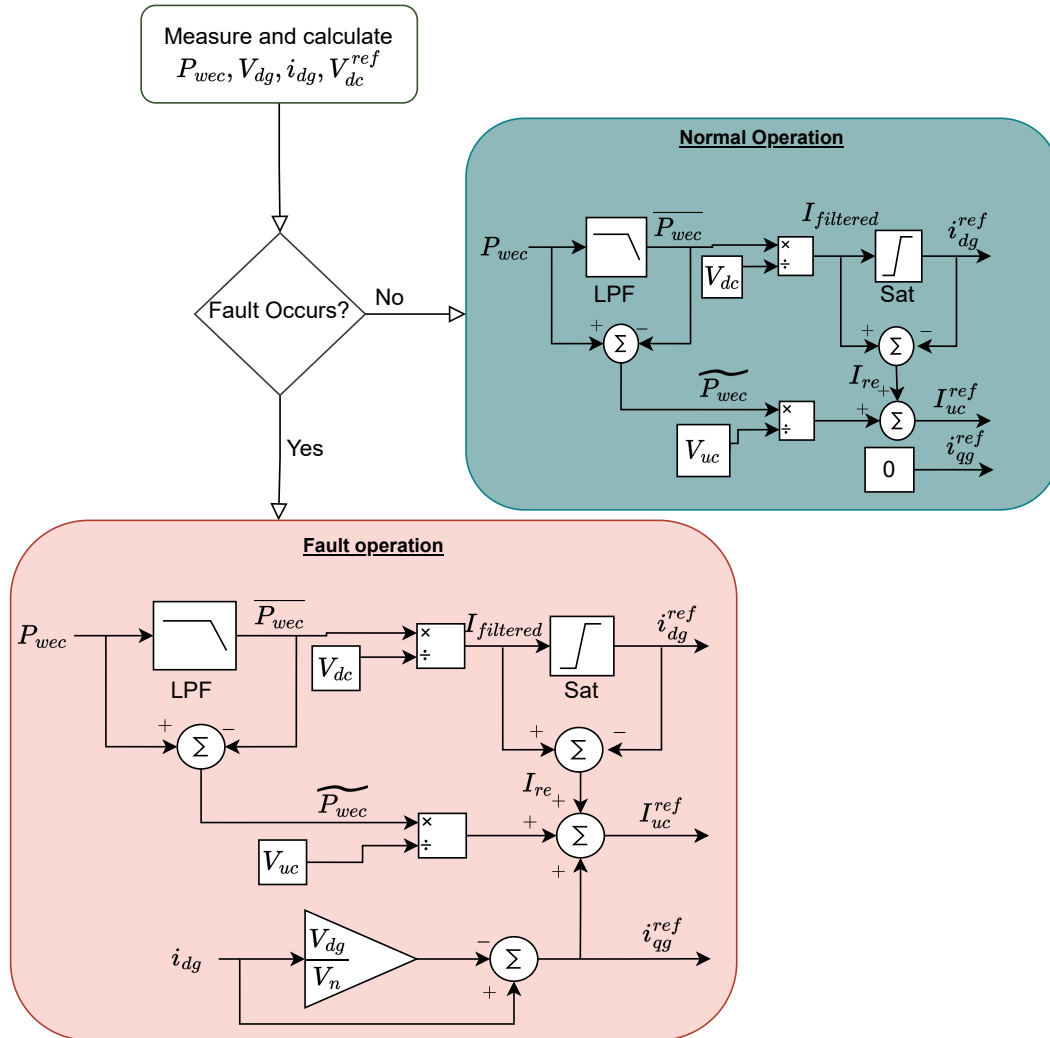


**Figure 7.4:** Energy management system overview.

enabling maximum active power and zero reactive electrical power injection into the grid. The power extracted from the WEC, denoted as  $P_{wec}$ , is divided into two components using a low-pass filter (LPF) as follows:

$$P_{wec} = \widetilde{P_{wec}} + \overline{P_{wec}}. \quad (7.25)$$

Implementing filter-based power splitting methods is a common approach in the literature, particularly for applications involving hybrid energy storage systems (HESS) [17, 200]. However, determining the optimal cut-off frequency (time constant) for the low-pass filter to maximise DC bus voltage regulation performance is a challenging task. The relationship between DC bus voltage regulation and the filter cut-off frequency is complex, and selecting the cut-off frequency for the EMS involves a trial-and-error process. Consequently, the cut-off frequency selection for the EMS is ultimately achieved by trial and error, with minimum DC bus voltage variance

achieved with a cut-off frequency of 0.02 [Hz]. The high-frequency component of power, denoted as  $\widetilde{P}_{wec}$  in (7.25), is utilised to derive a reference signal for the UC (storage) controller. The UC controller absorbs the high-frequency fluctuations in  $P_{wec}$  and regulates the DC bus voltage. The saturation block, depicted in Fig. 7.4, ensures that the UC storage meets the necessary negative power (reactive mechanical power) required for LiTe-Con (or LiTe-Con+). On the other hand, the low-frequency (averaged) component  $\overline{P}_{wec}$  of the power is fed into the inverter and used to generate the current reference signal  $i_{dg}^{ref}$  for the Grid-SC control.

During a grid fault event, the EMS ensures that the grid is supported by providing a reactive current  $i_{qg}$  proportional to the voltage sag caused by the fault using the UC storage. As a result, the reference current  $i_{qg}^{ref}$  is non-zero throughout the duration of grid faults. Therefore, in addition to the reactive LiTe-Con and DC bus voltage regulation components, the UC reference current  $I_{uc}^{ref}$  also includes a third component that provides grid fault support, as illustrated in Fig. 7.4.

## 7.5 Results

In this section, the performance of the Grid-SC and storage controllers are assessed by analysing time-series plots. Similar to the Gen-SC controller, the time-series plots presented here correspond to an irregular sea-state characterised by a JONSWAP spectrum[152], with  $H_s = 2$  [m],  $T_p = 8.5$  [s] and  $\gamma = 3.3$ .

The tracking performance of the Grid-SC control is presented in Fig. 7.5. Both  $d$ -axis and  $q$ -axis currents are accurately tracked, with minimal errors achieved through Lyapunov control. Fig. 7.5 also illustrates a significant degradation in tracking performance when an alternative benchmark PI controller is used, primarily due to its inability to handle system nonlinearities. The objective of achieving maximum active power injection is accomplished by accurately tracking the  $d$ -axis current  $x_3(t)$  to its reference value  $i_{dg}^{ref}$ , which is generated by the EMS at the DC bus. Fig. 7.5(a) demonstrates that the injected current varies according to the wave profile. Furthermore, regulating the  $q$ -axis current  $x_4(t)$  to zero ensures zero electrical reactive power injection, resulting in a unity power factor for the injected grid power.

The tracking performance of the storage controller is presented in Fig. 7.6. In particular, Fig. 7.6(a) depicts the absorption of high-frequency power components by the UC storage at the DC bus, as allocated by the EMS. It is worth noting that, once again, the Lyapunov controller outperforms the benchmark PI controller in terms of tracking ability, resulting in a considerably tighter regulation of the DC bus voltage  $V_{dc}^{bus}$ , as demonstrated in Fig. 7.6. The indirect control of the UC storage current  $x_5(t)$  effectively achieves the objective of maintaining a tightly regulated DC bus voltage,

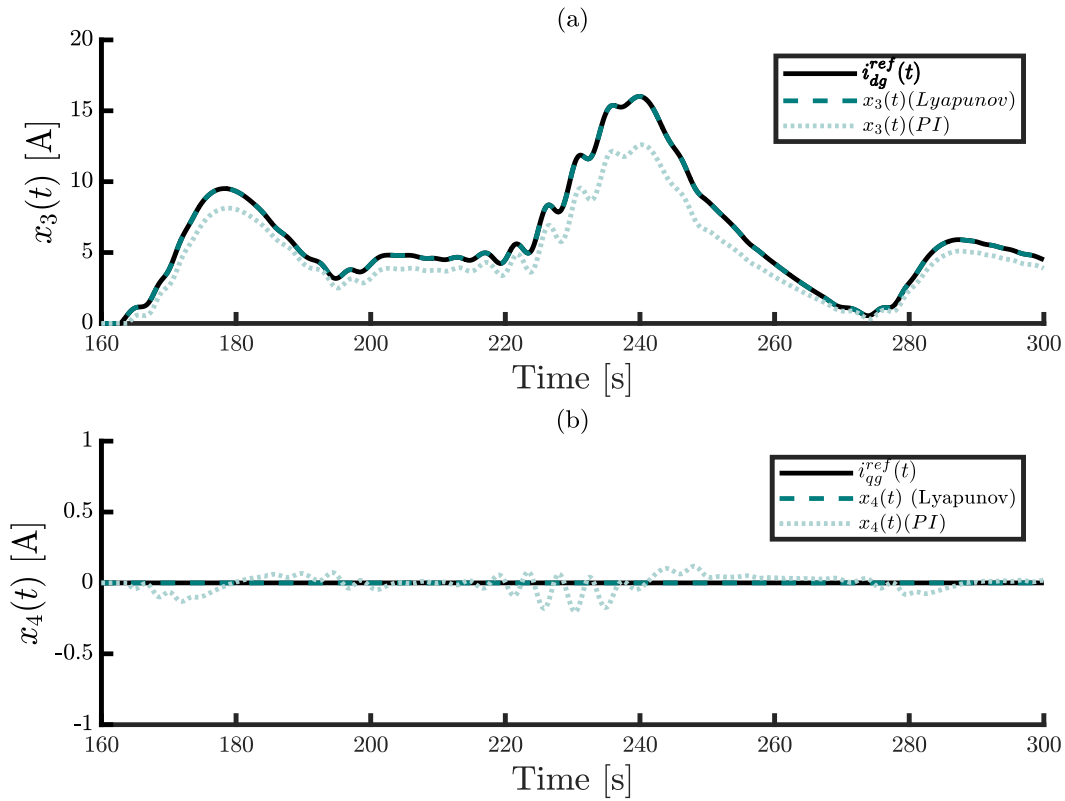


**Figure 7.5:** Tracking performance of the Grid-SC controller (a) d-axis current [A] (b) q-axis current [A].

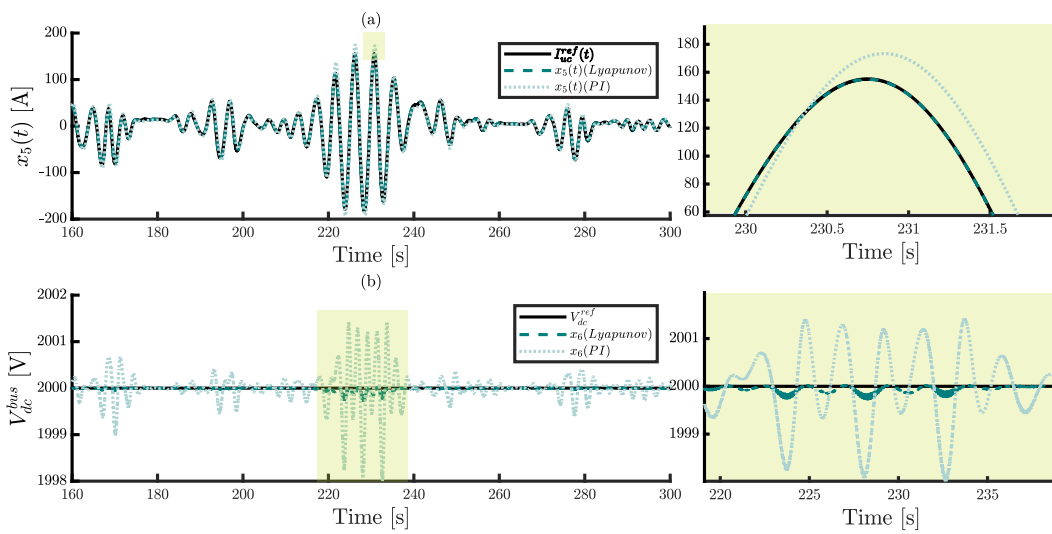


**Figure 7.6:** Tracking performance of the UC storage controller (a) Ultra-capacitor current [A] (b) DC bus voltage [V].



as presented in Fig. 7.6(b). Moreover, integration of the UC system offers several advantages, including an increase in the captured power through reactive control and an enhancement in the quality of the supplied grid power by reducing variability. The quality of injected power is illustrated in Fig. 7.7, with Fig. 7.7(a) showing the three-phase grid currents. Fig. 7.7(b) confirms the in-phase relationship between the scaled-down Phase A grid voltage and current, ensuring a unity power factor. The frequency excursions of the grid power are depicted in Fig. 7.7(c), demonstrating that the frequency remains within the contingency band of  $50 \pm 0.5$  [Hz] as specified by the Irish grid codes. Additionally, Fig. 7.8 showcases the grid voltage and current harmonics for Phase A. According to IEEE Standard 519-1992, the maximum permissible Total Harmonic Distortion (THD) level for grid voltage and current is 5%. It is evident from Fig. 7.8 that the current harmonics (0.92%) and voltage harmonics (0.13%) are well below the limits established by IEEE Standard 519-1992. Hence, the proposed system complies with grid regulations and exhibits satisfactory power quality.

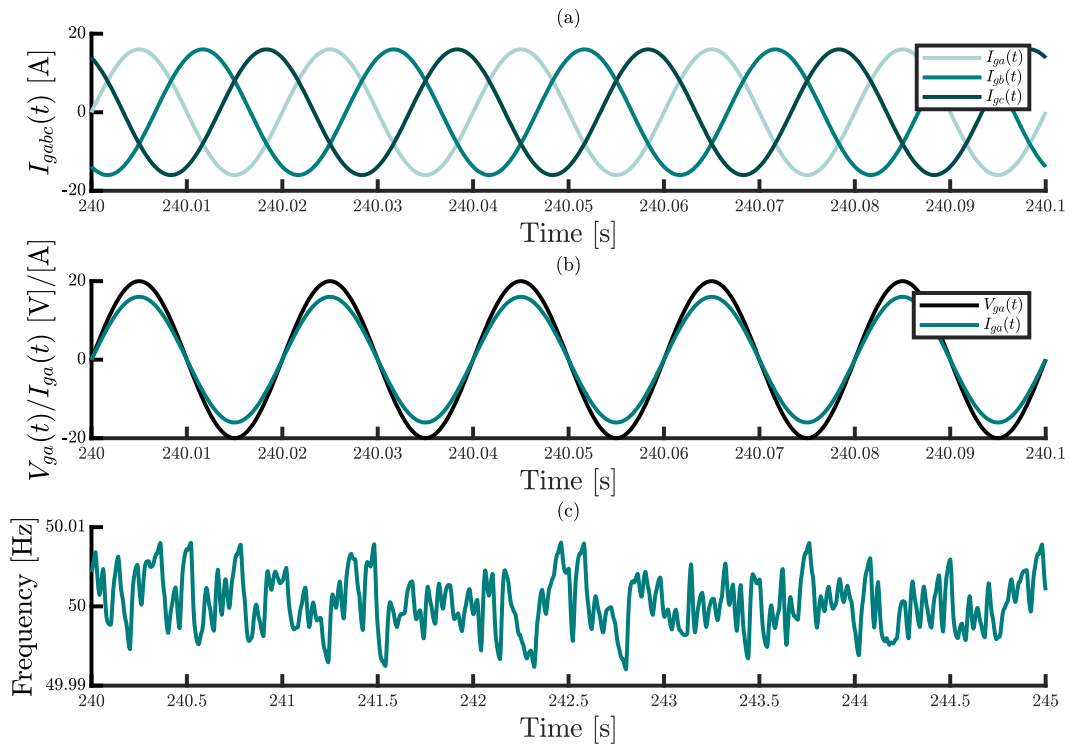


**Figure 7.7:** Power quality plots (a) Three-phase injected current [A] (b) Scaled Phase A grid voltage [V] and Phase A current [A] (c) Frequency variations [Hz].

In the following part of this Section, the low-voltage ride-through (LVRT) performance of the proposed system is assessed under both symmetric (three line-to-ground or 3-LG) and asymmetric (single line-to-ground or 1-LG) fault conditions. Faults are simulated at various time instances to evaluate the effectiveness of the control scheme.

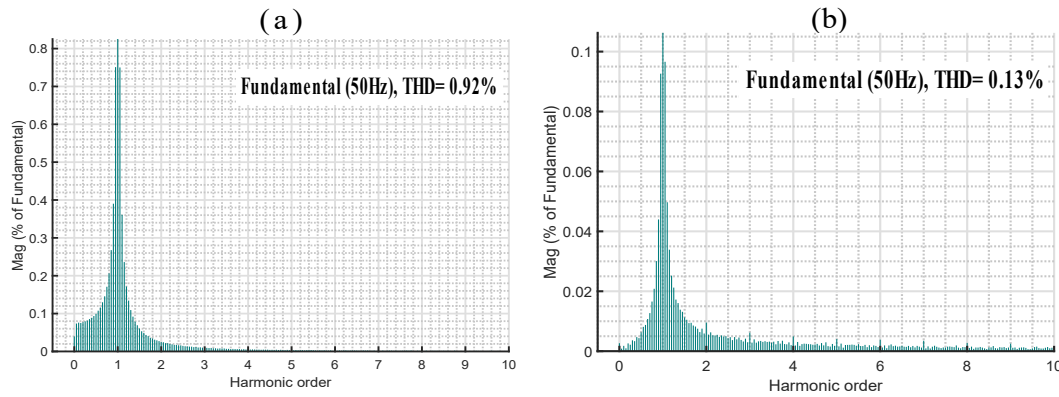


**Figure 7.8:** Harmonic spectrum: (a) Magnitude of grid current harmonics (b) Magnitude of grid voltage harmonics.

The timing of the faults is determined based on different injected power values  $P_g$ , and the specific fault times are provided in Table 7.1.

**Table 7.1:** The Fault event times for both symmetric and asymmetric faults.

Fault No.	Fault times [s]	Injected grid power $P_g$
1.	210-210.625	Constant
2.	232-232.625	Increasing
3.	251-251.625	Decreasing

Fig. 7.9 illustrates the response during a symmetrical three-phase ( $3-\phi$ ) voltage sag. Specifically, Fig.7.9(a) presents the voltage at the Point of Common Connection (PCC), denoted as  $V_{PCC}$ , and it shows that the  $V_{PCC}$  consistently remains within limits prescribed by the grid codes. Consequently, the proposed coordinated control scheme exhibits a robust dynamic response and promptly restores  $V_{PCC}$  to its nominal value, once the fault is cleared. In Fig.7.9(b), there is a slight increase in the DC bus voltage,  $V_{dc}^{bus}$ , which nevertheless remains in close proximity to the reference value throughout and after the voltage sags. The output active power  $P_g$  experiences a drop due to the fault, while reactive power  $Q_g$  is injected using UC storage to ensure that  $V_{PCC}$  remains within limits stipulated by the grid codes, as depicted in Fig. 7.9(c) and Fig. 7.9(d), respectively.

The performance of the proposed control scheme is also validated under an asymmetric (1-LG) fault condition. Fig. 7.10 depicts the results obtained during a 1-LG voltage sag. In particular, Fig. 7.10(a) presents the PCC voltage  $V_{PCC}$ , which remains within the permissible limits during the fault events. However, the voltage exhibits harmonics due to the presence of an unbalanced fault. Additionally, the magnitude of the voltage dip is lower compared to that observed during a symmetrical 3-LG

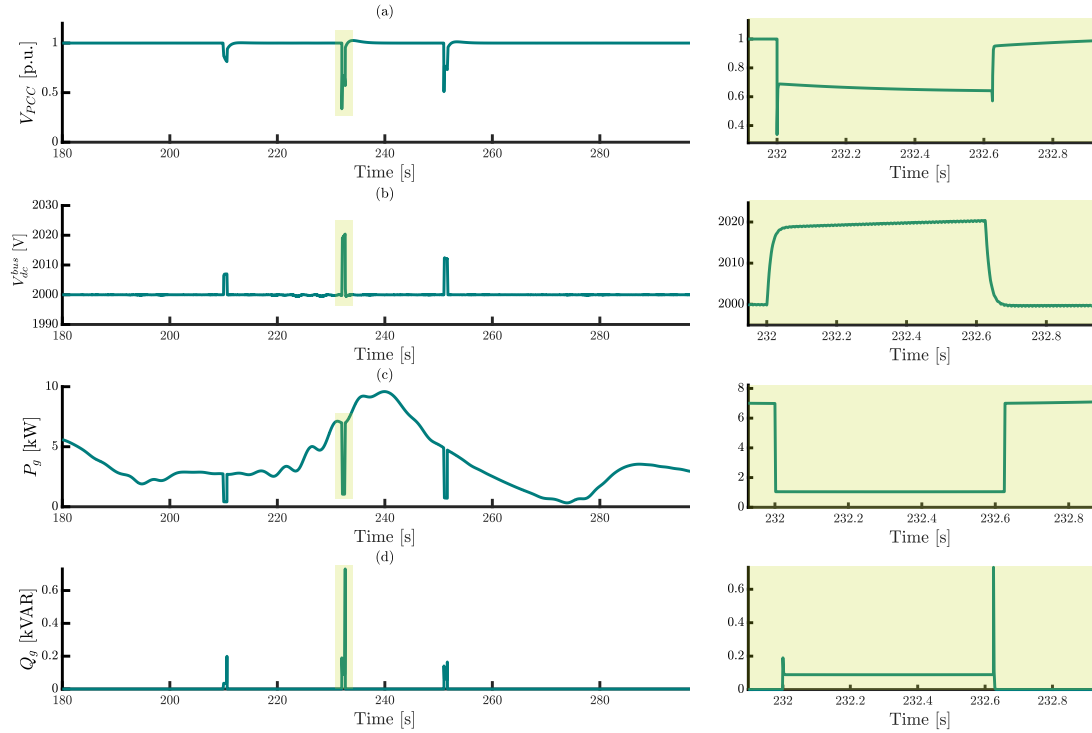


**Figure 7.9:** LVRT response of the proposed control scheme under symmetrical 3-LG fault (a) PCC voltage [p.u.] (b) DC bus voltage [V] (c) Active power  $P_g$  injected into the grid [kW] (d) Reactive power  $Q_g$  injected into the grid [kVAR].

fault. The DC bus voltage  $V_{dc}^{bus}$ , the injected active power  $P_g$ , and the reactive power  $Q_g$ , display similar responses as shown in Fig.7.10(b), Fig.7.10(c), and Fig. 7.10(d) respectively. Thus, the proposed control scheme ensures a robust LVRT response for both symmetric and asymmetric fault scenarios. It is worth noting that the magnitudes of the output responses vary depending on the fault occurrence times. For instance, when the fault occurs during an increasing interval of injected active power, such as at fault time 232-232.625 [s], the magnitude variations in  $V_{PCC}$ ,  $V_{dc}$ , and  $Q_g$  are the largest. Conversely, the magnitude of the variations is lowest when  $P_g$  is relatively constant (fault time = 210-210.625 [s]).

## 7.6 Conclusions

This chapter focuses on the grid-side and storage control components of the high-performance W2G control framework for a direct-drive heaving point absorber-based wave energy conversion system. Similar to the device-side control, Lyapunov-based nonlinear controllers are designed for the Grid-SC and the DC/DC buck-boost storage converter. Once again, it is observed that Lyapunov-based controllers outperform the benchmark PI controllers typically proposed in the existing literature, particularly in

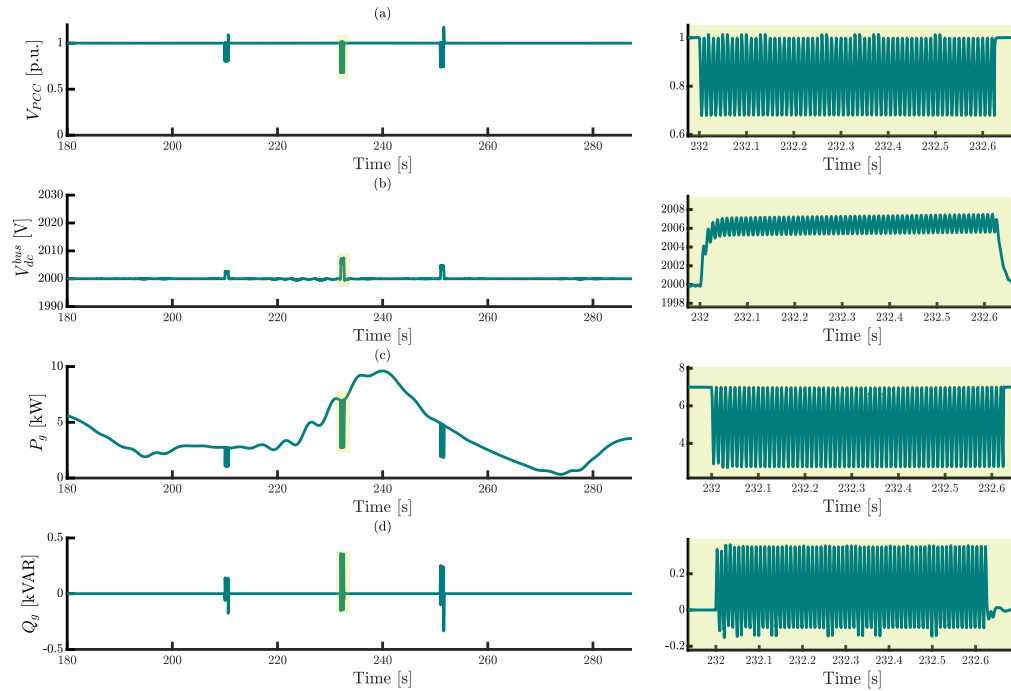


**Figure 7.10:** LVRT response of the proposed control scheme under asymmetrical 1-LG fault (a) PCC voltage [p.u.] (b) DC bus voltage [V] (c) Active power  $P_g$  injected into the grid [kW] (d) Reactive power  $Q_g$  injected into the grid [kVAR].

terms of tracking performance. The use of an EMS ensures that the storage system can support both device-side and grid-side requirements. Specifically, a rule-based EMS is added to the control scheme to perform three tasks: (1) DC bus voltage regulation, (2) the mechanical reactive power requirements of LiTe-Con (or LiTe-Con+), and (3) to support the grid during voltage sags (both symmetric and asymmetric), via an ultra-capacitor storage system. Furthermore, the proposed control scheme guarantees compliance with power quality standards, including power fluctuations, frequency variations, and THD levels, which remain well within limits specified by typical grid codes and IEEE standards.

The applicability of the proposed W2G control approach can be easily extended to other WECs, especially on the grid-side of the powertrain. However, it is important to note that different WECs may respond differently under controlled conditions on the device side.

# 8

## On the reactive power requirements of reactive hydrodynamic WEC control

### Contents

---

<b>8.1</b>	<b>Reactive power peak phenomena</b>	<b>114</b>
8.1.1	Notation and conventions	116
<b>8.2</b>	<b>Optimal WEC control</b>	<b>116</b>
8.2.1	Reactive PI control	117
<b>8.3</b>	<b>Reactive power peak analysis</b>	<b>118</b>
8.3.1	Preliminaries	119
8.3.2	Instantaneous power calculations	120
8.3.3	Energy results	125
<b>8.4</b>	<b>Illustrative case studies</b>	<b>126</b>
8.4.1	Matched cases	127
8.4.2	Mismatched cases	128
<b>8.5</b>	<b>Discussion</b>	<b>135</b>
8.5.1	Discussion of results	135
8.5.2	Effect of a non-ideal PTO	137
<b>8.6</b>	<b>Conclusions</b>	<b>138</b>

---

As discussed in Chapter 6, reactive hydrodynamic WEC controllers require reactive (negative) power at various points in the wave cycle, resulting in an overall better power absorption than passive damping controllers. Recent experimental results have revealed a noteworthy occurrence whereby reactive power peaks can surpass active power levels, posing a challenge for device developers in determining the PTO rating

of the system. The dilemma lies in deciding whether to accommodate these high reactive power peaks, or restrict the power flow to rated (active) levels. The causes underlying these excessive power peaks are poorly understood, leading to considerable uncertainty regarding their management and mitigation strategies. In this regard, this chapter presents analytical results on the reactive power requirements for a reactively controlled WEC. In particular, the reactive power peaks phenomenon is explained in Section 8.1, and Section 8.2 recalls optimal WEC control fundamentals and describes a finite order realisation, i.e. reactive proportional-integral (PI) controller, which is used for analysis in addition to the LiTe-Con. In Section 8.3, reactive power peak analysis, including the derivation of analytical results, is presented. Section 8.4 presents illustrative case studies for both matched and mismatched cases (control synthesis and modelling errors), while Section 8.5 provides a comprehensive discussion on the significance of the result. Finally, Section 8.6 concludes this chapter.

## 8.1 Reactive power peak phenomena

Optimal WEC control has been shown to require occasional reverse (*reactive*) power flow [151] from the grid side. However, it is important to note that this term differs from the definition of reactive power in electrical power networks, which is caused

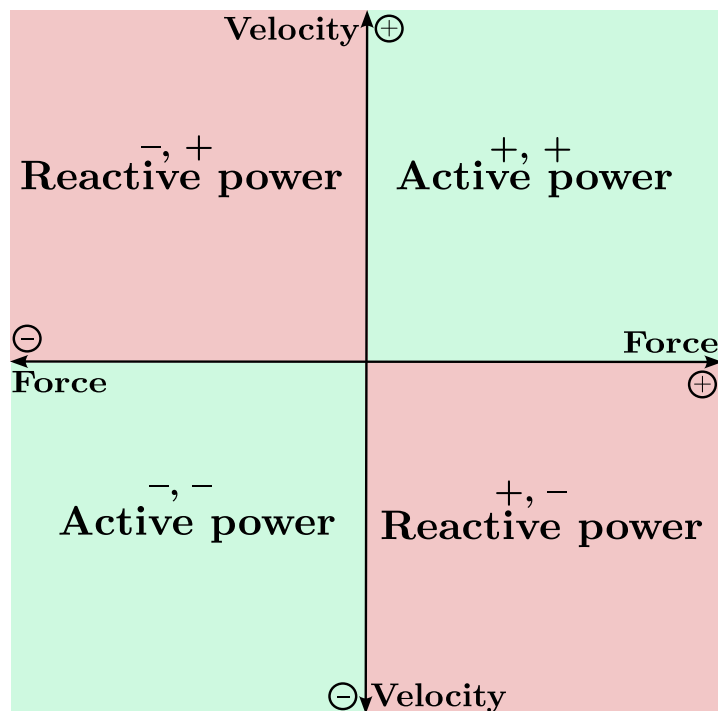


**Figure 8.1:** Active, and reactive, power flow regions for a wave energy converter under optimal control.

by a phase difference between voltage and current (see, for example, Fig. 6.2). In the case of WECs, reactive power is identified by a *sign difference* between force and velocity (mechanical power) or voltage and current (electrical power). This distinction is illustrated in Fig.8.1.

In Fig. 8.2, a typical instantaneous power flow profile, for an optimally controlled WEC, is presented. The green and red shaded areas represent the active (forward) and reactive (reverse) power flow regions, respectively. It is important to note that not all WEC control algorithms incorporate reactive power flow, as it requires a bi-directional wave-to-wire powertrain. For instance, some systems employ a (suboptimal) passive WEC damping controller [201], which does not rely on reactive power. However, it should be noted that the power absorption capability of a passive WEC controller is significantly lower than a reactive WEC controller [18]. Therefore, reactive WEC controllers are crucial in maximising power absorption from existing WEC infrastructure, leading to improved overall economic performance. Although reactive control incurs a small cost overhead relative to the main WEC structure and PTO, their inclusion is essential for optimal utilisation of the available capital WEC infrastructure.

In a reactively controlled wave energy conversion system, the PTO system must be capable of handling both active and reactive power peaks while enabling bi-directional power flow. However, to achieve a cost-effective design, it is crucial to accurately evaluate the active/reactive peak power requirements of a reactively controlled WEC system. This assessment is essential for properly sizing the PTO system to maximise economic value by balancing energy capture capability with capital cost, with the capacity factor being a key parameter [18, 202]. When reactive power peaks exceed active power peaks, meaning that the reactive-to-active peak power ratio exceeds unity, there are significant cost implications for the capacity of the PTO system. Excessive reactive power peaks may result in over-sizing the PTO system, leading to

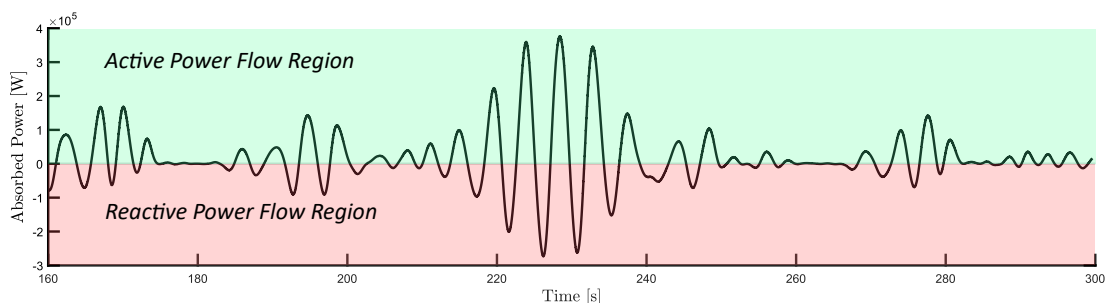


**Figure 8.2:** A typical instantaneous power flow profile for an optimally controlled WEC operating in irregular waves. The green shaded region represents active power flow region, while the red shaded region represents reactive power flow region. However, mean power flow (energy) is positive overall.

increased capital costs. Moreover, over-sizing the PTO system can lead to inefficient operation of the overall system, as the generator may operate in a region where its efficiency is lower than the optimal operating point. This chapter examines the occurrence of extreme reactive power peaks in reactive WEC control through analytical results and illustrative case studies.

### 8.1.1 Notation and conventions

The notation and conventions followed in this chapter are as follows:

$\mathbb{R}^+(\mathbb{R}^-)$  denotes the set of non-negative (non-positive) real numbers.  $(Z(\omega), z(t))$  denotes a Fourier transform pair. The symbol  $\oplus$  is used to represent the direct sum of  $N$  matrices, *i.e.*  $\oplus_{p=1}^N B_p = \text{diag}(B_1, B_2, \dots, B_N)$ . Finally, when required, the abbreviations  $c_\omega \equiv \cos(\omega t)$  and  $s_\omega \equiv \sin(\omega t)$  are adopted for notational convenience.

## 8.2 Optimal WEC control

Recall, from Section 4.2.3, the equation of motion for a *controlled* WEC (1-DoF), using the linear potential theory (LPT) assumptions, is given as follows:

$$\Sigma_c : \begin{cases} \ddot{z}(t) = \mathcal{M}(-K_h z(t) - k_r(t) * \dot{z}(t) + f_e(t) - f_u(t)), \\ y(t) = \dot{z}(t), \end{cases} \quad (8.1)$$

where  $\mathcal{M} = (M + m_\infty)^{-1}$  is generalised mass matrix (a scalar in this case),  $f_e(t)$  is the excitation force,  $k_r(t)$  is the radiation impulse response function.  $f_u$  represents the control force applied by the PTO system. The general energy maximising control problem for WECs can be informally posed as follows [162]:

Maximise  $\int_{f_u(t)}^{} \text{Energy absorption from incoming waves.}$

Then, from a mathematical perspective, the absorbed energy  $\mathcal{J}$  over the time interval  $[0, T]$ , where  $T \in \mathbb{R}^+$ , can be expressed as:

$$\mathcal{J} = \int_0^T P_{abs}(t) dt, \quad (8.2)$$

where  $P_{abs}(t) = v(t)f_u(t)$  denotes the instantaneous mechanical absorbed power, and  $v(t)$  and  $f_u(t)$  are the WEC velocity and control force, respectively, with  $v(t) = \dot{z}(t)$ . Thus, the general solution for the energy maximising control problem can be stated in terms of the optimal control force profile [162], as follows:

$$F_u^{opt}(\omega) = Z_i^*(\omega)V(\omega). \quad (8.3)$$



Similarly, the impedance-matching condition of (8.3) can be formulated in terms of an optimal velocity profile, represented by a purely real mapping, as follows:

$$V^{opt}(\omega) = \frac{1}{Z_i(\omega) + Z_i^*(\omega)} F_e(\omega) = \frac{1}{2B_r(\omega)} F_e(\omega). \quad (8.4)$$

Furthermore, recalling the optimal impedance-matching condition (as a feedforward structure), presented in Section 6.2, as

$$\frac{V^{opt}(\omega)}{F_e(\omega)} = T_{f_e \rightarrow v}^{opt}(\omega) = \frac{\Re(G)^2 + \Im(G)^2}{2\Re(G)}, \quad (8.5)$$

and,

$$H_{ff}(\omega) = H_{f_e \rightarrow f_u}^{opt}(\omega) = \frac{\Re(G) + j\Im(G)}{2\Re(G)}, \quad (8.6)$$

where  $G$  is the input-output frequency response of the WEC dynamics given in (6.2). It is worth noting that the excitation to control force mapping denoted as  $H_{f_e \rightarrow f_u}^{opt}(\omega)$  in (8.6), corresponds to a feedforward control structure. On the other hand, the force-to-velocity mapping denoted as  $T_{f_e \rightarrow v}^{opt}(\omega)$  in (8.5) represents the mapping between  $f_e$  (or  $F_e(\omega)$  in the frequency domain) and  $V^{opt}(\omega)$ , which is unique regardless of the control scheme employed, whether feedback or feedforward. Therefore, the following two conditions

$$\mathbf{(C1)} \quad T_{f_e \rightarrow v}^{opt}(\omega) = \Re(T_{f_e \rightarrow v}^{opt}) \in \mathbb{R}^+ \quad \wedge \quad \mathbf{(C2)} \quad \Re(H_{f_e \rightarrow f_u}^{opt}) = 1/2, \quad (8.7)$$

are valid,  $\forall \omega \in \mathbb{R}$ . It should be noted that **(C1)** is derived from the positive-real nature of the map  $G$  for WEC applications (see, for example, [203]).

### 8.2.1 Reactive PI control

This section introduces a feedback finite-order realisation of the optimal impedance-matching condition, i.e., a ‘reactive’ PI controller, since it is used for a comparative simulation analysis with the LiTe-Con presented in Section 8.4. The reactive PI controller is widely recognised as a standard feedback control solution in the WEC literature, and computes the control force as a linear combination of the WEC system position and velocity:

$$f_u(t) = \begin{bmatrix} k_z & k_v \end{bmatrix} \begin{bmatrix} z(t) \\ \dot{z}(t) \end{bmatrix}, \quad (8.8)$$

which, by employing standard properties of the Laplace transform, can be expressed as:

$$H_{PI}(s) = \frac{k_z s + k_v}{s}. \quad (8.9)$$

Equivalently, the representation of the control force in the frequency domain is given by:

$$F_u(\omega) = -H_{PI}(j\omega)V(\omega). \quad (8.10)$$

Within the WEC literature, the PI controllers are often tuned through exhaustive search procedures. The performance of the PI controllers, measured in terms of absorbed energy, is normally assessed over a sufficiently large grid of values for  $k_z$  and  $k_v$ . However, considering the impedance-matching condition discussed in Section 8.2, it is possible to derive analytical conditions for maximising the absorbed energy in unconstrained scenarios with monochromatic waves. Consequently, the parameters of the reactive PI controller can be computed as follows:

$$k_z = \Re\{\Gamma(\omega^*)\}, \quad k_v = -\omega^* \Im\{\Gamma(\omega^*)\} \quad (8.11)$$

with,

$$\Gamma(\omega^*) = \frac{1}{T_{f_e \rightarrow v}^{opt}(\omega^*)} - \frac{1}{G(j\omega^*)}, \quad (8.12)$$

and  $\omega^*$  a particular frequency where the energy absorption maximisation is targeted. Hence, the impedance-matching condition is fulfilled for  $\omega^*$ , when considering  $H_{PI}(s)$  with  $s = j\omega$  and  $\omega \in \mathbb{R}^+$ . By utilising the reactive PI controller structure defined in Eqs. (8.8) and (8.12), the resulting force-to-velocity mapping corresponds to a band-pass (resonant) system. The resonance frequency of this system is  $\omega^*$ , and its frequency response aligns with the optimal mapping  $T_{f_e \rightarrow v}^{opt}(\omega)$  exclusively at  $\omega = \omega^*$ . This alignment preserves the zero phase-locking property the purely real mapping provided in (8.4). It is important to note that, with the parameter definitions specified in (8.11), the resulting force-to-velocity mapping can be expressed as follows:

$$T_{f_e \rightarrow v}^{PI}(j\omega^*) = \frac{G(j\omega^*)}{1 + G(j\omega^*)H_{PI}(j\omega^*)} = T_{f_e \rightarrow v}^{opt}(\omega^*). \quad (8.13)$$

### 8.3 Reactive power peak analysis

In this section, analytical results are derived for the matched optimal WEC control conditions presented in Section 8.2. These analytical results contribute to a deeper understanding of the requirements for reactive power peaks in optimal WEC control.

### 8.3.1 Preliminaries

In accordance with standard numerical generation methods for ocean waves (see, for example, [155]), we assume that the wave excitation force in the time-domain can be expressed, without loss of generality, as a  $T_0$ -periodic function defined in an  $N$ -dimensional space, as

$$f_e(t) = \sum_{p=1}^N [\alpha_p \cos(p\omega_0 t) - \beta_p \sin(p\omega_0 t)], \quad (8.14)$$

where  $\omega_0 = 2\pi/T_0$  is the fundamental frequency associated with  $f_e(t)$ . It is important to note that  $f_e(t)$  can be expressed in a more concise form, as

$$f_e(t) = L_f \xi(t), \quad (8.15)$$

where  $\{L_f^T, \xi(t)\} \subset \mathbb{R}^{2N}$  are defined as

$$\begin{aligned} L_f &= [\alpha_1 \quad \beta_1 \quad \dots \quad \alpha_N \quad \beta_N], \\ \xi(t) &= [c_{\omega_0} \quad -s_{\omega_0} \quad \dots \quad c_{\omega_N} \quad -s_{\omega_N}]^T. \end{aligned} \quad (8.16)$$

where, from now on, the abbreviations  $c_\omega \equiv \cos(\omega t)$  and  $s_\omega \equiv \sin(\omega t)$  are adopted for notational convenience.

**Remark 8.3.1.** *The condition  $\xi(t) \neq 0$  holds for any  $t \in \mathbb{R}$ . This is, in fact, linked to the persistence of excitation condition on the set of functions composing the entries of  $\xi$ .*

Based on the definition of  $f_e$  in (8.15), and following similar arguments as in, for example, [204], we can express the time-domain equivalents of  $V^{opt}(\omega)$  and  $F_u^{opt}(\omega)$  in (8.4) and (8.3) using (8.15) as:

$$v(t) = L_f \Phi_T \xi(t), \quad f_u(t) = L_f \Phi_H \xi(t), \quad (8.17)$$

with  $\{\Phi_T, \Phi_H\} \subset \mathbb{R}^{2N \times 2N}$  defined as

$$\begin{aligned} \Phi_T &= \bigoplus_{p=1}^N \begin{bmatrix} T_{f_e \rightarrow v}^{opt}(p\omega_0) & 0 \\ 0 & T_{f_e \rightarrow v}^{opt}(p\omega_0) \end{bmatrix}, \\ \Phi_H &= \bigoplus_{p=1}^N \begin{bmatrix} 1/2 & \Im(H_{f_e \rightarrow f_u}^{opt}(p\omega_0)) \\ -\Im(H_{f_e \rightarrow f_u}^{opt}(p\omega_0)) & 1/2 \end{bmatrix}. \end{aligned} \quad (8.18)$$

**Remark 8.3.2.** *Given the set of conditions (C1) and (C2) in (8.7), it can be easily verified that the matrices  $\Phi_T$  and  $\Phi_H$  in (8.18) are always full rank.*

We can now demonstrate that the instantaneous power  $P_{abs}(t)$  can be expressed in terms of a time-dependent quadratic form. Using the expressions in (8.15) and (8.17), note that

$$P_{abs}(t) = (L_f \Phi_T \xi(t)) (L_f \Phi_H \xi(t))^\top = L_f A(t) L_f^\top, \quad (8.19)$$

where the matrix  $A(t) \in \mathbb{R}^{2N \times 2N}$  is defined as<sup>8.1</sup>

$$A = \Phi_T \xi \xi^\top \Phi_H^\top = \Phi_T \Xi \Phi_H^\top, \quad (8.20)$$

with  $\Xi = \xi \xi^\top$ .

### 8.3.2 Instantaneous power calculations

Before presenting our main proposition, we introduce several intermediate results. We begin by expressing the matrix  $A$  in (8.20) as a sum of two components:

$$A = \underline{A} + \overline{A}, \quad (8.21)$$

where

$$\underline{A} = \frac{A + A^\top}{2}, \quad \overline{A} = \frac{A - A^\top}{2}, \quad (8.22)$$

represent the symmetric and skew-symmetric parts of  $A$ , respectively. Note that  $\underline{A} = \underline{A}^\top$  and  $\overline{A} = -\overline{A}^\top$ . Since (8.19) is quadratic in nature, we can deduce that

$$P_{abs} = L_f A L_f^\top = L_f (\underline{A} + \overline{A}) L_f^\top = L_f \underline{A} L_f^\top. \quad (8.23)$$

Now we present our first two important propositions. These results are instrumental in substantiating our principal assertion (Proposition 8.3.3), establishing a connection between the minimum and maximum instantaneous power absorption.

**Proposition 8.3.1.** Consider  $\underline{A}$  as in (8.23). Then,  $\text{rank}(\underline{A}) \leq 2$ , for any  $t \in \mathbb{R}$ .

*Proof.* We observe that  $\Xi$  in equation (8.20) can be expressed as an outer product operation, implying that  $\text{rank}(\Xi) = 1$  for any  $\xi$ , given that  $\xi \neq 0 \forall t$  (as stated in Remark 8.3.1). The proof can be established using standard rank arguments in finite-dimensional spaces, *i.e.* note that

$$\begin{aligned} \text{rank}(A) &= \text{rank}(\Phi_T \Xi \Phi_H^\top) \\ &\leq \min(\text{rank}(\Phi_T), \text{rank}(\Xi), \text{rank}(\Phi_H)) \\ &= \min(2N, 1, 2N) = 1, \end{aligned} \quad (8.24)$$

<sup>8.1</sup>From now on, we omit the dependence on  $t$  when it is clear from the context.

since both  $\Phi_T$  and  $\Phi_H$  are always full rank (see Remark 8.3.2). Thus,

$$\text{rank}(\underline{A}) = \text{rank}(A + A^\top) \leq 2 \text{rank}(A) = 2, \quad (8.25)$$

which proves our claim.  $\square$

**Proposition 8.3.2.** *The trace of the matrix  $\underline{A}$ , denoted as  $\text{tr}(\underline{A})$ , is always positive for all  $t \in \mathbb{R}$ .*

*Proof.* Firstly, we observe that it is straightforward to show that  $\text{tr}(\underline{A}) = \text{tr}(A)$ . By manipulating the matrix  $A$ , we can see that its diagonal elements, denoted as  $d(A) \subset \mathbb{R}$ , are the union of two sets, *i.e.*

$$d(A) = d_1 \cup d_2, \quad (8.26)$$

where the sets  $d_1$  and  $d_2$  are

$$\begin{aligned} d_1 &= \left\{ T_{f_e \rightarrow v}^{\text{opt}}(p\omega_0) \left( \frac{1}{2} c_{p\omega_0}^2 - \Im(H_{f_e \rightarrow f_u}^{\text{opt}}(p\omega_0)) c_{p\omega_0} s_{p\omega_0} \right) \right\}_{p=1}^N, \\ d_2 &= \left\{ T_{f_e \rightarrow v}^{\text{opt}}(p\omega_0) \left( \frac{1}{2} s_{p\omega_0}^2 + \Im(H_{f_e \rightarrow f_u}^{\text{opt}}(p\omega_0)) c_{p\omega_0} s_{p\omega_0} \right) \right\}_{p=1}^N. \end{aligned} \quad (8.27)$$

By utilising the formal definition of trace, *i.e.* the sum of the elements in  $d(A)$ , we can evaluate  $\text{tr}(A)$  as follows:

$$\begin{aligned} \text{tr}(A) &= \sum_{p=1}^N \frac{1}{2} (c_{p\omega_0}^2 + s_{p\omega_0}^2) T_{f_e \rightarrow v}^{\text{opt}}(p\omega_0) \\ &= \sum_{p=1}^N \frac{1}{2} T_{f_e \rightarrow v}^{\text{opt}}(p\omega_0). \end{aligned} \quad (8.28)$$

Since the terms inside the sum are positive (since  $T_{f_e \rightarrow v}^{\text{opt}}(p\omega_0)$  is strictly positive for all  $p$  due to condition **(C1)**), and the sum is a finite sum, it follows that  $\text{tr}(A)$  is strictly positive for all  $t \in \mathbb{R}$ , which proves our claim.  $\square$

After introducing Propositions 8.3.1 and 8.3.2, we proceed to define the key quantities of interest based on (8.19). Let  $P^l$  and  $P^u$  be defined as follows:

$$P^l = \min_{L_f} \frac{1}{\|L_f\|} L_f \underline{A} L_f^\top, \quad P^u = \max_{L_f} \frac{1}{\|L_f\|} L_f \underline{A} L_f^\top, \quad (8.29)$$

In other words,  $P^l$  and  $P^u$  represent the (normalised) minimum and maximum achievable values of the instantaneous power  $P_{\text{abs}}$  under optimal controlled conditions, respectively. These values are obtained for any admissible wave excitation force vector  $L_f^\top \in \mathbb{R}^{2N}$  and  $t \in \mathbb{R}$ , considering all possible realisations of the wave excitation force according to a given spectrum (see Section 8.4). Additionally, we introduce the definition of the peak power ratio  $P_{\text{ratio}}$  as

$$P_{\text{ratio}} = \frac{|P^l|}{|P^u|}. \quad (8.30)$$

Our main proposition can be stated as follows.

**Proposition 8.3.3.** *Let  $P^l$  and  $P^u$  be defined as in (8.29). Then,  $P^u > 0$  for all  $t \in \mathbb{R}$ . Furthermore,  $|P^u| > |P^l|$ , and hence  $P_{ratio} < 1$ , for all  $t \in \mathbb{R}$ .*

*Proof.* Suppose, for the time being, that the value of  $t$  is fixed at  $t = t^*$ . It is important to note that, by employing variational arguments [205], the quantities  $P^l$  and  $P^u$  in (8.29) can be precisely computed in relation to the spectrum of  $\underline{A}$ , i.e.

$$\begin{aligned} P^l &= \min_{L_f} \frac{1}{\|L_f\|^2} L_f \underline{A} L_f^\top = \lambda^l, \\ P^u &= \max_{L_f} \frac{1}{\|L_f\|^2} L_f \underline{A} L_f^\top = \lambda^u, \end{aligned} \quad (8.31)$$

with<sup>8.2</sup>  $\{\lambda^l, \lambda^u\} \subset \mathbb{R}$  being the smallest and largest eigenvalues of  $\underline{A}$ , respectively. According to Proposition 8.3.1, it follows that  $\text{rank}(\underline{A}) \leq 2$ , and thus the spectrum of  $\underline{A}$  can always be decomposed as

$$\lambda(\underline{A}) = \{\lambda^l, \lambda^u\} \cup \underbrace{\{0, \dots, 0\}}_{2(N-1)}. \quad (8.32)$$

Furthermore, utilising the well-known property that the trace of a matrix equals the sum of its eigenvalues, we can establish the following relation:

$$\text{tr}(\underline{A}) = \lambda^l + \lambda^u. \quad (8.33)$$

Moreover, according to Proposition 8.3.2, we have

$$\text{tr}(\underline{A}) = \sum_{p=1}^N \frac{1}{2} T_{f_e \mapsto v}^{opt}(p\omega_0) = \lambda^l + \lambda^u > 0, \quad (8.34)$$

and consequently, it is evident that  $\lambda^u > 0$  and  $|\lambda^u| > |\lambda^l|$  for any possible  $t^* \in \mathbb{R}$  (since the trace condition (8.28) is indeed independent of time), which proves our main claim.  $\square$

<sup>8.2</sup>We recall that the eigenvalues of a symmetric matrix are always real (see e.g. [205]).

**Remark 8.3.3.** The result in Proposition 8.3.3 can be seen as a ‘worst-case scenario’ measure, and essentially states that the absolute value associated with the maximum instantaneous power achieved over the set of admissible  $L_f$ , i.e.  $|P^u|$ , is always larger than its minimum counterpart, i.e.  $|P^l|$ . Note that  $P^u$  and  $P^l$  do not, in general, take place for the same excitation force vector  $L_f$ . Furthermore, Proposition 8.3.3, clearly, does not imply that the instantaneous power for a given realisation is always positive for a given  $L_f$ , but rather states a relation between maximum and minimum values over admissible  $L_f$  vectors. This is illustrated via Fig. 8.3, where maximum and minimum (normalised with respect to  $P^u$ ) instantaneous power values can be appreciated (left), for 500 random realisations of  $L_f$  vectors according to a typical wave spectrum, for the device presented in Section 8.4, under optimal control conditions. Furthermore, a snippet of the time trace of instantaneous power corresponding with the realisation linked to  $P^u$  (centre) and  $P^l$  (right) is presented, showing both maximum and minimum values attained (with circles). Note that, clearly, even for these limit-case realisations, reactive power flow is effectively present.

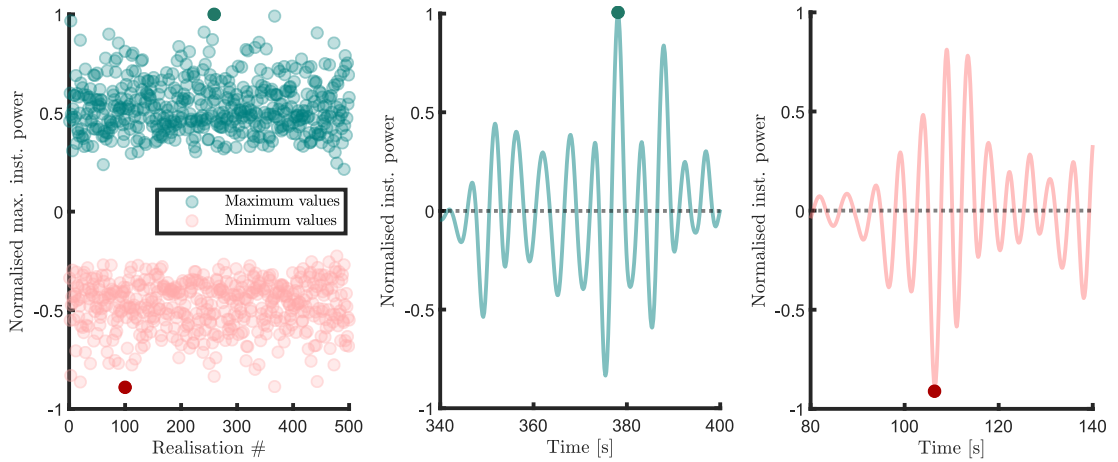


**Figure 8.3:** Maximum and minimum (normalised with respect to  $P^u$ ) instantaneous power values for 500 random realisations of  $L_f$  vectors according to a typical wave spectrum, for the device presented in Section 8.4, under optimal control conditions. A snippet of the time trace of instantaneous power, corresponding with the realisation linked to  $P^u$  (centre) and  $P^l$  (right), is presented, showing both maximum and minimum values attained (with circles).

**Remark 8.3.4.** From the results of Proposition 8.3.3, we can deduce straightforwardly that the above results hold for the monochromatic case ( $N = 1$  in (8.14)), i.e.  $|\lambda^u| > |\lambda^l|$  and peak power ratio  $P_{ratio} < 1$ .

In the subsequent discussion, we delve into specific cases of interest, encapsulated

in the form of Corollary 8.3.1 and Corollary 8.3.2, are presented.

**Corollary 8.3.1** (Asymptotic cases).  $\lambda^l \rightarrow -\lambda^u$  as  $\omega_0 \rightarrow 0$  or  $\omega_0 \rightarrow +\infty$ .

*Proof.* Let's consider the case when  $\omega_0 \rightarrow 0$ . We note that

$$\lim_{\omega_0 \rightarrow 0} \lambda^l + \lambda^u = \lim_{\omega_0 \rightarrow 0} \sum_{p=1}^N \frac{1}{2} T_{f_e \rightarrow v}^{opt}(p\omega_0) = 0, \quad (8.35)$$

due to the fact that  $G(j\omega)$  is zero at the origin, see, for example, [203]. Thus, we can conclude that  $\lambda^l \rightarrow -\lambda^u$  as  $\omega_0 \rightarrow 0$ . A similar reasoning can be followed for the case  $\omega_0 \rightarrow +\infty$ , considering that  $G(j\omega)$  is strictly proper, and it is hence omitted.  $\square$

**Remark 8.3.5.** *The result of Corollary 8.3.1 implies that as  $\omega_0$  approaches 0 or infinity, the peak power ratio  $P_{ratio}$  of the instantaneous power tends to 1.*

**Corollary 8.3.2.** *When  $N = 1$  and  $\omega_0 = \omega_r$ , with  $\omega_r$  representing the resonant frequency of the WEC system. Then, the smallest and largest eigenvalues of  $\underline{A}$  are  $\lambda^l = 0$  and  $\lambda^u = \frac{1}{4}\Re(G(\omega_r))$ , respectively.*

*Proof.* Firstly, we note that, at resonance,  $\Im(G(\omega_r)) = 0$ , and therefore

$$T_{f_e \rightarrow v}^{opt}(\omega_r) = \frac{1}{2}\Re(G(\omega_r)). \quad (8.36)$$

Straightforward calculations show that  $\underline{A}$  reduces to

$$\underline{A} = \frac{1}{4}\Re(G(\omega_r)) \begin{bmatrix} c_{\omega_r}^2 & -c_{\omega_r}s_{\omega_r} \\ -c_{\omega_r}s_{\omega_r} & s_{\omega_r}^2 \end{bmatrix}, \quad (8.37)$$

which has a characteristic polynomial  $P_{\underline{A}}(\lambda)$  represented by

$$P_{\underline{A}}(\lambda) = \frac{1}{4}\Re(G(\omega_r))\lambda(\lambda - 1). \quad (8.38)$$

Since  $\Re(G(\omega_r)) > 0$ , due to the positive-real nature of  $G$ , the resultant smallest and largest eigenvalues of  $\underline{A}$  are

$$\lambda^l = 0 \quad \wedge \quad \lambda^u = \frac{1}{4}\Re(G(\omega_r)), \quad (8.39)$$

proving our claim.  $\square$

**Remark 8.3.6.** *Corollary 8.3.2 presents a key practical finding: The minimum possible value for instantaneous power, over the space of admissible (monochromatic) excitation forces, at resonance, is always zero, meaning that only active instantaneous power is necessary for optimal control at  $\omega_r$  within the range of permitted excitation forces. Therefore, the  $P_{ratio} = 0$  for this particular case.*



### 8.3.3 Energy results

Recall the definition of the absorbed mechanical energy  $\mathcal{J}$  in (8.40), representing the integral of the instantaneous power over a period  $T_0$ , as

$$\mathcal{J} = \int_0^{T_0} P_{abs}(t) dt, \quad (8.40)$$

where  $P_{abs}$  defined as in (8.19)-(8.23), i.e. WEC instantaneous mechanical power under frequency-domain optimality conditions. We make the following proposition in relation to  $\mathcal{J}$ .

**Proposition 8.3.4.** *For any admissible excitation force vector  $L_f \in \mathbb{R}^{1 \times 2N}$ , the mechanical energy  $\mathcal{J}$  is strictly positive.*

*Proof.* Let us re-write (8.40) in terms of (8.23) as

$$\begin{aligned} \mathcal{J} &= \int_0^{T_0} L_f \Phi_T \Xi(t) \Phi_H^T L_f^T dt \\ &= L_f \Phi_T \left( \int_0^{T_0} \Xi(t) dt \right) \Phi_H^T L_f^T, \end{aligned} \quad (8.41)$$

and note that the equality

$$\begin{aligned} \int_0^{T_0} \Xi(t) dt &= \int_0^{T_0} \bigoplus_{p=1}^N \begin{bmatrix} c_{p\omega_0}^2 & -c_{p\omega_0} s_{p\omega_0} \\ -c_{p\omega_0} s_{p\omega_0} & s_{p\omega_0}^2 \end{bmatrix} dt \\ &= \frac{T_0}{2} \mathbb{I}_{2N}, \end{aligned} \quad (8.42)$$

holds, since each element of the matrix in (8.42) represents a standard inner-product operation between a set of orthogonal functions in  $L^2$ . It suffices to note that, using (8.42), the mechanical energy can be expressed as

$$\mathcal{J} = \frac{T_0}{2} L_f \Phi_T \Phi_H^T L_f^T. \quad (8.43)$$

Now, defining a matrix  $\Phi \in \mathbb{R}^{2N \times 2N}$  is as

$$\Phi = \Phi_T \Phi_H^T = \bigoplus_{p=1}^N \begin{bmatrix} \frac{1}{2} T_{f_e \rightarrow v}^{opt}(p\omega_0) & -\mathfrak{Im}(H_{f_e \rightarrow f_u}^{opt}(p\omega_0)) \\ \mathfrak{Im}(H_{f_e \rightarrow f_u}^{opt}(p\omega_0)) & \frac{1}{2} T_{f_e \rightarrow v}^{opt}(p\omega_0) \end{bmatrix}, \quad (8.44)$$

then the mechanical energy  $\mathcal{J}$  can now be expressed as

$$\mathcal{J} = \frac{T_0}{2} L_f \left( \frac{\Phi + \Phi^T}{2} \right) L_f^T, \quad (8.45)$$

The claim then follows immediately from the fact that the symmetric matrix

$$\frac{\Phi + \Phi^T}{2} = \bigoplus_{p=1}^N \begin{bmatrix} \frac{1}{2} T_{f_e \rightarrow v}^{opt}(p\omega_0) & 0 \\ 0 & \frac{1}{2} T_{f_e \rightarrow v}^{opt}(p\omega_0) \end{bmatrix}, \quad (8.46)$$

in (8.45) is always positive-definite, due to condition **(C1)** in (8.7), and thus the mechanical energy  $\mathcal{J}$  is always positive for any admissible excitation force vector  $L_f$ .  $\square$

## 8.4 Illustrative case studies

In this section, we conduct illustrative case studies to validate the analytical results presented in Section 8.3. The simulation results also illustrate the effects of possible system/controller mismatch on the peak power ratio and absorbed power. A cylindrical heaving (1-DoF) point absorber WEC, with a hemispherical bottom, as depicted in Fig. 8.4, is considered here. In this section, we consider both monochromatic and

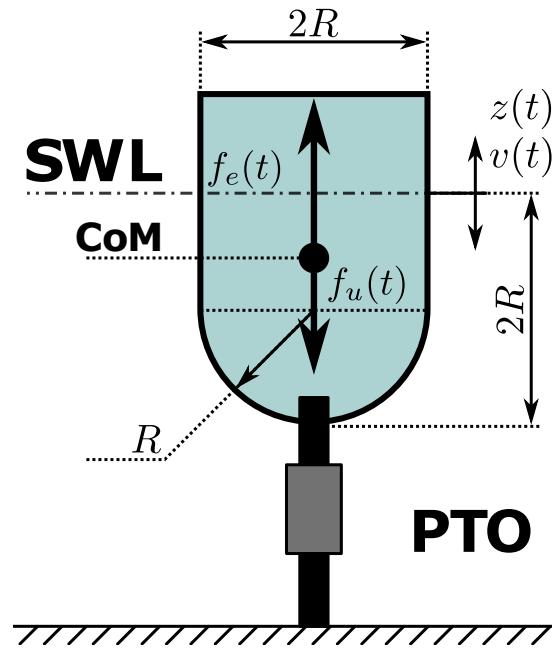


**Figure 8.4:** Schematic diagram of cylindrical WEC with hemispherical bottom. All the relevant dimensions are shown in the schematic, with  $R = 5$  [m]. SWL and CoM represent the still water level and centre of mass, respectively.

panchromatic wave conditions to analyse the performance of the WEC. The sea-states are characterised by a significant wave height  $H_s = 3$  [m] and a typical peak period  $T_p \in [4, 20]$  [s], or equivalently, a typical peak frequency  $\omega_p \in [0.31, 1.57]$  [rad/s]. A panchromatic wave spectrum is continuous and contains infinite spectral components (*i.e.* a continuous spectrum). However, for simulation purposes, a polychromatic representation with limited frequencies is used to approximate the continuous spectrum. A JONSWAP spectrum [152] is employed to generate the corresponding free surface elevation, which is then used to calculate the excitation force  $f_e$ . The wave-to-force convolution kernel is obtained from hydrodynamic parameters computed using the NEMOH tool [161], which is based on boundary-element methods. Recall that the corresponding SDF of the JONSWAP spectrum [152] is given by:

$$S(\omega) = \frac{\alpha g^2}{\omega^5} \exp\left[-\beta \frac{\omega_p^4}{\omega^4}\right] \gamma^{a(\omega)}, \quad (8.47)$$

where  $\alpha$  and  $\beta$  are constant values,  $g$  is gravitational acceleration,  $a(\omega)$  is a frequency dependent function, and  $\gamma$  is the peak enhancement factor, respectively. Moreover, to ensure statistically consistent results, we consider 30 realisations of each sea state in our simulations. The length of time associated with each realisation is set to be 300 times the typical peak wave period.

### 8.4.1 Matched cases

The results presented in this section assume that the system operates under the matched case, where there is no mismatch between the nominal model used for optimal control design and the actual WEC system. Furthermore, the results are computed under theoretically ideal impedance-matching condition using a non-causal, optimal controller, as discussed in Section 8.2. Fig.8.5 presents the peak power

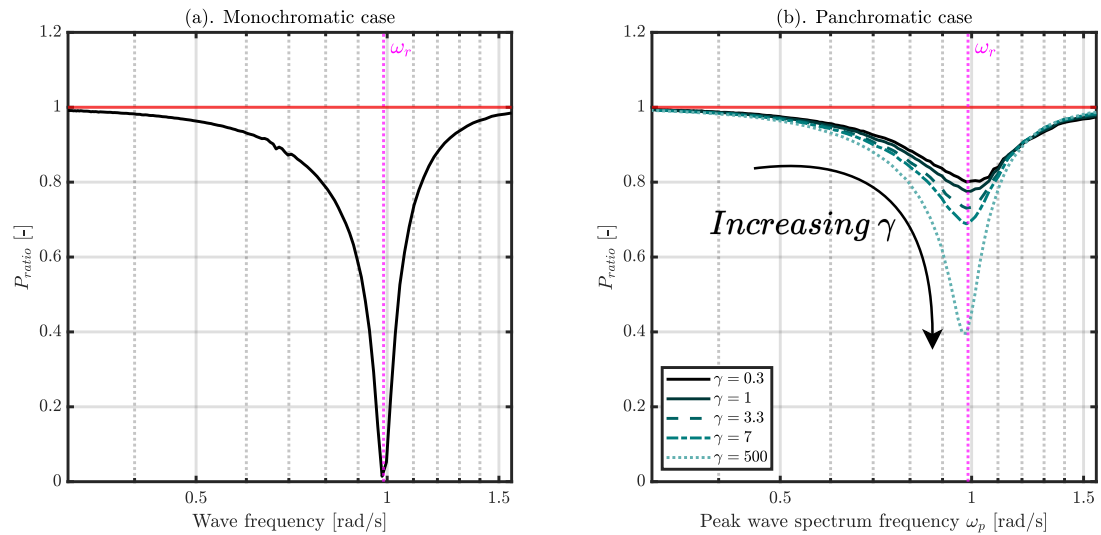


**Figure 8.5:** Peak power ratio  $P_{ratio}$ , for the range of wave frequencies considered, for optimal controller (a). Monochromatic case (b). Panchromatic case. The vertical purple dotted line depicts the resonant frequency  $\omega_r$  of the WEC.

ratio  $P_{ratio}$  for the range of wave frequencies considered. In particular, Fig.8.5(a) shows the results for the monochromatic case, and Fig. 8.5(b) shows the results for the panchromatic case. In both monochromatic and panchromatic cases, it is observed, from Fig.8.5, that the peak power ratio  $P_{ratio}$  never exceeds unity, which is in accordance with the analytical results presented in Proposition 8.3.3 and Remark 8.3.4. Furthermore, in the monochromatic case (Fig. 8.5(a)), it is observed that, as the wave frequency approaches the resonant frequency  $\omega_r$  of the WEC device,  $P_{ratio}$  tends to zero. This is consistent with Corollary 8.3.2, which states that the optimal controller does not require any reactive power at resonance under monochromatic

wave excitation. Since panchromatic wave spectra are broad-banded,  $P_{\text{ratio}}$  never reaches zero at resonant frequency (it is, however, at minimum). Moreover, the shape of the wave spectrum, characterised by the parameter  $\gamma$  in (8.47), has an impact on  $P_{\text{ratio}}$ . Increasing  $\gamma$  leads to a more concentrated and peaky spectrum, with a smaller effective bandwidth. Unsurprisingly, as shown in Fig. 8.5(b), as  $\gamma$  increases,  $P_{\text{ratio}}$  tends to approach the monochromatic case since a larger  $\gamma \rightarrow \infty$  gives rise to an effective monochromatic wave spectrum. It is worth noting that values of  $\gamma > 7$  are unusual for a JONSWAP spectrum, but are used here to effectively demonstrate the impact of increasing  $\gamma$  on  $P_{\text{ratio}}$ . Additionally, it can be observed from Fig. 8.5 that as the wave frequency approaches asymptotic values (*i.e.*  $\omega \rightarrow 0, \infty$ ),  $P_{\text{ratio}}$  approaches 1, which verifies Corollary 8.3.1.

## 8.4.2 Mismatched cases

Section 8.4.1 presents the case study results for a fully-matched case, where there is no mismatch between the model and the controller. However, in practice, mismatches are inevitable due to various sources of errors and uncertainty. In this section, we consider two main types of mismatch cases: modelling errors, also referred to as the *parametric mismatch*, and errors in the controller synthesis procedure, referred to as the *controller mismatch*.

### 8.4.2.1 Modelling errors

To demonstrate the impact of modelling uncertainty in the WEC model, we consider the main hydrodynamic parameters, *i.e.* mass  $M$ , hydrostatic stiffness  $K_h$ , and radiation damping  $B_r(\omega)$ , are subject to multiplicative modelling errors, expressed as follows:

$$\begin{aligned}\hat{M} &= \delta m \cdot M, \\ \hat{K}_h &= \delta k \cdot K_h, \\ \hat{B}_r(\omega) &= \delta b \cdot B_r(\omega),\end{aligned}\tag{8.48}$$

where  $[\delta m, \delta k, \delta b] \subset [0.5, 2]$ . These values represent a variation of 50-200% in the hydrodynamic parameters  $M$ ,  $K_h$ , and  $B_r(\omega)$ , respectively. In accordance with the frequency domain nominal WEC model presented in (6.2), the actual (mismatched) model  $\hat{G}(j\omega)$ , accounting for parametric variations, can be expressed as follows:

$$\hat{G}(j\omega) = \frac{1}{\hat{Z}_i(\omega)} = \frac{1}{\hat{B}_r(\omega) + j\omega(\hat{M} + A_r(\omega) - \frac{\hat{K}_h}{\omega^2})}.\tag{8.49}$$

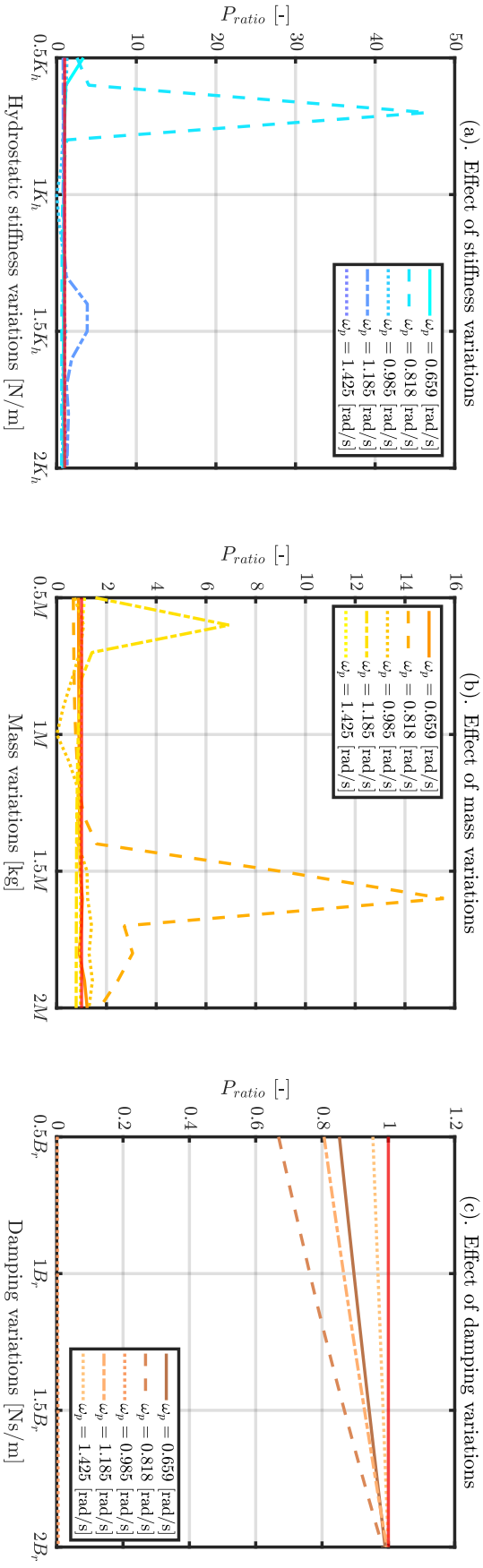
The optimal impedance-matching condition  $H_{f_e \rightarrow f_u}^{\text{opt}}(\omega)$ , as defined in (8.6), is applied to the actual (mismatched) model  $\hat{G}(j\omega)$  described in (8.49). The modelling errors

are articulated entirely in the frequency domain, where all signals and dynamic system responses, including the excitation force  $f_e(t)$ , control force  $f_u(t)$ , velocity  $v(t)$ , and frequency responses of the systems such as the actual system  $\hat{G}(j\omega)$  in (8.49) and the analysed control structure, such as the optimal feedforward control mapping  $H_{f_e \rightarrow f_u}^{opt}(\omega)$  in (8.6) are expressed in their spectral representations. By utilising these spectral representations, we compute the interactions based on their corresponding input-output relationships. Subsequently, the time-domain signals are obtained through an inverse Fourier transform.

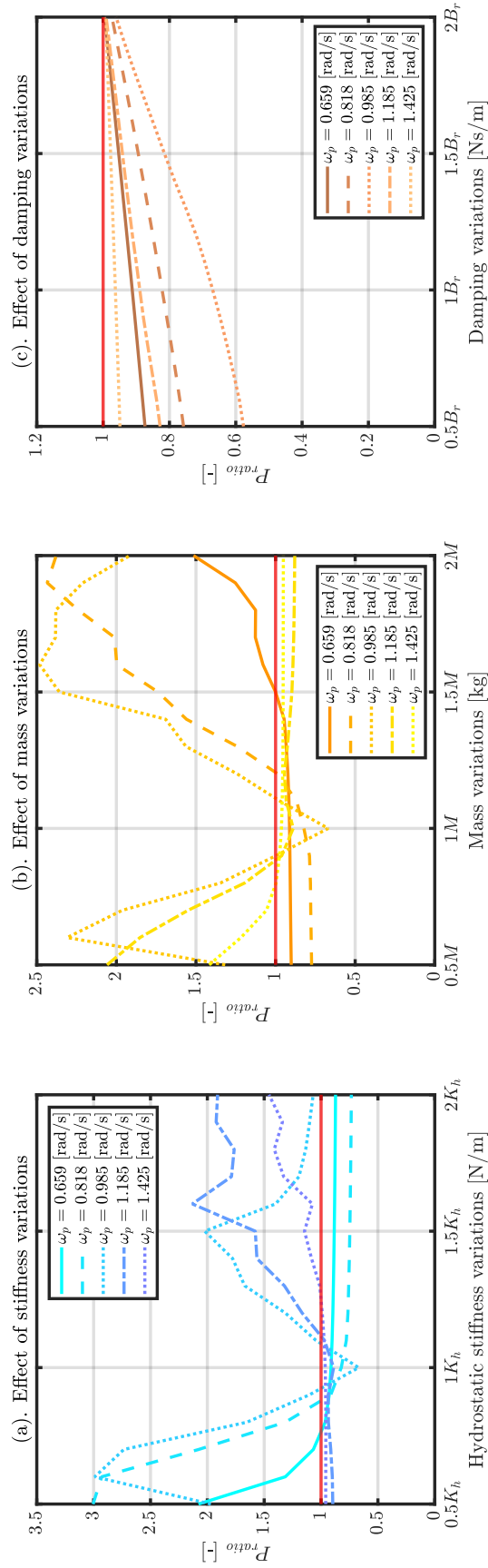
Fig. 8.6 illustrates the impact of parametric variations on peak power ratio  $P_{ratio}$  for different monochromatic waves. In particular, Fig. 8.6(a) demonstrates the effect of hydrostatic stiffness variations  $\hat{K}_h$  on  $P_{ratio}$ . It is evident that  $\hat{K}_h$  has a detrimental effect on the  $P_{ratio}$ , with some cases requiring reactive power peaks up to 47 times higher than the active power peak. Similarly, Fig. 8.6(b) shows the negative impact of mass variations  $\hat{M}$  on  $P_{ratio}$ , with reactive power peaks reaching nearly 16 times the active power peak in some cases. On the other hand, the effects of radiation damping variations  $\hat{B}_r(\omega)$  on  $P_{ratio}$  are not as severe as those of stiffness and mass variations, as depicted in Fig. 8.6(c). For the same variation in radiation damping  $\hat{B}_r(\omega)$ ,  $P_{ratio}$  never exceeds 1, meaning that the reactive power peaks are always lower than the active power peaks. However, it can be observed, from Fig. 8.6(c), that  $P_{ratio}$  increases with higher values of  $\hat{B}_r(\omega)$  and will surpass 1 when  $\hat{B}_r(\omega) > 2B_r(\omega)$ .

Fig. 8.7 showcases the results for parametric mismatch under panchromatic waves, which exhibit similar trends to the monochromatic case. However, the magnitudes of the reactive power peaks are significantly lower than in the monochromatic cases. Specifically, for stiffness variations  $\hat{K}_h$ ,  $P_{ratio}$  is approximately 3, which is significantly lower than the monochromatic case where  $P_{ratio}$  reaches around 47 in the worst-case scenario. Similar trends can be observed for mass variations ( $\hat{M}$ ) in Fig. 8.7(b) and damping variations ( $\hat{B}_r(\omega)$ ) in Fig. 8.7(c).

It is important to consider the relationship between the effects of mass and stiffness variations and the frequency of the incoming wave (or peak spectrum frequency for panchromatic cases), denoted as  $\omega_p$ , relative to the WEC resonant frequency  $\omega_r$  (approximately 0.987 [rad/s]). When  $\omega_p < \omega_r$ , stiffness variations  $\hat{K}_h$  below the nominal  $K_h$  result in a higher  $P_{ratio}$ , while mass variations  $\hat{M}$  greater than the nominal mass  $M$  also lead to a higher  $P_{ratio}$ . Conversely, when  $\omega_p > \omega_r$ , the effects on  $P_{ratio}$  are opposite: A higher  $\hat{K}_h$  and lower  $\hat{M}$  result in more significant impacts and lead to a higher  $P_{ratio}$ . For cases where  $\omega_p \approx \omega_r$ , both stiffness and mass variations have adverse effects on  $P_{ratio}$ , regardless of the specific variations in  $K_h$  and  $M$ , as depicted in Figs. 8.6 and 8.7. However, radiation damping variations  $\hat{B}_r(\omega)$  do not exhibit such



**Figure 8.6:** Effects of parametric mismatch on peak power ratio  $P_{ratio}$  for optimal controller under monochromatic waves: (a). Peak power ratio  $P_{ratio}$  for the range of hydrostatic stiffness variations  $\hat{K}_h \in [0.5K_h, 2K_h]$  [N/m], where  $K_h = 7.8868 \times 10^5$  [N/m] (b). Peak power ratio  $P_{ratio}$  for the range of mass variations  $\hat{M} \in [0.5M, 2M]$  [kg], where  $M = 6.6792 \times 10^5$  [kg] (c). Peak power ratio  $P_{ratio}$  for the range of damping variations  $\hat{B}_r(\omega) \in [0.5B_r(\omega), 2B_r(\omega)]$  [Ns/m].  $\omega_p$  represents wave frequency.



**Figure 8.7:** Effects of parametric mismatch on peak power ratio  $P_{ratio}$  for optimal controller under panchromatic waves: (a). Peak power ratio  $P_{ratio}$  for the range of hydrostatic stiffness variations  $\hat{K}_h \in [0.5K_h, 2K_h]$  [N/m], where  $K_h = 7.8868 \times 10^5$  [N/m] (b). Peak power ratio  $P_{ratio}$  for the range of mass variations  $\hat{M} \in [0.5M, 2M]$  [kg], where  $M = 6.6792 \times 10^5$  [kg] (c). Peak power ratio  $P_{ratio}$  for the range of damping variations  $\hat{B}_r(\omega) \in [0.5B_r(\omega), 2B_r(\omega)]$  [Ns/m].  $\omega_p$  represents peak wave spectrum frequency.

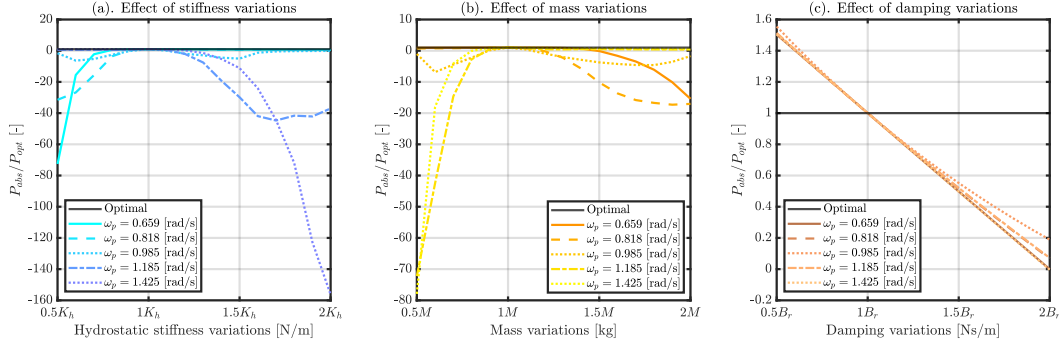


**Figure 8.8:** Effects of parametric mismatch on relative absorbed power  $P_{abs}/P_{opt}$  under panchromatic waves: (a).  $P_{abs}/P_{opt}$  for the range of hydrostatic stiffness variations  $\hat{K}_h \in [0.5K_h, 2K_h]$  [N/m], where  $K_h = 7.8868 \times 10^5$  [N/m] (b).  $P_{abs}/P_{opt}$  for the range of mass variations  $\hat{M} \in [0.5M, 2M]$  [kg], where  $M = 6.6792 \times 10^5$  [kg] (c).  $P_{abs}/P_{opt}$  for the range of damping variations  $\hat{B}_r(\omega) \in [0.5B_r(\omega), 2B_r(\omega)]$  [Ns/m].  $\omega_p$  depicts the peak frequency of a wave spectrum, and  $P_{opt}$  represents the optimal absorbed power for fully matched case.

frequency-dependent effects. Since radiation damping variations only affect the real part of the transfer function  $\hat{G}(j\omega)$  in (8.49), and do not impact the phase of the system, their effects on  $P_{ratio}$  are minimal compared to mass and stiffness variations, which is consistent with the sensitivity results presented in [206].

Fig. 8.8 illustrates the effects of parametric mismatch on the absorbed power  $P_{abs}$  compared to the optimal (fully-matched) case  $P_{opt}$ . In Fig. 8.8(a), the impact of stiffness variations  $\hat{K}_h$  on the relative absorbed hydrodynamic power  $P_{abs}/P_{opt}$  is depicted, which clearly shows that  $\hat{K}_h$  adversely affect the absorbed hydrodynamic power. Similarly, Fig. 8.8(b) demonstrates the negative impact of mass variations  $\hat{M}$  on the absorbed hydrodynamic power, showing negative power absorption for mismatch cases. The negative power absorption magnitude corresponds directly to the magnitude of the  $P_{ratio}$  shown in Fig. 8.7. Furthermore, Fig. 8.8(c) illustrates the effects of radiation damping variations  $\hat{B}_r(\omega)$  on the relative absorbed power. Unlike mass and stiffness variations, radiation damping variations exhibit slightly different behaviour. When  $\hat{B}_r(\omega) > B_r(\omega)$ , the relative absorbed power drops almost linearly. Conversely, for  $\hat{B}_r(\omega) < B_r(\omega)$  variations, a moderate increase in absorbed power is observed. It should be noted that parametric uncertainty can also lead to higher power absorption, as demonstrated in [207]. Note that the effects of parametric variations on relative absorbed power, for monochromatic cases, are very similar to the panchromatic case, and therefore are not included, for brevity.

### 8.4.2.2 Controller synthesis errors

This section focuses on the effects of controller synthesis mismatches on the reactive power requirements of a WEC under controlled conditions. Controller mismatch occurs



due to the finite-order realisation of the impedance-matching condition. Three specific finite-order realisations are considered: Two based on the LiTe-Con (referred to as *LiTeCon-V1* and *LiTeCon-V2*) and a *Reactive PI* controller.

In Fig. 8.9, the force-to-velocity responses for each of the considered controllers are presented. These controllers aim to approximate the optimal impedance-matching force-to-velocity response  $T_{f_e \rightarrow v}^{opt}$ . However, each controller exhibits different approximation errors due to the various synthesis procedures employed. Even within the same type of controller, such as LiTe-Con, the selection of different frequencies in the synthesis procedure leads to significantly different realisations and, consequently, diverse mapping characteristics, as illustrated in Fig. 8.9. In particular, the force-to-velocity response  $T_{f_e \rightarrow v}^{LCV1}$  performs better in terms of accurately mapping the optimal force-to-velocity condition  $T_{f_e \rightarrow v}^{opt}$  within the considered frequency range (indicated by the shaded green region in Fig.8.9). On the other hand, the *Reactive PI* controller, which only maps a single frequency as described in Section 8.2.1, exhibits the largest approximation error. It is worth noting that all controllers face challenges in achieving synthesis

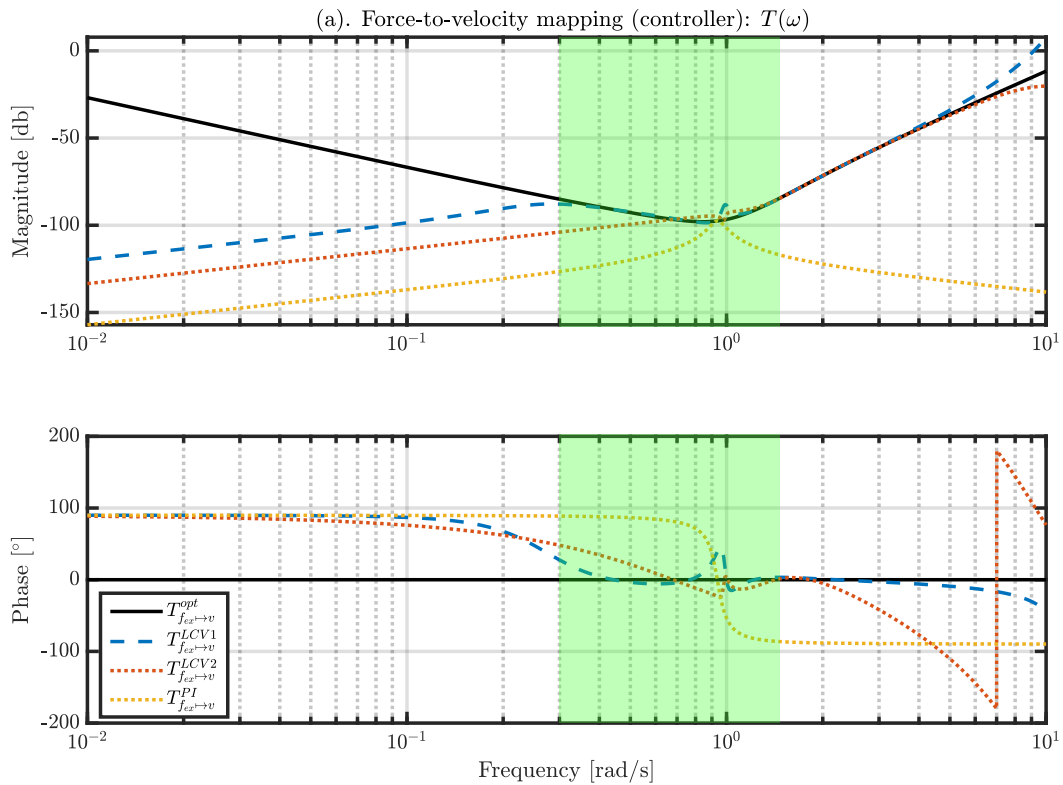


**Figure 8.9:** Force-to-velocity mapping  $T(\omega)$  for the controllers considered here, *i.e.*, *Optimal*  $T_{f_e \rightarrow v}^{opt}$  (Black solid line), *LiTeCon-V1*  $T_{f_e \rightarrow v}^{LCV1}$  (blue dashed line), *LiTeCon-V2*  $T_{f_e \rightarrow v}^{LCV2}$  (orange dotted line), and *Reactive PI*  $T_{f_e \rightarrow v}^{PI}$  (yellow dash-dot line), respectively. The shaded green region represents the wave frequency range considered for the analysis, *i.e.*, the area of interest.

fidelity, particularly around the resonant frequency, especially in capturing the phase response. These discrepancies in the phase response can impact the peak power requirements, as discussed in the following paragraphs.

Figs. 8.10 and 8.11 demonstrate how controller mismatch, resulting from different controller synthesis procedures, has an adverse effect on the peak power ratios  $P_{\text{ratio}}$  and relative absorbed power  $P_{\text{abs}}/P_{\text{opt}}$ , particularly at frequencies where the controller force-to-velocity response deviates from the optimal force-to-velocity response (as shown in Fig.8.9). In Fig.8.10(a), the values of  $P_{\text{ratio}}$  are presented for the three controller realisations (*LiTeCon-V1*, *LiTeCon-V2*, and *Reactive PI*) compared to the optimal fully matched case (*Optimal*) under monochromatic waves. It is evident that  $P_{\text{ratio}}$  is particularly affected by mismatch around the resonance frequency  $\omega_r$ , especially for the *LiTeCon-V1* controller realisation, which fails to accurately capture the optimal force-to-velocity response in both magnitude and phase at these frequencies, resulting in  $P_{\text{ratio}} > 1$ . On the other hand, *LiTeCon-V2* exhibits inferior matching characteristics compared to *LiTeCon-V1*, but the mismatch around the resonance frequency is not as significant as *LiTeCon-V1*. As a result,  $P_{\text{ratio}}$  is always less than 1 for this controller realisation. It is important to note that the power capture performance of *LiTeCon-V2* is considerably worse than *LiTeCon-V1*, as depicted in Fig.8.10(b). The *Reactive PI* controller realisation, which can only map a single frequency on the optimal impedance-matching condition, exhibits the lowest relative absorbed power  $P_{\text{abs}}/P_{\text{opt}}$  and the lowest values of  $P_{\text{ratio}}$  among the considered controller realisations, as shown in Fig. 8.10.

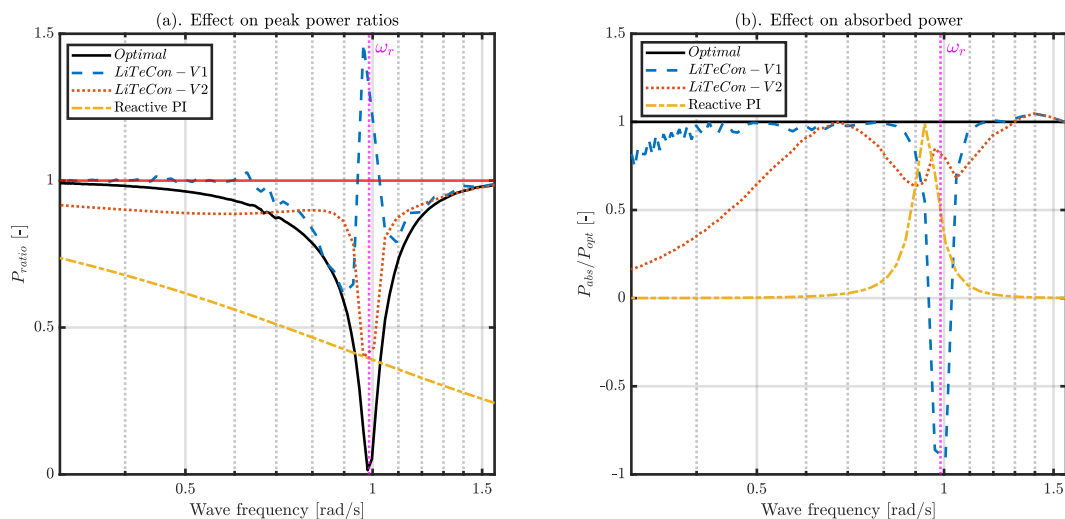


**Figure 8.10:** Effects of controller synthesis mismatch under monochromatic waves: (a) Peak power ratio  $P_{\text{ratio}}$  of three controllers for the range of wave frequencies considered. (b) Relative absorbed power  $P_{\text{abs}}/P_{\text{opt}}$  of the controllers for the range of wave frequencies considered. The vertical purple dotted line depicts the resonant frequency  $\omega_r$  of the WEC.

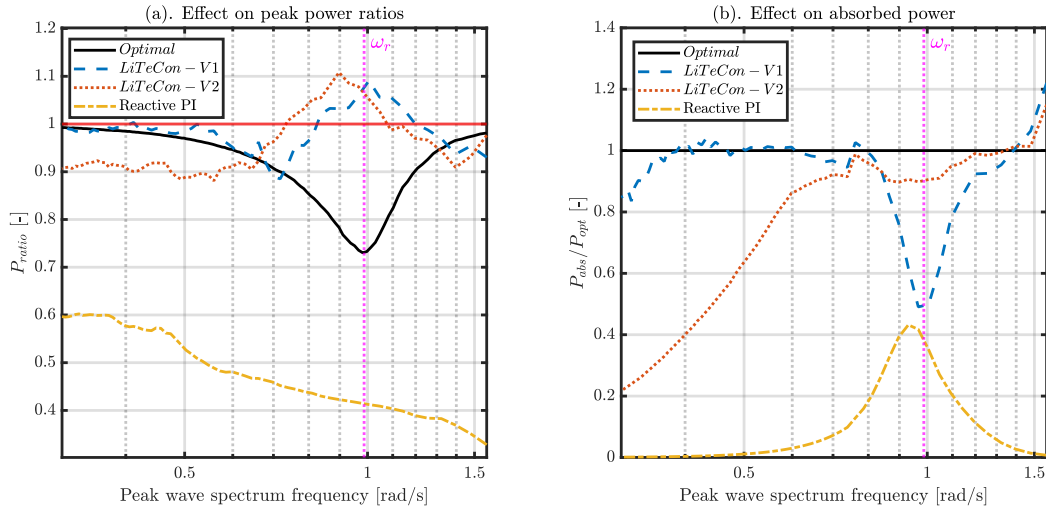


**Figure 8.11:** Effects of controller synthesis mismatch under panchromatic waves: (a) Peak power ratio  $P_{\text{ratio}}$  of the controllers for the range of wave frequencies considered. (b) Relative absorbed power  $P_{\text{abs}}/P_{\text{opt}}$  of the controllers for the range of wave frequencies considered. The vertical purple dotted line depicts the resonant frequency  $\omega_r$  of the WEC.

In the case of panchromatic waves, the effects of controller mismatch on  $P_{\text{ratio}}$  are more pronounced, as shown in Fig.8.11. In Fig. 8.11(a), it can be observed that both *LiTeCon-V1* and *LiTeCon-V2* result in  $P_{\text{ratio}} > 1$  for mismatches around the resonant frequency ( $\omega_r$ ) of the WEC, indicating that the controllers fail to adequately match the optimal force-to-velocity response, leading to increased reactive power requirements. Consequently, the negative impact of the increased  $P_{\text{ratio}}$  on the relative absorbed power  $P_{\text{abs}}/P_{\text{opt}}$  is illustrated in Fig. 8.11(b), where a significant drop in relative absorbed power is observed. For the Reactive PI controller, the performance under panchromatic waves is similar to the monochromatic case, in terms of the peak power ratio  $P_{\text{ratio}}$ . However, a further decrease in the relative absorbed power  $P_{\text{abs}}/P_{\text{opt}}$  is observed for panchromatic waves, primarily due to the *bandpass* nature of the Reactive PI controller.

## 8.5 Discussion

### 8.5.1 Discussion of results

Fig.8.12 provides further analysis of the data presented in Fig.8.5 by examining the occurrence probability of  $P_{\text{ratio}}$  for both monochromatic and panchromatic ( $\gamma = 3.3$ ) cases. The analysis shows that the majority of the matched cases have  $P_{\text{ratio}}$  values greater than 0.7, indicating that the reactive power peaks are generally in the range of 70-100% of the active power peak, which holds true for most cases, except for those occurring near the WEC resonance frequency. The occurrence probability of  $P_{\text{ratio}}$  is

highest (around 70%) when  $0.90 < P_{ratio} < 1$ , indicating that reactive power peaks are frequently close to, or even exceed, the active power peaks, highlighting the importance of considering reactive power peaks and designing PTO and energy storage systems to handle reactive power peaks in addition to active power peaks. In the mismatched cases, the occurrence of  $P_{ratio} > 1$ , due to controller or parametric mismatch, indicates that the reactive power requirements can be even higher than the active power peak. Indeed, an increased peak power ratio  $P_{ratio} > 1$  is consistently associated with a significant drop in absorbed power, as demonstrated in Section 8.4.2. Higher reactive power peaks, indicative of mismatch, occur for various reasons (see Section 8.4.2) and can be dealt with differently by addressing the mismatch. Firstly, improving the accuracy of the control design model is crucial in reducing modelling uncertainty and preventing extreme reactive power peaks. This involves refining the mathematical model used for control synthesis to better capture the dynamics of WEC system. Alternatively, model-free or data-based control approaches for WECs, as mentioned in [208], can be explored. However, it should be noted that model-free controllers are still in the early stages of development (and constraint handling is an issue) [209]. Another option is to constrain reactive power flow using constrained optimal control methods, such as the approach presented in [197]. Excessive reactive power peaks can be limited by incorporating constraints on reactive power. However, this

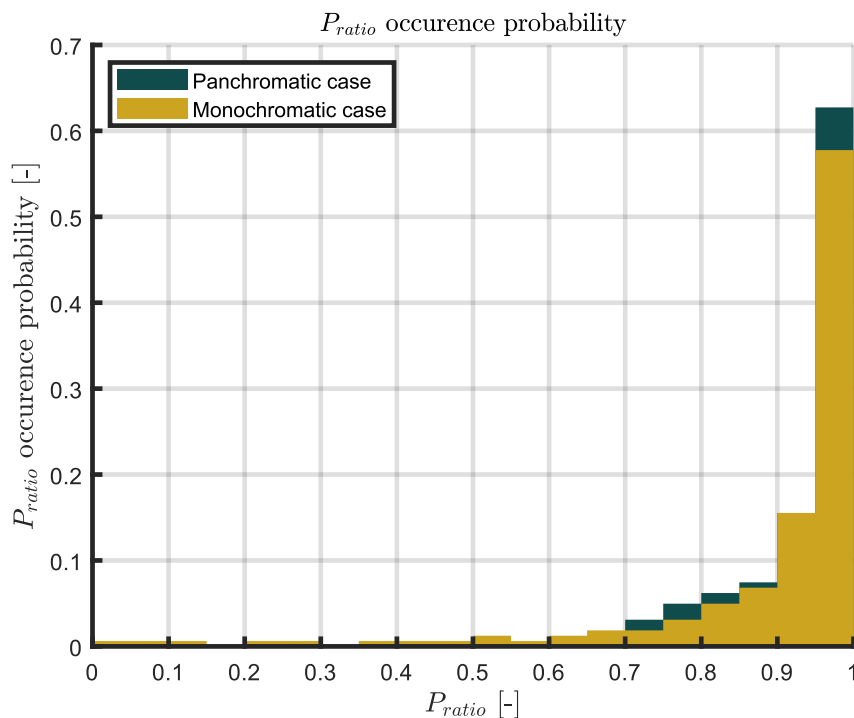


**Figure 8.12:** Occurrence probability of  $P_{ratio}$  values for both monochromatic and panchromatic cases.

solution involves nonlinear constraints, can be computationally expensive, and cannot guarantee a solution 100% of the time.

The sensitivity of peak power ratios  $P_{\text{ratio}}$  to different types of mismatch varies. The results indicate that variations in mass  $M$  and stiffness  $K_h$  have a more significant impact on  $P_{\text{ratio}}$  than variations in damping  $B_r(\omega)$ . Therefore, correctly modelling the mass and stiffness parameters of the WEC can help minimise the adverse effects of increased reactive power peaks. Regarding controller mismatch, the sensitivity of  $P_{\text{ratio}}$  is most pronounced when the controller fails to match the optimal impedance-matching condition near the resonant frequency of the device, resulting in a drop in the relative absorbed power, as shown in Figs. 8.10 and 8.11. In order to mitigate the effects of controller mismatch, it is crucial to design finite-order controller realisations that accurately capture the optimal impedance-matching condition, particularly in the vicinity of the WEC resonant frequency.

It is important to note that the findings presented in this chapter are applicable to MPC/MPC-like WEC controller [183], with the primary goal of achieving impedance-matching (complex-conjugate) condition. However, it should be acknowledged that the introduction of displacement and force constraints will likely reduce the extent of controller action and, therefore, the peak power ratio.

### 8.5.2 Effect of a non-ideal PTO

The analysis and the presented results primarily address modelling and controller synthesis errors in WEC systems. However, it is essential to acknowledge the presence of non-ideal behaviour in the PTO part of the powertrain, particularly concerning the efficiency of converting mechanical energy to electrical energy. While this paper focuses on generic system and controller mismatch issues, it is worth emphasising the significance of non-ideal PTO efficiency, particularly in the context of electricity production, where a generator is connected to the mechanical prime-mover using an appropriate coupling. In practical WEC systems, converting mechanical energy to electrical energy involves energy losses due to friction, electrical losses, and other inefficiencies in the PTO chain. These losses can have an impact on the overall system performance and efficiency. It is therefore relevant to examine the behaviour of reactive power peaks, in the light of such circumstances, and discuss the implications. As a starting point, the studies conducted by Genest *et al.* [211, 212] provide valuable insights into the significant impact of non-ideal PTO efficiency on generated power which demonstrate that, in specific scenarios, the system becomes an overall power *consumer* when the non-ideal PTO efficiency is not considered in the controller model. In the mismatched case, it is essential to note that the problem of reactive power peaks

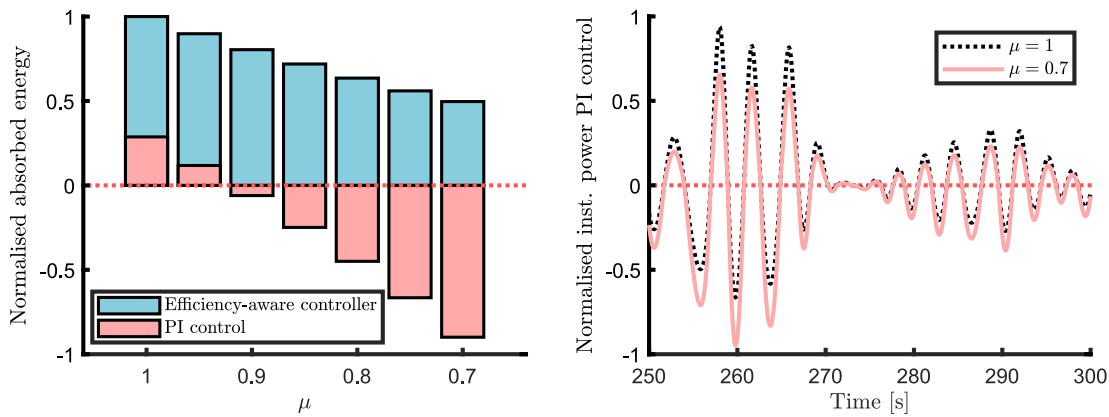


**Figure 8.13:** Ranges of positive and negative energy absorption for non-ideal PTO case, using an efficiency-aware (moment-based), and efficiency-ignorant (reference) PI controller, using the methodology of [210] (left). Sample time trace of power flow with non-ideal PTO for an efficiency-ignorant (reference) PI controller, showing large excursions in reactive power flow (right).

becomes more significant when dealing with a non-ideal ( $\mu < 1$ ) PTO efficiency since *even more* reactive power is required at the electrical stage (from the grid or storage) to provide the required mechanical reactive power to ‘maximise’ hydrodynamic conversion. The findings presented in studies such as [210–213] (which also utilises an efficiency-aware controller) emphasise the importance of incorporating system/controller mismatch, resulting from non-ideal PTO efficiency, into the controller model. Specifically, the consideration of system/controller mismatch due to non-ideal PTO efficiency is crucial, particularly when assessing the impact of reactive power peaks on the power capacity of the generator and power converters in the powertrain.

## 8.6 Conclusions

This chapter investigates the causes of excessive reactive power peaks in reactive WEC control through theoretical analysis and an illustrative case study. The peak power ratio  $P_{\text{ratio}}$  is used as a key metric to assess the occurrence of these peaks.

For matched system/controller cases,  $P_{\text{ratio}} < 1$ , i.e. the reactive power peak is always less than the active power peak, proven analytically and with simulation results. Additionally, energy absorption is always positive for matched cases. The findings also suggest that instances where  $P_{\text{ratio}} > 1$  are solely attributed to various types of mismatch. This mismatch arises from various factors, including unmodelled dynamics, model uncertainty, errors in controller synthesis due to finite-order realisations, and the omission of non-ideal PTO efficiency. An increased  $P_{\text{ratio}}$  has implications for both the capital costs of powertrain equipment, such as PTO and storage systems, and the

power absorption capacity of the wave energy conversion system. Furthermore, the chapter reveals that power absorption is negatively affected by an elevated  $P_{\text{ratio}}$  in all the analysed cases.

This chapter adopts a fundamental linear approach, establishing the essential groundwork for future research. To mitigate excessive reactive power peaks resulting from system/controller mismatch, a better model/controller matching is required. However, the effective implementation of such a mechanism and its implications for power absorption requires further investigation.





## **Part IV**

# **Conclusions and Future work**



# 9

## Conclusions

### Contents

---

<b>9.1 Conclusions</b> . . . . .	<b>143</b>
<b>9.2 Future work</b> . . . . .	<b>145</b>

---

This thesis contributes to developing a control-oriented modelling and high-performance control framework for a grid-connected wave energy conversion system, which addresses both device- and grid-side requirements. Furthermore, the thesis explores other grid integration aspects related to the value of wave energy to the electricity grid in terms of complementarity to other renewable resources and load requirements in a jurisdiction, particularly the Island of Ireland (including Northern Ireland), in this case.

The primary findings and conclusions<sup>9.1</sup> of this thesis are summarised in Section 9.1, while potential areas for future research are discussed in Section 9.2.

### 9.1 Conclusions

Initially, a complementarity assessment of wave energy with other renewable energy modalities (tidal, wind and solar), for the Island of Ireland, is presented, providing a case for the potential value of wave energy on the Irish electric grid. The complementarity analysis indicates a direct relationship between complementarity and the diversity of supply systems. Integrating marine energy resources like wave and tidal power

---

<sup>9.1</sup>Indeed, specific conclusions are provided at the end of each chapter, summarising the findings and outcomes of that particular chapter.

into the wind-solar mix results in a more diverse energy supply system for Ireland. This diversification may lead to reduced storage and reserve requirements, which enhances the overall resilience and efficiency of the energy supply system, offering potential advantages in terms of system reliability and stability. Moreover, a preliminary balancing costs analysis emphasises the importance of integrating wave energy into the primarily wind-powered Irish electricity system, revealing the wave energy potential to reduce balancing costs by reducing the variability associated with other renewable energy sources like wind. As a result, the inclusion of wave energy can contribute to a more stable and consistent generation profiles in Ireland.

Following the state-of-the-art review of grid integration studies in the literature in Part II, it is concluded that, in general, many grid integration studies have some drawbacks, such as the use of

- (i) simplified hydrodynamic models,
- (ii) regular wave models,
- (iii) simplified power converter models,
- (iv) passive damping hydrodynamic control,
- (v) and relatively rudimentary PI power converter control,

where one, or more, of these issues is prevalent in the majority of the studies. In addition, drawing from the classification presented in Chapter 3, it is concluded that the inertial characteristics of a wave energy conversion system depends upon both the wave absorber technology and its associated PTO mechanism.

To this end, in Part III of the thesis, a W2G coordinated control framework, for a direct-drive heaving point absorber wave energy converter, is proposed. First of all, *control-oriented models* for each component of the W2G powertrain are developed, including a hydrodynamic WEC model with appropriate radiation force quantification rather than mass-spring-damper models typically used in the literature and computationally efficient state-space averaged power converters models. Furthermore, irregular wave models are also utilised instead of commonly used regular wave models to model ocean waves. The framework provides *high-performance controllers* for device-side, grid-side and storage subsystems in the powertrain. On the device-side, LiTe-Con (and LiTe-Con+) reactive hydrodynamic controllers are proposed, which not only provide significantly more absorbed power, from ocean waves, compared to passive damping controllers, they also offer a position constraint handling mechanism essential for device safety. Lyapunov-based nonlinear controllers are employed for the power converters control in the powertrain, demonstrating satisfactory performance across

range of operating conditions (range of sea-states, grid faults etc.) and outperforms typically proposed PI controllers. In addition, the use of a Lyapunov-based control synthesis procedure ensures the stability of the electrical components of the powertrain, providing a *guarantee* of stability during operation. Another important part of the W2G control framework is the energy management system or EMS, as a supervisory control mechanism, which ensures that the storage subsystem performs DC bus voltage regulation, reactive hydrodynamic control support and grid LVRT support, by providing low-level current references for Grid-SC and storage power converters. The proposed W2G control scheme also ensures that power quality standards, including power fluctuations, frequency variations, and THD levels, are maintained within the limits specified by typical grid codes and IEEE standards.

Though the reactive hydrodynamic controllers (LiTe-Con and LiTe-Con+) delivers more power compared to passive damping controllers. However, implementing these reactive hydrodynamic controllers in a W2G control scheme comes with implications, such as the requirement for negative (reactive<sup>9.2</sup>) power and additional storage or power sources to provide this power. It also necessitates bi-directional PTO (for bi-direction power flow requirements) and higher ratings for PTO and power converters in the powertrain. Realising the significance of the implications, reactive power peaks are analysed, for reactively controlled wave energy conversion system, in Chapter 8. In particular, analytical (and simulation) results show that, for matched cases, the reactive power peaks are always less than that of active power peaks and energy absorption is always positive. However, under mismatched cases, as demonstrated by the illustrative case studies in Chapter 8, reactive power peaks can exceed positive active power peaks, leading to a negative impact on the absorbed power. Several factors contribute to this mismatch, such as unmodelled dynamics, model uncertainty, controller synthesis errors arising from finite-order realisations, and the omission of non-ideal PTO efficiency in the controller model. Thus, a better model/controller matching is required in order to mitigate the excessive reactive power peaks. Furthermore, these results also highlights the importance using *validated models under controlled conditions* in order to avoid such excessive reactive power peaks.

## 9.2 Future work

The work presented in this thesis opens up several directions for further research and investigation:

---

<sup>9.2</sup>Specifically, the reactive power in reactive hydrodynamic control sense, as detailed in Section 8.1.

- ▶ The significance of energy storage systems for grid-connected wave energy conversion systems cannot be overemphasised. These storage systems serve various crucial functions, including supporting reactive hydrodynamic control, enhancing power quality, and providing grid support during faults. Moreover, long-term storage can complement wave energy generation during periods of low or no generation. Thus, optimally sizing the storage system is crucial to maximising its benefits. Therefore, it is imperative to explore *control-informed* optimal sizing of storage systems (both short-term and long-term), as an *economic evaluation*, for grid-connected wave energy applications, as this area remains relatively unexplored in the existing wave energy literature and presents a promising direction for future research.
- ▶ As discussed in [16], utilising combined resources offers several advantages. One promising application is the use of co-located combined renewable power plants, incorporating wave energy, for microgrid applications, particularly in areas distant from the main electricity grid, such as remote islands seeking electrification (see, for example, [214]). The investigation of feasibility, control strategies, and energy management for these *marine microgrids* represents a promising future research direction.
- ▶ Analysing the W2G controlled system by considering nonlinearities/losses in each part of the W2G powertrain. This is particularly important for the hydrodynamic model of the WECs, since the energy-maximising WEC control violates the small-motion assumption associated with the linear WEC models [160], resulting in overestimating the power absorption capability. Hence, the inclusion of nonlinear effects in the hydrodynamic model is important. Additionally, inclusion of generator losses (Iron losses, Cu-losses and saturation etc.) and power converters losses (switching, conduction losses etc.) in the W2G model will help realise the true potential of grid-connected wave energy conversion systems (see, for instance, [215]).
- ▶ The deployment of wave energy is expected to be in the form of wave farms or WEC arrays. Therefore, it becomes essential to analyse the grid integration aspects of WEC arrays and their implications for grid-connected systems. In particular, WEC arrays offer the potential to reduce the negative (reactive) power requirements of hydrodynamic control through the aggregation effect, and they can also reduce storage requirements by minimising the need for power output smoothing [216, 217]. An important question is whether the other WECs in a WEC array can meet the reactive power requirements of each individual

WEC within the same array. To answer such questions, the development of control mechanisms requires further research and constitutes essential areas for future investigation.





# Bibliography

- [1] J. Flanagan, P. Nolan, R. McGrath, and C. Werner. Towards a definitive historical high-resolution climate dataset for Ireland – promoting climate research in Ireland. *Adv. Sci. Res.*, 15:263–276, 2019.
- [2] Bingyong Guo and John V Ringwood. A review of wave energy technology from a research and commercial perspective. *IET Renew. Power Gener.*, 15(14):3065–3090, 2021.
- [3] BG Reguero, IJ Losada, and FJ Méndez. A global wave power resource and its seasonal, interannual and long-term variability. *Appl Energ*, 148:366–380, 2015.
- [4] Francisco Taveira-Pinto, Paulo Rosa-Santos, and Tiago Fazerer-Ferradosa. Marine renewable energy. *Renew. Energy*, 150:1160–1164, 2020.
- [5] Christina Kalogeri, George Galanis, Christos Spyrou, Dimitris Diamantis, Foteini Baladima, Marika Koukoura, and George Kallos. Assessing the European offshore wind and wave energy resource for combined exploitation. *Renew. Energy*, 101:244–264, 2017.
- [6] Francesco Fusco, Gary Nolan, and John V Ringwood. Variability reduction through optimal combination of wind/wave resources—An Irish case study. *Energy*, 35(1):314–325, 2010.
- [7] Gordon Reikard, Bryson Robertson, and Jean-Raymond Bidlot. Combining wave energy with wind and solar: Short-term forecasting. *Renew. Energy*, 81:442–456, 2015.
- [8] Gunnar Mork, Stephen Barstow, Alina Kabuth, and M Teresa Pontes. Assessing the global wave energy potential. In *International Conference on Offshore Mechanics and Arctic Engineering*, volume 49118, pages 447–454, 2010.
- [9] J. Hals. *Modelling and phase control of wave-energy converters*. PhD thesis, Norges teknisk-naturvitenskapelige universitet, 2010.
- [10] Jennifer DeCesaro, Kevin Porter, and Michael Milligan. Wind energy and power system operations: A review of wind integration studies to date. *Electr. J.*, 22(10):34–43, 2009.
- [11] Tarek Ahmed, Katsumi Nishida, and Mutsuo Nakaoka. Grid power integration technologies for offshore ocean wave energy. In *2010 IEEE Energy Convers. Congr. Expo.*, pages 2378–2385. IEEE, 2010.

- [12] EirGrid. Grid Code, Version 6.0. Technical report, EirGrid, 2015.
- [13] THE GRID CODE, Issue 5, Revision 38. Technical report, National Grid Electricity System Operator (ESO),UK, 2019.
- [14] Mansour Mohseni and Syed M Islam. Review of international grid codes for wind power integration: Diversity, technology and a case for global standard. *Renew. Sustain. Energy Rev.*, 16(6):3876–3890, 2012.
- [15] Hafiz Ahsan Said and John V Ringwood. Grid integration aspects of wave energy—Overview and perspectives. *IET Renew. Power Gener.*, 15:3045–3064, 2021.
- [16] Hafiz Ahsan Said, Shaun Costello, and John Ringwood. On the complementarity of wave, tidal, wind and solar resources in ireland. In *Proceedings of the Eur. Wave Tidal Energy Conf.*, pages 340–1:340–6, September 2023.
- [17] Hafiz Ahsan Said and John V Ringwood. Intelligent control of a DC microgrid consisting of Wave Energy Converter (WEC) and Hybrid Energy Storage System (HESS). In *14th European Wave and Tidal Energy Conference (EWTEC), Plymouth.*, pages 1884–1:1884–9, 2021.
- [18] Hafiz Ahsan Said, Demián García-Violini, and John V Ringwood. Wave-to-grid (W2G) control of a wave energy converter. *Energ. Convers. Manage. : X*, 14:100190, 2022.
- [19] Hafiz Ahsan Said and John V Ringwood. Low voltage ride-through capability enhancement of a grid-connected wave energy conversion system. *Trends in Renewable Energies Offshore (RENEW 2022)*, pages 267–275, 2022.
- [20] Hafiz Ahsan Said, Demián García-Violini, and John V Ringwood. An improved linear time-varying reactive hydrodynamic control for a grid-connected wave energy conversion system. In *OCEANS 2023-Limerick*, pages 1–9. IEEE, 2023.
- [21] Hafiz Ahsan Said, Demián García-Violini, Nicolás Faedo, and John V. Ringwood. On the ratio of reactive to active power in wave energy converter control. *IEEE Open Journal of Control Systems*, 3:14–31, 2024.
- [22] Saptarshi Bhattacharya, Shona Pennock, Bryson Robertson, Sarmad Hanif, Md Jan E Alam, Dhruv Bhatnagar, Danielle Preziuso, and Rebecca O’Neil. Timing value of marine renewable energy resources for potential grid applications. *Appl Energ*, 299:117281, 2021.
- [23] Shona Pennock, Daniel Coles, Athanasios Angeloudis, Saptarshi Bhattacharya, and Henry Jeffrey. Temporal complementarity of marine renewables with wind and solar generation: implications for GB system benefits. *Appl Energ*, 319:119276, 2022.
- [24] A González, E McKeogh, and BO Gallachoir. The role of hydrogen in high wind energy penetration electricity systems: The irish case. *Renew. Energy*, 29(4):471–489, 2004.

- [25] K Martins and James G Carton. Prospective roles for green hydrogen as part of Ireland's decarbonisation strategy. *Results Engg.*, 18:101030, 2023.
- [26] Luciano De Tommasi and Pádraig Lyons. Towards the integration of flexible green hydrogen demand and production in Ireland: Opportunities, barriers, and recommendations. *Energies*, 16(1):352, 2022.
- [27] Diana Cantor, Andrés Ochoa, and Oscar Mesa. Total Variation-Based Metrics for Assessing Complementarity in Energy Resources Time Series. *Sustainability*, 14(14):8514, January 2022.
- [28] *Marine Institute ERDDAP Data Portal*. Accessed; January 9, 2023.
- [29] Alan Lapworth. Wind against tide. *Weather*, 66(4):100–102, 2011.
- [30] *ERA5 hourly data on single levels from 1940 to present*. Accessed; May 16, 2023.
- [31] F de O Antonio. Wave energy utilization: A review of the technologies. *Renew. Sustain. Energy Rev.*, 14(3):899–918, 2010.
- [32] Gordon J Dalton, Raymond Alcorn, and T Lewis. Case study feasibility analysis of the pelamis wave energy convertor in Ireland, Portugal and North America. *Renew. Energ.*, 35(2):443–455, 2010.
- [33] Alexis Mérigaud and John V Ringwood. Power production assessment for wave energy converters: Overcoming the perils of the power matrix. *Proc. Inst. Mech. Eng. Part M J. Eng. Marit. Environ.*, 232(1):50–70, 2018.
- [34] Simone Giorgi and John V Ringwood. Can tidal current energy provide base load? *Energies*, 6(6):2840–2858, 2013.
- [35] *W2E Wind to Energy W2E-215/9.0*. Accessed; May 16, 2023.
- [36] B. François, B. Hingray, D. Raynaud, M. Borga, and J.D. Creutin. Increasing climate-related-energy penetration by integrating run-of-the river hydropower to wind/solar mix. *Renew. Energy*, 87:686–696, March 2016.
- [37] Yang Zhang, Pietro Elia Campana, Anders Lundblad, Lei Wang, and Jinyue Yan. The influence of photovoltaic models and battery models in system simulation and optimization. *Energy Proced.*, 105:1184–1191, 2017.
- [38] Jakub Jurasz, FA Canales, Alexander Kies, Mohammed Guezgouz, and Alexandre Beluco. A review on the complementarity of renewable energy sources: Concept, metrics, application and future research directions. *Solar Energy*, 195:703–724, 2020.
- [39] Fausto Alfredo Canales and Guillermo J. Acuña. Chapter 2 - Metrics and indices used for the evaluation of energetic complementarity—a review. In Jakub Jurasz and Alexandre Beluco, editors, *Complementarity of Variable Renewable Energy Sources*, pages 35–55. Academic Press, January 2022.

- [40] Dominik Heide, Lueder Von Bremen, Martin Greiner, Clemens Hoffmann, Markus Speckmann, and Stefan Bofinger. Seasonal optimal mix of wind and solar power in a future, highly renewable Europe. *Renew Energy*, 35(11):2483–2489, 2010.
- [41] Baptiste Francois, Marco Borga, Jean-Dominique Creutin, Benoit Hingray, Damien Raynaud, and Julian-Friedrich Sauterleute. Complementarity between solar and hydro power: Sensitivity study to climate characteristics in Northern-Italy. *Renewable energy*, 86:543–553, 2016.
- [42] Solar energy in Ireland.  
<https://www.energyireland.ie/solar-energy-in-ireland/>, 2023. Accessed; July 10.
- [43] Yeraí Peña-Sánchez. *Hydrodynamic excitation force estimation and forecasting for wave energy applications*. PhD thesis, National University of Ireland, Maynooth (Ireland), 2020.
- [44] Anne Blavette. *Grid integration of wave energy & generic modelling of ocean devices for power system studies*. PhD thesis, University College Cork, 2013.
- [45] Dara L O’Sullivan and Anthony W Lewis. Generator requirements and functionality for ocean energy converters. In *XIX Int. Conf. Electr. Mach. 2010*, pages 1–7. IEEE, 2010.
- [46] A F de O Falcão. Control of an oscillating-water-column wave power plant for maximum energy production. *Appl. Ocean Res.*, 24(2):73–82, 2002.
- [47] António FO Falcão, João CC Henriques, and Luís MC Gato. Self-rectifying air turbines for wave energy conversion: A comparative analysis. *Renew. Sustain. Energy Rev*, 91:1231–1241, 2018.
- [48] M Rosati, JV Ringwood, and JCC Henriques. A comprehensive wave-to-wire control formulation for oscillating water column wave energy converters. *Trends in Renewable Energies Offshore*, pages 329–337, 2022.
- [49] Mikel Alberdi, Modesto Amundarain, Aitor J Garrido, Izaskun Garrido, and Francisco Javier Maseda. Fault-ride-through capability of oscillating-water-column-based wave-power-generation plants equipped with doubly fed induction generator and airflow control. *IEEE Trans. Ind. Electron.*, 58(5):1501–1517, 2010.
- [50] FD Mosquera, Carolina Alejandra Evangelista, Pablo Federico Puleston, and JV Ringwood. Optimal wave energy extraction for oscillating water columns using second-order sliding mode control. *IET Renew. Power Gener.*, 14(9):1512–1519, 2020.
- [51] Belfast TQsUo. Islay LIMPET wave power plant, non-nuclear energy programme joule III, CORDIS. Technical report, JOR3-CT98-0312, 2002.

- [52] R Curran. Ocean wave energy systems design: Conceptual design methodology for the operational matching of the wells air turbine. In *Collab. Prod. Serv. Life Cycle Manag. a Sustain. World*, pages 601–615. Springer, 2008.
- [53] Y Torre-Enciso, I Ortubia, L I López De Aguilera, and J Marqués. Mutriku wave power plant: from the thinking out to the reality. In *Proc. 8th Eur. wave tidal energy Conf. Uppsala, Sweden*, volume 710, pages 319–329. EWTEC, 2009.
- [54] *Wave Dragon - Home*. Accessed; March 17, 2023. <[http://www.wavedragon.net/?Option=com\\_frontpage&Itemid=1](http://www.wavedragon.net/?Option=com_frontpage&Itemid=1)>.
- [55] *CORPOWER'S WAVE ENERGY CONCEPT*. Accessed; March 27, 2023. <<http://www.corpowerocean.com/technology/#corpowerConcept>>.
- [56] *ARCHIMEDES WAVESWING SUBMERGED WAVE POWER BUOY*. Accessed; March 27, 2020. <<http://www.awsocean.com/archimedes-waveswing.html>>.
- [57] J Weber, F Mouwen, A Parish, and D Robertson. Wavebob—research & development network and tools in the context of systems engineering. In *Proc. 8th Eur. wave tidal energy Conf. Uppsala, Sweden*, volume 8, pages 416–420, 2009.
- [58] Trevor Whittaker and Matt Folley. Nearshore oscillating wave surge converters and the development of Oyster. *Philos. Trans. R. Soc. A Math. Phys. Eng. Sci.*, 370(1959):345–364, 2012.
- [59] Ross Henderson. Design, simulation, and testing of a novel hydraulic power take-off system for the Pelamis wave energy converter. *Renew. Energy*, 31(2):271–283, 2006.
- [60] J Cameron McNatt and Christopher H Retzler. The performance of the mocean m100 wave energy converter described through numerical and physical modelling. *Int. Mar. Energy J.*, 3(1):11–19, 2020.
- [61] *EMEC-Wave Devices*. Accessed; January 9, 2020. <<http://www.emec.org.uk/marine-energy/wave-devices/>>.
- [62] *WEPTOS Technology*. Accessed; April 29, 2023. <<http://www.weptos.com/technology>>.
- [63] Andrei Ermakov and John V Ringwood. Rotors for wave energy conversion—practice and possibilities. *IET Renew. Power Gener.*, 15(14):3091–3108, 2021.
- [64] *Wello Penguin Technology*. Accessed; April 29, 2023. <<https://wello.eu/technology/>>.
- [65] *CycWEC Design Features*. Accessed; June 29, 2023. <<https://atargis.com/CycWEC.html>>.
- [66] *The Salter Duck*. Accessed; June 29, 2023. <<https://technologystudent.com/energy1/tidal7.htm>>.

- [67] Markel Penalba and John V Ringwood. A review of wave-to-wire models for wave energy converters. *Energies*, 9(7):506, 2016.
- [68] Kristof Schlemmer, Franz Fuchshumer, Norbert Böhmer, Ronan Costello, and Carlos Villegas. Design and control of a hydraulic power take-off for an axi-symmetric heaving point absorber. In *Proc. Nineth Eur. Wave Tidal Energy Conf. Southampt.* EWTEC, 2011.
- [69] Markus Mueller, Ricardo Lopez, Alasdair McDonald, and Godwin Jimmy. Reliability analysis of wave energy converters. In *2016 IEEE Int. Conf. Renew. Energy Res. Appl.*, pages 667–672. IEEE, 2016.
- [70] Nicholas Jon Baker. *Linear generators for direct drive marine renewable energy converters*. PhD thesis, Durham University, 2003.
- [71] M A Mueller. Electrical generators for direct drive wave energy converters. *IEE Proceedings-generation, Transm. Distrib.*, 149(4):446–456, 2002.
- [72] Shohel Amin. Design and analysis of a bidirectional rack and pinion wave energy converter (WEC). Master's thesis, 2021.
- [73] NJ Baker, L Chambers, C Retzler, M Galbraith, and E Spooner. Developing a direct drive power take off for the mocean wave energy converter. In *11th International Conference on Power Electronics, Machines and Drives (PEMD 2022)*. IET, 2022.
- [74] Alla Weinstein, G Fredrikson, MJ Parks, and K Nielsen. Aquabuoy-the offshore wave energy converter numerical modeling and optimization. In *Oceans' 04 MTS/IEEE Techno-Ocean'04 (IEEE Cat. No. 04CH37600)*, volume 4, pages 1854–1859. IEEE, 2004.
- [75] Raju Ahamed, Kristoffer McKee, and Ian Howard. Advancements of wave energy converters based on power take off (PTO) systems: A review. *Ocean Eng.*, 204:107248, 2020.
- [76] Feng Wu, Xiao Ping Zhang, Ping Ju, and Michael J H Sterling. Optimal control for AWS-based wave energy conversion system. *IEEE Trans. Power Syst.*, 24(4):1747–1755, 2009.
- [77] Henk Polinder, Michiel E C Damen, and Fred Gardner. Linear PM generator system for wave energy conversion in the AWS. *IEEE Trans. Energy Convers.*, 19(3):583–589, 2004.
- [78] H Polinder, M E C Damen, and F Gardner. Design, modelling and test results of the AWS PM linear generator. *Eur. Trans. Electr. Power*, 15(3):245–256, 2005.
- [79] Feng Wu, Xiao-Ping Zhang, Ping Ju, and Michael J H Sterling. Modeling and control of AWS-based wave energy conversion system integrated into power grid. *IEEE Trans. Power Syst.*, 23(3):1196–1204, 2008.

- [80] Biswarup Das and Bikash C Pal. Voltage control performance of AWS connected for grid operation. *IEEE Trans. Energy Convers.*, 21(2):353–361, 2006.
- [81] Feng Wu, Ping Ju, Xiao-Ping Zhang, Chuan Qin, Guo-Jing Peng, Hua Huang, and Jing Fang. Modeling, control strategy, and power conditioning for direct-drive wave energy conversion to operate with power grid. *Proc. IEEE*, 101(4):925–941, 2013.
- [82] Mostafa I Marei, Mohamed Mokhtar, and Ahmed A El-Sattar. MPPT strategy based on speed control for AWS-based wave energy conversion system. *Renew. Energy*, 83:305–317, 2015.
- [83] Hany M Hasanien. Gravitational search algorithm-based optimal control of Archimedes wave swing-based wave energy conversion system supplying a DC microgrid under uncertain dynamics. *IET Renew. Power Gener.*, 11(6):763–770, 2016.
- [84] Li Wang, Jhih-Hsin Lin, Anton V Prokhorov, Hazlie Mokhlis, and Chua Kein Huat. Stability analysis of a hybrid wave-energy conversion system with linear permanent-magnet generator driven by Archimedes wave swing and induction generator driven by wells turbine. In *2018 IEEE Ind. Appl. Soc. Annu. Meet.*, pages 1–9. IEEE, 2018.
- [85] Hany M Hasanien. Transient stability augmentation of a wave energy conversion system using a water cycle algorithm-based multiobjective optimal control strategy. *IEEE Trans. Ind. Informatics*, 15(6):3411–3419, 2018.
- [86] Safdar Rasool, Md Rabiul Islam, Kashem M Muttaqi, and Danny Sutanto. An advanced control strategy for a smooth integration of linear generator based wave energy conversion system with distribution power grids. In *2019 IEEE Ind. Appl. Soc. Ann. Meeting*, pages 1–6. IEEE, 2019.
- [87] Safdar Rasool, Md Rabiul Islam, Kashem M Muttaqi, and Danny Sutanto. Coupled modeling and advanced control for smooth operation of a grid-connected linear electric generator based wave-to-wire system. *IEEE Trans. Ind. Appl.*, 56(5):5575–5584, 2020.
- [88] Safdar Rasool, Kashem M Muttaqi, and Danny Sutanto. Modelling of a wave-to-wire system for a wave farm and its response analysis against power quality and grid codes. *Renew. Energy*, 162:2041–2055, 2020.
- [89] Safdar Rasool, Kashem M Muttaqi, and Danny Sutanto. A multi-filter based dynamic power sharing control for a hybrid energy storage system integrated to a wave energy converter for output power smoothing. *IEEE Trans. Sustain. Energy*, 13(3):1693–1706, 2022.
- [90] Rania A. Turkey, Hany M. Hasanien, and Abdulaziz Alkuhayli. Dynamic stability improvement of aws-based wave energy systems using a multiobjective salp swarm algorithm-based optimal control scheme. *IEEE Syst. Journal*, 16(1):79–87, 2022.

- [91] Ahmed Mahdy, Hany M Hasanien, Walid Helmy Abdel Hameed, Rania A Turkey, Shady HE Abdel Aleem, and Essamudin Ali Ebrahim. Nonlinear modeling and real-time simulation of a grid-connected aws wave energy conversion system. *IEEE Trans. Sustain. Energy*, 13(3):1744–1755, 2022.
- [92] Ahmed Mahdy, Hany M Hasanien, Waleed Helmy, Rania A Turkey, and Shady HE Abdel Aleem. Transient stability improvement of wave energy conversion systems connected to power grid using anti-windup-coot optimization strategy. *Energy*, 245:123321, 2022.
- [93] Thibaut Kovaltchouk, Bernard Multon, Hamid Ben Ahmed, Judicael Aubry, François Rongère, and Alain Glumineau. Influence of control strategy on the global efficiency of a Direct Wave Energy Converter with electric Power Take-Off. In *2013 Eighth Int. Conf. Exhib. Ecol. Veh. Renew. Energies*, pages 1–10. IEEE, 2013.
- [94] Antonio de la Villa Jaén, Agustín García-Santana, and Others. Considering linear generator copper losses on model predictive control for a point absorber wave energy converter. *Energy Convers. Manag.*, 78:173–183, 2014.
- [95] Remya Krishna, Sasi K Kottayil, and Mats Leijon. Direct predictive current control of grid connected neutral point clamped inverter for wave power extraction. In *SPEEDAM 2010*, pages 175–179. IEEE, 2010.
- [96] F Martinez-Rodrigo, D Ramirez, H Mendonça, and S de Pablo. MMC as nonlinear vector current source for grid connection of wave energy generation. *Int. J. Electr. Power Energy Syst.*, 113:686–698, 2019.
- [97] Arvind Parwal, Martin Fregelius, Jennifer Leijon, Maria Chatzigiannakou, Olle Svensson, Irina Temiz, Cecilia Boström, Janaina G de Oliveira, and Mats Leijon. Experimental test of grid connected VSC to improve the power quality in a wave power system. In *2018 5th Int. Conf. Electr. Power Energy Convers. Syst.*, pages 1–7. IEEE, 2018.
- [98] Arvind Parwal, Martin Fregelius, Jennifer Leijon, Maria Chatzigiannakou, Olle Svensson, Erland Strömstedt, Irina Temiz, Janaina Goncalves de Oliveira, Cecilia Boström, and Mats Leijon. Grid integration and a power quality assessment of a wave-energy park. *IET Smart Grid*, 2(4):625–634, 2019.
- [99] Seyyedmahdi Jafarishiadeh, Mehdi Farasat, and Shahab Mehraeen. Grid-connected operation of direct-drive wave energy converter by using HVDC line and undersea storage system. In *2017 IEEE Energy Convers. Congr. Expo.*, pages 5565–5571. IEEE, 2017.
- [100] Maider Santos, Elisabetta Tedeschi, Pierpaolo Ricci, Marta Molinas, and Jose L Martin. Grid connection improvements by control strategy selection for wave energy converters. In *Int. Conf. Renew. Energy Power Qual. , Las Palmas Gran Canar. Spain. ICREPQ11*, 2011.



- [101] Elisabetta Tedeschi, Matteo Carraro, Marta Molinas, and Paolo Mattavelli. Effect of control strategies and power take-off efficiency on the power capture from sea waves. *IEEE Trans. Energy Convers.*, 26(4):1088–1098, 2011.
- [102] Elisabetta Tedeschi and Mainer Santos-Mugica. Modeling and control of a wave energy farm including energy storage for power quality enhancement: the BIMEP case study. *IEEE Trans. Power Syst.*, 29(3):1489–1497, 2013.
- [103] Gianluca Brando, Adolfo Dannier, Andrea Del Pizzo, Luigi Pio Di Noia, and Cosimo Pisani. Grid connection of wave energy converter in heaving mode operation by supercapacitor storage technology. *IET Renew. Power Gener.*, 10(1):88–97, 2016.
- [104] Ali S Haider, Ted KA Brekken, Ryan G Coe, Giorgio Bacelli, and Alan McCall. On real-time hybrid testing of ocean wave energy conversion systems: An experimental study. *IEEE Open J. Ind. Appl.*, 3:30–40, 2022.
- [105] Gimara Rajapakse, Shantha Jayasinghe, Alan Fleming, and Michael Negnevitsky. A model predictive control-based power converter system for oscillating water column wave energy converters. *Energies*, 10(10):1631, 2017.
- [106] Gimara Rajapakse, Shantha Jayasinghe, Alan Fleming, and Michael Negnevitsky. Grid integration and power smoothing of an oscillating water column wave energy converter. *Energies*, 11(7):1871, 2018.
- [107] Dónal B Murray, M G Egan, J G Hayes, and D L O’Sullivan. Applications of supercapacitor energy storage for a wave energy converter system. In *7th Eur. Wave Tidal Energy Conf. EWTEC*, 2009.
- [108] Mikel Alberdi, Modesto Amundarain, Aitor J Garrido, Izaskun Garrido, and Francisco Javier Sainz. Control of oscillating water column-based wave power generation plants for grid connection. In *2012 20th Mediterr. Conf. Control Autom.*, pages 1485–1490. IEEE, 2012.
- [109] Modesto Amundarain, Mikel Alberdi, Aitor Garrido, Izaskun Garrido, and Manuel de la Sen. Neural control for wave power plant during voltage dips. *Electr. Power Syst. Res.*, 92:96–105, 2012.
- [110] Mikel Alberdi, Modesto Amundarain, Aitor Garrido, and Izaskun Garrido. Neural control for voltage dips ride-through of oscillating water column-based wave energy converter equipped with doubly-fed induction generator. *Renew. Energy*, 48:16–26, 2012.
- [111] Ehsan Enferad, Daryoush Nazarpour, Sajjad Golshannavaz, and Farrokh Aminifar. Direct drive surge wave energy converter with grid integration functionality. *Int. Trans. Electr. Energy Syst.*, 26(5):1066–1084, 2016.
- [112] Kai Rothenhagen, Marek Jasinski, and Marian P Kazmierkowski. Grid connection of multi-megawatt clean wave energy power plant under weak grid condition. In *2008 13th Int. Power Electronics and Motion Control Conf.*, pages 1904–1910. IEEE, 2008.

- [113] Jonathan Robinson and Geza Joos. VSC HVDC transmission and offshore grid design for a linear generator based wave farm. In *2009 Can. Conf. Electr. Comput. Eng.*, pages 54–58. IEEE, 2009.
- [114] J K H Shek, D E Macpherson, and M A Mueller. Experimental verification of linear generator control for direct drive wave energy conversion. *IET Renew. Power Gener.*, 4(5):395–403, 2010.
- [115] Haojie Luan, Omer C Onar, and Alireza Khaligh. Dynamic modeling and optimum load control of a PM linear generator for ocean wave energy harvesting application. In *Twenty-Fourth Annu. IEEE Appl. Power Electron. Conf. Expo.*, pages 739–743. IEEE, 2009.
- [116] H Lendenmann, K C Strømsem, M Dai Pre, W Arshad, A Leirbukt, G Tjensvoll, and T Gulli. Direct generation wave energy converters for optimized electrical power production. In *Proc. 7th Eur. Wave Tidal Energy Conf. EWTEC*, 2007.
- [117] Ramon Zamora and Anurag K Srivastava. Controls for microgrids with storage: Review, challenges, and research needs. *Renew. Sustain. Energy Rev.*, 14(7):2009–2018, 2010.
- [118] Zhiwen Wang, Rupp Carriveau, David S-K Ting, Wei Xiong, and Zuwen Wang. A review of marine renewable energy storage. *Int. J. Energy Res.*, 43(12):6108–6150, 2019.
- [119] Annette Evans, Vladimir Strezov, and Tim J Evans. Assessment of utility energy storage options for increased renewable energy penetration. *Renew. Sustain. Energy Rev.*, 16(6):4141–4147, 2012.
- [120] Abdulwahab Alhamali, Mohamed Emad Farrag, Geraint Bevan, and Donald M Hepburn. Review of energy storage systems in electric grid and their potential in distribution networks. In *2016 Eighteenth Int. Middle East Power Syst. Conf.*, pages 546–551. IEEE, 2016.
- [121] P Medina, Abebe W Bizuayehu, João P S Catalão, Eduardo M G Rodrigues, and Javier Contreras. Electrical energy storage systems: technologies’ state-of-the-art, techno-economic benefits and applications analysis. In *2014 47th Hawaii Int. Conf. Syst. Sci.*, pages 2295–2304. IEEE, 2014.
- [122] D O Akinyele and R K Rayudu. Review of energy storage technologies for sustainable power networks. *Sustain. Energy Technol. Assessments*, 8:74–91, 2014.
- [123] Sergio Vazquez, Srdjan M Lukic, Eduardo Galvan, Leopoldo G Franquelo, and Juan M Carrasco. Energy storage systems for transport and grid applications. *IEEE Trans. Ind. Electron.*, 57(12):3881–3895, 2010.
- [124] Arvind Parwal. Virtual Synchronous Generator Based Current Synchronous Detection Scheme for a Virtual Inertia Emulation in SmartGrids. *Energy Power Eng.*, 11(3):99–131, 2019.

- [125] Apoorv Agarwal, Vishnu Mahadeva Iyer, Anup Anurag, and Subhashish Bhattacharya. Adaptive Control of a Hybrid Energy Storage System for Wave Energy Conversion Application. In *2019 IEEE Energy Convers. Congr. Expo.*, pages 4994–5001. IEEE, 2019.
- [126] Fergus Sharkey, Joe MacEnri, Elva Bannon, Michael Conlon, and Kevin Gaughan. Resource-induced voltage flicker for wave energy converters—assessment tools. *IET Renew. Power Gener.*, 7(6):623–630, 2013.
- [127] Samir Hazra and Subhashish Bhattacharya. Control of squirrel cage induction generator in an oscillating point absorber based wave energy conversion system. In *2014 IEEE Appl. Power Electron. Conf. Expo. 2014*, pages 3174–3180. IEEE, 2014.
- [128] Antonio de la Villa Jaén, Agustín García-Santana, and Dan El Montoya-Andrade. Maximizing output power of linear generators for wave energy conversion. *Int. Trans. Electr. Energy Syst.*, 24(6):875–890, 2014.
- [129] Ean A Amon, Ted K A Brekken, and Alphonse A Schacher. Maximum power point tracking for ocean wave energy conversion. *IEEE Trans. Ind. Appl.*, 48(3):1079–1086, 2012.
- [130] Rico Hjerm Hansen, Torben O Andersen, and Henrik C Pedersen. Model based design of efficient power take-off systems for wave energy converters. In *Proc. 12th Scand. Int. Conf. Fluid Power, Tampere, Finl.*, pages 18–20, 2011.
- [131] Hugo Mendonca and Sergio Martinez. A resistance emulation approach to optimize the wave energy harvesting for a direct drive point absorber. *IEEE Trans. Sustain. Energy*, 7(1):3–11, 2015.
- [132] Adrian C M O Sullivan and Gordon Lightbody. Predictive control of a wave to wire energy conversion system—The importance of field weakening. In *2016 UKACC 11th Int. Conf. Control*, pages 1–6. IEEE, 2016.
- [133] Ligu Wang, Jan Isberg, and Elisabetta Tedeschi. Review of control strategies for wave energy conversion systems and their validation: the wave-to-wire approach. *Renew. Sustain. Energy Rev.*, 81:366–379, 2018.
- [134] Josef Schachner. Power connections for offshore wind farms, 2004.
- [135] Iraide López, Jon Andreu, Salvador Ceballos, Iñigo Martínez de Alegría, and Iñigo Kortabarria. Review of wave energy technologies and the necessary power-equipment. *Renew. Sustain. Energy Rev.*, 27:413–434, 2013.
- [136] Marina Tsili and S Papathanassiou. A review of grid code technical requirements for wind farms. *IET Renew. Power Gener.*, 3(3):308–332, 2009.
- [137] The Grid Code. Technical report, National Transmission and Dispatch Company, Lahore, Pakistan, 2005.

- [138] IEEE Standards Association and Others. 1159-2009. IEEE Recommended Practice for Monitoring Electric Power Quality Industrial and Commercial Applications, 2009.
- [139] IEEE. IEEE Approved Draft Recommended Practice for Monitoring Electric Power Quality. *IEEE P1159/D7*, April 2019, pages 1–104, jun.
- [140] Anne Blavette, Dara L O'Sullivan, Ray Alcorn, Michael G Egan, and Tony W Lewis. Simplified estimation of the flicker level induced by wave energy farms. *IEEE Trans. Sustain. Energy*, 7(3):1216–1223, 2016.
- [141] Henk Polinder and Mattia Scuotto. Wave energy converters and their impact on power systems. In *2005 Int. Conf. Futur. Power Syst.* IEEE, 2005.
- [142] Anne Blavette, Dara L O'Sullivan, Antony W Lewis, and Michael G Egan. Impact of a wave farm on its local grid: Voltage limits, flicker level and power fluctuations. In *2012 Ocean.*, pages 1–9. IEEE, 2012.
- [143] I M Dudurych, M Holly, and M Power. Integration of wind power generation in the Irish grid. In *2006 IEEE Power Eng. Soc. Gen. Meet.*, pages 8–pp. IEEE, 2006.
- [144] Istvan Erlich, Wilhelm Winter, and Andreas Dittrich. Advanced grid requirements for the integration of wind turbines into the German transmission system. In *2006 IEEE Power Eng. Soc. Gen. Meet.*, pages 7–pp. IEEE, 2006.
- [145] A Morales, X Robe, M Sala, P Prats, C Aguerri, and E Torres. Advanced grid requirements for the integration of wind farms into the Spanish transmission system. *IET Renew. Power Gener.*, 2(1):47–59, 2008.
- [146] Christian Windt, Nicolás Faedo, Markel Penalba, Frederic Dias, and John V Ringwood. Reactive control of wave energy devices—the modelling paradox. *Appl. Ocean Res.*, 109:102574, 2021.
- [147] Giuseppe Giorgi and John V Ringwood. Comparing nonlinear hydrodynamic forces in heaving point absorbers and oscillating wave surge converters. *Journal of Ocean Engineering and Marine Energy*, 4:25–35, 2018.
- [148] W Cummins. The impulse response function and ship motions. DTIC Document. In *Proceeding Symp. Sh. Theory Inst. für Schiffbau der Univ. Hambg.*, pages 25–27, 1962.
- [149] Lothar Birk. *Fundamentals of ship hydrodynamics: Fluid mechanics, ship resistance and propulsion*. John Wiley & Sons, 2019.
- [150] Ochi MK. *Ocean Waves: The Stochastic Approach*, volume 6. Cambridge University Press, 2005.
- [151] John V Ringwood, Giorgio Bacelli, and Francesco Fusco. Energy-maximizing control of wave-energy converters: The development of control system technology to optimize their operation. *IEEE Control Syst. Mag.*, 34(5):30–55, 2014.

- [152] Klaus F Hasselmann, Tim P Barnett, E Bouws, H Carlson, David E Cartwright, K Eake, J A Euring, A Gicnapp, D E Hasselmann, P Kruseman, and Others. Measurements of wind-wave growth and swell decay during the Joint North Sea Wave Project (JONSWAP). *Ergaenzungsh. zur Dtsch. Hydrogr. Zeitschrift, R. A.*, 1973.
- [153] Charles L Bretschneider. *Wave variability and wave spectra for wind-generated gravity waves*. Number 118. The Board, 1959.
- [154] Willard J Pierson Jr and Lionel Moskowitz. A proposed spectral form for fully developed wind seas based on the similarity theory of sa kitaigorodskii. *J. Geophys. Res.*, 69(24):5181–5190, 1964.
- [155] Alexis Mérigaud and John V Ringwood. Free-surface time-series generation for wave energy applications. *IEEE J. Oceanic Eng.*, 43(1):19–35, 2017.
- [156] Odd Faltinsen. *Sea loads on ships and offshore structures*, volume 1. Cambridge University Press, 1993.
- [157] Christian Windt, Josh Davidson, and John V Ringwood. High-fidelity numerical modelling of ocean wave energy systems: A review of computational fluid dynamics-based numerical wave tanks. *Renew. Sustain. Energy Rev.*, 93:610–630, 2018.
- [158] M Alves. Frequency-domain models. In *Numerical Modelling of Wave Energy Converters*, pages 11–30. Elsevier, 2016.
- [159] Marc Bonnet. Boundary Integral Equation Methods for Solids and Fluids. *Meccanica*, 34(4):301–302, October 1999.
- [160] Giuseppe Giorgi. *Nonlinear hydrodynamic modelling of wave energy converters under controlled conditions*. PhD thesis, National University of Ireland, Maynooth (Ireland), 2018.
- [161] LHEEA, NEMOH-Presentation. Laboratoire de Recherche en Hydrodynamique Énergétique et Environnement Atmosphérique. <https://goo.gl/yX8nFu>, 2017. [Online accessed 1-Aug-2022].
- [162] Umesh A Korde and John Ringwood. *Hydrodynamic control of wave energy devices*. Cambridge University Press, 2016.
- [163] T Francis Ogilvie. Recent progress toward the understanding and prediction of ship motions. In *5th Symp. on Naval Hydr.*, volume 1, pages 2–5. Bergen, 1964.
- [164] Nicolás Faedo, Yeraí Peña-Sánchez, and John V Ringwood. Finite-order hydrodynamic model determination for wave energy applications using moment-matching. *Ocean Eng.*, 163:251–263, 2018.
- [165] István Kollár, Rik Pintelon, and Johan Schoukens. Frequency domain system identification toolbox for matlab. *IFAC Proceedings Volumes*, 24(3):1243–1247, 1991.

- [166] Michael Lawson, Yi-Hsiang Yu, Kelley Ruehl, Carlos Michelen, et al. Development and demonstration of the wec-sim wave energy converter simulation tool. In *2nd Marine Energy Technology Symposium, METS, Seattle, WA, USA*, page pages 1–8, 2014.
- [167] Yerai Peña-Sanchez, Nicolás Faedo, Markel Penalba, Giuseppe Giorgi, Alexis Mérigaud, Christian Windt, Demián García Violini, Liguó Wang, and John V Ringwood. Finite-Order hydrodynamic Approximation by Moment-Matching (FOAMM) toolbox for wave energy applications. In *13th Eur. Wave Tidal Energy Conf. EWTEC, Naples, Italy*, pages 1448–1:1448–9, 2019.
- [168] Gaspard Riche de Prony. Essai experimental et analytique: sur les lois de la dilatabilité des fluides elastique et sur celles de la force expansive de la vapeur de l'eau et de la vapeur de l'alkool, a differentes temperatures. *Journal Polytechnique ou Bulletin du Travail fait a l'Ecole Centrale des Travaux Publics*, 1795.
- [169] Robert H Park. Two-reaction theory of synchronous machines generalized method of analysis-part i. *Trans. Am. Inst. Electr. Eng.*, 48(3):716–727, 1929.
- [170] Ned Mohan. *Advanced electric drives: analysis, control, and modeling using MATLAB/Simulink*. John Wiley & Sons, 2014.
- [171] Remya Krishna, Olle Svensson, Magnus Rahm, Sasi K Kottayil, Rafeal Waters, and Mats Leijon. Analysis of linear wave power generator model with real sea experimental results. *IET Renew. Power Gener.*, 7(5):574–581, 2013.
- [172] Abdelmounime El Magri, Fouad Giri, Gildas Besancon, Abderrahim El Fadili, Luc Dugard, and Fatima Zara Chaoui. Sensorless adaptive output feedback control of wind energy systems with PMS generators. *Control Eng. Pract.*, 21(4):530–543, 2013.
- [173] Zhuxian Xu, Di Zhang, Fei Wang, and Dushan Boroyevich. A unified control for the combined permanent magnet generator and active rectifier system. *IEEE Trans. Power Electron.*, 29(10):5644–5656, 2014.
- [174] Robert W Erickson and Dragan Maksimovic. *Fundamentals of power electronics*. Springer Science & Business Media, 2007.
- [175] Mudasser Hassan, Zahir Javed Paracha, Hammad Armghan, Naghmash Ali, Hafiz Ahsan Said, Umar Farooq, Ammar Afzal, and Muhammad Arshad Shehzad Hassan. Lyapunov based adaptive controller for power converters used in hybrid energy storage systems. *Sustain . Energy Technol. Assess.*, 42:100853, 2020.
- [176] H.Y. Kanaan and K. Al-Haddad. A comparison between three modeling approaches for computer implementation of high-fixed-switching-frequency power converters operating in a continuous mode. In *IEEE CCECE2002. Canadian Conference on Electrical and Computer Engineering. Conference Proceedings (Cat. No.02CH37373)*, volume 1, pages 274–279 vol.1, 2002.

- [177] Seth R Sanders, J Mark Noworolski, Xiaojun Z Liu, and George C Verghese. Generalized averaging method for power conversion circuits. *IEEE Trans. Power Electron.*, 6(2):251–259, 1991.
- [178] Pawel Szczesniak. A Comparison Between Two Average Modelling Techniques of AC-AC Power Converters. *Int. J. Power Electron. Drive Syst.*, 6(1):32, 2015.
- [179] Thomas L Floyd and Elizabeth Pownell. *Principles of electric circuits*. Prentice Hall Upper Saddle River, NJ, USA:, 1997.
- [180] Johannes Falnes and Adi Kurniawan. *Ocean waves and oscillating systems: linear interactions including wave-energy extraction*, volume 8. Cambridge University Press, 2020.
- [181] Francesco Fusco and John V. Ringwood. A simple and effective real-time controller for wave energy converters. *IEEE Trans. Sust. Energ.*, 4(1):21–30, 2013.
- [182] Demián García-Violini, Nicolás Faedo, Fernando Jaramillo-Lopez, and John V Ringwood. Simple controllers for wave energy devices compared. *J. Mar. Sci. Eng.*, 8(10):793, 2020.
- [183] Nicolás Faedo, Sébastien Olaya, and John V Ringwood. Optimal control, MPC and MPC-like algorithms for wave energy systems: An overview. *IFAC J. Syst. Control*, 1:37–56, 2017.
- [184] Demián García-Violini, Yeraí Peña-Sanchez, Nicolás Faedo, and John V Ringwood. An energy-maximising linear time invariant controller (LiTe-Con) for wave energy devices. *IEEE Trans. Sustain. Energy*, 11(4):2713–2721, 2020.
- [185] Demián García-Violini, Yeraí Peña-Sanchez, Nicolás Faedo, Christian Windt, Francesco Ferri, and John V Ringwood. Experimental Implementation and Validation of a Broadband LTI Energy-Maximizing Control Strategy for the Wavestar Device. *IEEE Trans. Control Syst. Technol.*, 2021.
- [186] Nicolás Faedo, Demián García-Violini, Yeraí Peña-Sanchez, and John V Ringwood. Optimisation-vs. non-optimisation-based energy-maximising control for wave energy converters: A case study. In *2020 Eur. Control Conf.*, pages 843–848. IEEE, 2020.
- [187] Peter Van Overschee and Bart De Moor. *Subspace Identification for Linear Systems - Theory Implication Applications*. Springer, 1996.
- [188] Lennart Ljung. *System Identification - Theory for the User*. Prentice Hall, 1999.
- [189] Demián García-Violini, Yeraí Peña-Sanchez, Nicolás Faedo, Francesco Ferri, and John V Ringwood. A broadband time-varying energy maximising control for wave energy systems (LiTe-Con+): Framework and experimental assessment. *IEEE Trans. Sustain. Energy*, 2023.

- [190] Mahmoud Kabalan, Pritpal Singh, and Dagmar Niebur. Large signal Lyapunov-based stability studies in microgrids: A review. *IEEE Trans. Smart Grid*, 8(5):2287–2295, 2016.
- [191] Warren E Dixon, Aman Behal, Darren M Dawson, and Siddharth P Nagarkatti. *Nonlinear control of engineering systems: a Lyapunov-based approach*. Springer Science & Business Media, 2013.
- [192] Seth Robert Sanders and George C Verghese. Lyapunov-based control for switched power converters. *IEEE Trans. Power Electron.*, 7(1):17–24, 1992.
- [193] Addy Wahyudie, Omsalama Saeed, Mohammed Jama, Hassan Noura, and Khalifa Harib. Maximising power conversion for heaving point absorbers using a reference-based control technique. *IET Renew. power Gener.*, 11(3):271–280, 2017.
- [194] Mohammed Jama, Bisni Fahad Mon, Addy Wahyudie, and Saad Mekhilef. Maximum Energy Capturing Approach for Heaving Wave Energy Converters Using an Estimator-Based Finite Control Set Model Predictive Control. *IEEE Access*, 9:67648–67659, 2021.
- [195] Francesco Paparella and John V Ringwood. Optimal control of a three-body hinge-barge wave energy device using pseudospectral methods. *IEEE Trans. Sustain. Energy*, 8(1):200–207, 2016.
- [196] Dan Montoya, Elisabetta Tedeschi, Luca Castellini, and Tiago Martins. Passive Model Predictive Control on a Two-Body Self-Referenced Point Absorber Wave Energy Converter. *Energies*, 14(6):1731, 2021.
- [197] Jitendra K Jain, Oliver Mason, Hafiz A Said, and John V Ringwood. Limiting reactive power flow peaks in wave energy systems. *IFAC-PapersOnLine*, 55(31):427–432, 2022.
- [198] Saeed Golestan, Josep M Guerrero, and Juan C Vasquez. Three-phase PLLs: A review of recent advances. *IEEE Trans. Power Electron.*, 32(3):1894–1907, 2016.
- [199] WC Duesterhoeft, Max W Schulz, and Edith Clarke. Determination of instantaneous currents and voltages by means of alpha, beta, and zero components. *Transactions of the American Institute of Electrical Engineers*, 70(2):1248–1255, 1951.
- [200] E Maximiliano Asensio, Guillermo A Magallán, Cristian H De Angelo, and Federico M Serra. Energy management on battery/ultracapacitor hybrid energy storage system based on adjustable bandwidth filter and sliding-mode control. *J. Energy Stor.*, 30:101569, 2020.
- [201] John V Ringwood, Siyuan Zhan, and Nicolás Faedo. Empowering wave energy with control technology: Possibilities and pitfalls. *Annu. Rev. Control*, 2023.
- [202] Nataliia Y Sergiienko, Mathieu Cocho, Benjamin S Cazzolato, and Alexandre Pichard. Effect of a model predictive control on the design of a power take-off system for wave energy converters. *Appl. Ocean Res.*, 115:102836, 2021.



- [203] Nicolás Faedo, Fabio Carapellese, Edoardo Pasta, and Giuliana Mattiazzo. On the principle of impedance-matching for underactuated wave energy harvesting systems. *Appl. Ocean Res.*, 118:102958, 2022.
- [204] N Faedo, G Giorgi, JV Ringwood, and G Mattiazzo. Optimal control of wave energy systems considering nonlinear froude–krylov effects: control-oriented modelling and moment-based control. *Nonlinear Dynam.*, pages 1–28, 2022.
- [205] Roger A Horn and Charles R Johnson. *Matrix analysis*. Cambridge University Press, 2012.
- [206] John V Ringwood, Alexis Mérigaud, Nicolás Faedo, and Francesco Fusco. An analytical and numerical sensitivity and robustness analysis of wave energy control systems. *IEEE Trans. Control Syst. Technol.*, 28(4):1337–1348, 2019.
- [207] Demián Garcia-Violini and John V Ringwood. Energy maximising robust control for spectral and pseudospectral methods with application to wave energy systems. *Int. J. Control*, 94(4):1102–1113, 2021.
- [208] Edoardo Pasta, Fabio Carapellese, Paolo Brandimarte, Luca Parrinello, and Giuliana Mattiazzo. A model-free control strategy based on artificial neural networks for PeWEC. In *14th European Wave and Tidal Energy Conference (EWTEC), Plymouth, UK*, 2021.
- [209] E Pasta, G Papini, N Faedo, G Mattiazzo, and JV Ringwood. On optimization-based strategies in data-driven control of wave energy systems. In *Trends in Renewable Energies Offshore: Proceedings of the 5th International Conference on Renewable Energies Offshore (RENEW 2022)*, page 401. CRC Press, 2022.
- [210] Nicolás Faedo, Giuseppe Giorgi, John V Ringwood, and Giuliana Mattiazzo. Nonlinear moment-based optimal control of wave energy converters with non-ideal power take-off systems. In *ASME Intl. Conf. on Offshore Mechanics and Arctic Eng.*, volume 85932, page V008T09A082, 2022.
- [211] Romain Genest, Félicien Bonnefoy, Alain H Clément, and Aurélien Babarit. Effect of non-ideal power take-off on the energy absorption of a reactively controlled one degree of freedom wave energy converter. *Appl. Ocean Res.*, 48:236–243, 2014.
- [212] Giorgio Bacelli, Romain Genest, and John V Ringwood. Nonlinear control of flap-type wave energy converter with a non-ideal power take-off system. *Annu. Rev. Control*, 40:116–126, 2015.
- [213] Nataliia Y Sergiienko, Giorgio Bacelli, Ryan G Coe, and Benjamin S Cazzolato. A comparison of efficiency-aware model-predictive control approaches for wave energy devices. *J. of Ocean Eng. and Mar. Energ.*, pages 1–13, 2021.
- [214] Nahidul Hoque Samrat, Norhafizan Bin Ahmad, Imtiaz Ahmed Choudhury, and Zahari Bin Taha. Modeling, control, and simulation of battery storage photovoltaic-wave energy hybrid renewable power generation systems for island electrification in Malaysia. *Sci. World J.*, 2014, 2014.

- [215] Markel Penalba and John V Ringwood. A high-fidelity wave-to-wire model for wave energy converters. *Renew. Energy*, 134:367–378, 2019.
- [216] J Tissandier, A Babarit, and AH Clément. Study of the smoothing effect on the power production in an array of SEAREV wave energy converters. In *The Eighteenth International Offshore and Polar Engineering Conference*. OnePetro, 2008.
- [217] M Molinas, O Skjervheim, B Sørby, P Andreasen, S Lundberg, and T Undeland. Power smoothing by aggregation of wave energy converters for minimizing electrical energy storage requirements. In *Proceedings of the 7th European Wave and tidal energy conference*, pages 3–8, 2007.